

DISS. ETH NO. 26856

**Development of Image Processing Tools for the Simultaneous
Analysis of Brain and Spinal Cord Multi-Parametric Maps:
implication for Spinal Cord Injury**

A thesis submitted to attain the degree of

DOCTOR OF SCIENCES of ETH ZURICH

(Dr. sc. ETH Zurich)

presented by

Michela Azzarito

M.Sc. in Biomedical Engineering, Turin Polytechnic

born on 30.11.1987

citizen of Italy

accepted on the recommendation of

Prof. Dr. Nicole Wenderoth (examiner)

Prof. Dr. Patrick Freund (co-examiner)

2020

Abstract

Magnetic resonance imaging (MRI) allows to non-invasively characterize brain and spinal cord tissue, in-vivo. This has proven to be a powerful mean to improve diagnostics.

Quantitative MRI (qMRI) is an emerging field in MRI which can provide information, not only on the macrostructural aspects of the central nervous systems, as does conventional MRI, but also provides insights into the underlying microstructure. Specifically, quantitative multi-parameter mapping (MPM) provides several maps which are sensitive to myelin, iron and water content.

The application of qMRI in the brain has provided crucial insights into how, for example, myelin content is distributed across cortical layers in the visual cortex. However, the application of qMRI techniques in the spinal cord lags behind the brain due to the inherent small size of the cord, low signal-to-noise ratio and the particularly challenging imaging environment characterized by cardiac and respiratory pulsation, proximity of bones, air, cartilage, and fat around the spinal cord. Together, these factors have greatly impacted the quality of spinal cord qMRI and limited its clinical application. Recent technical advances such as specialized acquisition sequences, complex shimming, custom receive coils and substantial post-processing for artefacts correction (i.e. motion, aliasing and others) have made this approach more applicable to the spinal cord.

Despite these advances in imaging sequences, few postprocessing tools are available for the analysis of spinal cord qMRI. Common brain software's are unfortunately not optimized for spinal cord image processing. For example, the deformation of the spinal cord does not allow the application of standard motion-correction algorithms based on rigid or affine transformation, as well as segmentation and registration/normalization tools. In addition, common brain MRI templates and atlases do not include the spinal cord and therefore cannot be used for spinal cord analysis.

The aim of this thesis is to promote the clinical adoption of spinal cord qMRI. Specifically, based on brain approaches, new tools for the simultaneous analysis of brain and spinal cord are optimized and applied to investigate microstructural changes after a spinal cord injury (SCI) across the brain and spinal cord, simultaneously. The developed tools are also used to detect the microstructural signature of neuropathic pain in SCI-patients. Additionally, longitudinal pre-processing pipelines were optimized and used to investigate training-induced neuroplasticity in healthy subjects. The methodological and clinical advances from this work have resulted in four studies.

In the first study, a processing tool for the simultaneous analysis of brain and cervical spinal cord was implemented in the statistical parametric mapping (SPM) framework. This open source tool allows the investigation of macro- and microstructural changes using voxel-based morphometry (VBM) and voxel-based quantification (VBQ) pipelines, respectively. In order to extend available brain VBM/VBQ pipelines, a new template covering brain and cervical spinal cord was generated using a generative semi-supervised modelling approach. The template was incorporated in the pre-processing pipeline of VBM/VBQ analysis in SPM and was validated on T1-weighted MRI and multi-parameter mapping (MPM) maps, by assessing trauma-induced changes in SCI patients and comparing the findings with the existing outcome from analytical tools assessing the brain and cord, separately. Validation based on a SCI cohort demonstrated that the new processing approach based on the brain and spinal cord is as sensitive as available processing tools in detecting changes in SCI-patients offering the advantage of performing the analysis and statistics simultaneously, in the brain and spinal cord.

In the second study, the developed tool for the simultaneous analysis of brain and cervical spinal cord was used to assess the microstructural changes associated with neuropathic-pain (NP) in SCI-patients. In this study, myelin- and iron-sensitive changes along the ascending and descending nociceptive pathways are identified in those patients who suffer from NP when compared to pain-free patients. Crucially, myelin- and iron changes were associated with NP intensity suggesting specific maladaptive plastic processes in the ascending and descending nociceptive pathways. Therefore, tracking microstructural plasticity might facilitate the understanding and monitoring of the complex pathophysiology of NP.

In the third study, a longitudinal processing pipeline was optimized for qMRI of the brain and cervical cord and used to assess training induced changes in healthy subjects and SCI-patients. In this thesis we only report findings from healthy controls. This study was motivated by the fact that even if motor training induces neuroplastic changes in the brain, still little is known about the underlying microstructural changes and their dynamics. In this study, training-induced neuroplasticity was investigated in terms of myelin and volume changes. During the acquisition of a motor skill task, transient changes within the motor cortex and its descending projections and in the hippocampus were shown. Performance improvements related to the transient myelin-sensitive changes across the hippocampus suggesting experience-dependent microstructural changes. Interestingly training lower limbs led to greater changes in the myelin-sensitive MT in the posterior part of the internal capsula when compared to upper limb trained participants, suggesting a somatotopy of learning. This study

showed that MPM maps can be used not only as a biomarker of neurodegeneration but also for neuroplasticity.

In the fourth and last study, MPM maps in the cervical cord of chronic SCI patients were used to quantify a gradient of neurodegenerative changes along the cervical cord by taking advantage of available routines which were optimized for the assessment of MPM from the spinal cord toolbox (SCT). In this study a gradient of neurodegeneration was evident after traumatic SCI; its magnitude is reduced with increasing distance from the lesion level. In addition, the degeneration was more pronounced in the ascending as compared to the descending spinal pathways. The associations with clinical measurements suggest that remote secondary neurodegenerative changes are clinically eloquent and that monitoring the neurodegenerative gradient could track treatment effects of regenerative and neuroprotective agents.

In conclusion, several methodological developments and improvements have been addressed in this thesis to facilitate the use of qMRI for spinal cord imaging in health and disease. Specifically, the development of tools for the simultaneous analysis of brain and cervical spinal cord can be used to assess trauma-induced changes, as well as the underlying pathophysiological changes related to neuropathic pain, in SCI-patients; and provide valuable biomarkers that might facilitate patient monitoring, and track treatment effects of regenerative and neuroprotective agents. The optimization of longitudinal processing pipelines for MPM maps provides for the first-time evidence of subtle and transient microstructural changes across a motor-hippocampus loop. Such approach could therefore be used to track the efficacy of rehabilitation.

Sommario

Le immagini di risonanza magnetica (MRI) permettono di investigare in modo non-invasivo il cervello e la colonna spinale; e questo ha offerto un potente mezzo di diagnostica.

Le MRI quantitative (qMRI), fanno parte di un emergente campo di ricerca e forniscono non solo informazioni sulla macrostruttura del sistema nervoso, come le MRI convenzionali, ma anche informazioni sulle sottostanti microstrutture. In particolare, le mappe quantitative multiparametriche (MPM) offrono delle immagini che sono sensibili al contenuto di mielina, ferro e acqua.

L'applicazione di qMRI nel cervello ha fornito informazioni cruciali sul come, per esempio il contenuto di mielina è distribuito lungo la corteccia cerebrale visiva. Tuttavia l'applicazione delle tecniche di qMRI nella colonna vertebrale sono piuttosto primitive rispetto al cervello, questo è dovuto alla piccola dimensione della colonna vertebrale, al basso rapporto segnale-rumore, e all'ambiente particolarmente ostile caratterizzato dalla pulsazione cardiaca e respiratoria, la prossimità delle strutture ossee, aria, cartilagine e tessuto adiposo che circonda la colonna spinale. Tutti questi fattori hanno influenzato la qualità delle qMRI nella colonna spinale e ne hanno limitato l'applicazione clinica. Recenti sviluppi tecnici sulle sequenze di acquisizione, complessi metodi di correzione del bias (shimming), lo sviluppo di bobine di ricezione e metodi per la correzione di artefatti (i.e. movimento, aliasing e altro) hanno reso questo approccio maggiormente applicabile alla colonna spinale.

Nonostante tutti questi miglioramenti nell'acquisizione delle immagini, esistono pochi software per il processamento delle immagini della colonna spinale. Inoltre, i comuni software per l'analisi delle immagini del cervello non sono applicabili alla colonna vertebrale per una serie di motivi. Ad esempio, la grande flessibilità della colonna vertebrale, non ammette l'applicazione dei comuni metodi di correzione del movimento usati nel cervello, perché basati su deformazioni rigide o affini; così come anche i metodi di segmentazione e normalizzazione. Inoltre, i comuni template ed atlanti dedicati al cervello, non includono la colonna spinale e pertanto non possono essere usati per l'analisi della stessa.

L'obiettivo di questa tesi, è di promuovere l'uso delle qMRI per la colonna vertebrale. In particolare nuovi metodi, basati sugli approcci già usati per l'analisi cervello, sono stati ottimizzati per l'analisi simultanea del cervello e della colonna vertebrale cervicale; e utilizzati per investigare i cambiamenti microstrutturali del cervello e colonna spinale simultaneamente.

I metodi sviluppati sono stati anche usati per investigare i meccanismi microstrutturali del dolore neuropatico in pazienti con lesioni al midollo spinale. Inoltre, i metodi per il processamento delle immagini longitudinali sono stati ottimizzati e usati per investigare la neuroplasticità indotta dall'esercizio fisico in soggetti sani. Gli sviluppi tecnologici e clinici di questa tesi hanno fornito supporto per quattro studi.

Nel primo studio, lo sviluppo di un nuovo software per la simultanea analysis del cervello e colonna vertebrale è stato implementato in SPM. Questo software di libero accesso (open source), ha permesso l'investigazione di cambiamenti macro- e micro-strutturali utilizzando i celebri metodi denominati voxel-based morphometry (VBM) e voxel-based quantification (VBQ). Per poter estendere l'analisi del cervello includendo anche la colonna vertebrale, una nuova template che include anche la colonna vertebrale è stata realizzata usando modelli generative semi-supervisionati. La nuova template è stata incorporata nei metodi di processamento VBM/VBQ in SPM. Tali metodi sono stati validati usando T1-weighted e le mappe multi parametriche (MPM), investigando i cambiamenti indotti dalla lesione alla colonna vertebrale e confrontandone i risultati con quelli che analizzano il cervello e la colonna vertebrale separatamente. La validazione basata su soggetti con lesione alla colonna vertebrale ha dimostrato che il nuovo metodo di processamento delle immagini è capace di fornire gli stessi risultati offerti dai software disponibili; offrendo il vantaggio di effettuare l'analisi e la statistica del cervello e colonna vertebrale nello stesso ambiente e simultaneamente.

Nel secondo studio, il software sviluppato per la simultanea analisi del cervello e colonna vertebrale, è stato ulteriormente usato per investigare i cambiamenti strutturali associati al dolore neuropatico dopo una lesione alla colonna vertebrale. In questo studio, confrontando soggetti affetti da dolore neuropatico con quelli non affetti, sono stati identificati cambiamenti strutturali relativi alla mielina e alla concentrazione del ferro, lungo le vie nocicettive ascendenti e discendenti. I cambiamenti strutturali relativi a mielina e alla concentrazione di ferro sono associati all'intensità del dolore neuropatico suggerendo la presenza di un meccanismo di plasticità maladattativa nelle vie nocicettive ascendenti e discendenti. Perciò l'analisi dei cambiamenti microstrutturali potrebbe facilitare la comprensione e il monitoraggio del complesso fenomeno del dolore neuropatico.

Nel terzo studio, un nuovo metodo per l'analisi di immagini longitudinali del cervello e della colonna vertebrale, è stato ottimizzato per qMRI; ed usato per l'investigazione dei cambiamenti plastici dovuti all'esercizio fisico/motorio in soggetti sani e quelli con una lesione alla colonna vertebrale. Nel contesto di questa tesi, vengono riportati solo i risultati dei soggetti sani. Questo studio è stato motivato dal

fatto che, anche se l'esercizio motorio induce cambiamenti plastici nel cervello, in realtà i meccanismi microstrutturali e le dinamiche coinvolte sono ancora sconosciuti. In questo studio la plasticità cerebrale indotta dall'esercizio fisico è stata investigata in termini di cambiamenti volumetrici e di mielina. Mentre si migliora nell'esercizio fisico, vari cambiamenti temporanei sono stati individuati nella corteccia motoria, nelle sue proiezioni discendenti e nell'ippocampo. I miglioramenti delle prestazioni fisiche sono associati a cambiamenti temporanei nella mielina dell'ippocampo, suggerendo un meccanismo di plasticità microstrutturale indotta dall'esercizio fisico. Inoltre maggiori cambiamenti strutturali legati alla mielina sono stati osservati nella parte posteriore della capsula interna, nei soggetti che si esercitano con le gambe rispetto a quelli che si esercitano con le braccia; suggerendo una somatotopia legata all'apprendimento. Questo studio ha dimostrato che MPM possono essere usate non solo per investigare i cambiamenti strutturali indotti da una lesione alla colonna vertebrale ma anche per fenomeni di plasticità cerebrale.

Nel quarto e ultimo studio, le MPM sono state usate per indagare i cambiamenti strutturali lungo la colonna vertebrale utilizzando metodi già sviluppati ma ottimizzati per MPM. In questo studio un gradiente di degenerazione è stato individuato in soggetti con una lesione alla colonna vertebrale. Tale degenerazione risulta ridotta con l'aumentare della distanza dalla zona della lesione definendo un gradiente. Inoltre tale gradiente risulta più accentuato nelle vie ascendenti rispetto a quelle discendenti. L'associazione con le misure cliniche, suggerisce che i cambiamenti neurodegenerativi secondari forniscono importanti informazioni cliniche e che il monitoraggio di tale gradiente neurodegenerativo potrebbe offrire informazioni rilevanti sugli effetti degli agenti regenerativi o protettivi.

In conclusione, nel contesto di questa tesi, diversi metodi sono stati ottimizzati e sviluppati per facilitare l'uso delle qMRI in condizioni sane e patologiche. In particolare, il metodo sviluppato per la simultanea analisi del cervello e della colonna vertebrale può essere usato per indagare i cambiamenti dovuti ad una lesione alla colonna vertebrale, così come anche i cambiamenti relativi allo sviluppo di dolore neuropatico; tale metodo fornisce biomarker che possono facilitare il monitoraggio degli effetti di agenti regenerativi e neuroprotettivi. L'ottimizzazione del processo di analisi longitudinale per MPM fornisce la prima evidenza di cambiamenti microstrutturali temporanei, lungo il sistema ippocampo-motorio. Questi metodi possono essere usati per valutare l'efficacia di trattamenti riabilitativi.

Contents

Abstract	2
Sommario	5
Contents	8
1 General Introduction.....	16
1.1 Background.....	16
1.2 Problem statement	18
1.3 Main goals of the thesis	19
1.4 Structure of the thesis.....	20
2 Background I: Quantitative MRI (qMRI).....	22
2.1 Spin Physics	22
2.2 Relaxation Effects.....	24
2.2.1 The T1 relaxation.....	24
2.2.2 The T2 relaxation.....	25
2.3 Pulse sequence.....	26
2.3.1 Gradient Echo (GRE) Sequence	26
2.3.2 Multi-echo GRE.....	28
2.3.3 Spoiled gradient echo: image contrast	28
2.4 Multi-parametric mapping.....	31
2.4.1 Theory of MPM signal model	32
2.4.2 R1 and PD estimation	33
2.4.3 Estimation of the magnetisation transfer saturation.....	34
2.4.4 The ESTATICS model and R2* estimation	35
2.4.5 Bias correction.....	35
2.5 hMRI-toolbox	36
2.5.1 Map generations in hMRI toolbox	37

2.5.2	hMRI implementations for bias corrections	38
2.5.3	Post-processing of MPM maps.....	39
2.5.4	Statistical analysis.....	41
2.6	Interpretation of MPM maps	41
2.7	Limitations of MPM.....	44
2.8	Future developments.....	45
2.9	Conclusion background I.....	45
3	Background II: Spinal Cord Injury	47
3.1	The anatomy of the spinal cord	47
3.2	Epidemiology of traumatic SCI	49
3.3	Pathophysiology of traumatic SCI	49
3.3.1	Acute stage.....	50
3.3.2	Subacute stage	50
3.3.3	Intermediate stage	50
3.3.4	Chronic stage.....	52
3.4	Recovery and Plasticity after SCI.....	52
3.4.1	Spontaneous adaptive and maladaptive plasticity after SCI.....	53
3.4.2	Training-induced plasticity after SCI.....	54
3.4.3	Underlying cellular and molecular mechanisms	55
3.5	Diagnostic tools	58
3.5.1	Clinical examination	58
3.5.2	Electrophysiological measurements	61
3.5.3	Spinal Cord Imaging.....	61
3.6	Conclusion background II	64
4	Study I: Simultaneous analysis of brain and spinal cord multi-parametric maps based on SPM framework.....	66
4.1	Abstract	67

4.2	Introduction	68
4.3	Materials and Methods	69
4.3.1	Participants and study design	70
4.3.2	Image acquisition	71
4.3.3	Brain-neck template	71
4.3.4	VBM/VBQ pipeline for the simultaneous analysis of brain and spinal cord	72
4.3.5	Statistical analysis.....	75
4.4	Results	77
4.4.1	Structural changes in the brain using SPM-BSC	77
4.4.2	Structural changes in the brain using SPM-BO.....	78
4.4.3	Brain map reliability: SPM-BSC vs SPM-BO	78
4.4.4	Assessing spinal cord changes using voxel-wise analysis in template space	80
4.4.5	Assess spinal cord changes using extracted metrics.....	81
4.4.6	Associations between spinal cord MPM maps and clinical outcomes.....	82
4.5	Discussion.....	83
4.6	Conclusion	86
5	Study II: Microstructural signature of neuropathic pain across the neuraxis after spinal cord injury 87	
5.1	Abstract	88
5.2	Introduction	89
5.3	Materials and Methods	90
5.3.1	Participants.....	90
5.3.2	Clinical assessment.....	91
5.3.3	Data acquisition.....	91
5.3.4	Data analysis.....	92
5.3.5	Trauma-associated changes in SCI patients compared to healthy controls	94
5.3.6	Pain-associated changes in SCI patients with NP compared to pain-free SCI patients	97

5.4	Discussion.....	100
5.4.1	Limitations.....	103
5.5	Conclusion.....	103
6	Study III: The interplay between corticomotor system and hippocampus circuit changes during procedural learning.....	105
6.1	Abstract.....	106
6.2	Introduction.....	107
6.3	Materials and Methods.....	108
6.3.1	Participants.....	108
6.3.2	Standard protocol approvals, registrations, and patient consents.....	108
6.3.3	Experimental design and training task.....	108
6.3.4	Behavioural analysis.....	109
6.3.5	MRI acquisition.....	110
6.3.6	MRI processing.....	111
6.3.7	MRI Statistics.....	111
6.4	Results.....	113
6.4.1	Demographics and behavioural results.....	113
6.4.2	Training induced structural changes.....	114
6.4.3	Temporal association between the motor cortex, the corticospinal tract and the hippocampus.....	117
6.4.4	Somatotopy of lower vs upper limb training.....	118
6.4.5	MRI correlations with behavioural improvements.....	118
6.5	Discussion.....	120
6.5.1	Training-induced structural changes.....	120
6.5.2	Temporal association between the motor cortex, the corticospinal tract and the hippocampus.....	122
6.5.3	MRI correlations with behavioural improvements.....	122
6.5.4	Limitations.....	123

6.6	Conclusion	124
7	Study IV: Tracking the neurodegenerative gradient after spinal cord injury.....	125
7.1	Abstract	126
7.2	Introduction	126
7.3	Materials and methods	127
7.3.1	Participants and study design	127
7.3.2	Standard protocol approvals, registrations, and patient consents.....	129
7.3.3	Clinical assessments	129
7.3.4	Image acquisition	129
7.3.5	MRI Data processing.....	130
7.3.6	Statistical analysis.....	131
7.4	Results	132
7.5	Demographic, clinical, and radiologic characteristics	132
7.5.1	Neurodegenerative gradient.....	132
7.5.2	Pathophysiological changes	135
7.5.3	Associations between structural changes, lesion level and clinical outcome.....	136
	Figure.....	137
7.6	Discussion.....	137
7.6.1	Characteristics of the neurodegenerative gradient.....	138
7.6.2	Pathophysiological changes	139
7.6.3	Associations between structural changes and clinical outcome	139
7.6.4	Limitations.....	139
7.7	Conclusion	140
8	General discussion	141
8.1	Key findings	141
8.2	Discussion of methodological improvements.....	142

8.2.1	Simultaneous analysis of brain and cervical spinal cord	143
8.2.2	Optimization of longitudinal pipeline	144
8.2.3	Optimization of SCT routines for MPM maps analysis.....	145
8.3	Discussion of clinical studies	146
8.3.1	Trauma-induced changes in SCI	146
8.3.2	Microstructural signature of neuropathic pain after SCI	148
8.3.3	Training-induced plastic changes in SCI	149
8.4	Limitations and considerations	151
8.4.1	Technical limitations for the spinal cord analysis	151
8.4.2	MPM maps as indirect measure of microstructural changes	152
8.5	Outlook and future directions.....	152
8.5.1	Generation of a brain and spinal cord template covering more spinal cord segments 152	
8.5.2	Improvement in the generation of MPM map in the spinal cord	153
8.5.3	Multi-contrast MPM data.....	153
8.6	Concluding remarks.....	154
	References.....	156
	Acknowledgments.....	184
	Curriculum vitae	185

List of Abbreviations

ACC anterior cingulate cortex
AIS American Spinal Injury Association Impairment Scale
APW anterior-posterior width
ASIA American Spinal Injury Association
BSC brain and spinal cord
CA Cornu Ammonis
CE cluster extent
CNS central nervous system
CoV coefficient of variation
CSF cerebrospinal fluid
CST corticospinal tracts
CT computed tomography
DG Dentate Gyrus
DLPFC dorsolateral prefrontal cortex
EC entorhinal cortex
EPI echo planar imaging
FA flip angle
FDR false discovery rate
FID free induction decay
FLASH fast low-angle shot
FoV field of view
FWE family-wise error
FWHM full width at half maximum
GLM general linear model
GM gray matter
GRE Gradient Echo
hMRI in-vivo histology using MRI
ICC intraclass correlation coefficients
ISNCSCI International Standards for Neurological Classification of Spinal Cord Injury
LA lesion area
LEMS lower extremity motor score
LL lesion length
LRW=left-right width; MPM = multi-parameter mapping;
LW lesion width
MEP motor evoked potential
MPM multi-parameter mapping
MPRAGE magnetization-prepared rapid acquisition gradient echo
MR magnetic resonance
MRI magnetic resonance imaging
MT magnetization transfer
MTR MT ratio
 M_{xy} transverse component
Mz longitudinal magnetization
M1 motor cortex
NP neuropathic pain
NT neural tissue
PAG periaqueductal gray
PD proton density
PP pinprick score
pSCI paraplegics;
p.u. percentage unit;

qMT quantitative MT
qMRI quantitative magnetic resonance imaging
RF radiofrequency
ROI region of interest
R1 longitudinal relaxation rate
R2*effective transverse relaxation rate
SBM source based morphometry
SC spinal cord
SCA = Spinal Cord Area
SCI spinal cord injury
SCIM spinal cord independence measure
SCT= spinal cord toolbox
SEP somatosensory evoked potential
SNR signal-to-noise ratio
SPM= Statistical Parametric Mapping
SPM-BSC SPM brain and spinal cord
SPM-BO SPM brain only
SwE sandwich estimator
S1 primary sensory
TE echo time
TIV total intracranial volume
TMS transcranial magnetic stimulation
TPMs tissue probability maps
TR repetition time
tSCI tetraplegics
VBM voxel based morphometry;
VBQ voxel based quantification.
WM white matter

1 General Introduction

1.1 Background

The development of medical imaging tools is essential for the diagnostic and prognostic of spinal cord disorders. Pathologies of the spinal cord can result from neurodegenerative and vascular diseases, disc degeneration, trauma and cancer and often lead to permanent sensory or motor disfunctions (Adams and Salam-Adams 1991; Rowland et al. 2008). The precise assessment of the spinal cord structure is critical for the prediction of recovery and for tracking treatment effects in interventional trails but also rehabilitation (Bozzo et al. 2011a; van Middendorp et al. 2011). Moreover, the identification of neuroimaging biomarkers might help to assess the efficiency and effects of these treatments, e.g., regeneration and axonal growth (Bradbury and McMahon 2006) or remyelination (Harlow, Honce, and Miravalle 2015).

While conventional MRI sequences, such as T1- or T2-weghted images provide useful structural information about the location and the extend of the pathology, that complement clinical and neurophysiological exams (Freund et al. 2019a; Huber et al. 2017; Pfyffer et al. 2019; Vallotton et al. 2019); they are not specific and sensitive to more subtle microstructural changes such as axonal degeneration (Mac Donald et al. 2007; Zhang et al. 2009) or demyelination (Vavasour et al. 2011; West 2014).

Quantitative MRI (qMRI) aims at overcoming these limitations by providing metrics that are more specific to tissue microstructure (Freund et al. 2013; Stroman et al. 2014a; Weiskopf 2013; Weiskopf et al. 2015), with the potential for deeper insights and understanding of the pathophysiology of diseases (Freund et al. 2013). Furthermore, qMRI provide imaging biomarkers that correlate well with neurological and functional impairment (better prognosis), predict outcomes (better prediction), reflect specific aberrant processes within the cord tissue (improve diagnosis) and help in surgical decision (Freund et al. 2013; Freund, et al. 2019a). These techniques might also specifically show reversible and irreversible components of damage by differentiating between processes such as demyelination, axonal loss, and grey matter loss. In addition, qMRI provide quantitative metrics that allow reliable comparison across sites (multi-centre trials) (Seif et al. 2019) , and the investigation of subtle changes over time (longitudinal studies) (Deoni et al. 2008; Weiskopf et al. 2013). Therefore, the ongoing development of qMRI techniques aims to improve the non-invasive characterization of tissue microstructure.

Although we cannot directly image the microstructural tissue components using MRI in vivo, we can make some inferences about the microstructure within a voxel using biophysical models (Weiskopf et al. 2015). Therefore the MPM protocol was developed and optimized (Helms, et al. 2008; Weiskopf et al. 2013; Weiskopf and Helms 2008) in order to provide new qMRI parameters sensitive to myelin, water, or iron content (Edwards et al. 2018) such as the longitudinal relaxation rate ($R1 = 1/T1$), the proton density (PD), the magnetisation transfer (MT) saturation and the effective transverse relaxation rate ($R2^* = 1/T2^*$). MPM maps have been already applied to a multitude of studies, for example for (a) the combined investigation of myelin and iron concentration in brain tissue (Callaghan et al. 2014; Freund et al. 2013), (b) the study of brain atrophy using improved delineation of tissue boundaries (Freund et al. 2013; Lorio et al. 2014) and (c) assessment of layer-specific microstructure (Lutti et al. 2014) acquiring high-resolution data (800 μm in 25 min. @3T Callaghan et al. 2015b), 400 μm in 70 min. @7T (Trampel et al. 2019)).

One of the clinical aetiologies that can potentially benefit from brain and spinal cord MPM is the management of traumatic SCI. Traumatic SCI is a devastating event that leads to permanent motor and sensory impairments. After the initial mechanical insult, secondary injury mechanisms lead to further damage in the pathways, which propagate further along the neuraxis due to anterograde (Wallerian) and retrograde degeneration. Unfortunately, there is no cure for SCI and all treatments aim at minimising secondary complications and maximising residual function by rehabilitation. The prognosis depends primarily on the initial severity and level of the injury. The investigation of the extent of the injury at the epicentre is possible by conventional MRI techniques, clinical tests, and electrophysiological measurements. However, each method is sensitive to a specific aspect of the disease and presents some limitations. Conventional MRI is the best choice for the imaging of the spinal cord and provides great anatomical details about the injury type, level, and extent, but does not provide quantitative and specific measures of microstructural damage, limiting the diagnostic and prognostic capability of MRI (Seif et al. 2019). Clinical tests such as ISNCSCI or GRASSP (Duff et al. 2011), provide measurements related to the motor and sensory functions or to the capability of the patients to perform some tasks, however they are subjective measurements and do not provide information on the location or structure of the damage. Electrophysiological recordings such as motor evoked potential (MEP) or somatosensory evoked potential (SEP) are able to measure the electrical conductivity of neurons and allow the functional investigation of spinal cord tracts (Curt and Dietz 1996). However, they cannot provide information regarding the extent, localization and structure of the damage. The application on MPM maps in the investigation of the SCI-patients offers several advantages over the aforementioned approaches used so far in the clinical routine. Specifically, MPM

maps provides more information on the pathophysiological changes at the injury site and along the spinal cord in terms of retrograde and anterograde degeneration, myelin changes and iron content. These microstructural changes offer the ability to improve patients' stratification and define personalized rehabilitation strategies. Furthermore, since these maps are sensitive to microstructural changes, they are more sensitive to detect subtle changes along the central nervous system and offer predictive imaging biomarkers that correlate with clinical recovery.

1.2 Problem statement

The application of qMRI in the spinal cord is limited by numerous anatomical, physiological and technical factors that affect the quality of the spinal cord scans. The quality of qMRI in the spinal cord is affected by the (i) susceptibility artifacts created by the close proximity of bones (spine), air-filled structures (lungs), and fat around the spinal canal; (ii) the small cross-sectional dimensions of the spinal cord requiring high-resolution sequences, (iii) motion of the spinal cord and adjacent structures due to respiration, pulsation of cerebrospinal fluid, swallowing, etc.; and (iv) the relatively low signal-to-noise ratio due to the less efficient coil coverage (Stroman et al. 2014b). In addition, these factors can greatly vary across spinal levels making the acquisition more challenging and complex. However, in the past few years researchers have developed methods to overcome these challenges, such as advanced coil designs (Cohen-Adad et al. 2011) and pulse sequences (Dowell et al. 2009; Finsterbusch 2009; Wilm et al. 2007).

Another limitation for spinal cord imaging is the limited number of tools dedicated to the processing of spinal cord images (Stroman et al. 2014a). Moreover, brain software packages (e.g., FSL, SPM, BrainVoyager, FreeSurfer, AFNI, MINC Toolkit) are not optimized for spinal cord image processing because of the s-shape morphology of the spinal cord which does not allow the application of standard motion-correction algorithms based on rigid or affine transformation, as well as segmentation and registration/normalization tools. Common brain MRI templates (Evans et al. 1992; Fonov et al. 2011) and atlases do not include the spinal cord and therefore cannot be used for spinal cord analysis. The lack of a standard processing tools had a negative impact on the spinal cord neuroimaging community as it has limited the ability of researchers to compare and reproduce published results, as well as to conduct collaborative and multi-center studies. Only in 2017, the spinal cord toolbox (SCT (De Leener et al. 2016)), which is a comprehensive software dedicated to the processing of spinal cord MRI data was released. SCT is built on previously validated methods and provides standard templates and analysis procedures. However this toolbox presents some limitations: (i) the templates such as PAM50

(De Leener et al. 2018) covers only the spinal cord (no brain), therefore combined brain and spinal cord analysis is not possible; (ii) the SCT provides only post-processing tools for qMRI, it does not include a statistics environment; (iii) and it was specifically developed to analyse DTI and fMRI data, therefore SCT routines are not optimized or tested using data from other acquisition protocols (such as the MPM); and finally (iv) the analysis implies a straightening of the spinal cord which involves great deformation of the spinal cord. However, dedicated tools for the analysis of MPM maps in the spinal cord are missing and there are no available tools for the simultaneous analysis of brain and spinal cord in the same framework.

1.3 Main goals of the thesis

In this thesis several tools and processing routines were developed or optimized in order to incorporate the use of MPM maps for the assessments of spinal cord tissue changes. These tools were applied in clinical studies to investigate neurodegenerative changes after a traumatic SCI. Specifically, the main technical improvements can be summarized in three techniques and were applied in four different clinical studies.

Methodological improvements addressed in this thesis and corresponding clinical applications (see table 1 for a summary):

- (1) Development of a tool for the simultaneous analysis of brain and spinal cord in the SPM framework, offering the possibility to perform pre-processing and statistics in the same framework. The incorporation of a template covering brain and spinal cord offered the possibility to perform VBM/VBQ analysis including brain and cervical spinal cord. The developed tool was used to investigate trauma-induced changes in SCI patients (study I) as well as the underlying microstructural changes that characterize maladaptive plastic changes in chronic SCI-patients (study II).
- (2) Optimization of longitudinal processing pipelines, with and without the incorporation of the cervical spinal cord, in order to be more sensitive to subtle macro- and microstructural changes over time. These procedures were used to investigate training-induced changes in healthy controls and the corresponding association with the behavioural improvement (study III).

- (3) Optimization of SCT procedures for the analysis of MPM maps. MPM maps can be warped in template space (PAM50), as well as quantified in subject space, allowing the investigation of micro-structural changes along the full spinal cord (study IV).

Methodological development or improvement	Corresponding clinical applications	Dedicated chapter in the thesis
Development of image processing tools for the simultaneous analysis of brain and spinal cord	Investigate macro- and micro-structural changes in the brain and cervical spinal cord in SCI patients	Chapter 4
	Investigate the underlying microstructural changes that characterize maladaptive plastic changes in chronic SCI-patients with neuropathic pain	Chapter 5
Optimization of longitudinal processing procedures for MPM maps (with and without the spinal cord)	Investigate training induces myelin changes in healthy subjects (only brain)	Chapter 6
Optimization of SCT procedures for the analysis of MPM maps	Investigate macro- and micro-structural changes in the spinal cord of SCI-patients spanning over the levels C1 to C4	Chapter 7

Table 1: Methodological improvements and corresponding clinical applications covered in this thesis

1.4 Structure of the thesis

In this thesis, first the methodological and biological background are covered in chapters 2 and 3, respectively. Specifically, chapter 2 deals with the technical background of MRI including spin physics, excitation and relaxation phenomena with a more detailed description of the sequence used for the acquisition of MPM protocol. MPM protocol provides qMRI parameters sensitive to myelin, water, or iron content (Edwards et al. 2018) such as the longitudinal relaxation rate (R_1), the proton density (PD), the magnetisation transfer (MT) saturation and the effective transverse relaxation rate (R_2^*). In this chapter the biophysical model of MPM maps (MT; R_1 , PD and R_2^*) are described, followed by the tool that is used to generate the maps. At the end of the chapter the interpretation and limitations of these maps are also discussed.

Chapter 3 provides an overview of the spinal cord anatomy and the pathological changes after a SCI. After the primary injury to the spinal cord, several secondary changes are triggered, and the corresponding stages and characteristics are described. The third chapter also provides an overview of

the conventional diagnostic tools used to investigate the level and extend of the injury, track changes and predict the outcome of SCI patients.

Each of the following chapters (4-7) are dedicated to a single peer reviewed publication. Specifically, chapter 4 focuses on the simultaneous analysis of brain and spinal cord multi-parametric maps based on SPM framework (Study I), chapter 5 is related to the microstructural signature of neuropathic pain across the neuraxis after spinal cord injury (Study II); chapter 6 focuses on the interplay between corticomotor system and hippocampus circuit changes during procedural learning (Study III) and chapter 7 is related to tracking the neurodegenerative gradient after spinal cord injury (Study IV). Finally, chapter 8 provides a general discussion, highlighting the scientific relevance of all the studies and discussing the limitations, outlook and future developments.

2 Background I: Quantitative MRI (qMRI)

MRI is a non-invasive technique which uses magnetic fields, magnetic field gradients and radio waves to produce detailed medical images. These images are used for diagnosis, treatments planning and efficacy assessment. MRI techniques allow the investigation not only of the anatomy and pathology but also of organ function, probe in vivo chemistry and even the visualization of the thinking brain.

The MR signal was discovered in 1946 by two separate groups, Bloch et al. (Bloch 1946) and Purcell et al. (Purcell et al. 1946). They jointly received the Nobel Prize for physics in 1952. The theory of MRI relaxation was described by Bloembergen, Purcell and Pound (Bloembergen, Purcell, and Pound 1948) which is known with their initials BPP. The technique for generating images using spatial encoding with magnetic field gradients was discovered by Lauterbur (Lauterbur 1973) and Mansfield et al. (Mansfield and Grannell 1973) and they were awarded with the Nobel prize in medicine in 2003.

In this chapter the basic principles of MRI are described, focusing on the techniques used in qMRI. The quantitative nature of qMRI allows reliable comparison across sites (multi-centre trials), and the investigation of subtle changes over time (longitudinal studies) (Sean C L Deoni et al. 2008; Weiskopf et al. 2013). Combining qMRI with biophysical modelling provides the possibility to characterize key microscopic soft tissue parameters such as iron or myelin density (Stüber et al. 2014), which previously could only be achieved with ex vivo histology. The possibility to perform in-vivo histology was named hMRI, meaning in vivo histology using MRI (hMRI (Weiskopf et al. 2015)). Finally, one of the main qMRI acquisition protocol (the MPM approach), and corresponding biophysical models are described in more details.

2.1 Spin Physics

All MRI phenomena are based on the interaction between an external magnetic field B_0 , and the magnetic properties of atomic nuclei such as hydrogen protons (even if other elements can be used). Hydrogen protons can be represented as tiny magnetic bars spinning around their own axes. In absence of an external magnetic field, these tiny bar magnets are randomly distributed (figure 2.1A). As soon as an external magnetic field B_0 along the z-axis of the scanner (direction of the magnet bore) is applied, they align with the magnetic field (predominantly parallel to B_0) generating a **net magnetization**, and they precess or “wobble” at the Larmor frequency (figure 2.1B), which can be described as

(2.1)

$$\omega_0 = \gamma B_0$$

where:

ω_0 = Precessional or Larmor frequency. (MHz)

γ = Gyro Magnetic Ratio. (MHz/T)

B_0 = Magnetic field strength. (T)

The net magnetization, also called M_z or longitudinal magnetization can be described as a vector (figure 2.1C). A measurable MR signal is generated when the net magnetization, is perturbed or “excite” by a radiofrequency (RF) pulse and the corresponding relaxation (going back to initial state, before sending the RF pulse) is measured (figure 2.1D). By sending an RF pulse (excitation) with a certain strength (amplitude) and for a certain period, the net magnetization is flipped in the X-Y plane by a certain angle (i.e. 90°) called Flip Angle α (FA). The resulting magnetization vector can be characterized by its remaining longitudinal component M_z along the direction of the main magnetic field (Z-axis) and a transverse component M_{xy} in the orthogonal plane (X-Y plane). Only the protons that spins with the same frequency as the RF pulse are excited absorbing energy from the RF pulse and flipping the net magnetization in the X-Y plane. This energy is released during the relaxation phase and the initial state (before RF pulse) is recovered. After RF pulse, M_{xy} continuously rotates around the main magnetic field B_0 with the Larmor frequency ω_0 and induces a detectable MR signal, the so-called free induction decay (FID) in a receive coil surrounding the object under investigation. The speed of the M_{xy} rotation is determined by the local magnetic field, i.e. due to tissue properties or hardware imperfections.

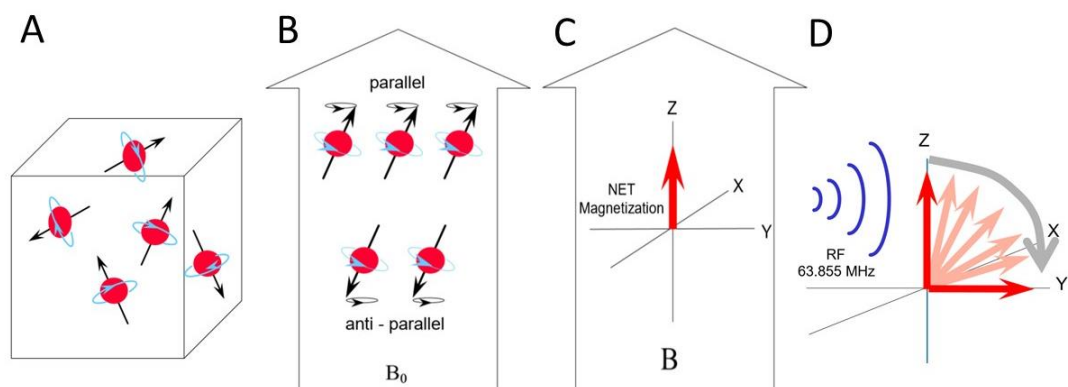


Figure 2.1: Spin representation during an MRI experiment. In absence of an external magnetic field hydrogen protons represented by spins, are randomly distributed (A); as soon as an external magnetic field B_0 is applied along the z-axis of the scanner (B), these spins align with the magnetic field (predominantly parallel to B_0) generating a net magnetization M_z (C), and they precess at the Larmor frequency. In an MRI experiment a radiofrequency (RF) pulse is given and the net magnetization is flipped in the X-Y plane by a certain angle (i.e. 90°) (D).

2.2 Relaxation Effects

As long as M_{xy} has a non-zero component, the MR signal will persist, and its amplitude is affected by two different relaxation effects: T1- recovery and T2*-decay. For a more comprehensive description refer to the excellent books by (McRobbie, Moore, and Graves 2017).

2.2.1 The T1 relaxation

The T1 relaxation or T1-recovery characterizes the recovery of the longitudinal magnetization M_z (describes what happens in the Z direction), which returns to thermal equilibrium (M_z directed along B_0) by exchanging energy with its environment. T1 relaxation is the time it takes for the longitudinal magnetization (M_z) to reach 63 % of the original magnetization. Every tissue has a different T1 relaxation depending on how strong protons are bounded, i.e. tightly bound protons will release their energy much quicker to their surroundings than protons, which are bound loosely (see figure 2.2).

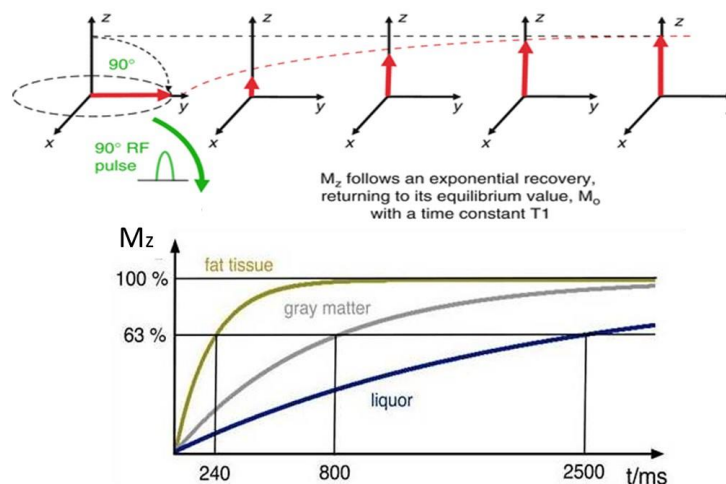


Figure 2.2: T1 relaxation. Following a 90 RF pulse, the z component of the Net Magnetisation, M_z is reduced to zero, but then recovers gradually back to its equilibrium value if no further pulses are applied. The recovery of M_z is an exponential process with a time constant T1. This is the time at which the magnetization has recovered to 63 % of its original value. Different tissues have different T1 values. Fat has the shortest T1 value of all tissues (fat recovers the fastest) while fluid has the longest T1 value (fluid recovers the slowest). The figure is adapted from (Ridgway 2010).

2.2.2 The T2 relaxation

The T2 relaxation or T2-decay describes the dephasing of the transverse magnetization M_{XY} (describes what happens in the XY plane). Right after the RF pulse the net magnetization is flipped into the X-Y plane and protons are spinning in-phase (i.e. after a 90° RF pulse the magnetization vector is rotating in the X-Y plane around the Z-axis). But immediately after the RF pulse, spins rotate at different speeds and start to de-phase. This process of getting from a total in-phase situation to a total out-of-phase situation is called T2 relaxation. T2 relaxation is a time constant and depends on how the hydrogen protons are bound in its molecule and therefore it is different for each tissue (fat tissue will de-phase quickly, while water will de-phase much slower). T2 relaxation is also called spin-spin relaxation because it describes interactions between protons in their immediate surroundings (molecules) and it is defined as the time it takes for the spins to de-phase to 37% of the original value. T2 relaxation is a decaying process, which means phase coherence is strong at the beginning, but rapidly it decays (becomes less intensive) until there is no phase coherence left (figure 2.3). Consequently, the signal that is received from the receive coil (FID), is strong at the beginning and quickly becomes weaker due to T2 relaxation. In the real case, the T2 relaxation is affected by local (microscopic) magnetic field inhomogeneity and chemical shift which result in a faster decay known as T2* effects.

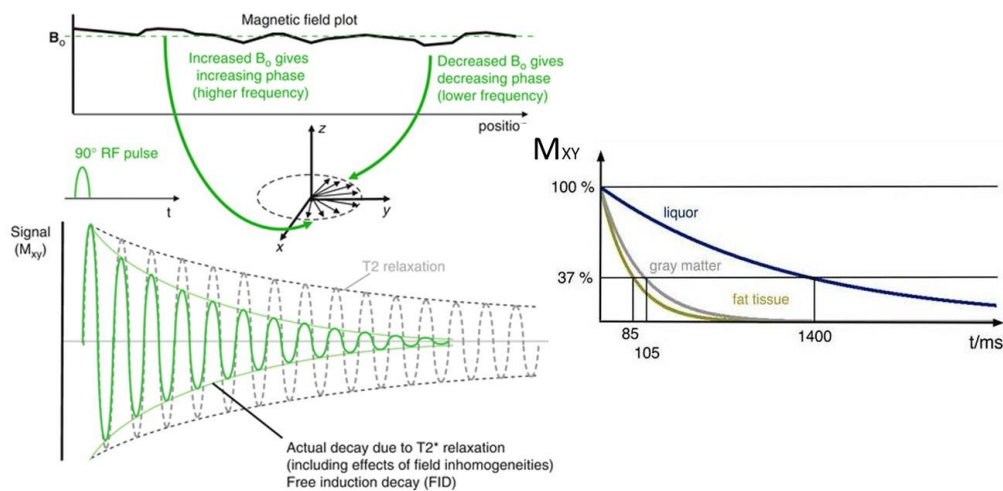


Figure 2.3: T2 and T2* relaxation. The FID signal decays due to spin-spin interactions, causing a loss of phase coherence (de-phasing) at T2 relaxation time. However, local magnetic field inhomogeneity induces additional de-phasing and induce a rapid decay of the FID signal, known as T2* decay. The figure is adapted from (Ridgway 2010).

2.3 Pulse sequence

In the MR experiment the signal is acquired by repeatedly applying RF pulses and sampling the resulting FID at specific time-points. The time between subsequent repetitions of the RF pulses is termed the repetition time (TR); whereas, the time from the generation of the FID to the acquisition of the MR signal is termed the echo time, TE (figure 2.4). If the magnetisation is not allowed to return to thermal equilibrium in between subsequent repetitions, the spin system reaches a steady-state.

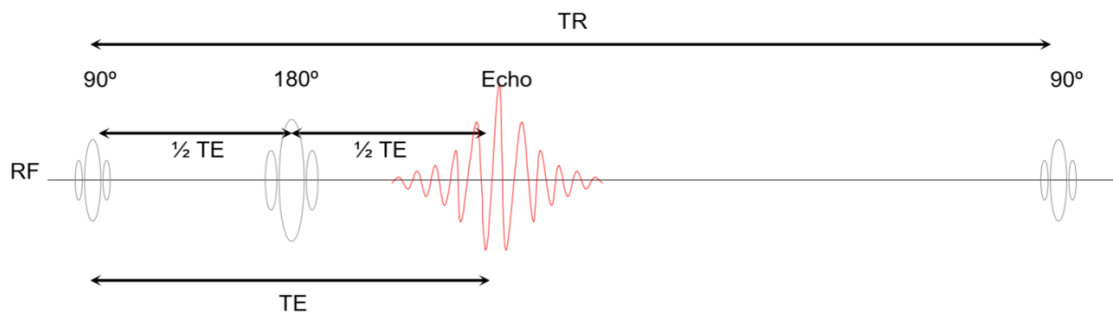


Figure 2.4: Graphical representation of the Repetition Time (TR) and Echo Time (TE). The figure is adapted from (Brown, Semelka, and Nishino 2004).

In order to understand where the signal is coming from, spatial encoding is necessary. This is done by applying different gradients in the three directions (Z, X and Y). These variations can be decoded as variations in phase and frequency in the measured MR signal. For a detailed explanation of spatial encoding, refer to (Matt & Kevin). The combination of RF pulses, gradient switches and signal collecting defines the **MR pulse sequence**. Depending on MR scanner settings and the specific pulse sequence used, different image contrasts are generated.

2.3.1 Gradient Echo (GRE) Sequence

The Gradient Echo sequence (GRE) uses a gradient polarity reversal to manipulate the FID as presented in figure 2.5 where changing the polarity of the G_{RO} rephases the spins. A better illustration of the effect of sequence on the spins is given in figure 2.6.

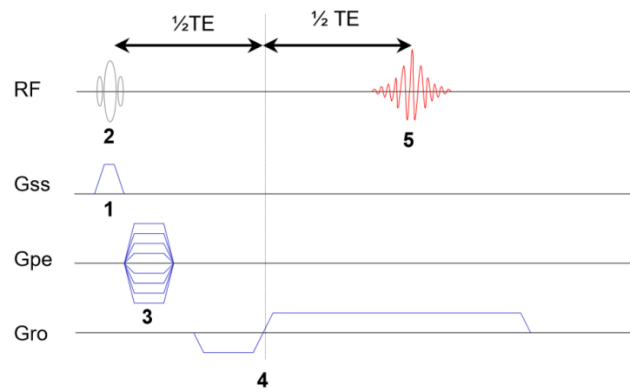


Figure 2.5: Sequence diagram for GRE. This sequence consists of (1) switching on the Slice Select gradient (GSS) and simultaneously (2) apply a RF-pulse to ‘flip’ the net magnetization into the X-Y plane. Then (3) the Phase Encoding gradient (GRE) is switched on (first phase encoding) and (4) the read out gradient G_{RO} is switch on. First negative polarity, and then change polarity to positive, during which (5) the signal, the Free Induction Decay (FID), is sampled. The figure is adapted from (Brown et al. 2004).

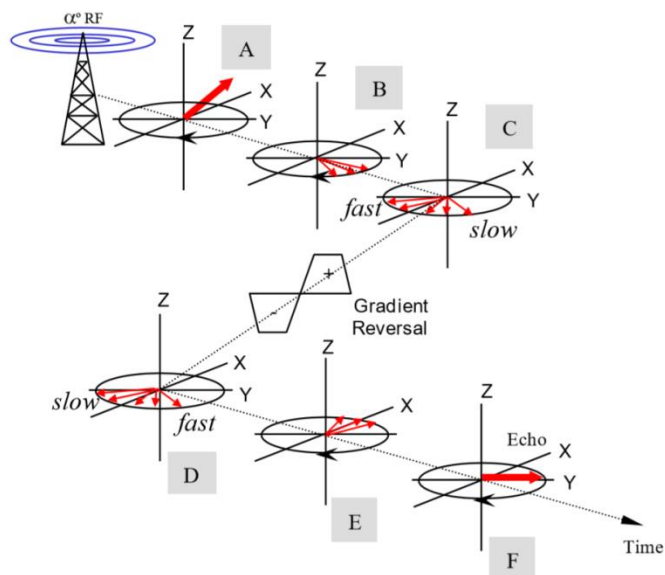


Figure 2.6: GRE sequence and spins. After the RF pulse, the spins are dephasing (A-B) with different speeds, by applying the gradient polarity reversal, reverses the dephasing speed of the spins; therefore, the fast ones will slow down and the slow ones will speed up (C-D). At a certain moment (F) all spins are in phase again (this is the echo). The figure is adapted from (Brown et al. 2004).

The gradient echo sequence allows very short repetition times and therefore faster imaging is feasible. The disadvantage is that it does not correct for local magnetic field inhomogeneities (i.e. imperfections of the main magnetic field, shim or tissue properties), which translates into the presence of artifacts in the image. However, advanced hardware, such as improved shimming and gradient performance,

permits the successful application of GRE imaging with reliable and reproducible image quality (Markl and Leupold 2012).

2.3.2 Multi-echo GRE

The same gradient reversal process used to create a single gradient echo can be repeated to produce two or more additional GREs after a single RF-pulse. This is known as dual (or multi-) echo GRE. This multi-echo acquisition is possible as long as complete the transverse magnetization by $T2^*$ relaxation has completely occurred. Usually data from these echoes are combined to create a single image that has been shown to have excellent suppression of CSF flow artefacts and is useful for displaying internal structures. Multi-echo GRE sequence is used for spinal cord imaging using a relatively new technique known as MERGE (GE), MEDIC (Siemens), or M-FFE (Philips).

2.3.3 Spoiled gradient echo: image contrast

Gradient echoes imaging is particularly used in clinical applications because it allows fast imaging. However, even images acquired with the most common sequences employing the gradient echo for data acquisition can significantly differ in signal, contrast, artefact behaviour, and sensitivity. This is due to the different use of sequence timing and basic sequence building blocks such as spoiler gradients or specific radiofrequency (RF) pulse phase patterns. The spoiled-GRE technique is specifically designed to disrupt transverse ($T2$) coherences, and therefore produce good $T1w$ images. However, this technique can be used to acquire $T2^*$ -weighted and PD images as well, using appropriate parameters. The signal (S) of a spoiled GRE sequence, assuming perfect spoiling and reached longitudinal steady state can be described as:

$$(2.2) \quad S = k [H] \frac{\sin\alpha(1 - e^{-TR/T1})}{(1 - \cos\alpha * e^{-TR/T1})} e^{-TE/T2^*}$$

where k is a scaling factor, α is the flip angle, TR repetition time, TE echo time, $T1$ and $T2^*$ are the longitudinal and transverse relaxation time, respectively.

As you may noticed from equation, the signal from a spoiled-GRE sequence depends on three operator-selectable parameters (TR , TE , and flip angle α) and three intrinsic tissue parameters ($T1$, $T2^*$, and spin-density $[H]$). In particular:

- the signal is always proportional to spin density $[H]$
- TE controls $T2^*$ -weighting [from the term $\exp(-TE/T2^*)$], specifically for small TE values, the $T2^*$ contribution is minimized.
- Flip angle (α) controls $T1$ -weighting, i.e. using a small α , $\cos\alpha$ can be approximated as 1 so the denominator term is cancelled, removing the $T1$ effects resulting in $[H]$ and $T2^*$ weighted. Conversely, as $\alpha \rightarrow 90^\circ$ $T1$ -weighting increases.
- TR controls $T1$ -weighting [from the term $\exp(-TR/T1)$], i.e. for small TR the exponential term becomes large and the $T1$ -weighting increases. Conversely, when TR is long, $T1$ -weighting is minimized.

The signal is maximized at the **Ernst angle** α_E (computed by setting $dS/d\alpha = 0$), which corresponds to:

$$(2.3) \quad \alpha_E = \arccos(e^{-TR/T1})$$

Note that the Ernst angle gives the highest signal for a given tissue for a certain $TR/T1$ combination, but it does not necessary offer the best contrast between different tissues. To better understand the effect of the TE , α and TR , figures 2.7 to 2.9 are showing the effect of each parameter and corresponding image contrast; and in Table 3.1 typical spoiled GRE-parameters for each contrast are presented.

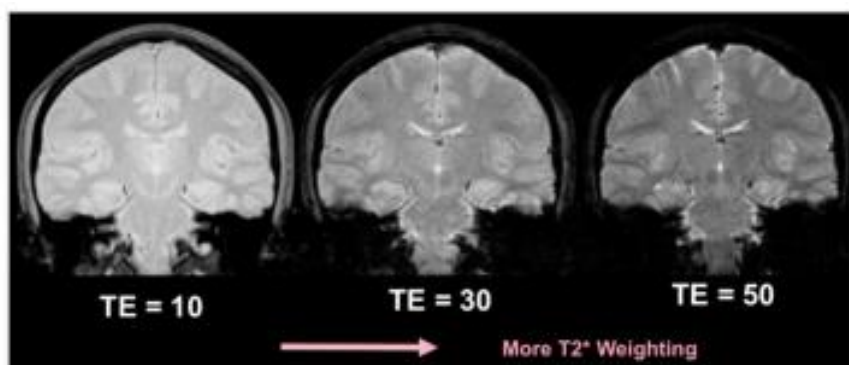


Figure 2.7: Effect of echo time (TE) on GRE sequence: if TE is longer, more time for dephasing is allowed and the resulting image presents increased $T2^*$ -weighting. (The figure is adapted from <http://mriquestions.com/spoiled-gre-parameters.html>).

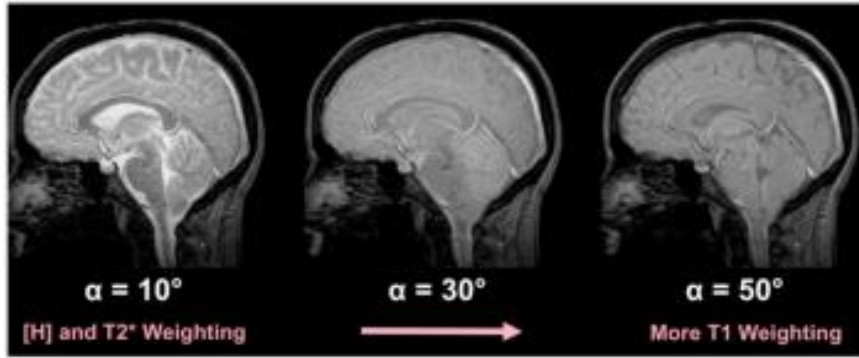


Figure 2.8: Effect of the flip angle (α) on GRE sequence: if α is small, the net magnetization is flipped by a small angle and steady state of the longitudinal magnetization is slightly changed; therefore, only a small differentiation based on the intrinsic T1 properties is allowed. Thus, for small α , [H] and T2* effects predominate, whereas for $\alpha \rightarrow 90^\circ$, T1-weighting increases. (The figure is adapted from <http://mriquestions.com/spoiled-gre-parameters.html>).

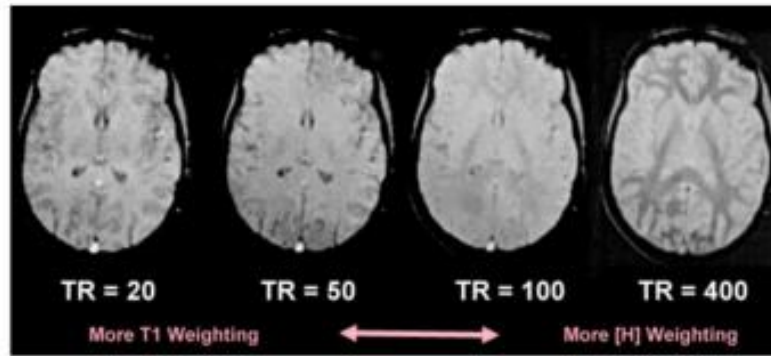


Figure 2.9: Effect of repetition time (TR) on GRE sequence: if TR is short, the T1-weighting is accentuated; whereas for long TRs the T1 effects are minimized allowing [H] and T2*-weighting to become dominant. (The figure is adapted from <http://mriquestions.com/spoiled-gre-parameters.html>).

Desired Image Contrast	Parameter Selection	Reason
T1-weighting	Short TR (5-10 ms) Short TE (2-5 ms) Intermediate α (30-50°)	T1 contrast would theoretically be better with $\alpha=60-90^\circ$, but signal would be weak because far from Ernst angle; $\alpha = 30-50^\circ$ is compromise for good signal and T1-weighting at short TR
[H]-weighting (PD)	Long TR (100-400ms) Short TE (2-5 ms) small α (2-20°)	Long TR and small α minimize T1 weighting; shorter TE minimizes T2* effects
T2*-weighting	Long TR (200-800 ms) long TE (20-50ms) small α (5-20°)	Long TR and small α minimize T1 weighting; long TE maximizes T2* effects

Table 2.1: typical spoiled GRE-parameters at 1.5T for different contrasts (from <http://mriquestions.com/spoiled-gre-parameters.html>).

The image contrast of GE sequences is determined mainly by FA and TE as shown in Figure 2.10. A high FA and short TE gives T1 weighted contrast. A medium FA and short TE gives PD contrast. A low FA and long TE gives T2 weighted contrast. Typically, FA can be anything in the range of 1° to 180° but usually values between 1° and 90° are used.

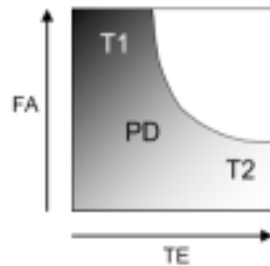


Figure 2.10: Illustration of image contrast for GE sequence as a function of flip angle (FA) and echo time (TE). For high FA and short TE, the GE sequence gives T1w contrast; for medium FA and short TE, it gives PD contrast; and for low FA and long TE it gives T2w contrast.

2.4 Multi-parametric mapping

In order to estimate absolute physical metrics, which are independent from the hardware and are sensitive to microstructural properties such as axons, myelin, iron and water concentration (Draganski et al. 2011; Lorio et al. 2014, 2016), the MPM protocol was developed. This protocol allows the measurement of qMRI. The quantitative nature of this data allows reliable comparison across sites (multi-centre trials), and the investigation of subtle changes over time (longitudinal studies) (Deoni et al. 2008; Weiskopf et al. 2013).

The MPM protocol was introduced by Weiskopf and Helms 2008 (Helms, et al. 2008a; Helms et al. 2009; Weiskopf et al. 2011a, 2013) for estimating the longitudinal relaxation rate R_1 , the effective transverse relaxation rate R_2^* , the proton density PD and the magnetisation transfer saturation MT (figure 2.11). This approach was developed at 3T and includes data acquisition, modelling and bias correction of three multi-echo spoiled gradient echo volumes (multi-echo FLASH sequence).

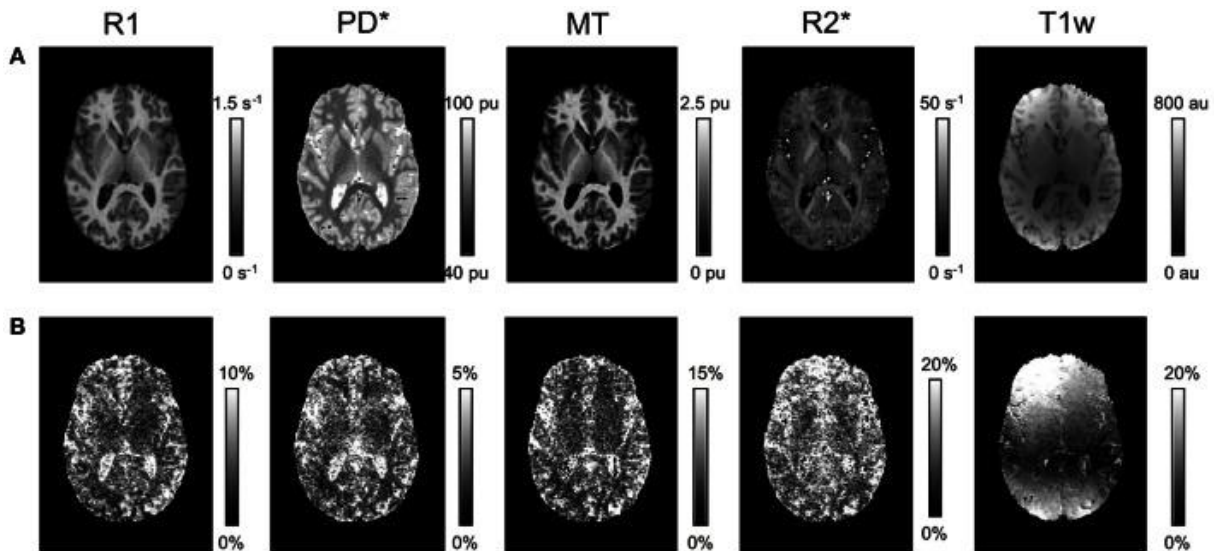


Figure 2.11: Axial slice through R1, PD*, MT, and R2* parameter maps and T1w images for a single volunteer. (A) Mean and (B) inter-site coefficient of variation (CoV) across the three different sites from (Weiskopf et al. 2013).

The initial framework was further developed enabling time-efficient whole brain mapping with 3 different resolutions: (i) resolution of 800 μm in 24 min Callaghan et al. 2015b); (ii) 1 mm isotropic resolution in 18 min at 3T (Papp et al. 2016); and (iii) ultra-high-resolution quantitative maps at 400 μm at 7T (Trampel et al. 2019). The MPM protocol was used in several studies focusing on: (a) the combined study of myelin and iron concentration in the brain and spinal cord (Callaghan et al. 2014; Freund et al. 2013); (b) the study of brain atrophy using improved delineation of tissue boundaries (Freund et al. 2013; Lorio et al. 2014), thanks to the improvement of the segmentation of deep gray matter structures; (c) assessment of layer-specific microstructure (Lutti et al. 2014) acquiring high-resolution data (800 μm in 25 min. at 3T Callaghan et al. 2015b), 400 μm in 70 min. at 7T (Trampel et al. 2019).

2.4.1 Theory of MPM signal model

Data from the multi-echo FLASH sequence are processed in order to generate maps of R1, R2*, PD, as well as semi-quantitative MT saturation maps (figure 2.12).

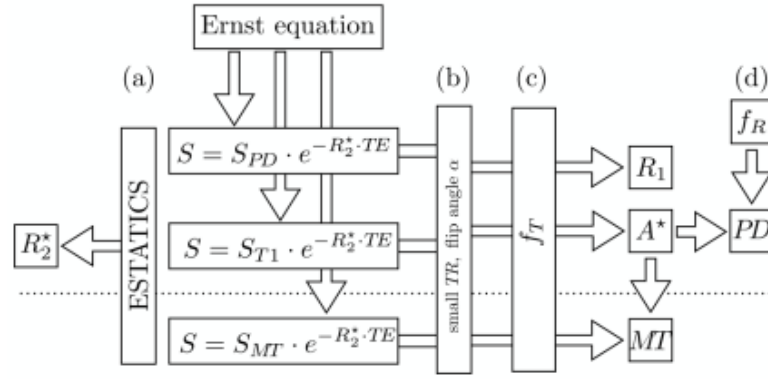


Figure 2.12: Schematic representation of qMRI maps generation from MPM protocol. The acquired signal S is modelled by the Ernst equation with an exponential decay (which depend on the echo time TE acquired). The longitudinal relaxation rate R_1 , the effective transverse relaxation rate R_2^* , the proton density PD and the magnetisation transfer saturation MT are computed from the acquired data, using some approximations for small repetition time TR and small flip angles α . Additional bias correction is based on the acquired transmit and receive bias fields, f_T and f_R respectively (Balteau et al. 2018).

2.4.2 R_1 and PD estimation

The signal S from the multi-echo PDw and T1w acquisitions can be described by the Ernst equation for an ideal spoiled gradient echo acquisition (Ernst and Anderson 1966; Helms, et al. 2008a; Helms, et al. 2008).

$$(2.4) \quad S = A \cdot \sin \alpha \cdot \frac{1 - e^{-R_1 \cdot TR}}{1 - \cos \alpha \cdot e^{-R_1 \cdot TR}} e^{-R_2^* \cdot TE}$$

TR denotes the repetition time, α is the flip angle and A is proportional to the equilibrium magnetisation and thus to the proton density PD (Helms, et al. 2008a).

For short TR (i.e. $R_1 \cdot TR \ll 1$) the exponential can be liberalized using:

$$(2.5) \quad e^{-R_1 \cdot TR} \sim 1 - R_1 \cdot TR$$

Leading to (3):

$$(2.6) \quad S = A^* \cdot \sin \alpha \cdot \frac{R_1 \cdot TR}{1 - \cos \alpha \cdot (R_1 \cdot TR)}$$

With

$$(2.7) \quad A^* = \frac{A}{\#echoes} \sum_{TE} e^{-R_2^* \cdot TE}$$

There are two alternatives to compute the A^* : (i) using several echoes, i.e. the sum in Eq. (4) is calculated across all echoes introducing an $R2^*$ bias which depends on the TE and increases with the number of echoes included; in this case an additional correction using the $R2^*$ estimate is needed; (ii) using only the signal at TE = 0, which is free from $R2^*$ weighting. Both methods perform similarly (Balteau et al. 2018).

For small flip angles, the approximation $\sin(\alpha) = \alpha$ and $\cos(\alpha) = 1 - \alpha^2/2$ can be used, and neglecting the $\alpha^2 \cdot R1 \cdot TR$ term, Eq. (1) simplifies to:

$$(2.8) \quad S = A^* \cdot \alpha \cdot \frac{R1 \cdot TR}{\frac{\alpha^2}{2} + R1 \cdot TR}$$

from which R1 and A^* are estimated using the signals from the PDw and T1w sequences:

$$(2.9) \quad R1 = \frac{S_{PD}\alpha_{PD}/TR_{PD} - S_{T1}\alpha_{T1}/TR_{T1}}{2 \cdot (S_{T1}/\alpha_{T1} - S_{PD}/\alpha_{PD})}$$

$$(2.10) \quad A^* = \frac{S_{T1}S_{PD}(TR_{T1}\alpha_{PD}/\alpha_{T1} - TR_{PD}\alpha_{T1}/\alpha_{PD})}{S_{PD}TR_{T1}\alpha_{PD} - S_{T1}TR_{PD}\alpha_{T1}}$$

where signals S_{T1} and S_{PD} are either averaged over a number of echoes (Helms, et al. 2008a) (in this a $\sum_{TE} e^{-R2^* \cdot TE}$ correction factor must be included), or extrapolated to TE = 0.

2.4.3 Estimation of the magnetisation transfer saturation

The MT (magnetisation transfer) saturation measure is derived in analogy to a dual-excitation spoiled gradient echo sequence where the second excitation is replaced by the MT pulse. Using a heuristic approximation, the closed form solution for the acquired signal S can be written (Helms and Hagberg 2009; Helms et al. 2008) as

$$(2.11) \quad S = A \cdot \sin \alpha_{MT} \cdot \frac{1 - e^{-R1 \cdot TR_{MT}} - \delta \cdot (e^{-R1 \cdot TR_2} - e^{-R1 \cdot TR_{MT}})}{1 - \cos \alpha_{MT} \cdot (1 - \delta) e^{-R1 \cdot TR_{MT}}} e^{-R2^* \cdot TE}$$

where $TR_{MT} = TR_1 + TR_2$ is the total repetition time, α_{MT} is the on-resonance flip angle of the MTw sequence and δ describes the MT saturation (more generally denoted MT in this theses). From an additional MTw signal S_{MT} and using the linearisation of the exponential term for short TR and the small angle approximation, we obtain (Helms, et al. 2008):

$$(2.12) \quad \delta = MT = (A \cdot \alpha_{MT} / S_{MT} - 1) \cdot R1 \cdot TR_{MT} - \alpha_{MT}^2 / 2$$

Note that the parameter maps R1, R2*, A and MT can alternatively be estimated from the ESTATICS model using analytic formulas and not relying on the linearization outlined above.

2.4.4 The ESTATICS model and R2* estimation

The effective transverse relaxation rate R2* can be derived from the exponential signal decay of the all signals. In this model, the signal decay of T1w, PDw and MTw acquisitions is assumed to identical and a unified description of the multi-echo is denoted as ESTATICS (Weiskopf et al. 2014). In ESTATICS data from all three contrasts are used in a single model as in the following equation (figure 2.12).

$$(2.13) \quad S = (S_{PD} \cdot I_{PD} + S_{T1} \cdot I_{T1} + S_{MT} \cdot I_{MT}) \cdot e^{-R2^* \cdot TE}$$

with indicator variables I_{PD} , I_{T1} , and I_{MT} for the differently weighted acquisitions. R2* map is computed using all signals from equation 2.13.

2.4.5 Bias correction

The generated maps (R1, A, MT and MT figure 2.11) need to be corrected for instrumental biases such as the B1 transmit f_T (figure 2.12c) and receive f_R (figure 2.12d) field inhomogeneities. There are 2 main methods for the bias fields correction: (i) based on specific B1 transmit and receive field measurements or (ii) based on image processing methods. In the first case, the MPM protocol includes additional acquisitions of the B1 transmit and receive field (Lutti et al. 2012; Weiskopf et al. 2011a). Usually, the B1 transmit field measurement involves eleven spin-echo with the nominal flip angles varying from 115° to 65° in 5° decrements prior the multi-echo acquisition of the maps. While f_T influences the local flip angle and hence all three (R1, PD, MT) maps, the RF sensitivity bias field f_R only influences the PD map (in the absence of subject motion). Therefore, the protocol includes a B1 mapping and RF sensitivity measurement prior PDw-echoes acquisition and only RF sensitivity measurements prior MTw- and T1-w -echoes acquisitions. If no measurements for field inhomogeneities are acquired, bias correction is still possible by estimating the inhomogeneity using some basis functions from the maps (image processing methods). More implementation details are presented in section 2.5.1.

2.5 hMRI-toolbox

The hMRI toolbox was developed in order to perform *in vivo* histology using MRI data. The idea is to investigate the microstructure of the brain based on MRI measurements and physical/biophysical models (Figure 2.13).

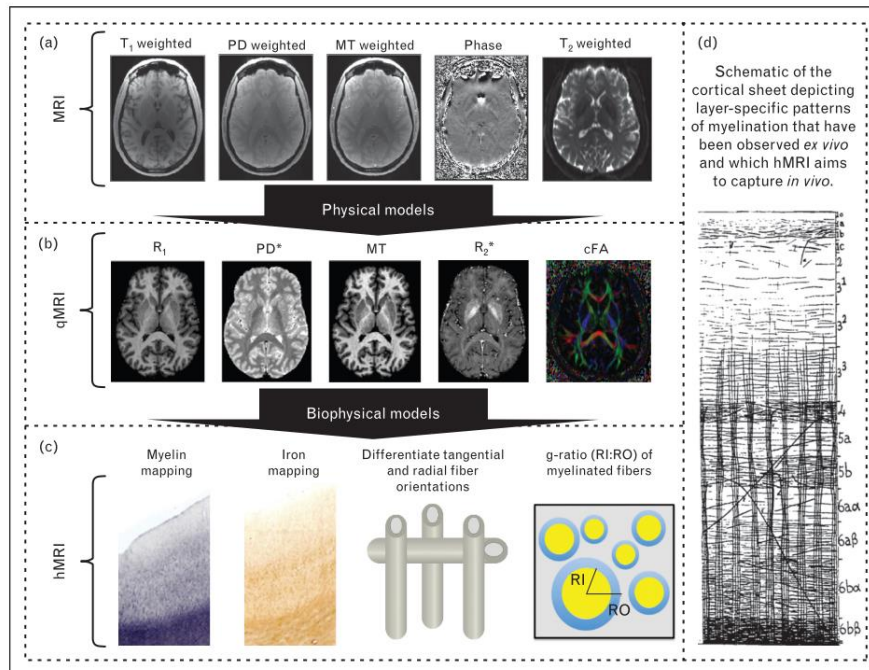


Figure 2.13: In-vivo histology using MRI (hMRI): (a) MRI measurements with weighted contrast to be more sensitive to specific MRI parameters (i.e. proton density (PD), magnetization transfer (MT) rate, longitudinal and transverse relation time (T₁ and T₂)); (b) from weighted MRI maps, using physical models, quantitative MRI (qMRI) maps, related to underlying tissue microstructure, can be computed; (c) then, using biophysical models, MRI or qMRI data are related to specific biological metrics such as myelin density, iron density, fibre orientation or g-ratio; finally (d) detailed microstructural description of the brain might be possible through hMRI (figure from (Weiskopf et al. 2015)).

To assess data from MPM protocol, first the voxel-based quantification (VBQ) toolbox was introduced by Draganski et al. 2011, and further developed (Balteau et al. 2018) under the name of hMRI toolbox (<http://hmri.info>). The hMRI toolbox is an easy-to-use open-source tool for handling and processing qMRI data and is available as an SPM toolbox in Matlab framework (tested in Matlab versions 8.0 (R2012b) to 9.3 (R2017b)). This toolbox allows the estimation of high-quality multi-parameter qMRI maps (i.e. R₁ R₂, PD and MT) that can be used for calculation of MRI biomarkers of tissue microstructure as well as improved delineation of subcortical brain structures. Embedded in the Statistical Parametric Mapping (SPM) framework in Matlab, it can be readily combined with existing

SPM tools and benefits from the extensive range of available tools for high-accuracy spatial registration and statistical inference. The general workflow to analyse MPM maps is depicted in figure 2.14 and includes: (i) map generation, (ii) post-processing and (iv) statistics in SPM. In the coming sections each step is described in more details providing some technical information.

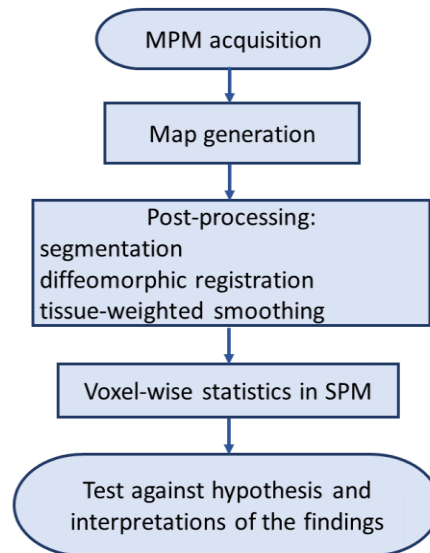


Figure 2.14: Schematic representation of the workflow to analyse MPM data. After the acquisition of MRI data using the MPM sequence, qMRI such as the longitudinal relaxation rate ($R1 = 1/T1$), the proton density (PD), the magnetisation transfer (MT) saturation and the effective transverse relaxation rate ($R2^* = 1/T2^*$) are generated using the Ernst equations. These qMRI maps are post-processed using tools from SPM toolbox including segmentation, registration and smoothing. After postprocessing MPM maps are warped in MNI space and can be used in a voxel-wise statistic in the framework of SPM.

2.5.1 Map generations in hMRI toolbox

As described in section 2.4, the MPM acquisition provides three (PDw, T1w and MTw) multi-echo spoiled gradient echo volumes (multi-echo FLASH sequence). These acquisitions can be described by the Ernst equation (Ernst and Anderson 1966; Helms, et al. 2008), and the corresponding qMRI can be computed using the equations described in sections 2.4.2-2.4.4.

The hMRI-toolbox provides more tools and options compared to the old VBQ in the generation of the MPM maps. Specifically, the hMRI toolbox can handle the situation where only a subset of data is available (or when some of the data are corrupted/poor quality). For example, $R2^*$, $R1$ and PD can still be estimated without MTw acquisitions, $R2^*$ alone can be estimated when neither MTw nor T1w acquisitions are available (single multi-echo PDw data). In addition, $R1$, PD and MT maps can be generated from single echo PDw, T1w and MTw images, not requiring multi-echo acquisitions.

In addition, hMRI toolbox can flexibly deal with a large range of site- and study-specific acquisition schemes, from the full MPM protocol to subsets of it, including single contrast echo trains for mapping $R2^*$ or variable flip angle data for mapping of $R1$ and PD using multi-echo or single-echo data (such as DESPOT1 (Deoni, Peters, and Rutt 2005)).

The hMRI toolbox provides some additional tools and suggestions for MPM processing. For example, to increase the consistency in individual head positions prior to normalisation or segmentation it is suggested to reorient the maps towards a standard pose, setting the anterior commissure at the origin (as defined in MNI space (Mazziotta et al. 1995a, 1995b, 2001)). The initial orientation of the maps is crucial for SPM's segmentation (Ashburner and Friston 2005) especially for longitudinal study, where multiple MRI acquisitions of the same subject need to be co-registered. Therefore, the reorientation of the images (using auto-reorient module) is highly suggested prior to any processing.

Finally, hMRI-toolbox provides metadata handling functionalities to retrieve parameter values and store processing parameters in the JSON-encoded metadata file (for more details, see Appendix B in (Balteau et al. 2018)).

2.5.2 hMRI implementations for bias corrections

By generating MPM maps, bias correction is also applied. The hMRI-toolbox provides correction methods for bias fields based on specific $B1$ transmit and receive field measurements or image processing methods. The bias corrections include the $B1$ (transmit) and the Receiver RF sensitivity bias correction.

B1 (transmit) bias correction

Several methods are implemented for the determination of $B1$ transmit bias field maps (fT expressed in p.u. of the nominal flip angle) for transmit bias correction of the quantitative data. Depending on the choice of the specific method, adequate input file and acquisition parameters must be given.

In the case of specific $B1$ transmit field measurements there are several methods such as the (i) EPI spin-echo (SE)/stimulated-echo (STE) method (Lutti et al. 2012); (ii) Actual Flip Angle Imaging (AFI) method (Yarnykh 2007); (iii) TFL $B1$ mapping based on a turbo flash (TFL) sequence with and without a pre-saturation pulse (Chung et al. 2010); or (iv) any of the previous methods with additional pre-processing (i.e. rescaling and smoothing). Further details on possible correction methods implemented in hMRI can be found in (Balteau et al. 2018) (Appendix C.3). If no additional bias transmit field is

acquired, then the UNICORT option is implemented in order to compute an inhomogeneity map using basis functions from the qMRI data.

Receiver RF sensitivity bias correction

In the hMRI toolbox, three options are available to correct for RF receive sensitivity bias (fR). Two of them rely on measured RF sensitivity maps (*Single* or *Per contrast* options) while the third method is data driven (Unified Segmentation). While options *Single* and *Unified Segmentation* assume that the sensitivity profile is consistent between contrasts (i.e. small inter-contrast subject movement) and the same correction is applied to all contrasts; the *Per contrast* option accounts for inter-contrast variation in RF sensitivity profile due to larger subject motion (Papp et al. 2016). In the latter case, field sensitivity measurements for each imaging contrast is included and applied to the corresponding contrast to correct for any coil sensitivity driven signal intensity modulation. In the *Single* case, the RF correction is computed from the single acquisition, whereas for the *Unified Segmentation* is computed from the image using Unified Segmentation algorithm (Ashburner and Friston 2005)). Details on the different RF sensitivity bias correction methods can be found in (Balteau et al. 2018) (Appendix C.4) and in the respective publications (Papp et al. 2016; Weiskopf et al. 2013).

2.5.3 Post-processing of MPM maps

The hMRI toolbox provides dedicated tools and tissue probability maps for the spatial processing of quantitative MRI maps based on the corresponding SPM framework. The spatial processing pipeline for hMRI data relies on three main operational steps: segmentation (Ashburner and Friston 2005), diffeomorphic registration (Ashburner 2007a) and tissue-weighted smoothing (Draganski et al. 2011). In hMRI, each step is implemented in a separate sub-module, but a fully integrated processing pipeline is provided as an additional option to facilitate standard data processing without the need to combine the individual steps. The segmentation and diffeomorphic registration rely on SPM functionalities tailored to the specific requirements of qMRI.

Segmentation of qMRI

The segmentation of the generated MPM maps (R1, R2*, PD and MT) is based on the unified segmentation algorithm as available in SPM12 (Ashburner and Friston 2005). The hMRI-segment allows the successive processing of a series of subjects and relies on one structural image per subject, (typically MT/R1 map or T1w image) and a set of tissue probability maps derived from multi-parametric maps (Lorio et al. 2014) denoted as extended TPMs (eTPM). The main outputs from the segmentation

step are probability maps of grey matter (GM), white matter (WM) and cerebro-spinal fluid (CSF) in native space (the c1/c2/c3 images); in Dartel-imported space (rc1/rc2 images) and in MNI space (classic elastic deformation, i.e. not with Dartel) with (wmc1/wmc2 images) and without (wc1/wc2 images) Jacobian modulation.

Diffeomorphic registration

The Diffeomorphic registration is based on the Dartel toolbox (Ashburner 2007a) and the key idea is to iteratively align the tissue class images (i.e. GM and WM) from a series of subjects to their own average by generating successive mean images with higher overlap and detail (i.e. increasing sharpness) called 'Templates'. By creating the Template, the corresponding deformation fields for each subject are generated encoding the nonlinear alignment from subject space to the final template (sub-module Run Dartel (create Templates)). Then, in all MPM maps are warped to MNI space (sub-module Normalise to MNI space) applying the estimated deformation fields. Note that unlike the standard Dartel toolbox in SPM, no smoothing and no modulation are applied at this stage.

Tissue-weighted smoothing

The tissue-weighted smoothing was proposed by Draganski et al. 2011 (Draganski, et al. 2011), in order to improve spatial realignment while accounting for the partial volume contribution (based on the tissue probability maps, WM/GM) in subject space. This combination of weighting and smoothing is expressed as:

$$(2.14) \quad v = \frac{g * (w s(\Phi)[e^{TPM(t)} > .05])}{g * w} [g * w > .05]$$

where:

- v is the resulting tissue-weighted smoothed image;
- $g*$ stands for convolution with a Gaussian smoothing kernel;
- ϕ encodes the spatial deformation from subject to standard space;
- $s(\phi)$ is a parameter map (e.g. MT, R1, R2*) in standard space warped by ϕ ;
- $w = |D\phi|t(\phi)$, the weights representing the tissue class density in standard space, accounting for volume changes;
- $t(\phi)$ represents subject's tissue class image, typically GM or WM, warped by ϕ ;
- $|D\phi|$ is a Jacobian determinants of deformation ϕ ;
- $[x > 0.05]$ is a masking operation where voxels with a value smaller than .05 are set to zero.

This step generates a tissue-weighted smoothed map (v) per tissue class (t) and parameter map (s) (i.e. smoothed GM and WM of MT map in MNI space) that can be used for the statistical analysis. Note, that since the threshold was defined as 5%, the tissue-weighted smoothed maps for GM and WM will

spatially overlap; therefore, an additional masking at the group-level is recommended to ensure that a given voxel is analysed only once. The main difference with VBM analyses, is that the tissue-weighted smoothing does not modulate the parameter maps (to account for volume changes), but instead preserves the quantitative values of the original qMRI maps in MNI space.

2.5.4 Statistical analysis

The statistical parametric mapping (SPM) analysis and modelling approaches can be applied to the spatially processed MPM maps, see, e.g., (Draganski et al. 2011; Freund et al. 2013). In this tool, parametric statistical models are assumed at each voxel using the general linear model. Data variability is described in terms of experimental and confounding effects, with residual variability. Hypotheses expressed in terms of the model parameters are assessed at each voxel with univariate statistics. For more details refer to SPM software (<https://www.fil.ion.ucl.ac.uk/spm/>).

2.6 Interpretation of MPM maps

The interpretation of MPM maps must be done carefully:

R2*

R2* maps is associated with different realisation of iron deposits (for a review, see e.g. (Edwards et al. 2018)), myelination of axons (Marques, et al. 2017), their orientation (Oh et al. 2013) and chemical exchange (Does 2018). The investigation of iron in the human cortex is important because cortical iron load is a risk factor for several neurodegenerative diseases (Bartzokis et al. 2004; van Duijn et al. 2017). Neocortical iron is inhomogeneously distributed among neocortical cells and sub-cellular compartments (Connor et al. 1990); and usually it is stored in the soluble paramagnetic iron-storage protein ferritin, iron clusters in mitochondria, and hæmoglobin (which is paramagnetic when deoxygenated). In addition, the distribution of iron is dynamic and can change under pathological condition (i.e. amyotrophic lateral sclerosis (ALS)) or in normal aging.

Interestingly, myelinated fibres are characterized by an increased iron concentration relative to the surrounding tissue in several primary cortical areas (primary visual, motor, and somatosensory cortex; (Stüber et al. 2014) and in the superior parietal lobe (Fukunaga et al. 2010; Stüber et al. 2014). This was shown using ex vivo histology where the distribution of iron and myelin have similar mesoscopic

lamellar structure. This might be due to iron's role as an enzymatic cofactor for the biosynthesis of cholesterol and other lipids, essential components of the myelin sheath (Connor and Menzies 1996; Morris et al. 1992). Probing the inhomogeneous iron distribution in vivo using $R2^*$, therefore has the potential to provide useful and specific biomarkers for compartments such as glial cells and iron rich fibres, with potential clinical impact. An alternative multi-compartment models can be used, e.g., to separately describe the orientation-dependence of myelinated fibre pathways in $R2^*$ parameter maps (Alonso-Ortiz, Levesque, and Pike 2018; Lee et al. 2017; Wharton and Bowtell 2012).

R1

$R1$ has been shown to be linearly depend on different microstructural tissue properties such as the local mobility of water molecules, the macromolecular content and the local concentration of paramagnetic ions such as iron or gadolinium-based contrast agents (Fatouros and Marmarou 1999; Fullerton, Potter, and Dornbluth 1982). A general linear relaxometry model was defined in order to describe the dependence of $R1$ on these components. Under the conditions of fast exchange, the cross-relaxation time between different water components is assumed to be much shorter than the MR relaxation times. In this case, the measured longitudinal relaxation rate is a weighted sum of the relaxation rates of the various contributory components (Fullerton et al. 1982):

$$(2.15) \quad R1 = \sum_i f_i R_{1i}$$

where f_i is the fraction of spins in pool i with relaxation rate R_{1i} . In the absence of any exogenous contrast agents, the measured $R1$ can be empirically modelled using the following equation:

$$(2.16) \quad R1 = R_{1f} + f_M r_{1M} + f_{FE} r_{1FE} + \sum_j f_j R_{1j}$$

Where R_{1f} is the relaxation rate of free water; f_M is the fraction of spins bound to macromolecules; r_{1M} is the relaxivity at macromolecular sites (i.e., $R_{1M} - R_{1f}$) where R_{1M} is the relaxation rate at macromolecular sites, f_{FE} is the fraction of spins at iron sites, and r_{1FE} is the relaxivity at iron sites; the index j sums over all potential unspecified contributions that remain. It was shown that $R1$ as depends on the magnetic intensity B_0 (Rooney et al. 2007).

In the MPM protocol, MT and $R2^*$ maps can be used as surrogate markers for the macromolecular and iron concentrations, respectively, and $R1$ map can be modelled as:

$$(2.17) \quad R1 = \beta_0 + \beta_1 MT(r) + \beta_2 R2^*(r) + \varepsilon(r)$$

Where β parameters are global constants and can be computed from a big cohort. Synthetic R1 maps can be computed using R2* and MT metrics (Callaghan et al. 2015ba). Even if R1 depends on different micro-structural tissue properties, the variation of T1 (which is the inverse of R1) values over the cortex, however, more strongly dependent on myelin concentration than on iron concentration (Rooney et al. 2007), making this a relatively sensitive and specific marker for changes in myelin content (Campbell et al. 2017; Dick et al. 2012; Lutti et al. 2014; Sereno et al. 2013). This is because iron in the brain is contained exclusively in ferritin-like proteins which are not very efficient in catalyzing T1 relaxation.

MT saturation

MT saturation is a semi-quantitative measure of the bound-pool water fraction (Helms, et al. 2008) and is often used as a marker for myelin content (Callaghan et al. 2014; Freund et al. 2013; Laule et al. 2007). The MT saturation map differs from the commonly used MT ratio (MTR) by explicitly removing the bias introduced by the spatially varying T1 relaxation time and B1-transmit field (Helms, et al. 2008a). Additional minor corrections for B1 transmit field inhomogeneity is also applied as described in Weiskopf et al. 2013. The main advantage in removing the spatially varying bias is the higher contrast in deep brain structures and reduced variance in the data (Callaghan, Mohammadi, and Weiskopf 2016) allowing better comparison across sites and over time (longitudinal studies). However, the MT saturation map does not depend only on the bound-pool fraction but also on the exchange between the bound and free water pools. It should be noted, in fact, that pathological processes unrelated to myelination can also affect these MT metrics (Vavasour et al. 2011).

A more direct measure of the bound-pool fraction is provided by quantitative MT (qMT), which requires more acquisition time and typically limiting the spatial resolution (e.g., 2mm isotropic in (Stikov et al. 2011a)).

Proton density

PD has been shown to be sensitive to white matter myelin content (Berman et al. 2018; Mezer et al. 2013). However, an investigation by Gomez et al. (2017) of maturation-related cortical PD change in a functionally-derived cortical area found a decrease in PD with age that seemed too large to be exclusively due to an increase in myelination. They speculated that this change could instead be driven by processes such as dendrite or glial cell proliferation.

2.7 Limitations of MPM

The ideal MPM protocol includes dedicated measurements of transmit and receive field inhomogeneities, which are typically based on customised sequences and might include imperfections (i.e. residual misalignment between measured receive (or transmit) field and the spoiled gradient echo images). Moreover, there are no available body coils for the implementation of RF sensitivity measurements and bias correction at 7T.

In the clinical settings, bias measurements are often not acquired due to time constraints, and B1 transmit bias correction (Weiskopf et al. 2011b) or RF sensitivity bias correction maps are based on Unified Segmentation approach which lead to lesser accuracy with some residual modulations. In addition, these corrections were optimised only for the Siemens TIM-TRIO MR system. The proposed MPM protocol uses RF and gradient spoiling to minimise unwanted transverse net magnetisation. Imperfect spoiling, which depends on the precise sequence protocol settings, can leave a residual bias in the R1 map if no further correction is used (Preibisch and Deichmann 2009; Yarnykh 2010).

Even if MPM map generations are based on Ernst equation and thus provides a comprehensive means of calculating a collection of physical quantitative (and semi-quantitative) parameters, including PD, R2*, R1 and MT; there are more sophisticated signal models that can be derived to relate the parameters more directly to the underlying biophysical mechanisms and tissue characteristics.

The major source of artefacts in MR images is the head motion, with severe consequences on qMRI and morphological measures of the brain (Callaghan et al. 2015b; Reuter et al. 2015; Weiskopf et al. 2014). The intra- and inter-scan head motion measures from hMRI toolbox, can be combined to objectively classify data according to quality. This quality measure might be used to exclude or down weight poor-quality data of individuals in a statistical group analysis. Note that even if hMRI toolbox offers quantitative measures of image quality, visual inspection remains largely considered as the gold-standard in the field (Rosen et al. 2018).

Additional limitations are coming from the post-processing including spatial normalisation accuracy, segmentation errors and partial volume effects (Ashburner, Andersson, and Friston 2000; Ridgway et al. 2008). The initial reorientation procedure can help in improving the segmentation however it might fail in those maps with poor signal-to-noise ratio, contrast-to-noise ratio, or outliers. In general, it is good practice to visually inspect the results of each step. The choice of the appropriate smoothing

kernel and its performance compared to alternative methods (e.g. TBSS (Smith et al. 2006) or TSPOON (Lee et al. 2009)) is still a subject of active research.

Finally, MPM was optimized for specific sequences and scanners, therefore appropriate inter-scanner calibration (Volz et al. 2012) might be needed.

2.8 Future developments

Future developments might include:

- Broad applicability of the toolbox handling multi-scanner and multi-vendor data, in this context protocol-specific correction parameters are required
- Application of ultra-high field MR systems
- Increase sensitivity to small inter-individual and intra-individual (e.g. plasticity) microstructural changes. In this context, the presence of motion has been investigated (Callaghan et al. 2015b; Weiskopf et al. 2014) retrospective robust estimation of $R2^*$ parameters have been suggested (Weiskopf et al. 2014) and could be implemented in future; or the use of adaptive noise removal methods along with appropriate handling of the Rician bias problem are important future improvements.
- Quantitative susceptibility mapping (QSM), taking advantage of the existing phase images acquired with the MPM protocol (Acosta-Cabronero et al. 2018)
- Including new biophysical models that take advantage of the multi-contrast MPM data for in vivo histology such as the MR g-ratio (the ratio between inner and outer diameter of a myelinated axon) model (Ellerbrock and Mohammadi 2018a; Mohammadi et al. 2015a); or the DTI & Fiber tools (Reisert et al. 2013).
- Improved robustness and spatial resolution

2.9 Conclusion background I

In this chapter the technical background of MRI techniques was described in order to understand the physical phenomena behind an image acquisition. Among the different MRI techniques, this chapter focused on the MPM protocols which provides qMRI parameters such as the longitudinal relaxation

rate ($R1 = 1/T1$), the proton density (PD), the magnetisation transfer (MT) saturation and the effective transverse relaxation rate ($R2^* = 1/T2^*$). Each map is computed using biophysical models that are sensitive to specific microstructural changes (i.e. myelin, water, or iron content). Additionally, the available tool for MPM processing named “hMRI” was also presented in order to understand the technical implementations and post-processing applied to the brain maps. These maps were used in clinical studies to investigate the microstructural changes, therefore the typical processing workflow for MPM maps and the corresponding biological interpretation was presented. However, further developments are still needed in order to apply such maps in the spinal cord and be able to investigate cord diseases.

3 Background II: Spinal Cord Injury

Temporal or permanent damage to the spinal cord is defined as spinal cord injury (SCI) and can be divided into traumatic and non-traumatic aetiologies. Traumatic SCI occurs when an external physical impact (i.e. a motor vehicle, fall, sports-related injury) damages the spinal cord; whereas non-traumatic SCI occurs when the primary injury is generated by an acute or chronic disease such as tumours, infections or neurodegenerative diseases (i.e. multiple sclerosis (MS), neuromyelitis optica (NMO)). Spinal cord injuries might lead to impairments to the normal motor, sensory and autonomous function and the corresponding symptoms and clinical outcomes vary widely depending on the level and severity of the injury. Although endogenous mechanisms exist for partial spinal cord regeneration, the overall capacity for spinal cord repair is rather limited (Ahuja et al. 2017) and no cures are available. Therefore, SCI has an enormous impact on the physical, psychological, social and economic aspect of the patient's life.

3.1 The anatomy of the spinal cord

The human spinal cord is part of the central nervous system and it includes several bundles of nervous tissue going from the brainstem to the lumbar region of the vertebral column. The spinal cord is located within the spinal canal and surrounded by a variable layer of cerebrospinal fluid (CSF) and protected by the vertebrae. In adult humans, the spinal cord has an average length of about 45 cm and is about 15 mm thick at its widest point at the cervical enlargement (Goto and Otsuka 1997). The spinal cord ensures the conduction of the neural signals from the brain to the peripheral nervous system (motor information) and from the peripheral nervous system to the brain (sensory information). Additionally, spinal cord reflexes play a crucial role in the control of muscle tone at rest and during movement (Turchick, et al 2012).

A transverse section of the spinal cord shows a highly organized structure, presenting an "H" or butterfly-shaped central grey matter surrounded by ascending and descending white matter columns, also called funiculi. Grey matter (GM) mainly contains neuronal cell bodies (which can belong to motor neurons or interneurons), glial cells (astrocytes and oligodendrocytes), and neuropil (dendrites and mostly unmyelinated axons). White matter (WM) consists of a very large number of axonal fibres which are organized into bundles (funiculus) and tracts (fasciculus) and other cell types such as astrocytes, oligodendrocytes, and microglia. The WM is divided into the dorsal (or posterior), lateral and ventral

(or anterior) column and presents a somatotopic organization including ascending (sensory related) and descending (motor related) tracts (figure 3.1).

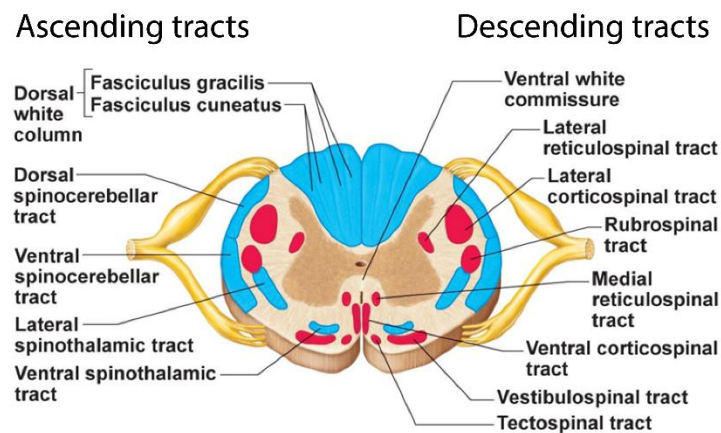


Figure 3.1 Transverse section of the spinal cord showing the main sensory pathways (ascending, afferent tracts) in blue; and motor pathways (descending, efferent tracts) in red. The spinal cord presents a topological organization and specialized tracts rising along specific regions. Specifically, sensory pathways located in the dorsal column are carrying information related to tactile, (i.e. pressure, vibration, position, and movement sense) and conscious proprioception such as the gracile and cuneate fasciculi. More anteriorly and laterally, the lateral column the lateral spinothalamic tract (or neospinothalamic tract) are carrying pain, temperature and crude touch information from somatic and visceral structures. Nearby laterally, the dorsal and ventral spinocerebellar tracts carry unconscious proprioception information from muscles and joints of the lower extremity to the cerebellum. In the ventral column (funiculus) there are four prominent sensory tracts: (i) the paleospinothalamic tract (or ventral spinothalamic tract) carrying pain, temperature, and information associated with touch to the brain stem nuclei and to the diencephalon, (ii) the spinoolivary tract carrying information from Golgi tendon organs to the cerebellum, (iii) the spinoreticular tract, and (iv) the spinotectal tract. The descending motor pathways are distributed mainly in the lateral and ventral columns. The lateral column includes the corticospinal and the rubrospinal tracts, carrying information associated with voluntary movement. The ventral column includes four tracts: the anterior corticospinal, the vestibulospinal, the reticulospinal, and the tectospinal tracts. These pathways control proximal axial and girdle muscles involved in postural tone, balance, orienting movements of the head and neck, and automatic gait-related movements (Diaz and Morales 2016).

Along its length, the spinal cord is divided into four regions (Figure 3.2) with distinguishable size and shape. The spinal cord presents two enlargements: the cervical enlargement stretching from the C5 to T1 vertebrae, and the lumbosacral enlargement located between T11 and L3, these enlargements give rise to the nerve plexus for the arms and legs, respectively. At each vertebral level, a pair of dorsal and ventral rootlets leaves the spinal cord and merges into a single spinal nerve outside the spinal cord (Figure 3.2c). These spinal nerves (31 pairs in total: 8 cervical, 12 thoracic, 5 lumbar, 5 sacral, and 1 pair of coccygeal nerves) contain both motor and sensory fibres.

The spinal cord is not a static structure, but it moves within the spinal canal due to the cerebrospinal fluid and arterial pulsation with an amplitude that diminishes with greater distance from the head (Figley and Stroman 2007).

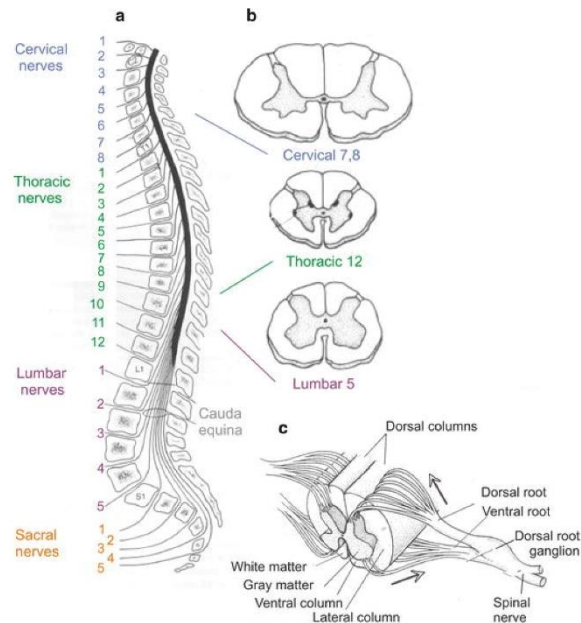


Figure 3.2: Sagittal view of spinal cord showing the cervical, thoracic, lumbar and sacral regions (a). Each region can be visually distinguished in the size and shape (b): the white matter, made up of longitudinal tracts, is thickest in the cervical level where most ascending fibres have already entered the cord and most descending fibres have not yet terminated on their targets, while the sacral cord is mostly grey matter. At each vertebral level, a pair of dorsal and ventral rootlets leaves the spinal cord and merges into a single spinal nerve outside the spinal cord (c). The figure is adapted from (Jankowska 2013).

3.2 Epidemiology of traumatic SCI

The incidence of traumatic SCI varies worldwide, with around 15 cases per million in Western Europe and around 39 cases in North America (Cripps et al. 2011). The incidence of SCI is approximately four times higher in males than in females (Chen et al. 2016) and the age profile shows a bimodal distribution with one peak between 15-29 years and the second peak (smaller but growing) for over-50 years old. In the general population, traumatic SCI occurs most frequently at the cervical level (~60%), followed by the thoracic (~30%) and lumbosacral level (~10%)(Chen et al. 2016).

3.3 Pathophysiology of traumatic SCI

The primary injury, coming from the direct physical trauma (e.g. contusion, compression, laceration) to the spinal cord triggers a cascade of changes at the cellular, structural, and functional level (Dumont et al. 2001). Although several definitions exist, the time course of these pathophysiological processes

are classified as acute (<48 hours), subacute (48 hours to 14 days), intermediate (14 days to 6 months), and chronic stage (>6 months) (Ahuja et al. 2017).

3.3.1 Acute stage

The acute stage of traumatic SCI is characterized by the primary injury and a cascade of secondary damages. The primary damage might lead to immediate cell death of neurons and oligodendrocytes, disruption of the vasculature and blood–spinal cord barrier. The destruction of the micro-vascular supply of the spinal cord initiates immediately (within minutes) a secondary injury cascade that leads to cell dysfunction and death due to cell permeabilization, pro-apoptotic signalling and ischaemic injury (Dumont et al. 2001). In addition, blood vessel injury can cause severe haemorrhages, which can expose the cord to an influx of inflammatory cells, cytokines and vaso-active peptides. The subsequent inflammatory response and the disrupted blood–spinal cord barrier, progressively add to spinal cord swelling which can lead to further mechanical compression and damage to multiple spinal segments (Bunge et al. 1993).

3.3.2 Subacute stage

In the subacute period, ischaemia, inflammation and excitotoxicity contribute to cell death of neurons and glia due to the loss of homeostasis and dysregulation of intracellular calcium. Furthermore, ongoing necrosis of neurons and glia releases ATP, DNA and potassium, which can activate microglial and other inflammatory cells (i.e. macrophages, polymorphonuclear cells and lymphocytes). These inflammatory cells infiltrate the injury site and propagate the inflammatory response and contribute to ongoing apoptosis of neurons and oligodendrocytes. The prolonged ischaemia contributes to further neuronal and glial (predominantly oligodendrocyte) cell death and the propagation of the injury (Dusart and Schwab 1994).

3.3.3 Intermediate stage

Several days after injury, microglia and blood monocytes are activated and transformed into rounded, polygonal cells referred to as macrophages. Macrophages can persist in injury sites for weeks to months and are involved in the removal of necrotic debris as well as being the major players in inflammatory and immunological responses. Astrocytes at the edge of the lesion undergo hypertrophy and their nuclei become larger and paler (most of the astrocytes within the lesion will die) (Gensel and Zhang 2015; O’Shea, et al. 2017). This profusion of processes ultimately results in a glial/astrocytic scar

formation. Seven to ten days post injury, an increased number of blood vessels are identified in the lesion site, probably due to angiogenesis (absolute increase) or loss of tissue with preservation of vascular structures (relative increase).

After the injury, the affected axons begin to degenerate. This axonal degeneration is characterized by the disintegration of the cytoskeletal proteins such as microtubules and neurofilaments, followed by breakdown of the axonal membrane and myelin sheath (Buss et al. 2004; Rotshenker 2011). This degeneration propagates from the lesion site, away or towards the cell body (soma). The degeneration of the distal part (away from the soma) is known as anterograde degeneration or Wallerian degeneration; whereas the degeneration of the proximal part (towards the soma) is called retrograde degeneration (Wang, et al. 2012) which is a slower process and can progress until years after the injury. In addition, trans-neuronal degeneration can also occur due to the disruption of input from (anterograde, “dying forward”) or output to other neurons (retrograde, “dying backward”), resulting in a more widespread remote degeneration pattern (Al-Louzi et al. 2017; Jindahra, Petrie, and Plant 2012). All the debris from the axons' breakdown are cleared by the macrophages (Neumann et al. 2009) (figure 2.3).

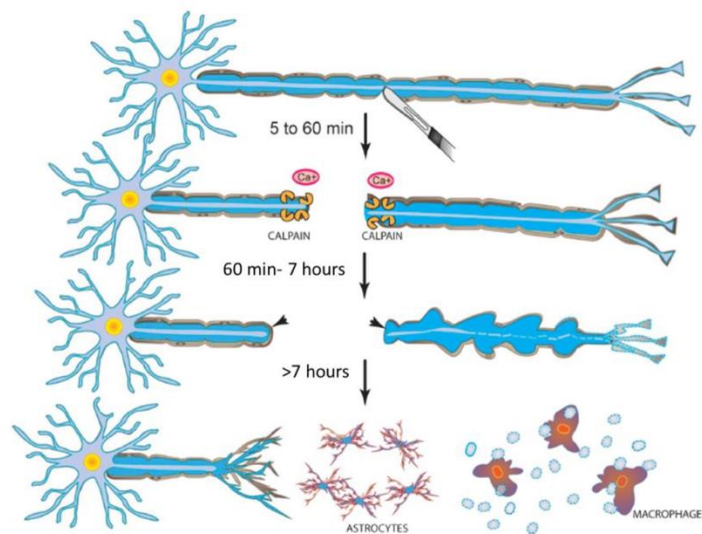


figure 3.3: Schematic representation of Wallerian axon degeneration from (Wang et al. 2012). After an injury to the spinal cord, the degeneration of the proximal (left) and distal (right) segments is principally mediated by extracellular Ca^{2+} influx and activation of the intracellular Ca^{2+} -dependent protease calpain (within 5–30 min). Then, the injured axon slowly retracts and forms axonal bulbs at the injury sites which remain morphologically stable and electrically excitable for approximately 24 to 48 h after injury. After 72 h from the injury, the cytoskeleton of the distal axon breaks down and fragments. Finally, these fragments are cleared by glia cells (i.e. astrocytes, macrophages) (blue circles).

3.3.4 Chronic stage

In the chronic stage the overwhelming cell death and degeneration promotes the ex vacuo (loss of tissue volume) and individual cavities coalesce to form a single cystic cavitation, which contain extracellular fluid, thin bands of connective tissue and macrophages (Norenberg, et al. 2004). These cystic cavities constitute a barrier to the directed axonal regrowth and are a poor substrate for cell migration (Milhorat et al. 1995; Tator 1995). Animal studies have shown that cystic cavities are surrounded by a perilesional zone in which reactive astrocytes proliferate and tightly interweave their processes, creating an inhibitory mesh-like array (Berry et al. 1983). In the chronic stage, most of the degenerative processes are already stabilized even if progressive degeneration is still visible after years from the injury (Blakemore 1974; Blight and Decrescito 1986). Partial regeneration of the injured spinal cord is possible due to the anatomical and synaptic plasticity, which might contribute to ongoing functional recovery (Lynskey, et al. 2008; Raineteau and Schwab 2001). Remyelination is also possible but is usually limited and incomplete (Blight and Decrescito 1986; Harrison and McDonald 1977; Totoiu and Keirstead 2005). Furthermore, neural precursor cell pools, which are mostly found in the ependymal layers of the central canal, as well as widely distributed oligodendrocyte precursor cells, can generate neurons, oligodendrocytes and astrocytes (including reactive astrocytes) (Barnabé-Heider et al. 2010; Meletis et al. 2008). However this regeneration is highly limited (limited clinical recovery) and most of the time SCI patients are left with significant degrees of impairment (Dietz and Fouad 2014; Fehlings and Tator 1995; Freund et al. 2011).

3.4 Recovery and Plasticity after SCI

Although spontaneous regeneration of lesioned fibres is limited in the adult central nervous system, significant recovery can still occur in the first year following incomplete SCIs (Burns et al. 1997; Raineteau and Schwab 2001). The prognosis depends primarily on the initial severity and level of the injury, but also postinjury medical and surgical care, and rehabilitative interventions have been shown to promote recovery after incomplete SCI in humans. The mechanism behind recovery and learning new skills is defined as “plasticity”. Plasticity or neuroplasticity refers to functional or structural changes occurring in the adult central nervous system (CNS) as a result of peripheral and internal input. From the biological point of view, plastic changes may include synaptic formations and synaptic strengthening (Rioult-Pedotti, et al. 2007), axonal sprouting (Bareyre et al. 2004) and changes of intracellular properties (Boulenguez et al. 2010). These mechanisms are crucial for learning, memory, and recovery from neural injury (Lawrence and Kuypers 1968; Raineteau and Schwab 2001; Weidner

et al. 2001; Zai and Wrathall 2005). After a SCI, spontaneous adaptive and maladaptive changes occur at several anatomical and physiological levels of the CNS, i.e. spinal cord, brainstem and cortex (Bruehlmeier et al. 1998; Jurkiewicz et al. n.d.). Synaptic plasticity in pre-existing pathways and the formation of new circuits through collateral sprouting of lesioned and unlesioned fibres are important components of the recovery process (Raineteau and Schwab 2001). Training and rehabilitation strategies have the general goal to promote plasticity for regaining function and improve the clinical outcome.

3.4.1 Spontaneous adaptive and maladaptive plasticity after SCI

After a SCI, spontaneous recovery of sensorimotor functions is possible within the first few months after a SCI (Curt et al. 2008). This spontaneous plasticity after SCI is not limited to the injury site, but it affects the full spinal cord including supraspinal structures (i.e. brain).

Animal studies showed that at the lesion site, motor fibres can surround the lesion and connect to commissural neurons lying in the opposite side of the lesion, or new intraspinal circuits can be formed and bridge the lesion site (Bareyre et al. 2004). In addition, proliferation of oligodendrocytes and astrocytes around the lesion can partially replace some of the damaged cell or remyelinate axons (Beattie et al. 1997; Zai and Wrathall 2005; Zai, Yoo, and Wrathall 2005). Thus, after a SCI the resolution of neuropraxia (Curt et al. 2008) and remyelination of spared axons is possible and novel pathways and substrates can re-establish the connection through the spinal cord surrounding the lesion and promoting some form of spontaneous recovery (Lawrence and Kuypers 1968; Raineteau and Schwab 2001; Weidner et al. 2001; Zai and Wrathall 2005).

Reorganization of brain cortex after SCIs in humans (Green et al. 1999) and rodents (Bareyre et al. 2004) was also reported. The hypothesized underlying mechanisms behind brain plasticity are related to disinhibition of latent cortical connections, axonal sprouting (Bareyre et al. 2004; Dobkin 2004; Nudo 1951), density and morphological changes in dendritic spines of cortical motoneurons (Kim et al. 2006; Nudo 1951). The described changes are “adaptive” in the sense that they promote recovery and are therefore desirable, however other plastic changes might be not beneficial for the patient and are defined “maladaptive” plasticity (Rosenkranz et al. 2005). This maladaptive plasticity can occur in the spinal cord and in the brain. In the spinal cord, the loss of circuits below the injury lead to imbalance of inhibitory and excitatory activity and, might increase excitability of the spinal cord by peripheral stimulation (Beauparlant et al. 2013; Dietz 2010) leading to neuropathic pain (Wrigley et al. 2009). In the brain, maladaptive changes were shown in the somatosensory cortex, corticospinal tracts and

visual-processing areas, showing a link between the degree of cortical reorganization and the intensity of persistent neuropathic pain following SCI (Jutzeler et al. 2016; Mole et al. 2014; Wrigley et al. 2009).

Plastic changes in the brain were also shown in absence of stimuli, as for example after limb amputation (Draganski et al. 2006) where the brain presented a decreased GM in the posterolateral thalamus contralateral to the side of the amputation which positively correlated with the time span after the amputation. Long-standing limb amputation can cause structural reorganization of brainstem, thalamic nuclei or in the somatosensory cortex (Florence, Taub, and Kaas 1998). Even short time immobilization influenced the sensorimotor representation and functional output for both arms (Debarnot et al. 2018).

Spontaneous brain plasticity is therefore a natural adaptation mechanism occurring in the adult CNS as a result of peripheral and internal input. In SCI patients this spontaneous neuroplasticity appears to be both adaptive (promoting recovery and providing targets for therapy) and maladaptive (inhibiting recovery and impairing function). Training and rehabilitative strategies can be used to enhance adaptive plasticity and/or mitigate maladaptive plasticity after SCI in order to enhance recovery.

3.4.2 Training-induced plasticity after SCI

Training and rehabilitative therapies can promote structural changes along the CNS. These plastic changes were initially shown from cross-sectional studies where group of experts (or trained subjects) were compared with group of controls (naïve to the training). In this context, taxi drivers showed larger posterior hippocampal volume compared to normal subjects (Maguire et al. 2000). The posterior hippocampus is related to spatial navigation and the increased volume correlated with years of experience. Musicians showed greater grey matter volume (Gaser and Schlaug 2003) and cortical thickness (Bermudez et al. 2009) in auditory cortices; and plastic changes in the motor regions and in white matter of the spinothalamic tract (Bengtsson et al. 2005). These training-induced changes were supported by the correlation between brain changes and years of musical practice.

However, cross-sectional studies cannot discriminate whether these plastic changes are related to groups differences or whether they are caused by learning new skills. Therefore, longitudinal studies were designed to better investigate training-induced changes and evaluate the complex relationship between anatomical changes and underlying functionality. One of the first longitudinal studies showed increased bilateral grey matter density in the visual motion area and occipito-parietal regions in people that learnt to juggle over a period of a 3 months (Draganski et al. 2004). Similarly, by practicing a

complex whole-body balancing task increased GM in frontal and parietal cortex were shown after 2 days of training (Taubert et al. 2010), and altered fractional anisotropy after 6 weeks of training (Sehm et al. 2014).

3.4.3 Underlying cellular and molecular mechanisms

Training-induced plasticity can occur in the GM and WM involving different cellular and molecular mechanisms. Even if the direct investigation of cellular changes are not possible in vivo, human neuroimaging studies detected structural changes in the brain that related to behavioural improvement. The cellular and molecular underlying mechanism were supported by animal studies and are broadly categorized into neuronal changes in GM, WM and extra-neuronal changes.

Training-induced neural changes in the grey matter

The grey matter is mainly characterized by neuronal cell bodies and unmyelinated axons, therefore training-induced changes include neurogenesis, synaptogenesis and changes in neuronal morphology (figure 3.4 a). Neurogenesis indicates growth of new neurons in adulthood and usually is reflected by an increased volume in MRI data. Evidence of adult training-induced neurogenesis was shown in the hippocampus (Eriksson and Perfilieva 1998; Tronel et al. 2010). In addition, animal studies with induced transient reduction of hippocampal neurons, showed impaired performance in memory tasks (Deng et al. 2009) and conversely, increasing adult hippocampal neurogenesis, by genetic manipulation, improved pattern separation learning (Deng et al. 2009). Although adult neurogenesis in the hippocampus was observed in animal studies, this is a relatively small increase compared to the total number of hippocampal neurons. Moreover, neurogenesis in the neocortex is complex and still not fully understood (Gould et al. 1999) making neurogenesis a minor candidate in training-induced changes particularly in regions outside the hippocampus.

Even if neurogenesis is unlikely to play a role in training-induced changes in the GM, changes in neuronal morphology may nevertheless contribute. It was shown that training can induce synaptogenesis (Kleim, et al. 2002) and changes in dendritic spine morphology (Kolb, et al. 2008). Synaptogenesis indicates the formation of new synapses between existing neurons; whereas changes

in the dendritic spine morphology include arborization. These changes may also persist after learning as shown in animal studies (Yang, et al. 2009).

Training-induced neural changes in the white matter

The white matter consists mainly of myelinated axons; therefore, training induces changes in the myelination and in the axons in terms of number, diameter, branching, trajectories and the packing density of fibers (figure 3.4 b). Training-induced changes in the WM are mainly related to increased or optimized speed or synchrony of impulse transmission (Fields 2008) in order to increase functional performance with learning.

Myelin is the external sheet surrounding axons and accelerating the action potential propagation, therefore myelin modulation, including myelination of unmyelinated axons or modification of the myelin sheaths, can alter or optimize brain circuitries according to experience. From animal studies it was shown that, 1/3 of oligodendrocyte progenitor cells (OPC) originate after adolescence (Psachoulia et al. 2009) and can participate in the repair of myelin and might participate in learning if myelination of unmyelinated axons is stimulated by functional activity. Another mechanism could go in the direction of decreased internodal lengths which was shown in visual cortex of rhesus monkeys (Peters, Verderosa, and Sethares 2008) during normal aging, suggesting active remyelination throughout life. A number of neuroimaging studies have reported changes in white matter structure with learning in adults (Scholz et al. 2009; Takeuchi et al. 2010; M Taubert et al. 2010) suggesting regulation of myelin as a novel form of brain plasticity (Lakhani et al. 2016).

Apart from myelin changes, in the WM activity-dependent axonal sprouting, pruning or re-routing are also possible. It was shown that in the hippocampus, sprouting of mossy fiber axons has been observed after induction of long-term potentiation (Adams et al. 1997), and spatial learning (Ramírez-Amaya and Escobar 1999). Using genetic manipulation in mice, in which restricted populations of neurons in the hippocampal circuit were inactivated, it was shown that inactive axons were eliminated through a competition with active axons (Yasuda et al. 2011); this suggests that pruning of axons is guided by activity-dependent competition to refine functional circuits. Rewiring of axons was shown in animal studies, for example macaque monkeys showed a novel pattern of anatomical connectivity between visual and parietal cortex in learning to use a rake to retrieve food pellets (Johansen-Berg 2007). In this study, inputs from certain visual areas were detected in trained animals but not in untrained animals,

suggesting the possibility of a re-branching of fibers in response to training. Similar rewiring has been observed after brain injury in a squirrel monkey model (Dancause et al. 2005).

Training-induced extra-neural changes in grey and white matter

Extra-neuronal changes include gliogenesis and angiogenesis, which can occur in both GM and WM (figure 3.4). Gliogenesis indicates an increase in the number and size of glial cells such as astrocytes and oligodendrocyte progenitor cells (OPCs). In fact glia cells, unlike mature neurons, retain the ability to divide in the adult brain (Rakic 2002); and it was shown that structural plasticity of non-neuronal cells, occurs in response to learning and experience (Dong and Greenough 2004). Specifically, astrocytes have an important role in synaptic function, ion homeostasis, neuroenergetics, and regulating blood flow in response to neuronal activity; whereas microglia, even if part of the immune system and traditionally involved in pathological conditions, are involved in the structural and functional plasticity of synapses and dendrites during development and learning (Tremblay, et al. 2010; Wake et al. 2009).

Angiogenesis indicates vascular changes. Training-induced vascular changes were shown in middle-aged monkeys where increased vasculature in the cerebral cortex was histologically-quantified after physical exercise in parallel with improved performance on cognitive tests, and interestingly these effects were lost after a sedentary period of 3 months (Kinam Park 2014; Rhyu et al. 2010).

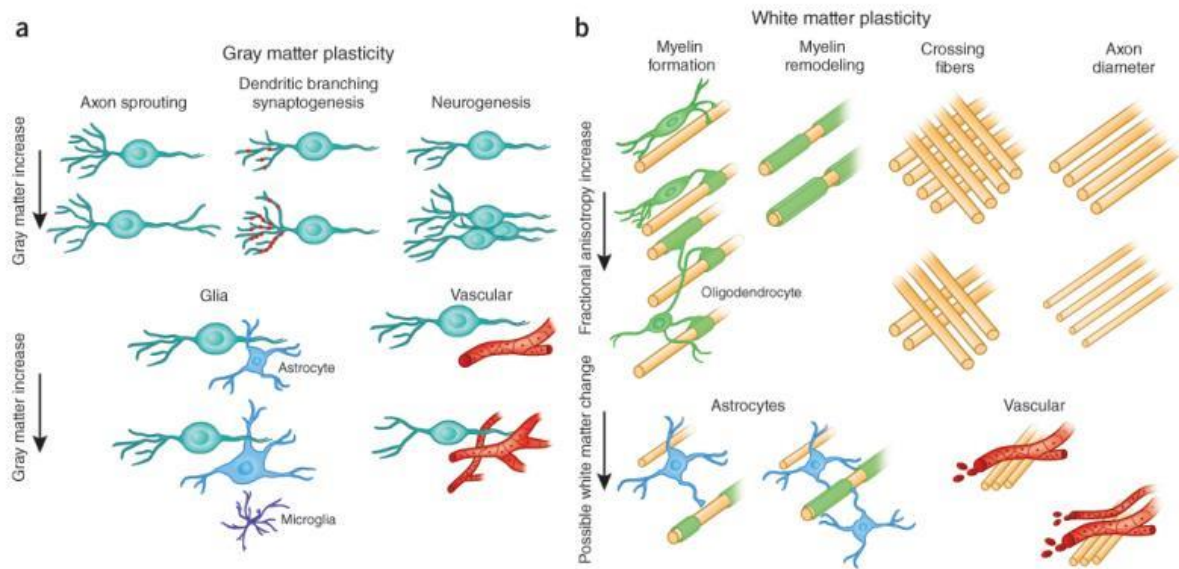


Figure 3.4: Schematic representation of possible cellular mechanism in the GM (a) and WM (b). Specifically, in the GM (a) training-induced neural changes might include axon sprouting, dendritic branching and synaptogenesis and neurogenesis (first row). In the WM (b) training-induced changes might induce changes in the myelination (myelination of unmyelinated axons, changes in myelin thickness and morphology) or in the axons (number of axon, diameter, branching, packing density, or fiber crossing) (first row). Non neural structure may also play a role in training-induced changes including changes in glial number and morphology, and angiogenesis (bottom row) in both GM and WM. The figure is adapted from (Zatorre, Fields, and Johansen-Berg 2012).

3.5 Diagnostic tools

The clinical manifestation of SCI is complex and heterogeneous; several diagnostic tools are used in order to investigate the neurological changes and prognosis of the disease. Typically, SCI patients are assessed using three main measurements: (i) Clinical examinations (ii) Electrophysiological measurements and (iii) spinal imaging.

3.5.1 Clinical examination

Clinical examinations are key to define the severity of injury and predict recovery. Specifically, improved neurological recovery should be linked to increased capacity to perform tasks such as walking, reaching and grasping, which results in meaningful gains in mobility and self-care. In this section the most popular clinical examinations are described such as the International Standards for Neurological Classification of SCI which is the clinical gold standard for measurement of severity; Graded Redefined Assessment of Strength Sensibility and Prehension (GRASSP), specific upper

extremity and the Spinal Cord Independence Measure (SCIM) which is a measure of self-care and independence.

International Standards for Neurological Classification of Spinal Cord Injury (ISNCSCI)

The International Standards for Neurological Classification of Spinal Cord Injury (ISNCSCI), revised in 2011 (Steven C. Kirshblum et al. 2011), was published by the American Spinal Injury Association (ASIA) and provides the gold standards for assessing motor and sensory deficits, the level and completeness of the injury. The motor assessment includes testing five key muscles in the upper (elbow flexors, wrist extensors, elbow extensor, finger flexors, finger abductors) and lower (hip flexors, knee extensors, ankle dorsiflexors, long toe extensors, ankle plantar flexors) extremities and grade them from zero (total paralysis) to five (active movement against full resistance). The sensory assessment includes light-touch and pin-prick on 28 pairs of dermatomes (left and right), graded from zero (absent sensation) to two (normal sensation). The light touch test is performed using a tapered wisp of cotton stroked once across a skin area less than 1 cm with the eyes closed or vision blocked. The pinprick test (sharp/dull discrimination) consists of touching a specific dermatome with a safety pin that is sharp on one end and rounded on the other and asking the patient to identify which side of the pin he has been touched with. The neurological level of the injury (NLI) refers to the most caudal spinal cord segment with intact sensation and antigravity muscle function strength. Since left and right side are tested separately, the neurological level of the injury can be defined for right/left sensory and right/left motor levels. Injuries are classified as being neurologically “complete” or “incomplete” based on the “Sacral Sparing”, which refers to the presence of sensory or motor function in the most caudal sacral segments (i.e. preservation of light touch or pin prick sensation at the S4-5 dermatome, Deep Anal Pressure (DAP) or voluntary anal sphincter contraction). The absence of motor and sensory perception at the most caudal sacral segments indicates a complete injury. The *American Spinal Injury Association Impairment Scale* (AIS), defined the following degree of impairments (Steven C. Kirshblum et al. 2011): “**A**(Complete), where the Sacral Sparing is not preserved (i.e. No sensory or motor functions are preserved in the sacral segments S4-S5); **B** (Sensory incomplete) where only the sensory function is preserved below the neurological level (including the sacral segments S4-S5), AND no motor function is preserved more than three levels below the motor level on either side of the body; **C** (Motor incomplete) where motor function is preserved below the neurological level, and more than half of key muscle functions below the NLI have a grade less than 3; **D** (Motor incomplete) where motor function is preserved below the neurological level, and at least half of key muscle functions below the

NLI have a muscle grade >3; E (Normal) if sensation and motor function are graded as normal in all segments, and the patient had prior deficits”.

The Graded Redefined Assessment of Strength Sensibility and Prehension (GRASSP)

The Graded Redefined Assessment of Strength Sensibility and Prehension (GRASSP) protocol provides a quantitative clinical measure specific for upper limb impairment designed for use in acute and chronic cervical SCI (Kalsi-Ryan, Curt, Mary C. Verrier, et al. 2012). The GRASSP was developed with the intent to be more responsive (sensitive) to changes over time, to assess the extent of spontaneous recovery and evaluate the effect of novel interventions. The GRASSP assessment focuses on three domains of hand function including (1) sensibility (2) strength and (3) prehension. The sensory aspects are tested using Semmes-Weinstein monofilaments on the dorsal and palmar surface of each hand and grading from 0 to 4 (with a total of 12 scores for each hand, and for dorsal and palmar surface). Muscle strength is tested on 10 arm & hand muscles of each side (anterior deltoid, biceps, wrist extensor, riceps, opponenspollicis, extensor digitorum; digit III finger flexor, flexor pollicis long- us T-1: digit V finger abductor, first dorsal interossei) and each muscle is graded from 0 (flaccid) to 5 (full range w/ maximal resistance) for a total grade of 50 for each upper limb. The prehension includes the prehension ability based on 3 grasps (Cylindrical Grasp, Lateral Key Pinch, and Tip to Tip Pinch) and scored from 0 to 4 (total score of 12); and prehension performance, which includes 6 prehension tasks (pour water from a bottle, open jars, pick up and turn a key, transfer 9 pegs board to board, pick up 4 coins & place in slot, screw 4 nuts onto bolts) scored from 0 to 5 (for a total score of 30). Higher GRASSP scores indicate better clinical outcome.

Spinal Cord Independence Measure (SCIM)

The Spinal Cord Independence Measure (SCIM) is a disability scale, specifically developed for patients with SCI to define daily-life independence (Itzkovich et al. 2007). The SCIM was defined to be more sensitive to functional changes and includes 19 items that assess three domains: (1) self-care such as feeding, grooming, bathing, and dressing(including 6 items with a total score range from 0-20); (2) respiration and sphincter management (4 items, scores from 0-40); and (3) mobility such as bed and transfers and indoor/outdoor (9 items, scores from 0-40). The total SCIM scores range from 0-100 with higher scores indicating more independence in self-management.

3.5.2 Electrophysiological measurements

Electrophysiological examinations provide functional assessment after SCI, offering a quantitative, objective measurements of nerve conductivity in a flexible and independent environment. In addition, they can assess specific parts of the spinal segments and peripheral nerve tracts and provide detailed quantitative information about a patient's condition that cannot be determined through standard clinical measurements. In this section we provide some example of electrophysiological examinations of the spinal cord such as Motor Evoked Potentials (MEP) and Somatosensory Evoked Potentials (SSEP).

Motor evoked potentials (MEP)

Motor evoked potentials (MEP) provide a tool to assess the function of the corticospinal tract using transcranial magnetic stimulation which induces an excitatory impulse in the motor cortex and a corresponding muscles contraction is recorded using surface electrodes (Groppa et al. 2012). MEPs latencies are related to the speed of conduction and may suggest the level of myelination and remyelination of the corticospinal tract over time. MEP amplitudes have been found to correlate with size and integrity of myelinated axons (Hendrix, et al. 2013; Jørgensen, et al. 2005); and with muscle movement velocity (Wirth, et al. 2008). In SCI patients, it was shown that MEPs latency remained unchanged over time, indicating that functional recovery occurs through compensation processes including neural plasticity rather than through physical repair (no improvements in spinal conductivity)(Curt and Dietz 1999).

Somatosensory Evoked Potentials (SSP)

Somatosensory Evoked Potentials (SSP) allow the assessment of ascending spinal tract function by stimulating peripheral nerves and recording the response from the patient's scalp. As a prognostic tool, SSEPs have been found to have predictive value in determining ambulation outcomes, although not to a degree more accurate than conventional clinical examination. Curt et al.(Curt and Dietz 1996) showed a positive relationship between median and ulnar nerve SSEP amplitude and outcome of hand function as well as an overall capability for SSEPs to assess level of injury. In a later work (Curt and Dietz 1999), they showed that SSEP measures are correlated with ASIA motor scores and that it can be used as a predictor of future ambulation.

3.5.3 Spinal Cord Imaging

Spinal cord imaging plays a critical role in the diagnosis, surgical treatment, and secondary complications, such as a syringomyelia, of SCI patients. Traditionally, non-invasive medical imaging

methods consists of plain radiography, computed tomography (CT), and MRI. Plain radiography (i.e. X-ray) and CT are the standard methods used immediately after injury for assessing the vertebral column and visualizing bone fractures and dislocations (Fehlings et al. 2017). However, they have limited sensitivity for detecting spinal cord trauma, ligaments, and intervertebral discs due to the low soft tissue contrast. MRI provides excellent soft tissue contrast, which makes it the gold standard imaging modality of diseases affecting the central nervous system (Bozzo et al. 2011b). Conventional MRI protocols applied in the diagnosis of SCI-patients, include T1-weighted (sagittal), T2-weighted (sagittal and axial), T2*-weighted (axial), and Short-TI Inversion Recovery (STIR, sagittal) sequences (Freund, et al. 2019a). These MRI modalities provide great anatomical detail regarding the level of injury, the degree of spinal canal and spinal cord compression, the presence of haemorrhage, the presence and length of edema, spinal cord swelling, as well as disc and ligamentous injury (Fehlings et al. 2017) and are crucial for the diagnosis and treatment planning of SCI-patients (Freund, et al. 2019a).

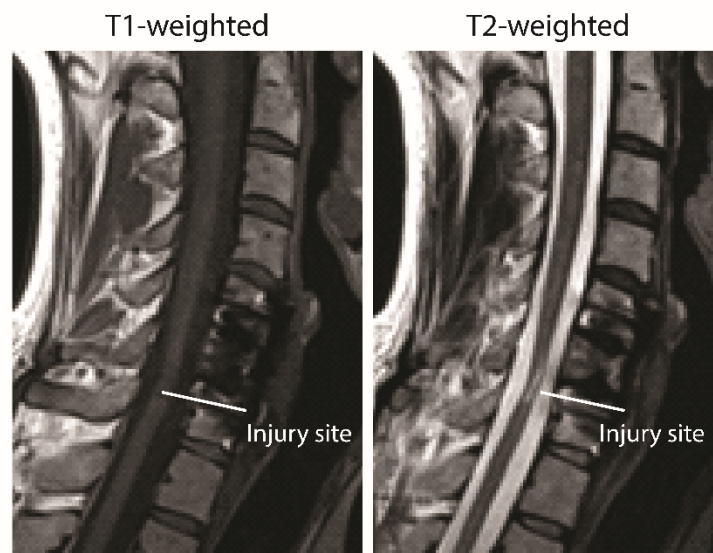


Figure 3.5: Examples of conventional T2-weighted MRI in sagittal view from a SCI patient. Note that these images provide information regarding the level, type and extent of the injury. T2-weighted image is generally considered the best diagnostic tool due to its higher contrast between the parenchyma and the lesion. However, these acquisitions are not sensitive to the underlying microstructural changes and therefore are not good predictors of long-term outcomes.

T1-weighted images are used to quantify spinal cord morphometry in terms of spinal cord area (SCA), anterior-posterior width (APW) and left-right width (LRW) (figure 3.6). It was shown that changes in the cords' LRW (Lundell 2011) have been associated with retrograde degeneration of the corticospinal tract (Lemon 2008); whereas changes in the APW (Grabher et al. 2015; Jutzeler et al. 2016; Lundell et

al. 2011) have been associated with anterograde degeneration in the posterior columns (Daniel and Strich 1969). These spinal cord parameters can be used to assess remote neurodegeneration above and below the lesion site.

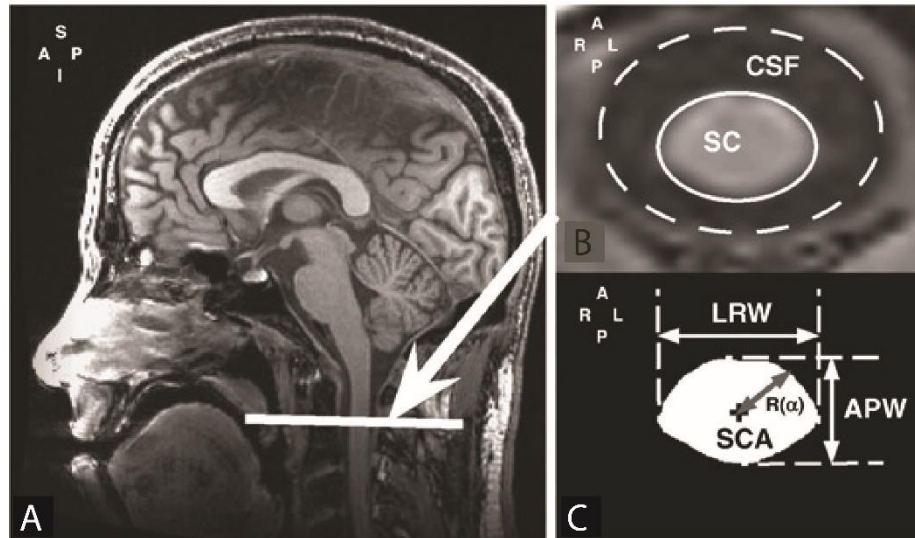


Figure 3.6: Examples of conventional T1-weighted (MPRAGE) in sagittal view in A and corresponding transverse section showing the spinal cord (SC) and surrounding cerebrospinal fluid (CSF) in B. The spinal cord morphometry is quantified in terms of spinal cord area (SCA), anterior-posterior width (APW) and left-right width (LRW) as shown in C. The figure is adapted from (Lundell et al. 2011).

In the T2-weighted MRI scans, the intramedullary damage can be detected (hyperintensity) and quantified in terms of lesion area (LA), lesion length (LL) and lesion width (LW) (figure 3.7). The small tissue bridges around the cyst can be measured dorsally and ventrally and they might predict long term recovery and electrophysiological functions (Huber et al. 2017; Pfyffer et al. 2019; Vallotton et al. 2019). Moreover, it was shown that atrophy in the dorsal horn has been associated with sensory outcome (eg, pain sensation, pin-prick score); whereas ventral horn atrophy has been associated with motor muscle strength score (Huber, et al. 2018).

However, these conventional techniques have several limitations: (i) the signal is highly variable across patients; (ii) imaging at the lesion site is still not feasible because of the artifacts induced by metal implants at the lesion site; and (iii) signal intensity changes are non-specific and do not correspond directly with aberrant physiological processes such as inflammation, gliosis, demyelination, axonal loss, and apoptosis. Therefore, conventional MRI provide a great tool to assess spinal cord anatomical details and allow the investigation of the soft tissue but are not able to characterize microstructural changes at the site of the injury. The development of new advanced imaging techniques, as the one

described in the previous chapter, have the potential to quantify changes in spinal cord microstructure and provide valuable biomarkers that correlate with disability and/or predict outcomes and may provide more sensitive and specific diagnostic tests.



Figure 3.7: Examples of conventional T2-weighted (MPRAGE) in sagittal view of a 51-year-old patient with incomplete spinal cord injury (male, tetraplegic, AIS grade C) on the left; and schematic drawing of the lesion parameters on the right including dorsal midsagittal tissue bridges (DB), lesion area (LA), lesion length (LL), lesion width (LW), ventral midsagittal tissue bridges (VB). The figure is adapted from (Freund, et al. 2019a).

3.6 Conclusion background II

In this chapter, the biological background of the spinal cord anatomy and the pathological changes after a SCI were presented. SCI is a devastating disease in which the primary injury to the spinal cord triggers a cascade of secondary injuries that affect the full central nervous system. Although spontaneous regeneration of lesioned fibres is limited in the adult central nervous system, significant recovery can still occur in the first year following incomplete SCI. The prognosis depends primarily on the initial severity and level of the injury, but also postinjury care and rehabilitative interventions have been shown to promote recovery after SCI. The functional or structural changes occurring in the adult brain in response to training/rehabilitation or environment changes is defined by the amount of neuroplasticity and functional compensation. However, spontaneous neuroplasticity after SCI can result in adaptive or maladaptive changes. The latter comes from spontaneous sprouting and hyperexcitability of neurons that lead to further impairment and neuropathic pain; whereas adaptive plasticity is the main goal of training and rehabilitation strategies for regaining function and improving

the clinical outcome. The investigation of these neurological changes over time can be done using several diagnostic tools. Typically, SCI patients are assessed by clinical examinations, electrophysiological measurements and spinal cord conventional MRI. In this chapter conventional MRI tools were described and used in the clinical practice to investigate macrostructural changes such as the level and extend of the injury. However, they are not able to characterize microstructural changes. Therefore, new advanced qMRI techniques were developed and used for the investigation of the brain. In the coming chapters, these tools are optimized in order to include the microstructural assessment of the cervical spinal cord.

4 Study I: Simultaneous analysis of brain and spinal cord multi-parametric maps based on SPM framework

Michela Azzarito, Sreenath P Kyathanahally, Yaël Balbastre, Maryam Seif, Claudia Blaiotta, Martina Callaghan, John Ashburner, Patrick Freund

This original article was submitted to Human Brain Mapping

4.1 Abstract

Objective: To provide and validate a simultaneous analysis tool of multi-parametric maps of the brain and cervical cord embedded in the SPM framework; (1) by assessing trauma-induced changes in spinal cord injury patients, (2) by comparing findings from available processing tools assessing the brain and spinal cord separately.

Methods: A probabilistic template of the brain and cervical spinal cord (BSC), named brain-neck template was generated using a generative semi-supervised modelling approach. The template was incorporated in the pre-processing pipeline of voxel-based morphometry (VBM) and voxel-based quantification (VBQ) analyses in SPM. The new approach was validated on T1-weighted MRI and multi-parameter mapping (MPM) maps, by assessing trauma-induced changes in SCI patients and comparing the findings with the outcome from existing analytical tools that assess the brain and cord separately. Reliability of the MRI measures was assessed using intraclass correlation coefficients (ICC).

Results: The SPM approach including the BSC template was able to simultaneously analyse the brain and cervical spinal cord of SCI patients and healthy controls. The results revealed trauma-induced changes along the entire projection of the corticospinal tracts in SCI patients. Similar findings were observed from the same data analysed using standard approaches covering brain or spinal cord, separately. The ICC in the brain was high ($ICC > 0.75$) within regions of interest such as sensory-motor cortex, thalamus and corticospinal tracts.

Conclusion: The simultaneous voxel-wise analysis of brain and cervical spinal cord was performed in a unique SPM-based framework incorporating pre-processing and statistical analysis in the same environment. Validation based on a SCI cohort demonstrated that the new processing approach based on the brain and spinal cord is as sensitive as available processing tools in detecting changes in SCI-patients offering the advantage of performing the analysis and statistics simultaneously in the brain and cervical spinal cord.

4.2 Introduction

A focal injury to the central nervous system produces widespread neurodegenerative changes, but also functional reorganization across the neuraxis (Freund et al. 2016). Quantitative MRI revealed that after traumatic spinal cord injury (SCI), not only does the injured spinal cord undergo progressive neurodegeneration, but with a time lag the cranial corticospinal tract and sensory-motor cortices also show signs of enduring neurodegeneration (Freund, Seif, Weiskopf, Friston, Michael G. Fehlings, et al. 2019b).

Currently, analyses are performed separately in the brain and at the level of the spinal cord. The gold standard for assessing spinal cord atrophy is to measure changes in the cross-sectional spinal cord area (SCA) at a single cervical level (C2/C3) (Papinutto et al. 2019) from T1 or T2-weighted MRI acquisitions using the JIM software (Horsfield et al. 2010) or the spinal cord toolbox (SCT) (De Leener et al. 2016). In the brain, volume changes (based on the segmentation of T1-weighted scans into tissue probabilities) or microstructural changes (via quantitative MRI, e.g. the multi-parametric mapping (MPM) protocol, or diffusion weighted imaging) are analysed using software toolboxes such as SPM (fil.ion.ucl.ac.uk/spm) or FSL (<https://fsl.fmrib.ox.ac.uk/>). In particular, volume changes can be analysed using voxel based morphometry (VBM) (Ashburner and Friston 2005) and microstructural changes, which include indirect measures of myelin (MT & R1) and iron content (R2*), can be analysed using voxel based quantification (VBQ) (Weiskopf et al. 2013).

However, there is no solution that enables the simultaneous assessment of changes occurring in the brain and cord. As a result, most imaging studies fail to implement and analyse the interactions between such remote areas across the central nervous system. Providing a tool that could assess the sequelae of a focal central nervous system (CNS) injury across the entire neuroaxis simultaneously would hold great potential to better understand the temporally and spatially distributed pathophysiological changes (Freund et al. 2016).

Anatomical templates are fundamental to group level comparisons because they naturally define a common space in which analyses can be performed. Templates typically either take the form of mean intensity images or of tissue probability maps (TPMs); the latter can further serve as anatomical priors in segmentation algorithms. A wide variety of brain templates have been developed, serving different purposes, but spinal cord templates are less common. Recently, a template that covers brainstem and spinal cord has been proposed (De Leener et al. 2018), using spinal cord specific tools that cannot be applied to the brain, so the conjoint analyses of the brain and cord is not possible. A principled way of

constructing a template is to consider it as an unknown variable in a generative model of large MR datasets (Blaiotta et al. 2018a). In this context, a brain-neck template has naturally been obtained by fitting the generative model to collections of images of the brain and spinal cord (Blaiotta et al. 2018a).

The present study implements a brain-neck template (covering brain and cervical spinal cord) and validates its use in the context of VBM (Ashburner and Friston 2005) and VBQ (Weiskopf et al. 2013) analyses as implemented in the SPM framework. The extended SPM framework for brain and spinal cord analyses, named 'SPM-BSC', offers the advantage of performing pre-processing and statistics simultaneously in the brain and cervical spinal cord. In addition to voxel-wise analyses in standard (group) space, cord-specific metrics were also computed in native space. These include: spinal cord area (SCA), anterior–posterior width (APW) and left–right width (LRW). Furthermore, mean values across the whole cervical spinal cord of the magnetization transfer saturation (MT), longitudinal relaxation rate ($R1=1/T1$) and effective transverse relaxation rate ($R2^*=1/T2^*$) were also computed. The SPM-BSC analysis was validated by assessing volume and microstructural changes in the brain and spinal cord in SCI-patients relative to healthy controls and comparing the results with pipelines separately optimised for the brain (SPM-BO for 'brain only'), or from the SCT covering only the spinal cord.

4.3 Materials and Methods

VBM/VBQ analyses in SPM (fil.ion.ucl.ac.uk/spm) were extended to include cervical spinal cord by incorporating a new probabilistic atlas of the brain and neck (Blaiotta et al. 2018a). Validation of this approach was performed by analysing a cohort of 53 individuals comprised of 30 patients with chronic traumatic SCI and 23 healthy participants. The SPM-BSC analysis was used to assess volume and microstructural differences within the brains and spinal cords of the SCI-patients relative to the healthy controls. Results obtained with the proposed SPM-BSC analysis were compared with those obtained using existing tools that separately assess either the brain or spinal cord only. Therefore, MRI data were analysed using:

1. SPM-BSC: the proposed VBM/VBQ pipeline implemented in SPM12 using a brain and spinal cord template enabling statistical analysis across the entire neuroaxis;
2. SPM-BO: the established VBM/VBQ pipelines available in SPM12 within the brain only;
3. SCT: the spinal cord toolbox (SCT) (De Leener et al. 2016) covering only the spinal cord.

4.3.1 Participants and study design

MRI from 30 patients (age: 44.67 years \pm 16.72; 29 men) with chronic traumatic SCI (mean years after injury 3.57 \pm 6.83) and 23 healthy controls (age: 36.87 years \pm 11.76; 13 men) were acquired at the University Hospital Balgrist between August 2011 and May 2015. There was no statistically significant age difference between the two groups (Mann-Whitney U test, $z = -1.92$, $p = 0.055$).

The exclusion criteria were: time since injury < 2 months, pregnancy, head or brain lesions associated with spinal cord injury, pre-existing neurological or medical disorders leading to functional impairments, mental disorder, or contraindications to MRI. All participants provided written informed consent prior to enrolment. The study protocols were in accordance with the Declaration of Helsinki and approved by the local ethics committee of Zurich the 'Kantonale Ethikkommission Zurich' (EK-2010-0271). Patients underwent a comprehensive clinical assessment protocol including the International Standards for Neurological Classification of Spinal Cord Injury (ISNCSCI) (Steven C Kirshblum et al. 2011a) for motor, light touch, and pinprick score; the Spinal Cord Independence Measure (SCIM)(Catz et al. 2007); and additionally for tetraplegic patients the Graded Redefined Assessment of Strength, Sensibility, (Table 4.1).

Participant	Age (years)	Time since injury (months)	Lesion Completeness	AIS	Level of impairment (motor/sensory)	ISNCSCI LEMS	ISNCSCI UEMS	ISNCSCI Pinprick	ISNCSCI Light Touch	SCIM
1	69	12.17	Incomplete	D	T11/T11	32	49	74	92	42
2	45	13.4	Incomplete	D	L3/L4	45	50	106	106	100
3	53	11.97	Incomplete	D	T10/T10	48	50	90	90	100
4	30	10.27	Complete	A	T10/T10	16	50	78	82	80
5	70	9.5	Complete	A	T7/T7	0	50	68	67	49
6	72	11.97	Incomplete	E	T3/T3	50	50	112	112	97
7	53	54.6	Complete	A	T3/T3	0	50	44	47	53
8	36	185.47	Complete	A	T12/T12	4	50	78	78	70
9	60	68.17	Complete	A	T1/T1	0	49	40	52	32
10	53	8.03	Complete	A	T9/T9	0	50	66	68	69
11	32	10.77	Incomplete	B	T11/T11	0	50	72	78	66
12	29	22.83	Incomplete	B	T6/T6	0	50	52	77	66
13	26	10.8	Complete	A	T4/T4	0	50	46	48	67
14	39	9.33	Complete	A	T7/T7	0	50	58	60	65
15	31	12.33	Incomplete	B	T4/T4	0	50	46	74	54
16	19	13.5	Complete	A	C6/C7	0	23	33	33	37
17	24	12.2	Incomplete	D	T1/C6	19	48	37	72	70
18	43	15.73	Complete	A	C6/C4	0	25	18	20	37
19	72	11.9	Incomplete	D	C6/C7	41	48	41	112	36
20	21	12.33	Complete	A	C6/C5	0	23	26	53	34
21	31	12.3	Incomplete	B	T1/C7	0	48	46	68	38
22	48	12.13	Incomplete	D	C5/C3	47	35	97	98	98
23	52	9.7	Incomplete	C	C7/C5	12	32	44	67	31
24	68	12.07	Incomplete	D	C3/C3	50	50	102	107	100

25	34	12.2	Complete	A	C7/C7	0	35	29	32	26
26	55	18.63	Incomplete	D	C3/C3	49	42	94	62	84
27	32	10.27	Complete	A	C6/C5	0	26	20	33	30
28	29	12.07	Complete	A	C5/C4	0	14	13	16	19
29	43	186.77	Incomplete	B	C6/C4	0	25	32	77	29
30	69	290.5	Incomplete	D	T1/C3	40	49	78	69	NA

Table 4.1: demographic information of patients with SCI included in the current study and corresponding clinical measurements.

4.3.2 Image acquisition

Participants underwent a T1-weighted 3D-MPRAGE sequence (whole-brain including the cervical cord up to C5 level) on a 3T MRI scanner (Magnetom Skyra^{Fit} or Verio, Siemens Healthcare, Erlangen, Germany) with the following parameters: field of view (FoV) of 224×256×176 mm², isotropic resolution of 1 mm³, repetition time (TR) =2420 ms, Echo time (TE)= 4.18 ms, flip angle (α) = 9°, inversion time = 960 ms, and readout bandwidth of 150 Hz per pixel. The system was equipped with a 16-channel radiofrequency (RF) receive head and neck coil and RF body transmit coil.

To assess microstructural changes, a multi-parameter mapping (MPM) protocol (Callaghan et al. 2015ba; Helms, et al. 2008a; Helms et al. 2009; Weiskopf et al. 2011a, 2013) was performed. These scans covered the whole brain and cervical spinal cord until level C4 with 1 mm isotropic resolution, FoV=240×256×176 mm³. Total acquisition time was 23 min applying parallel imaging in the phase-encoding direction using a generalized auto-calibration partially parallel acquisition algorithm (GRAPPA) factor 2×2 and readout bandwidth of 480 Hz/pixel. Each set of echoes was acquired using a different TR and flip angle (α) to achieve images with either T1-weighting: 25 ms / 23°, PD-weighting: 25 ms / 4°, or MT-weighting: 37 ms / 9° with off-resonance RF pulse prior to excitation. Echoes were acquired at six equidistant echo times (TE) from 2.46 ms to 17.22 ms for all weightings, with an additional echo at 19.68 ms for the PD-weighted and T1-weighted volumes.

4.3.3 Brain-neck template

The template incorporating brain and cervical spinal cord (named brain-neck template) was generated by Blaiotta et al. (Blaiotta et al. 2018a) using a generative semi-supervised modelling approach (Blaiotta, Jorge Cardoso, and Ashburner 2016). The algorithm is based on a Gaussian mixture model of MR intensities, where the intensity distribution within each tissue type is assumed Gaussian, and the

template encodes prior probabilities of belonging to each tissue (Blaiotta et al. 2016). A total of 12 Gaussian components were defined and, after algorithm convergence, they were combined into seven tissue maps based on visual inspection. In particular, a single Gaussian was assigned to each of grey matter (GM), white matter (WM), cerebrospinal fluid (CSF) and fat; three Gaussians were assigned to each of the non-neural tissues, soft tissues and to a mixture of bone and air. Finally, the template was registered to the existing SPM12 tissue probability template using a 12-parameter affine registration. This template covers the brain and spinal cord until level C3 (figure 4.1).

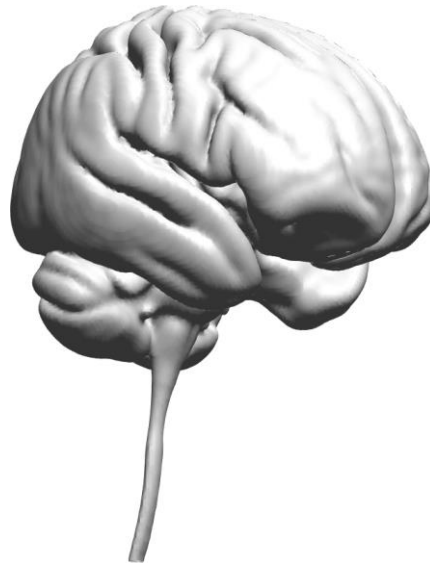


Figure 4.1: Surface rendering of the brain and spinal cord from the atlas, based on thresholding the sum of the gray and white probabilities at 0.5.

4.3.4 VBM/VBQ pipeline for the simultaneous analysis of brain and spinal cord

The brain-neck template (Blaiotta et al. 2018a) was used to segment the T1-weighted structural MPAGE images of each individual using the unified segmentation algorithm (Ashburner and Friston 2005). In order to incorporate the brain-neck template which contains seven tissue classes, one Gaussian was specified for GM, WM and CSF whereas three Gaussians were specified for the other tissue classes (non-neural tissues, soft tissues and a mixture of bone and air). To assess morphological changes in the spinal cord, the native-space GM and WM tissue maps were combined to form a neural tissue (NT) class. Then, the GM, WM and NT maps were spatially normalised to MNI space with Dartel (Ashburner 2007a), and modulated by the Jacobian determinants of the deformations (Good et al. 2001). Finally, an isotropic Gaussian kernel of 6 mm full width at half maximum (FWHM) was applied

to the modulated tissue maps (figure 4.2A). The total intracranial volume (TIV) was computed from the sum of the grey matter, white matter, and CSF volumes (Ridgway et al. 2011).

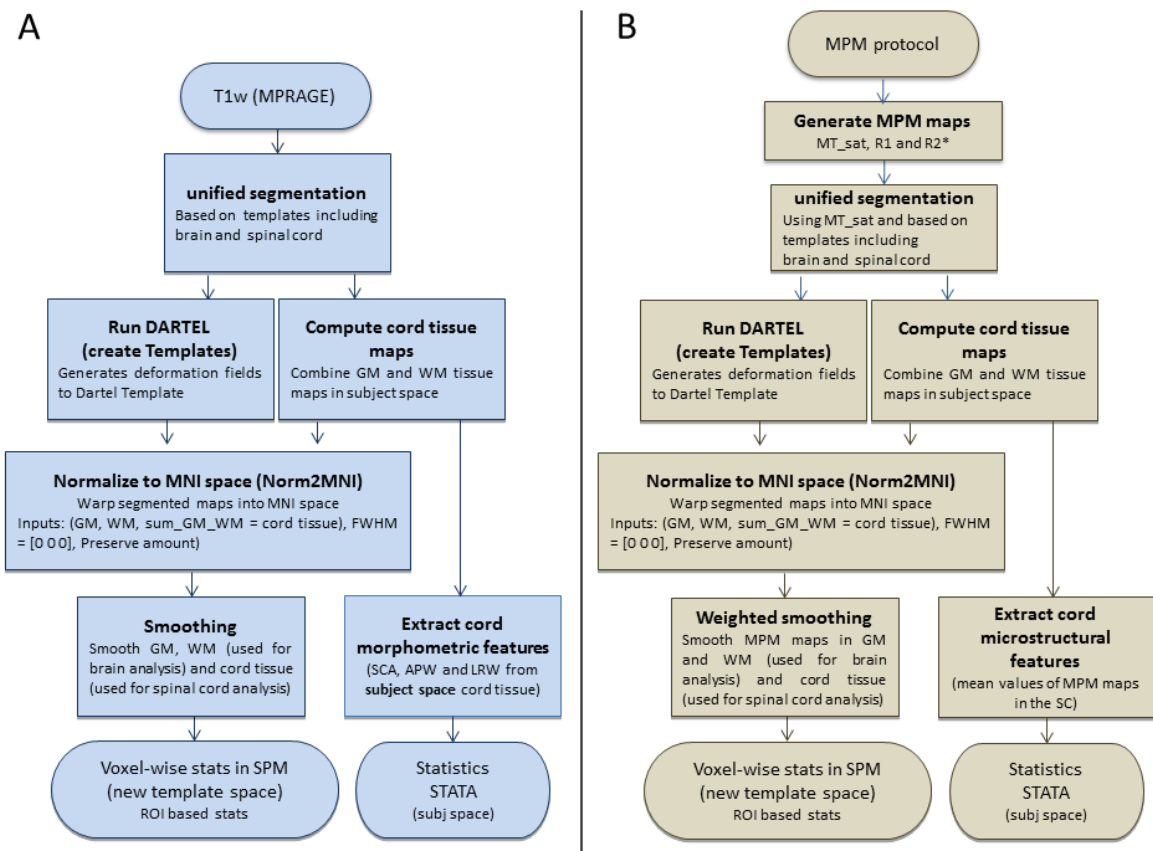


Figure 4.2: Pipeline describing the new SPM-BSC approach for VBM (in A) and VBQ (in B) analysis.

The VBQ analysis (Draganski, et al. 2011; Weiskopf et al. 2013) is based on the MPM protocol (Helms, et al. 2008; Weiskopf et al. 2013), which consists of 3D multi-echo fast low-angle shot (FLASH) gradient-echo sequences. The acquired T1-weighted, PD-weighted, and MT-weighted FLASH echoes were used to compute quantitative maps of MT, R1 and R2* using the *in vivo* histology using MRI (hMRI) toolbox (Tabelow et al. 2019). Inhomogeneity of the RF transmit field were corrected using UNICORT (Weiskopf et al. 2011). The VBQ analysis (Draganski, et al. 2011; Tabelow et al. 2019) included segmentation of the MT map into GM, WM and CSF, covering brain and spinal cord, using the unified segmentation approach (Ashburner and Friston 2005) and the brain-neck template (as used when segmenting the MPRAGE for the VBM analysis). Segmenting the MT map ensures that the MPM maps and the tissue probabilities are aligned in native space. To assess microstructural changes in the spinal cord, NT maps

were computed by again combining the GM and WM tissue maps from MT segmentation in native space. All tissue maps were transformed to MNI space using the Dartel algorithm (Ashburner 2007a). MPMs were warped to MNI space using participant-specific warping fields generated from the Dartel algorithm and finally smoothed using an isotropic Gaussian kernel filter with 6 mm FWHM using the VBQ smoothing approach with the corresponding tissue probability map (Draganski, et al. 2011) (Figure 4.2B).

Smoothing the spinal cord MRI leads to undesired partial volume effects with CSF. In order to identify the best scale space (Worsley et al. 1996), filters with different widths (from no smoothing to 6 mm FWHM isotropic smoothing) were applied prior to analysis using VBM or VBQ.

To compute macrostructural metrics in the spinal cord, such as SCA, APW and LRW, the native-space NT tissue probability maps were thresholded (at $p > 0.5$) to generate a mask of spinal cord. Next, an ellipse was fitted to the boundary of the mask in each transverse slice and the corresponding area (SCA) and main cord axes (LRW and APW) were extracted. Microstructural metrics were computed as the mean of the MT, R1 and R2* values within the masked region of the NT probability maps (computed from the MT map segmentation) covering cervical segments C1 to C3.

Standard VBM/VBQ analysis (SPM-BO)

MPRAGE anatomical images were analysed using the standard VBM approach, which segments and aligns the brain but does not account for the spinal cord. This procedure involved segmentation into GM, WM and CSF using unified segmentation (Ashburner and Friston 2005) with the tissue priors released with the SPM12 software. The GM and WM tissue probability maps were subsequently warped into standard MNI space using Dartel, before being smoothed with an isotropic Gaussian kernel with 6 mm FWHM.

Multi-parametric maps (MPMs) of MT, R1, and R2* were analysed using the standard voxel-based quantification (VBQ) pipeline as implemented in the hMRI toolbox in SPM12. Briefly, MT maps were segmented using the tissue priors released with SPM12, which enabled the brains of the MPMs to be normalized to MNI space using Dartel, but could not align the cords of the group. Finally, the spatially normalised MPMs were smoothed using the VBQ approach with an isotropic Gaussian kernel filter with 6 mm FWHM (Draganski, et al. 2011).

Spinal cord toolbox analysis (SCT)

All MRI data were also analysed using the SCT software (De Leener et al. 2016). Here, the cervical C1-C3 segments from T1-weighted images and MT maps (from the hMRI toolbox) were segmented automatically using deep segmentation (McCoy et al. 2019). Segmented data were carefully inspected and manually corrected for misclassification if necessary (using FSL; <https://fsl.fmrib.ox.ac.uk/>). Then, the generated spinal cord masks of each participant were registered to the MNI-Poly-AMU template (De Leener et al. 2018) using a combination of affine and nonlinear registrations, and the reverse deformation field (template to native) was applied to the WM and GM atlases, projecting them into the native space.

Next, macrostructural parameters were extracted from the spinal cord in the segmented T1-weighted image, across levels from C1 to C3 providing automatically APW, LRW and SCA. To perform microstructural analysis based on the MPM protocol, a pipeline was optimized based on SCT routines. Specifically the segmentation of MT maps provided a mask of the spinal cord which was aligned with all MPM maps in native space and used to extract microstructural parameters from the MT, R1 and R2* maps across levels C1 to C3. In addition, SCT smoothing along the centerline was applied to all MPMs using a Gaussian kernel with a standard deviation (sigma σ) of 3 mm (De Leener et al. 2016). The SCT smoothing algorithm works by straightening the cord, applying a 1-D Gaussian smoothing kernel and then un-straightening the cord back into the original space (De Leener et al. 2016). Finally the smoothed maps were warped into template space (PAM50) using the warping fields derived from the segmentation of the MT maps.

4.3.5 Statistical analysis

Morphometric and microstructural assessments in the brain and spinal cord

To assess morphometric and microstructural differences in the brain or spinal cord of SCI patients compared to healthy controls, a t-test within the framework of the general linear model (GLM) in SPM was applied. Age, gender, scanner and total intracranial volume (TIV) were included as covariates of no interest to control for confounding linear effects in all GLMs (Barnes et al. 2010). A family-wise error (FWE) correction using Gaussian Random Field theory was applied to account for multiple comparisons (Friston et al. 1994) within regions of interest (ROIs) using a threshold of $p=0.05$ at the peak-level. Only statistically significant results ($p < 0.05$) corrected for FWE are reported.

Additionally, spinal cord parameters in native space, such as SCA, APW, LRW and mean values from MT, R1 and R2*, extracted from both SCT and SPM-BSC approaches were used to assess differences between SCI-patients and healthy controls using an ANCOVA in Stata (Stata Corp 13.0, College Station, TX). All statistical tests were corrected for age, gender and scanner by including them as cofactors of no interest. Only results where $p < 0.05$ are reported.

Regions of interest (ROIs)

An ROI approach was applied based on literature findings (Freund, Seif, Weiskopf, Friston, Michael G. Fehlings, et al. 2019b). The following ROIs were used in the analysis of the brain: bilateral motor cortex M1 (precentral gyrus), bilateral somatosensory S1 cortices (postcentral gyrus), thalamus and corticospinal tract, which were extracted using the SPM Anatomy toolbox (Eickhoff et al. 2007). The ROI approach was also applied for the spinal cord analysis. This was necessary to be equally sensitive to cord changes for SCT and SPM-BSC approaches. For the analysis of SPM-BSC data, a group-specific spinal cord mask was computed by thresholding the average of the NT maps of all participants to include voxels with probability greater than 50% and further restricting this mask to the spinal cord from levels C1 to C3 (visually defined). For the SCT analysis, the ROI was defined from the PAM50_cord map limited to levels C1 to C3, as defined in the levels map provided with the SCT.

Comparison of brain maps: SPM-BSC vs SPM-BO

To evaluate the reliability of the spatially normalised maps computed with the SPM-BO and SPM-BSC approaches, the intra-class correlation coefficient (ICC) (McGraw and S. P. Wong 1996) was computed to define the degree of absolute agreement between the corresponding outputs from the two approaches. The mean values in each ROI used in the statistical analyses were used to compute inter-rater reliability using a two-way mixed-model, absolute agreement, and multiple raters ICC (McGraw and S. P. Wong 1996) in MATLAB 2016b. According to the ICC guidelines (Koo and Li 2016), ICC values can be partitioned to indicate poor (less than 0.5), moderate (between 0.5 and 0.75), good (between 0.75 and 0.9), and excellent (greater than 0.90) reliability between methods.

Associations between spinal cord MPM maps and clinical outcomes

Spinal cord MRI data in the template spaces (from both SPM-BSC and SCT analyses separately) were used to assess the associations between MPM measures and clinical outcomes (LEMS, light-touch, pinprick and SCIM scores), using regression models in SPM12. All tests were corrected for age, gender, scanner and total intracranial volume (TIV) as covariates of no interest and family-wise error (FWE)

correction was applied to account for multiple comparisons (Friston et al. 1994) using a threshold of $p=0.05$ at the peak-level.

4.4 Results

4.4.1 Structural changes in the brain using SPM-BSC

The ROI based analysis revealed myelin-sensitive R1 reduction (z -score=4.1, $x=9$, $y=-20$, $z=18$, $p=0.002$) in the thalamus of SCI-patients compared to healthy controls. Myelin-sensitive R1 and MT reductions were observed in the primary motor (MT: z -score=4.0, $x=45$, $y=-17$, $z=45$, $p=0.018$; R1: z -score=4.1, $x=45$, $y=-15$, $z=45$, $p=0.005$) and sensory cortex (MT: z -score=4.3, $x=51$, $y=-17$, $z=41$, $p=0.011$; R1: z -score=4.0, $x=-48$, $y=-35$, $z=47$, $p=0.015$) of SCI-patients compared to healthy controls. Furthermore myelin-sensitive R1 reduction (z -score=4.0, $x=24$, $y=-9$, $z=41$, $p=0.008$) was observed in the right corticospinal tract of SCI-patients compared to healthy controls (Figure 4.3A). All results are reported in Table 4.2.

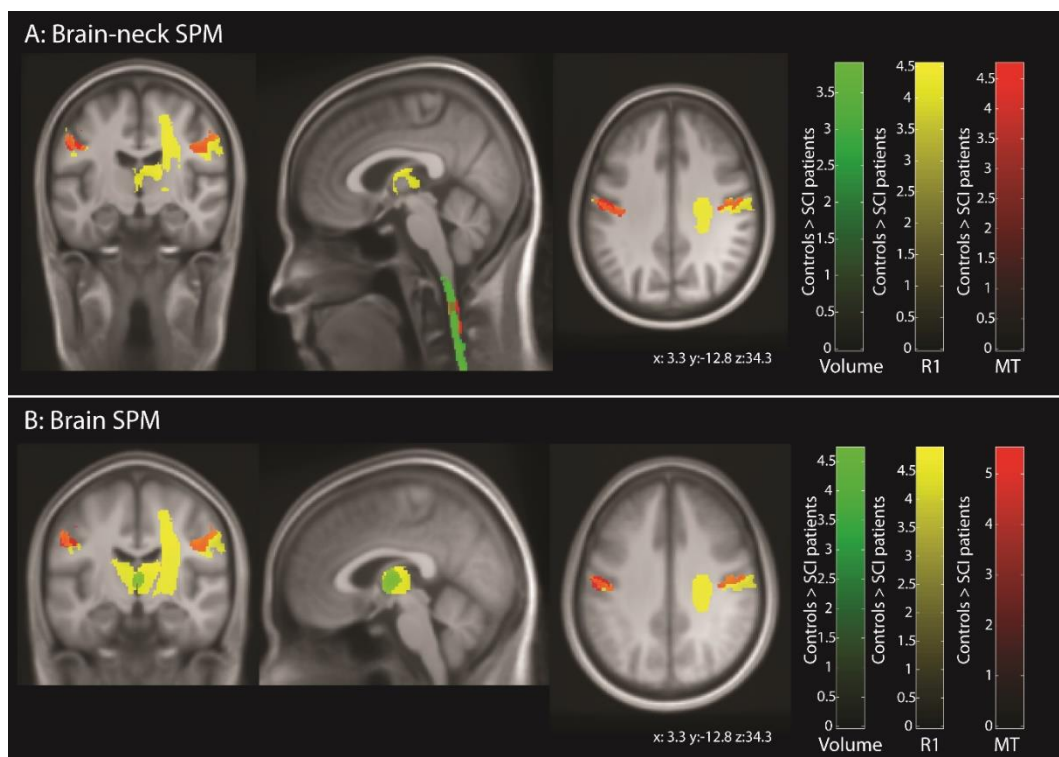


Figure 4.3: Overlay of statistical parametric maps (uncorrected $p < .001$, for illustrative purposes) showing morphometric and microstructural changes in SCI-patients compared to healthy controls using data pre-processed via the simultaneous brain and spinal cord (SPM-BSC) approach in (A) and the standard brain approach in (B). Both pre-processing methods showed myelin-sensitive R1 reduction in the thalamus (yellow); myelin-sensitive R1 and MT reduction in the bilateral sensory-motor cortex (R1, yellow; MT, red); and myelin-sensitive R1 reduction in right corticospinal tract in SCI-patients compared to healthy controls (R1, yellow; MT, red). In

addition, the SPM-BSC approach (A) showed atrophy (green) and myelin-sensitive MT reduction in the cervical spinal cord of SCI-patients compared to healthy controls. The colour bar indicates the t score.

4.4.2 Structural changes in the brain using SPM-BO

The ROI based analysis revealed significant atrophy (z-score=4.2, x=2, y=-11, z=5, p=0.011) and myelin-sensitive R1 reduction (z-score=4.4, x=5, y=-15, z=15, p<0.001) in the thalamus of SCI-patients compared to healthy controls. Myelin-sensitive R1 and MT reductions were observed in the primary motor (MT: z-score=4.8, x=45, y=-15, z=45, p<0.001; R1: z-score=4.6, x=45, y=-15, z=45, p<0.001) and sensory cortex (MT: z-score=5.0, x=48, y=-15, z=44, p<0.001; R1: z-score=4.2, x=-50, y=-35, z=50, p=0.007) of SCI-patients compared to healthy controls. Furthermore myelin-sensitive R1 reduction (z-score=4.1, x=26, y=-8, z=8, p=0.005) was observed in the right corticospinal tract of SCI-patients compared to healthy controls (Figure 4.3B). All These results are reported in Table 4.2.

	ROI	z-score	peak p-value (FWE corrected)	x	y	z
SPM-BSC						
R1	thalamus	4.1	0.002	9	-20	18
MT	Motor cortex	4.0	0.018	45	-17	45
R1	Motor cortex	4.1	0.005	45	-15	45
MT	Sensory cortex	4.3	0.011	51	-17	41
R1	Sensory cortex	4.0	0.015	-48	-35	47
R1	Corticospinal tract	4.0	0.008	24	-9	41
SPM-BO						
VBM	thalamus	4.2	0.011	2	-11	5
R1	thalamus	4.4	<0.001	5	-15	15
MT	Motor cortex	4.8	<0.001	45	-15	45
R1	Motor cortex	4.6	<0.001	45	-15	45
MT	Sensory cortex	5.0	<0.001	48	-15	44
R1	Sensory cortex	4.2	0.007	-50	-35	50
R1	Corticospinal tract	4.1	0.005	26	-8	8

Table 4.2: Results from region of interest (ROI) analysis using voxel based morphometry (VBM) and voxel based quantification (VBQ) from 'Brain-neck SPM' and 'Brain only' methods.

4.4.3 Brain map reliability: SPM-BSC vs SPM-BO

The ICC results are presented in table 4.3. The ICC was moderate to excellent in all cases. Excellent ICCs (ICC ≥ 0.9) were observed in the motor cortex and sensory cortex of the R1 map; in the thalamus and corticospinal tract of the R2* map; and in the corticospinal tract of the R1 map. Good ICCs (0.75 ≤ ICC < 0.9) were observed in M1 and S1 in the MT and volume maps; and in S1 of the R2* map. Moderate

ICCs ($0.5 \leq \text{ICC} < 0.75$) were observed in the thalamus and corticospinal tract of MT and volume maps; in the thalamus of the R1 map; and in M1 of the R2* map.

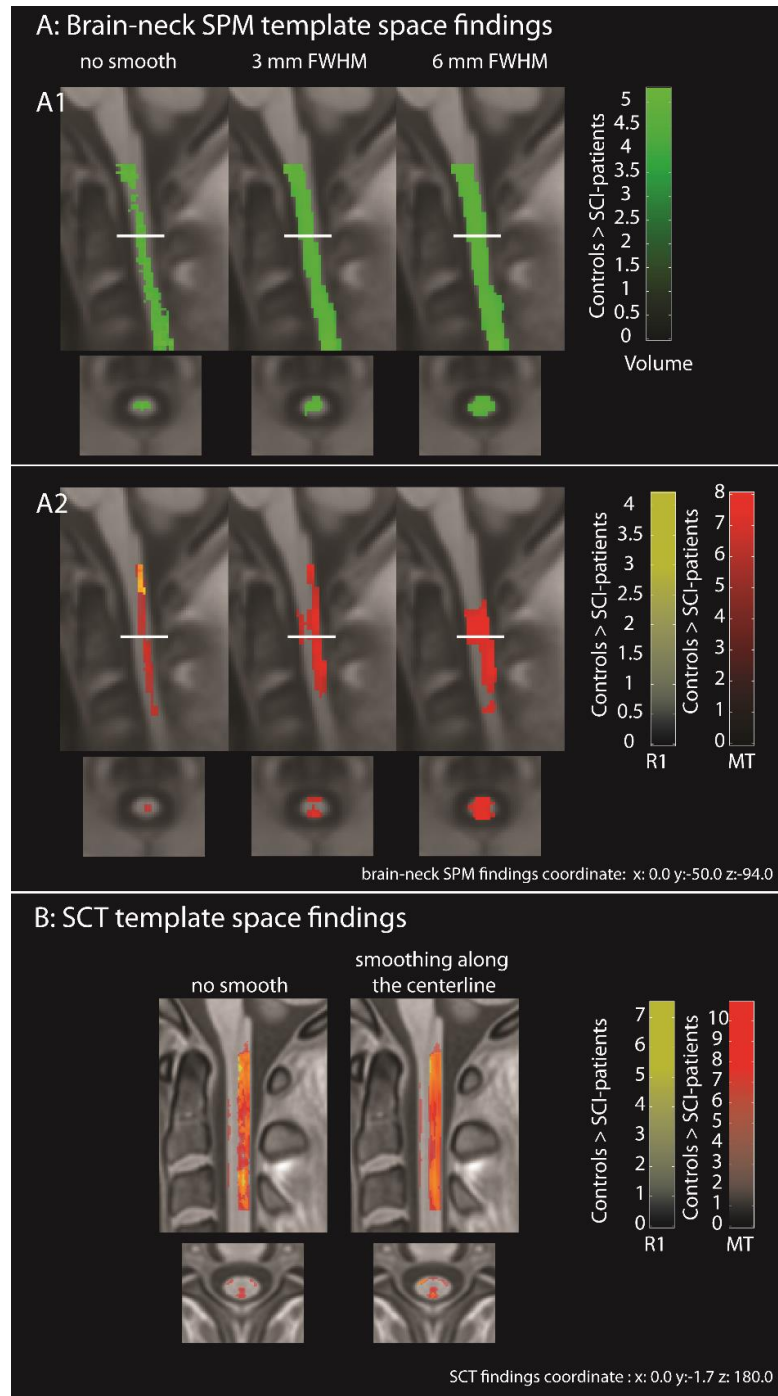


Figure 4.4: Overlay of statistical parametric maps (uncorrected $p < 0.001$, for illustrative purposes) showing significant differences in SCI-patients compared to healthy controls in the cervical spinal cord using different smoothing sizes and data analysed with SPM-BSC (in A) and SCT (in B) approaches. The colour bar indicates the t score.

ROI	MT	R1	R2*	Volume
M1	0.80	0.93	0.62	0.80
S1	0.88	0.98	0.85	0.88
Thalamus	0.56	0.56	0.95	0.56
corticospinal tract	0.50	0.90	0.97	0.50

Table 4.3: intraclass correlation coefficient (ICC) using the mean values in the ROIs from data smoothed with 6mm FWHM

4.4.4 Assessing spinal cord changes using voxel-wise analysis in template space

Data pre-processed using the SPM-BSC approach showed spinal cord atrophy (from the VBM analysis) and decreased MT (from the VBQ analysis) in SCI-patients compared to controls for all smoothing sizes, (Table 4.4). Decreased spinal cord R1 was found in SCI-patients compared to healthy controls only if no smoothing was applied (z-score= 3.82, x=0, y=-49.5, z=-78, p=0.042, in brain-neck template space) (Figure 4.4-A2).

Data pre-processed using the SCT approach showed reduced MT and R1 in SCI-patients compared to healthy controls (Figure 4.4B) using both, unsmoothed (MT: z-score= 7.01, x=0, y=-3, z=201 p<0.0001; R1: z-score= 5.94, x=-0.5, y=-3, z=215 p<0.0001, in PAM50 space) and smoothed data (MT: z-score= 7.61, x=-0.5, y=-3, z=201 p<0.0001; R1: z-score= 6.02, x=0, y=-3, z=213 p<0.0001, in PAM50 space).

Smoothing size FWHM	p-value (FWE-corrected)	Z score
VBM		
no smoothing	0.0035	4.63
1 mm	0.0019	4.70
2 mm	0.0007	4.70
3 mm	0.0006	4.59
4 mm	0.0004	4.56
5 mm	0.0003	4.54
6 mm	0.0003	4.50
MT		
no smoothing	<0.0001	6.28
1 mm	<0.0001	5.91
2 mm	0.0001	5.18
3 mm	0.0003	4.87
4 mm	0.0006	4.65
5 mm	0.0009	4.45
6 mm	0.0016	4.21
R1		
no smoothing	0.042	3.82

Table 4.4: Results from VBM and MT analyses of differences between patients and healthy controls in the spinal cord using different smoothing sizes.

4.4.5 Assess spinal cord changes using extracted metrics

Macrostructural analysis from data pre-processed with the SPM-BSC approach, revealed reduced SCA and APW in SCI-patients compared to healthy controls ($p < 0.05$); while the LRW showed only a trend ($p = 0.08$) in the cervical spinal cord. Similarly, data pre-processed with the SCT approach revealed reduced SCA and APW ($p < 0.05$) in SCI-patients compared to healthy controls; while the LRW showed only a trend ($p = 0.06$) (Figure 4.5A and Table 4.5). Microstructural analysis from data pre-processed with the SPM-BSC approach, revealed reduced myelin-sensitive MT and R1 ($p < 0.05$) in SCI-patients compared to healthy controls; whereas measures of R2* in the cervical cord were not significantly different ($p = 0.49$). Similarly, data pre-processed with the SCT approach revealed reduced myelin-sensitive MT ($p < 0.001$) in SCI-patients compared to healthy controls, but no significant differences were found in either the R2* maps ($p = 0.55$) or the R1 maps ($p = 0.62$) (Figure 4.5B and Table 4.5).

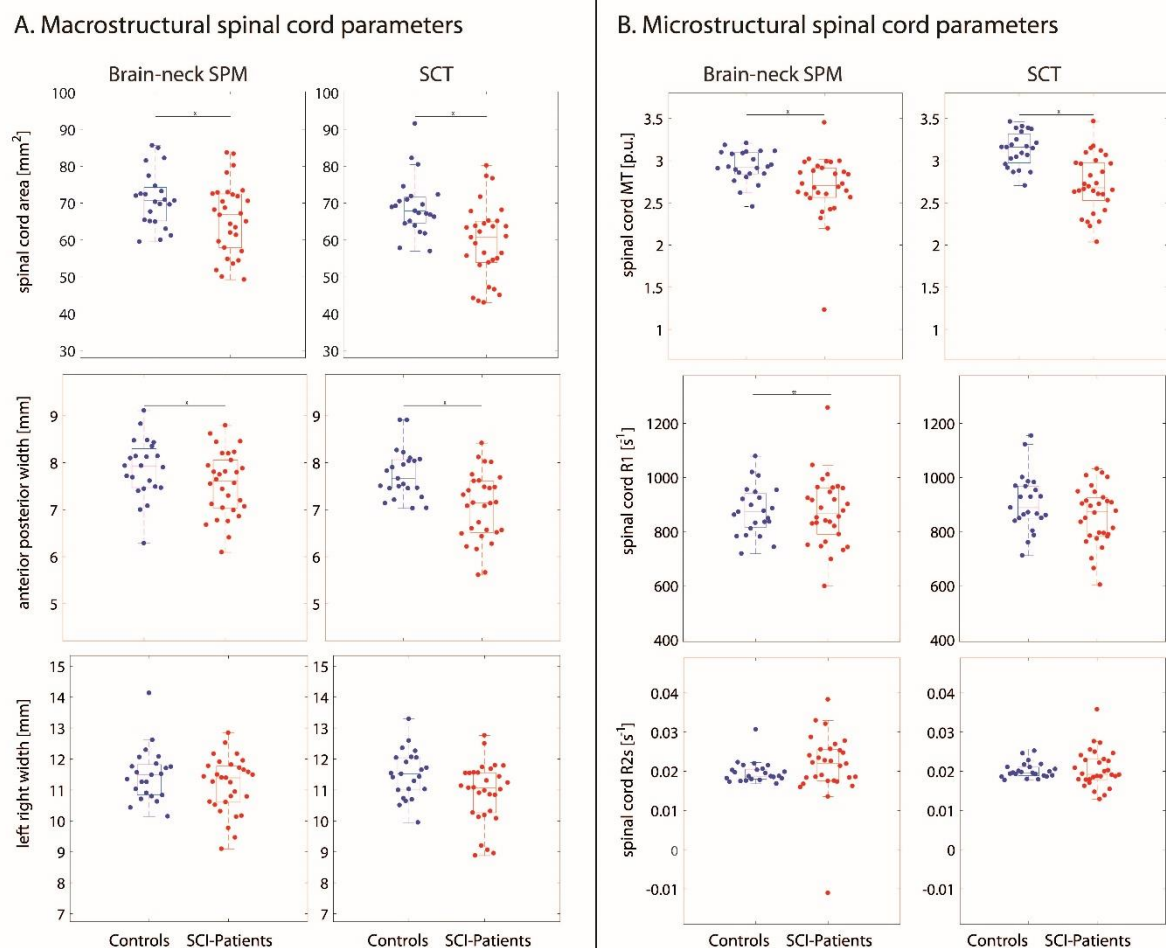


Figure 4.5: macrostructural changes in the cervical cord (A) using MRI data analysed with the SPM-BSC approach (left column) and SCT (right column), showing reduced cross-sectional area and anterior posterior width in SCI-patients compared to healthy controls ($p < 0.05$). Microstructural changes in the cervical cord (B) from MRI data

analysed using SPM-BSC approach (left column) and the SCT (right column), showing reduced MT in SCI-patients compared to healthy controls ($p < 0.05$). The * symbol indicates statistically significant differences ($p < 0.05$) between the connected groups.

SC metrics	Healthy controls mean \pm SD	SCI patients mean \pm SD	Group differences [%]	p-value
SPM-BSC				
SCA [mm ²]	71.05 \pm 7.51	65.91 \pm 9.61	7.23	0.019
APW [mm]	7.87 \pm 0.63	7.55 \pm 0.68	4.06	0.04
LRW [mm]	11.48 \pm 0.85	11.17 \pm 0.89	2.70	0.08
MT [p.u.]	2.93 \pm 0.19	2.69 \pm 0.38	8.19	0.004
R1 [s ⁻¹]	876.88 \pm 90.38	873.51 \pm 126.01	0.38	0.047
R2* [s ⁻¹]	0.02 \pm 0.003	0.02 \pm 0.008	0	0.49
SCT				
SCA [mm ²]	69.10 \pm 7.76	59.61 \pm 10.08	13.73	0.003
APW [mm]	7.76 \pm 0.52	7.06 \pm 0.72	9.02	0.002
LRW [mm]	11.51 \pm 0.77	10.91 \pm 0.98	5.21	0.059
MT [p.u.]	3.13 \pm 0.21	2.72 \pm 0.34	13.09	<0.001
R1 [s ⁻¹]	907.01 \pm 105.12	856.98 \pm 106.66	5.51	0.62
R2* [s ⁻¹]	0.02 \pm 0.002	0.02 \pm 0.005	0	0.55

Table 4.5: group comparison using spinal cord metrics computed from SPM-BSC and SCT approaches. SCA=spinal cord area, APW=anterior-posterior width; MT=magnetization transfer saturation; R1= longitudinal relaxation rate; R2*=effective transverse relaxation rate.

4.4.6 Associations between spinal cord MPM maps and clinical outcomes

Association analysis using MPMs analysed with the SPM-BSC approach showed that greater MT in the cervical cord was associated with better pinprick score (z-score=4.3, $x=0$, $y=-48$, $z=-108$, $p=0.003$, in brain-neck template space) and better SCIM score (z-score=3.9, $x=2$, $y=-56$, $z=-104$, $p=0.005$, in brain-neck template space) (Figure 4.6A). Similarly, MPMs analysed with the SCT approach showed that greater MT in the cervical cord was associated with better pinprick score (z-score=4.5, $x=-1$, $y=-3$, $z=202$, $p < 0.001$, in PAM50 space) and better SCIM score (z-score=4.7, $x=-1$, $y=-2$, $z=207$, $p < 0.001$, in PAM50 space) (Figure 4.6B).

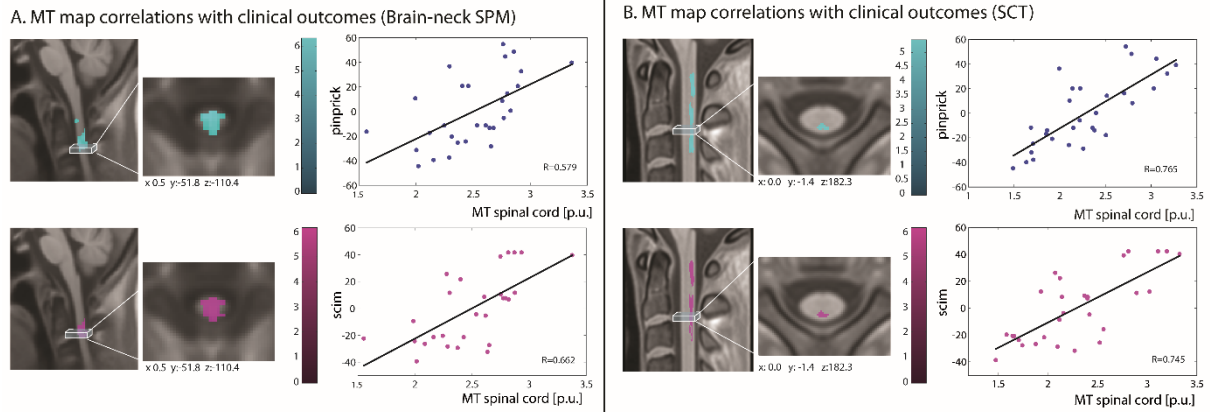


Figure 4.6: Associations between clinical measures and spinal cord MT maps pre-processed using SPM-BSC (in A) and SCT (in B); input data were smoothed with a 3 mm isotropic Gaussian kernel for SPM-BSC and with sigma 3 mm for SCT approach using SCT tools.

4.5 Discussion

In this study, a template covering the brain and the cervical spinal cord was validated within the SPM12 framework. This was done by comparing the results from the between-group effect of SCI patients and healthy controls on qMRI data in the brain and in the spinal cord using the new SPM-BSC analysis and established SPM brain and spinal cord toolbox analysis. In addition, good to excellent ICCs were observed in the majority of brain ROIs. Thus, the proposed SPM-BSC approach enables analysis of equivalent data, sensitive to disease-associated effects as brain or spinal cord, as established region-specific analysis tools but with the advantage of being embedded within the simple unified SPM framework.

SCI patients exhibited lower R1 values in the thalamus, corticospinal tract and sensory-motor cortex compared to healthy controls. Patients also displayed lower MT values than healthy controls in the sensory-motor cortex. These changes are consistently found across analysis methods (see Table 4.2), and are in line with previous studies (Freund et al. 2013; Grabher et al. 2015); supporting the conclusion that SPM-BSC approach is sensitive as SPM-BO in detecting group differences.

In addition, the ICC showed good to excellent values for most of the brain ROIs. Moderate ICCs were reported in the thalamus and corticospinal tract for MT and volume maps. These lower values might be due to discrepancies between the two templates, which were visually assessed by examining the difference between the standard and brain-neck templates. The observed discrepancies can be

attributed to the alignment strategy; in particular the standard brain template is smoother than the brain-neck template since the latter used more precise alignment during the template generation. More direct comparison would be aided by using the same alignment strategy during the generation of the template and subsequent segmentation for both analysis approaches.

Voxel-wise analysis in the spinal cord using the SPM-BSC approach showed that SCI patients exhibited lower MT values than healthy controls, regardless of the size of the smoothing kernel used. However, R1 maps did not show the same results over all smoothing sizes and reduced R1 values were found only for unsmoothed data (Figure 4.4). This suggests that only focal differences were present in the R1 map within the cord and were obscured by partial volume effects resulting from the smoothing process. The SCT analysis using the PAM50 template showed reductions in MT and R1 values in SCI-patients compared to healthy controls; and similar findings were found using smoothed data. The discrepancy between findings of reduced R1 between the two approaches in the smoothed case might be due to the smoothing algorithm applied: in the SPM-BSC analysis, weighted isotropic Gaussian kernel smoothing was applied within the NT tissue class using the same VBQ approach applied in the brain (Draganski, et al. 2011), enabling simultaneous assessment of the brain and neck using random field theory (Flandin and Friston 2016). By contrast, in the SCT approach a centerline smoothing algorithm was used, which works by straightening the cord, applying a 1-D Gaussian smoothing kernel along its length and then un-straightening the cord back into the original space (De Leener et al. 2016). The 1D nature of this latter approach may be more robust to partial volume effects, even within the cord, than the isotropic smoothing adopted in the VBQ approach. Nonetheless, both tools showed myelin sensitive MT changes that were consistent for all smoothing sizes. Further investigation of the impact of smoothing on voxel-wise analyses in the spinal cord is needed.

Spinal cord native-space analysis revealed atrophy and microstructural changes in SCI-patients compared to healthy controls. In particular, both approaches (SPM-BSC and SCT) showed atrophy in the spinal cord, more specifically in APW, and myelin-sensitive MT reduction in SCI-patients compared to healthy controls. However, different results were obtained for R1, where the SPM-BSC approach showed significant differences in SCI-patients compared to healthy controls, whereas in SCT this difference was not statistically significant. However, results from the analysis in PAM50 space (SCT) were more in line with those from the SPM-BSC approach. Atrophy and microstructural changes in the spinal cord observed with the SPM-BSC and SCT approaches in patients with SCI are in line those in the

literature (Freund, Seif, Weiskopf, Friston, Michael G. Fehlings, et al. 2019b). This demonstrates that the SPM-BSC approach can detect the same injury-related differences between SCI-patients and healthy controls as existing tools that are dedicated to either brain or cord. This is achieved without a loss of sensitivity and is the case for both native-space spinal cord metrics and template-space voxel-wise analyses.

The association analysis between spinal cord microstructure and clinical disability showed that higher MT values in the spinal cord were associated with better sensory and motor outcome. The SPM-BSC approach was able to replicate the associations between spinal cord microstructure and functional impairment in SCI-patients that were identified by the SCT analysis, though the latter did show stronger correlation (higher R values). This might again be due to the different smoothing approaches used by the two methods, i.e. SCT uses an adaptive Gaussian kernel oriented along the spinal cord centreline (De Leener et al. 2016). There are no standards for the correct shape and size of smoothing kernel to be used in the spinal cord, warranting further investigation on this topic.

A number of limitations must be considered when using the new SPM-BSC approach. Firstly, the brain-neck template covers only cervical spinal cord until level C3. However, a template spanning more spinal cord levels could be generated using the same algorithm (Blaiotta et al. 2018a) by including MRI data covering more spinal cord segments. This will be the focus of future work. Furthermore, the GM/WM classification in the spinal cord is sub-optimal. As a result, the probability maps of GM and WM were combined in the present study to generate a probability map of NT, which is a non-specific measure of spinal cord volume. In future, better GM/WM classification within the spinal cord might be achieved by combining ultra-high resolution spinal cord data and high resolution brain MRI during template creation. Lastly, results from data pre-processed with the standard brain-based SPM approach showed slightly higher z-scores (see Table 4.3), which could be due to differences in alignment due to the templates and segmentation inputs used.

4.6 Conclusion

This study presents a new approach for the simultaneous analysis of the brain and cervical spinal cord in the SPM framework. The proposed method yielded comparable results to more standard brain- or cord-specific approaches when used to analyse quantitative MRI. It offers a single tool for any MRI studies investigating neurological disease with spinal cord involvement. Validation based on comparing SCI-patients and healthy controls showed that the SPM-BSC analysis is as sensitive as available tools in detecting changes occurring in the brain and spinal cord separately. Template improvement, including better classification of GM/WM in the spinal cord and covering more spinal cord levels, will be the subject of future investigations. This approach provides a means of assessing brain and spinal cord interactions in health and disease.

5 Study II: Microstructural signature of neuropathic pain across the neuraxis after spinal cord injury

Michela Azzarito, Sreenath P Kyathanahally, Jan Rosner, Vince Calhoun, Claudia Blaiotta, John Ashburner, Nikolaus Weiskopf, Katja Wiech, Karl Friston, Gabriel Ziegler and Patrick Freund

This original article was submitted to BRAIN

Authors thank all participants for taking part in this study.

This study is funded by grants from European Research Council/ERC grant agreement n° 616905, grants from BMBF (01EW1711AB) in the framework of ERA-NET NEURON, grants from BRAINTRAIN European research network (Collaborative Project) supported by the European Commission (Grant agreement n° 602186), grants from NISCI supported by the European Union's Horizon 2020 research and innovation program under the grant agreement No 681094, and supported by the Swiss State Secretariat for Education, Research and Innovation (SERI) under contract number 15.0137, grants from UCL Impact Awards and Siemens Healthcare, during the conduct of the study; and The Wellcome Centre for Human Neuroimaging and Max Planck Institute for Human Cognitive and Brain Sciences have institutional research agreements with Siemens Healthcare. P.F. reports grants from ERA-NET NEURON (hMRIofSCIno: 32NE30_173678), grants from NISCI supported by the European Union's Horizon 2020 research and innovation program under the grant agreement No 681094, and supported by the Swiss State Secretariat for Education, Research and Innovation (SERI) under contract number 15.0137, grants from Wings for life charity (No WFL-CH-007/14), grants from International Foundation for Research (IRP-158).P.F. is funded by a SNF Eccellenza Professorial Fellowship grant (PCEFP3_181362/1). V.C. reports NIH grants R01EB020407 and R01MH118695.

K.F. and J.A. are funded by a Wellcome Trust Principal Research Fellowship (Ref: 088130/Z/09/Z). Open access of this publication is supported by the Wellcome Trust (091593/Z/10/Z) .S.K., M. A., J. R, C. B., K.W. have nothing to disclose.

5.1 Abstract

Background Neuropathic pain (NP) affects the majority of patients with spinal cord injury (SCI). In line with the construct of maladaptive plasticity, macrostructural alteration – reflected by changes in brain volume and spinal cord atrophy– have been associated with the occurrence of NP. The pathophysiological processes underlying maladaptive plasticity are thought to be reflected by changes in myelin and iron content.

Methods We assessed quantitative MRI (qMRI) datasets covering the brain and cervical cord of 13 SCI patients with NP, 17 pain-free SCI patients, and 23 healthy controls. Between-group differences in brain and spinal cord volume, myelin (by means of longitudinal relaxation (R1)) and iron content (by means of effective transverse relaxation rate [R2*]) were estimated using multivariate source-based computational anatomy.

Findings SCI patients with NP had lower myelin-sensitive R1 values in the primary motor cortex and dorsolateral prefrontal cortex and greater iron-sensitive R2* increases in the cervical cord, periaqueductal gray (PAG), thalamus, and anterior cingulate cortex when compared to pain-free patients. NP intensity was negatively associated with myelin-sensitive R1 in the PAG and iron-sensitive R2* in the cervical cord.

Interpretation This study illustrates the intimate relationships between neurodegenerative and compensatory processes across ascending and descending nociceptive pathways. Crucially, the degree of myelination and iron accumulation was directly associated with NP intensity. Maladaptive plastic processes affecting both the ascending and descending nociceptive pathways are therefore implicated in the maintenance of NP. Tracking microstructural plasticity may aid in unraveling the complex pathophysiology of NP and facilitate patient monitoring during clinical trials for NP.

5.2 Introduction

Neuropathic pain (NP) is a major secondary complication following spinal cord injury (SCI), affecting more than 50% of individuals (Burke et al. 2017; Kramer et al. 2017). Crucially, NP continues or even worsens over time (Siddall et al. 2003), and is often refractory to treatment. The underlying pathophysiology of NP is complex and involves alterations within “bottom-up” nociceptive processing (i.e., afferent integrity) and “top-down” endogenous pain modulation (Colloca et al. 2017), but is incompletely understood. Functional changes within descending modulatory pathways have been related to the presence of NP after SCI (Albu et al. 2015). The descending pain modulatory network encompasses a cortical-subcortical-brainstem network involved in the modulation of afferent nociceptive information (Huang et al. 2019). Key constituents involved in nociceptive information processing are the posterior insula, thalamus, periaqueductal grey (PAG), the anterior cingulate cortex (ACC), and dorsolateral prefrontal cortex (DLPFC) (for review see (Wiech 2016)), but also the corticospinal tract (Liu et al. 2018). Within ascending nociceptive pathways, inhibition and facilitation of afferent input already occurs at the level of the dorsal horn where primary afferent fibers synapse onto projection neurons (Bingel and Tracey 2008). Modulatory changes within these regions can precipitate a pro-nociceptive state (Tinnermann et al. 2017) and potentially contribute to the emergence and chronification of neuropathic pain (Treede 2016). Traumatic SCI triggers a cascade of trauma-induced secondary neurodegenerative processes, involving demyelination and iron accumulation in the spinal cord and brain (Freund, et al. 2019), which can be tracked using quantitative MRI (qMRI) (Weiskopf et al. 2013). To date, increases and decreases in brain and cord macrostructural (i.e., volumetric) changes have been associated with the occurrence of NP (Grabher et al. 2015; Jutzeler et al. 2016; Wrigley et al. 2009). However, microstructural correlates of these NP associated processes within areas undergoing atrophy and beyond are understudied. Based on recent studies illustrating that activity-dependent plasticity can translate into changes in myelin architecture (Fields 2015a), we hypothesized that such pathophysiological processes will be reflected in microstructural changes to myelin and iron content along nociceptive pathways.

Recent advances in magnetic resonance imaging now allow for the in-vivo investigation of microstructural changes (Cohen-Adad and Wheeler-Kingshott 2014; Weiskopf et al. 2013). We used a multiparametric mapping protocol (MPM) (Weiskopf et al. 2013) that provides indirect measures of myelination (via magnetisation transfer saturation (MT), longitudinal relaxation (R1)) (Callaghan et al. 2014; Natu et al. 2019), and iron content (using the effective transverse relaxation rate (R2*)) (Langkammer et al. 2010)) to carefully track the complex relationship between structural changes

along the trajectories of nociceptive pathways and its relation to the presence and intensity of NP. To characterise simultaneously NP related changes across the neuraxis, we used a combined brain and spinal cord template (Blaiotta et al. 2018b) embedded in the SPM framework. Finally, we applied multivariate source based morphometry (SBM), which estimates interrelationships among voxels across the neuraxis to identify naturally grouped patterns of structural variation between groups (Kasperek et al. 2010). To dissociate NP-associated changes from trauma-induced changes we first compared MRI indices between SCI patients and healthy controls and subsequently between SCI patients with and without NP.

5.3 Materials and Methods

5.3.1 Participants

Thirty chronic traumatic SCI patients (13 with neuropathic pain and 17 without, (Table 5.1)) and 23 healthy controls participated in the study (Supplementary Table 5.1). All participants provided written informed consent prior to enrolment and the study was approved by the Ethics Committee of the Canton Zurich (EK-2010-0271).

	Lesion level at scan	AIS	Age (in years)	Sex F=Female M = Male	Pain intensity (max. 10 points)	Pinprick (max. 122 points)	Light-touch (max. 122 points)	Motor (max. 100 points)
P01	T7	A	70.3	M	8	68	67	50
P02	T3	E	72.6	F	4	112	112	100
P03	T6	B	28.9	M	8	52	77	50
P04	T4	A	26.1	M	8	46	48	50
P05	T4	B	31.3	M	8	46	74	50
P06	C7	D	23.7	M	3	37	72	67
P07	C6	A	21.0	M	3	26	53	23
P08	C8	B	31.3	M	4	46	68	48
P09	C4	D	48.1	M	7	97	98	82
P10	C6	C	52.0	M	6	44	67	44
P11	L3	D	68.2	M	7	102	107	100
P12	C4	D	54.7	F	7	94	62	91
P13	C5	A	29.0	M	6	13	16	14
P14	T11	B	68.8	F	0	74	92	81
P15	L3	D	44.8	M	0	106	106	95
P16	T10	D	53.1	M	0	90	90	98
P17	T10	A	30.6	M	0	78	82	66
P18	T3	A	52.8	M	0	44	47	50
P19	T12	A	36.4	M	0	78	78	54
P20	T1	A	60.4	M	0	40	52	49
P21	T9	A	53.1	M	0	66	68	50
P22	T10	B	32.5	M	0	72	78	50

P23	T7	A	39.2	M	0	58	60	50
P24	C7	A	19.1	M	0	33	33	23
P25	C5	A	43.2	M	0	18	20	25
P26	T1	D	71.7	M	0	41	112	89
P27	C8	A	33.6	M	0	29	32	35
P28	C6	A	31.7	M	0	20	33	26
P29	C5	B	43.0	M	0	32	77	25
P30	C4	D	68.9	M	0	78	69	89

Table 5.1: Demographics of the patients with spinal cord injury

5.3.2 Clinical assessment

The neurological examination was performed according to the International Standards for Neurological Classification of Spinal Cord Injury (ISNCSCI)(Steven C Kirshblum et al. 2011b). In addition, post-SCI NP was assessed using the EMSCI pain questionnaire. On the self-report EMSCI questionnaire (V4.2, <http://www.emsci.org/index.php/project/the-assessments/pain>), patients rate various aspects of their spontaneous pain (e.g., current pain intensity, mean and maximal pain intensity during the last week before the assessment, location and quality of pain) as well as evoked symptoms (e.g., intensity of allodynia and paresthesia). The pain intensity was quantified using an 11-point numeric rating scale with “0” indicating no pain and “10” indicating the worst imaginable pain. Neuropathic pain was defined according to the standard taxonomy related to SCI (Bryce et al. 2012). We used ANOVA test to assess group differences for the demographic.

5.3.3 Data acquisition

Structural whole-brain data, including the cervical cord down to vertebra C5, were acquired on a 3T Magnetom-Verio MRI scanner (Siemens Healthcare, Erlangen, Germany) equipped with a 16-channel radiofrequency (RF) receive head and neck coil and RF body transmit coil. The scanner was upgraded during the study period (from Verio to Skyra^{fit}).

A T1-weighted structural scan was acquired using a 3D MPAGE (magnetization-prepared rapid acquisition gradient echo) sequence with the following: field of view (FoV) of 224 × 256 mm², matrix size 224 × 256, isotropic resolution of 1mm³, TR = 2420ms, TE = 4.18ms, flip angle(α) = 9°, inversion time = 960ms, and readout bandwidth of 150 Hz per pixel.

A whole-brain multi-parameter mapping (MPM) quantitative MRI protocol (Weiskopf et al. 2015), using a multi-echo 3D FLASH (fast low-angle shot) sequence, was performed. The following parameters

were used: FoV of $240 \times 256\text{mm}^2$, matrix size = 240×256 , isotropic resolution of 1mm^3 , GRAPPA parallel imaging in phase-encoding direction (anterior-posterior) with speed-up factor of 2, partial Fourier acquisition with 6/8 sampling factor in the partition direction (left-right), and a readout bandwidth of 480 Hz per pixel. Differently weighted MR images were achieved by choices of repetition time (TR) and flip angle (α): (1) T1-weighted (T1w): 25ms / 23° , (2) PD-weighted (PDw): 25ms / 4° , and (3) magnetization transfer (MT) weighted (MTw): 37ms / 9° with off-resonance MT saturation RF pulse prior to excitation. Echoes were acquired at seven equidistant echo times (TE), from 2.46ms to 17.22ms for all volumes and an additional echo at 19.68ms for PDw and T1w.

5.3.4 Data analysis

We used SPM12 spatial routines (www.fil.ion.ucl.ac.uk/spm) on the T1w images and MPM maps. As a novelty, we used a brain plus spinal cord (BSC) template (Blaiotta et al. 2018b) covering the brain and the cervical spinal cord in the unified segmentation approach (Ashburner and Friston 2005), which allowed us to assess brain and cervical cord changes within the same statistical framework. This BSC template was specified as a tissue probability map (i.e., spatial prior) in the unified segmentation step. This procedure assumes every voxel to be drawn from an unknown mixture of 12 Gaussians, which were grouped into 7 distinct tissue classes: grey matter (GM, using one Gaussian), white matter (WM, using one Gaussian), and cerebrospinal fluid (CSF, using one Gaussian), bone and air (using three Gaussians), soft tissue (using three Gaussians), non-neural tissues (using three Gaussians) and air/background (using three Gaussians)(Ashburner and Friston 2005). For volumetric analysis, we applied SPM12's unified segmentation, including the BSC template, to each subject's MPRAGE image (i.e. T1-weighted). T1w images were non-linearly transformed into standard MNI (Montreal Neurological Institute) space using diffeomorphic group-wise registration (Dartel) implemented in SPM12 (Ashburner 2007a). This defined the space for subsequent modelling steps. Finally, GM and WM probability maps were smoothed with an isotropic Gaussian kernel of 5mm full width at half maximum (FWHM).

For microstructural analysis, the acquired T1w, PDw, and MTw FLASH echoes from the MPM protocol, were first averaged to increase signal to noise ratio. UNICORT (Weiskopf et al. 2011b), was then used for correcting RF transmit field inhomogeneity and to calculate quantitative maps of magnetization transfer saturation (MT), longitudinal relaxation rate (R_1), and effective transverse relaxation rate (R_2^*) (Weiskopf et al. 2013). MT maps were segmented using the unified segmentation approach that included the BSC template. Segmented MT maps were then transformed non-linearly to standard MNI

space using Dartel, but without scaling by the Jacobian determinants (i.e., no “modulation” of parameter values). Additionally, all MPM maps (MT, R1 and R2*) were warped to the MNI space by using the participant specific flow fields from the MT maps and finally smoothed using a previously established tissue-weighted-smoothing procedure with a kernel of 5mm, in order to preserve quantitative values within the GM and WM tissue classes of each MPM map (Draganski, et al. 2011).

Subsequent modelling and analysis were performed for smoothed, normalized morphometric and microstructural parameter images (for WM and GM) across the brain and cervical cord, simultaneously. Each of the morphometric and microstructural parameter images were then individually analyzed using source based morphometry (SBM) (Gupta, et al. 2019). SBM (Gupta et al. 2019) is a multivariate analysis approach, implemented in the SBM toolbox within GIFT (<http://trendscenter.org/software>) that estimates covarying networks. SBM can be considered as a multivariate extension of VBM which accounts for spatial dependencies among different regions and increases sensitivity to effects distributed across the neuraxis. SBM applies spatial independent component analysis (Calhoun et al. 2001) (organized as subjects-by-voxels) to produce maximally independent components (components-by-voxels) and their associated mixing-matrices (subjects-by-components). The number of components (k) for subsequent ICA were estimated using a principled information theoretic approach (rather than arbitrarily selecting the number of components (Calhoun et al. 2001)). ICA was then applied to the T1w WM images of 23 HC, 12 NP and 17 without NP, which were arranged into one 53-row (subject-by-T1w-WMvoxels) data matrix. This data matrix was then decomposed into a mixing matrix (subjects by components) and a component matrix (components by voxels). The mixing matrix expresses the relationship between 53 subjects and k components. The rows of the mixing matrix indicate the contribution of each k component to a given subject, whereas the columns indicate how each component contributes to the 53 subjects. The component matrix on the other hand expresses the relationship between the k components and brain/cord voxels. The rows of the component matrix indicate how one component contributes to different voxels, whereas the columns of the component matrix indicate how one voxel contributes to each of the components.

The mixing matrix was used for subsequent statistical analysis, where every column of the mixing matrix quantifies the contribution of each component to the 53 subjects. An ANOVA with age, gender and scanner as covariates was applied to each column to assess which components showed a significant group difference. A false discovery rate (Benjamini and Hochberg 1995) controlling procedure with $q^* = 0.05$ was used to assess which components were statistically significant. A

significant component comprises clusters of voxels – with positive and negative values – reflecting group effects in different regions of brain & spinal cord that are interrelated to each other.

SBM was repeated for each of the volumetric and microstructural parameter maps. The number of components estimated were 8,8,7,7,6,3,5,5 for GM and WM maps from the MRPAGE, R1, R2* and MT maps, respectively. Components with loading scores that differed significantly between either controls and patients or neuropathic pain patients versus pain-free patients were identified. No significant components were found for MT maps. The significant components were scaled to unit standard deviation (SBM Z map), thresholded at a value of $|Z| > 3$ as described in (L. Xu et al. 2009) and rendered on the MNI-normalized BSC template for appropriate contrasts (Controls > Patients, Patients > Controls, NP Patients > Pain-free, Pain-free > NP Patients) (Figure 5.1 and 5.2). For illustrative purposes, the GM & WM are represented in the same color for each modality (e.g. volume, R1, R2*) of the significant components.

Finally, in order to explore the association between brain and spinal cord changes and pain intensity in patients with NP, we used SPM's multiple linear regression models adjusting for potentially confounding effects of age, gender and scanner upgrade. The explanatory variables in these analyses were pain intensities (range from 0-10), while the response variables were the volumetric and microstructural parameter maps above.

5.4 Results

5.4.1 Trauma-associated changes in SCI patients compared to healthy controls

We first confirmed previous reports showing trauma-induced macrostructural and microstructural changes across the motor, sensory and limbic system. Specifically, macroscopic changes (decreased volume) were observed in the cervical cord, thalamus, posterior cingulate, lingual gyrus, precuneus, superior and medial temporal gyrus and para-hippocampal gyrus (Figure 5.1 B & Table 5.2) when all patients (NP + Pain-free) were compared to controls. In these atrophied areas and beyond, myelin-sensitive R1 component was decreased in the sensorimotor cortices, middle frontal gyrus, precuneus and inferior parietal lobule when compared to healthy controls. The iron-sensitive R2* component showed an increase in the cervical cord, lentiform nucleus, cerebellum, posterior cingulate, middle temporal gyrus, right cerebellum and fusiform gyrus (Figure 5.2B, Table 5.3 & Table 5.4).

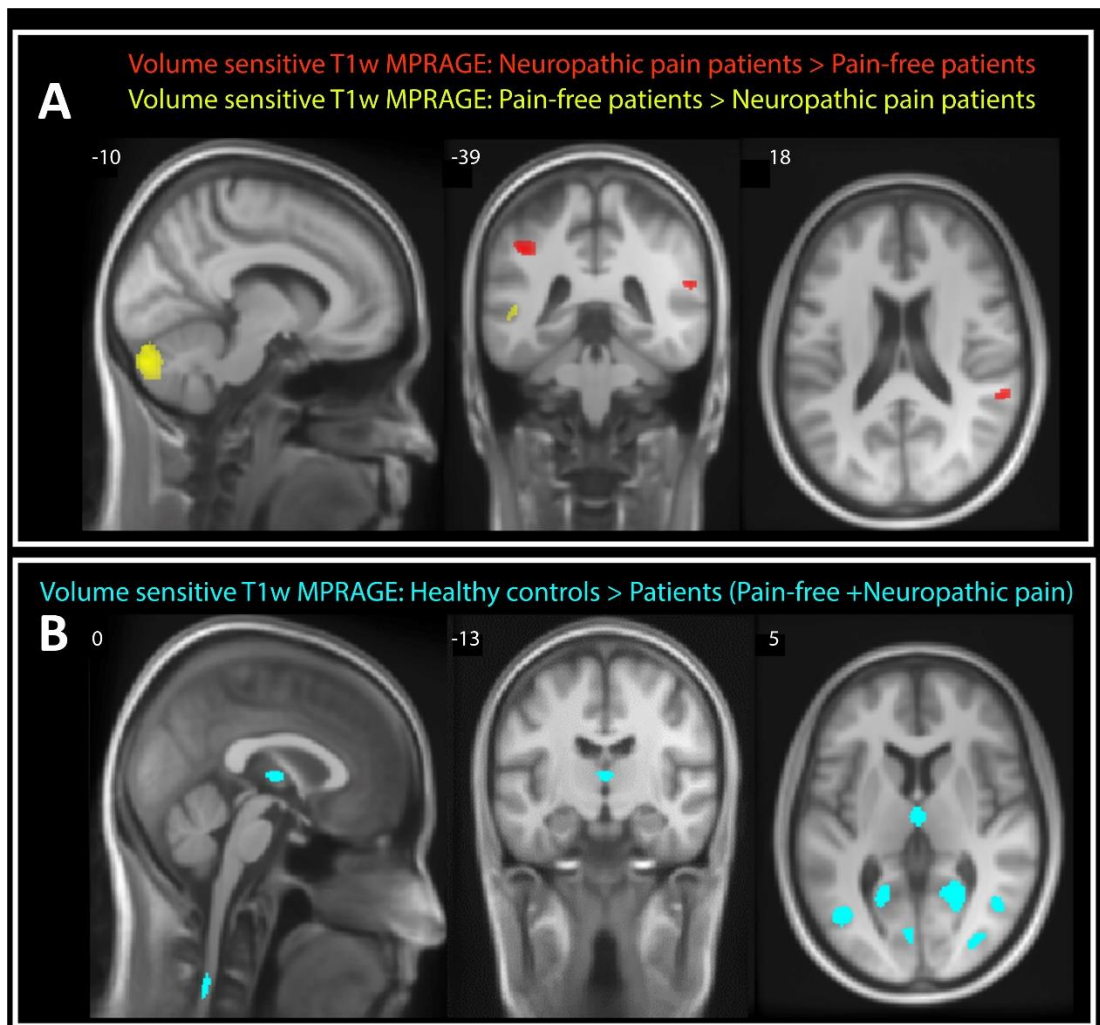


Figure 5.1: Source based morphometry (SBM) renderings showing trauma induced macrostructural changes along the neuroaxis, with key areas of the sensorimotor and limbic system affected by atrophy. (a) For patients with NP, atrophic changes (shown in yellow) associated with NP were observed in the cerebellum, middle temporal gyrus and occipital gyrus, while volume increases (shown in red) were observed in the posterior insula, superior temporal, occipital and middle frontal gyrus when compared to pain-free patients;(b) Trauma induced changes (i.e. all patients (NP + Pain-free) were compared to controls) the cervical cord, thalamus, posterior cingulate, lingual gyrus, precuneus, superior-, middle-, temporal gyrus and para-hippocampal gyrus showed significant atrophy (shown in blue).

Table 5.2: Volumetric changes based on the MPAGE T1-weighted sequence

Pain-free > NP patients			NP > Pain-free patients			Healthy controls > Patients (NP + Pain-free)		
No. of voxels	Peak cluster coordinates	Anatomical location	No. of voxels	Peak cluster coordinates	Anatomical location	No. of voxels	Peak cluster coordinates	Anatomical location
1159 423	-7.5,-85.5,-31 46.5,-67.5,-37	Left Cerebellum Right Cerebellum	364	-43.5,-28.5,8	Posterior insula	143	1.5, -54,-121	Cervical cord
47 81	52.5, -49.5, 0.5 -49.5,-36, 0.5	Middle Temporal Gyrus	165	-24,1.5, 51.5	Middle Frontal Gyrus	182	0 -12, 5	Thalamus
161	28.5,-87,6.5	Middle Occipital Gyrus	105 42	-42,-69, 5 40.5,-73.5,11	Middle Occipital Gyrus	179 66	39, -76.5,8 48,-42,14	Middle Occipital Gyrus
			64	58.5,-39, 18.5	Superior Temporal Gyrus and Posterior insula	331 83 160 72	-42,-67.5,3.5 49.5,-28.5, - 2.5 46.5, -60, 5 -28.5, -88.5, 3.5	Middle and Superior Temporal Gyrus
						67	18,-78, 36.5	Right Precuneus
						163 67	-21 -72,-7 6,-82.5, -5.5	Lingual gyrus
			423	-34.5,-43.5, 39.5	Left Parietal Lobe			
						1300 617	-19.5,-54,5 24,-57,6.5	Posterior Cingulate and Parahippocampal Gyrus

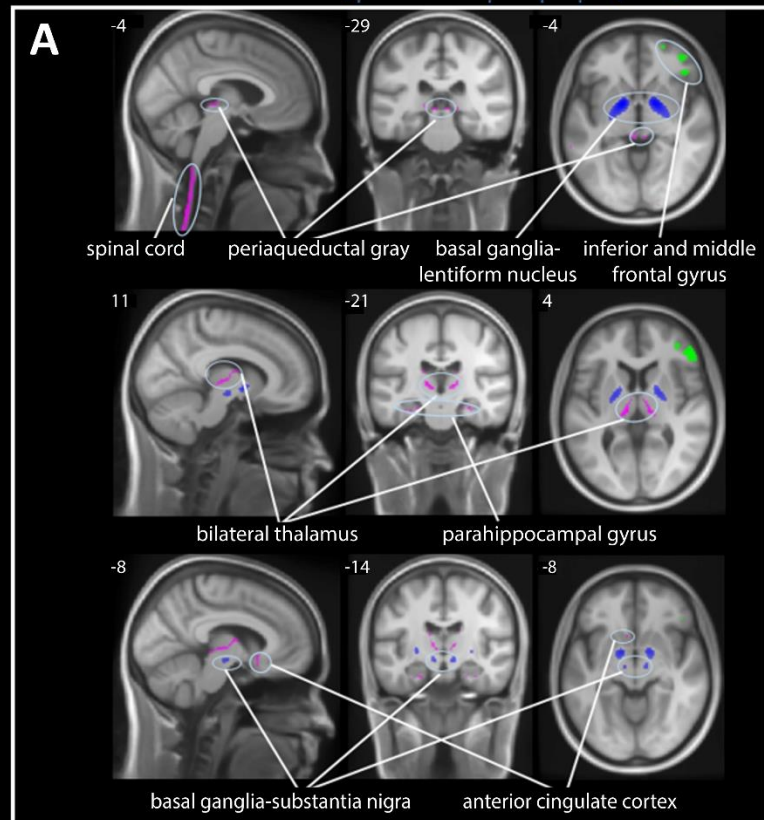
Table 5.3 Myelin-sensitive changes based on longitudinal relaxation rate (R1)

Pain-free > NP patients			Healthy controls > Patients (NP + Pain-free)		
No. of voxels	Peak cluster coordinates	Anatomical location	No. of voxels	Peak cluster coordinates	Anatomical location
1663	49.5, 36,2	Dorsolateral prefrontal cortex	58	0 -51 -79	Cervical cord
189 203	39, 48, -2.5 33, 3, 62	Middle Frontal Gyrus and Premotor cortex	221	6,-13.5, 71	Medial Frontal Gyrus
164	60, 6, 18.5	Inferior Frontal Gyrus and Precentral gyrus	592	-13.5,-34.5, 74	Left primary motor and sensory cortex
			155 306	10.5,-46.5, 63.5 28.5,-43.5, 60.5	Right primary sensory cortex
			323	-28.5,-43.5, 68	Left primary sensory cortex
			520 303	37.5,-27, 60.5 27,-12, 69.5	Right primary motor cortex
			514	-25.5,-13.5, 68	Left primary motor cortex
			276 84 69	-10.5,-81, 36.5 -21 -75, 47 -10.5, -46.5, 56	Left Precuneus
			322 293	13.5,-79.5, 36.5 19.5,-57, 65	Right Precuneus
			113 88 124	42,-48,47 -42,-58.5, 53 -49.5,-40.5, 53	Inferior Parietal Lobule

5.4.2 Pain-associated changes in SCI patients with NP compared to pain-free SCI patients

In NP patients, atrophic changes associated with NP were observed in the cerebellum, middle temporal gyrus and occipital gyrus, while volume increases were observed in the posterior insula, superior temporal, occipital and middle frontal gyrus when compared to pain-free patients (Figure 5.1 A & Table 5.2). Analysis of the myelin-sensitive R1 component showed signal decreases in primary motor cortex and DLPFC in NP patients when compared to pain-free patients (Figure 5.2A & Table 5.3). In NP patients, the iron-sensitive R2* component showed increased signal in the cervical cord, thalamus, anterior cingulate cortex, PAG, and para-hippocampal gyrus, while signal was decreased in the lentiform nucleus and substantia nigra when compared to pain-free patients (Figure 5.2A & Table 5.4). Note, that trauma-related differences were predominantly visible in the medial thalamus whereas pain-related changes were located in the lateral thalamus.

Myelin sensitive R1: Pain-free patients > Neuropathic pain patients
 Iron sensitive R2*: Neuropathic pain patients > Pain-free patients
 Iron sensitive R2*: Pain-free patients > Neuropathic pain patients



Myelin sensitive R1: Healthy controls > Patients (Pain-free + Neuropathic pain)
 Iron sensitive R2*: Patients (Pain-free + Neuropathic pain) > Healthy controls

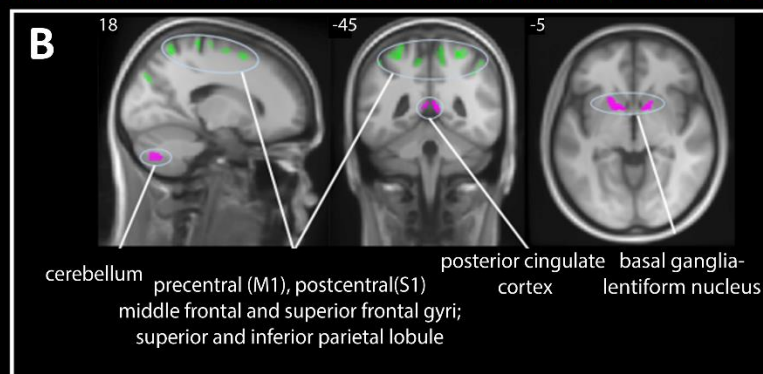


Figure 5.2: Source based morphometry (SBM) renderings showing pain-induced microstructural changes across the motor, sensory and limbic system ($|Z|=3$) in the brain and spinal cord. (a) For patients with NP when compared to pain-free patients, the myelin-sensitive R1 component showed signal decreases in primary motor cortex, dorsolateral prefrontal lobe, (shown in green), increase in iron-sensitive R2* component in the cervical cord, thalamus, anterior cingulate cortex, periaqueductal gray, and para-hippocampal gyrus (shown in pink), decrease in R2* (shown in blue) in the basal ganglia (i.e. lentiform nucleus) and substantia nigra. (b) For patients with and without NP when compared to healthy controls, myelin-sensitive R1 component (shown in green) was decreased in the sensorimotor cortices, middle frontal gyrus, precuneus and inferior parietal lobule, whereas iron-sensitive R2* component (shown in pink) showed increases in the cervical cord, lentiform nucleus, cerebellum, posterior cingulate, middle temporal gyrus, right cerebellum and fusiform gyrus.

Pain-free > NP patients			NP > Pain-free patients			Patients (NP + Pain-free) > Healthy controls		
No. of voxels	Peak cluster coordinates	Anatomical location	No. of voxels	Peak cluster coordinates	Anatomical location	No. of voxels	Peak cluster coordinates	Anatomical location
			1305	0, -56,-125.5	Cervical cord	876	3,-57 -130	Cervical cord
729	-15,1.5, -4	Left Lentiform nucleus				308	-12, 9,-4	Left Lentiform Nucleus
741	16.5, 3, -2.5	Right Lentiform nucleus				152	12 ,7.5,-8.5	Right Lentiform Nucleus
44	-9, -13.5,-11.5	Left Substantia nigra and Subthalamic nucleus	299	-9,-19.5,3.5	(Left) lateral prefrontal thalamus, sensory thalamus, medial prefrontal thalamus, PAG	164	4.5,-43.5,8	Posterior Cingulate
58	9, -13.5,-11.5	Right Substantia nigra and Subthalamic nucleus	219	12,-19.5,5	(Right) lateral prefrontal thalamus, sensory thalamus, medial prefrontal thalamus, PAG			
			85	-21,-10.5,-29.5	Left Parahippocampal Gyrus	60	45,-72, 12.5	Middle Temporal Gyrus
			70	22.5, -7.5,-31	Right Parahippocampal Gyrus	42	37.5, -4.5,-37	
						71	-55.5,-10.5,-38.5	
						91	-28.5,3,-37	
			62	-10.5, 12,-13	Anterior Cingulate cortex	137	19.5,-70.5,-43	Right Cerebellum
						99	-28.5,-54,-16	Fusiform gyrus
						42	37.5, -4.5,-37	

Table 5.4 Iron-sensitive changes based on effective transverse relaxation rate (R2*)

Magnitude of structural changes is associated with pain intensity

In NP patients, pain intensity was negatively associated with myelin-sensitive R1 in the PAG (Z-score=3.91, cluster extent voxels=77, p=0.004, FWE corrected) and positively correlated with iron-sensitive R2* in the cervical cord (Z-score=3.6, cluster extent voxels=32, p=0.042, FWE corrected) (Figure 5.3).

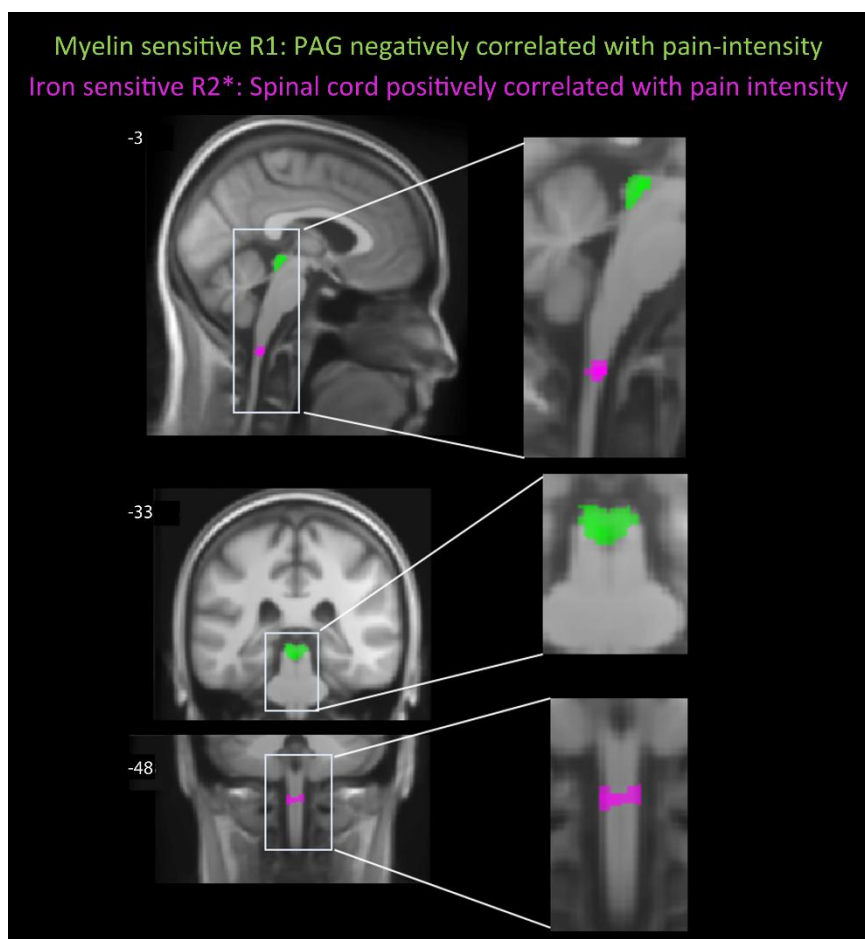


Figure 5.3: Statistical parametric maps (SPM) testing (i.e. linear regression) for an association between myelin-sensitive R1 and iron-sensitive R2* changes and pain intensity in the periaqueduct and medulla oblongata (t-values uncorrected $p < 0.005$, shown for descriptive purposes, masked by the union of the regions of interest).

5.5 Discussion

This study shows both decreased and increased myelin- and iron-sensitive content differences associated specifically with NP along the trajectory of ascending and descending nociceptive pathways after SCI. Most group effects are located within key structures involved in endogenous pain modulation (Huang et al. 2019; Wiech 2016). As SCI provides an ideal model to differentially study trauma-related and pain-related effects – following a defined lesion to the nervous system – these findings speak to specific pathophysiological mechanisms related to the development and maintenance of chronic neuropathic pain.

We first dissociated trauma-induced changes from NP associated (micro-) structural changes. In agreement with previous reports, trauma-induced atrophic changes, as well as myelin and iron changes, were evident across the sensorimotor and limbic system (for review, see (Freund, et al. 2019)). Accompanying trauma-induced changes, volumetric increases and decreases in the cervical cord, thalamus, primary somatosensory cortex, ACC, and DLPFC have been also associated with NP following SCI (Jutzeler et al. 2016; Wrigley et al. 2009). We demonstrate the microstructural substrates of such pain-associated volumetric changes by revealing changes in myelin and iron content along the trajectories of ascending and descending nociceptive pathways. Specifically, iron-sensitive R2* increases were detectable in the spinal cord, PAG, thalamus, ACC and para-hippocampal gyrus, suggesting iron accumulation due to neurodegenerative processes (Langkammer et al. 2010; Steiger, Weiskopf, and Bunzeck 2016) in regions that have previously been implicated in NP after SCI (Gustin et al. 2014; Jutzeler et al. 2016).

Communication between the prefrontal cortical areas and the PAG has been recently shown in functional MRI studies (Roy et al. 2014; Tinnermann et al. 2017). Here, we provide evidence for further downstream effects. Notably, microstructural alterations were detected within the spinal cord and also PAG. These effects were related to pain intensity; furnishing an important predictive validity to this imaging phenotype. The PAG is known to serve as a link between the forebrain and the lower brainstem (see (Benarroch 2012) for review) and is pivotal for the descending modulation of pain. It receives input from the frontal lobe, amygdala, hypothalamus, and anterior cingulate cortex and engages the rostral ventral medulla which in turn controls nociceptive processing in the spinal dorsal horn (Basbaum and Fields 1979). Direct stimulation of the PAG has successfully been trialed as a treatment option for NP including pain following SCI (Jermakowicz et al. 2017). Thus, it is anticipated that molecular changes in the PAG could compromise descending inhibition of nociceptive processing and subsequent increased spinal gain of incoming information. Such dysregulation in descending pain modulation has been shown to contribute to central sensitization as the hallmark of NP (Ossipov, Dussor, and Porreca 2010). Our study is the first to provide evidence for NP-related changes in PAG microstructure in humans, underscoring the clinical relevance of these changes for NP following SCI. In conjunction with microstructural alteration in the injured spinal cord, these findings are compatible with the notion of a dysfunctional spinal-bulbo-spinal loop, a key circuit of the descending pain modulatory system (Villanueva and Le Bars 1995).

Additional evidence for an impaired descending pain modulatory system can be inferred from microstructural changes in other key constituents of this network, namely the ACC (i.e., increased iron

accumulation) and DLPFC circuitry (Wiech 2016) (i.e., reduced myelin content). Previous studies had found structural and functional NP associations in the prefrontal cortex (Apkarian et al. 2005; Ong, Stohler, and Herr 2019), and particularly the DLPFC (Gustin et al. 2009) in those with NP. For example, reduced grey matter volume and hypometabolisms in the left DLPFC were observed in SCI patients suffering from NP when compared to healthy controls (Yoon et al. 2013). Here, we not only show that this reduction in volume is linked to a decrease in myelin-sensitive R1, but also that it is pain specific – as this reduction was not observed in pain-free patients. Of note, these anatomical alterations in the DLPFC not necessarily reflect an injury-induced change, but could instead be indicative of an individual's predisposition to develop persistent pain (Gustin et al. 2009). As the DLPFC is both involved in both top-down inhibition and facilitation of pain, the decreases in myelin content reported here in align well with the concept of pathological nociceptive gain control in NP after SCI (Albu et al. 2015; Finnerup and Jensen 2004).

Thalamic relay nuclei are not only key to central in afferent somatosensory processing, but are also densely connected with motor pathways – including the basal ganglia as well as cortical and subcortical regions – involved in pain processing (Gustin et al. 2011). Consequently, the thalamus is considered to play an important role in the pathophysiology of central neuropathic pain (Gustin et al. 2014). The impact of deafferentation on thalamic pathophysiology is complex and involves reduced GABAergic inhibition (Henderson et al. 2013), an imbalance between the medial and lateral thalamus with possible disinhibition of spinal projections to the medial thalamus (Tasker et al. 1987) and the release of abnormal thalamo-cortical patterns (Jeanmonod, Magnin, and Morel 1993). Intriguingly, our finding of iron accumulation in the thalamus in SCI patients with NP was confined to lateral thalamic nuclei, while volumetric changes in the medial thalamus were trauma-related (i.e., found in SCI with and without NP). These findings offer an essential line of evidence that structural plasticity within the thalamus is specifically linked to the pathophysiology of NP after SCI.

Finally, we observed an unexpected decrease of iron-sensitive R2* in the basal ganglia. The role of the basal ganglia in chronic pain conditions is still poorly understood, but its vast anatomical connections to a multitude of brain areas (including the thalamus) and cervical cord make it plausible that the basal ganglia could play an important role in aberrant nociceptive bottom-up and top-down signaling (for review see (Borsook et al. 2010)). The decrease in iron-sensitive R2* might indicate processes of functional compensation (Ghadery et al. 2015) in contrast to iron-sensitive R2* increases in atrophic central areas (Callaghan et al. 2014). Our findings warrant further studies into the role of basal ganglia

pathways in central neuropathic pain. At present, the implications of these findings remain highly speculative.

From a technical perspective, the multivariate (SBM) tests for group effects described above are, in principle, much more sensitive than the equivalent mass univariate (VBM) tests one would obtain from analysing the volumetric and microstructural images directly. This is because multivariate analyses do not try to assign a significance to each voxel or region – they test for distributed effects that covary among individuals (Gupta et al. 2019). Crucially, this multivariate analysis would not have been possible without combining the brain and spinal-cord within the same analysis. This speaks to the potential importance of the combined brain and spine template used to spatially normalize our data. This template is available through open access (<http://www.fil.ion.ucl.ac.uk/spm/toolbox/TPM/>) for related studies that test for distributed effects throughout the neural axis.

5.5.1 Limitations

Our study had some limitations. The cross-sectional nature of the study restricts conclusions to a single time point and thus the temporal evolution of the above-described microstructural changes remains uncertain. Despite the histological evidence that MT, R1 and R2* markers correspond to their biochemical counterparts (Langkammer et al. 2010; Natu et al. 2019)) they are indirect markers of myelin and iron content and any interpretation should take this into consideration. Thus, partial contributions of unexplored physiological/cellular processes occurring after SCI cannot be excluded. Moreover, current standardized neurological tests cannot account for unobserved latent lifestyle or genetic factors which might be different between SCI patients and controls, a-priori. To mitigate any potential effect of the scanner upgrade on our results, we ensured that the same number of patients and controls were measured before and after upgrade, allowing us to account for the upgrade effect (common to both cohorts). Finally, gender was not balanced across groups, with the majority of participants being male. However, this is representative of the general population of SCI patients, in which the male to female patients' ratio is 4:1 (Jackson et al. 2004).

5.6 Conclusion

This study evinces the microstructural signature of NP, affecting key constituents of the ascending and descending nociceptive pathways – its magnitude being directly linked to NP intensity. The complex interplay between myelin and iron changes in areas related to sensory and affective processing highlights maladaptive plastic processes likely involved in the maintenance of NP. Beyond unraveling

the intimate pathophysiology of NP, tracking microstructural plasticity may facilitate patient monitoring during clinical trials for NP.

6 Study III: The interplay between corticomotor system and hippocampus circuit changes during procedural learning

Manuscript in preparation.

6.1 Abstract

Background Plasticity in grey and white matter within and between the motor and limbic system are necessary for procedural learning. However, the spatial and temporal interplay of microstructural changes within and across these areas is still understudied.

Methods Eighteen healthy males performed a computer-controlled motion game on a dance platform four times a week using either their upper (n=9) or lower (n=9) limbs over a period of four weeks and underwent scans at baseline, 7, 14, 21 and at 84 days follow-up. Additionally, 14 healthy males were scanned following the same protocol, but without training. We used multivariate analysis of multiparametric mapping data to assess training-induced myelin and volumetric changes within and across the sensorimotor cortices, its descending projection and hippocampus. We further assessed the time lag of these changes and its somatotopic pattern and association with performance improvements.

Results Performance improvements were achieved in all participants and were maintained at follow-up. Transient myelin-sensitive longitudinal relaxation rate (R1) decrease was observed in the left sensorimotor cortex (M1) and bilateral corticospinal tracts (CST). In the hippocampus, transient decreased R1 and myelin-sensitive magnetization transfer (MT) accompanied transient volume increases in the left Cornu Ammonis (CA). Moreover, linear increased R1 and MT were observed in the bilateral entorhinal cortex (EC). Transient R1 decreases in the left CST was preceding the transient R1 decrease in left M1; and both R1 changes in the left M1 and left CA are preceding R1 changes in left EC. Along the cranial CSTs, greater changes in MT in the posterior part of the limb of the internal capsula occurred in lower-limb trainees when compared to upper limb trainees. Performance improvements were associated with volume and MT changes in bilateral hippocampus.

Conclusions Performance improvements are paralleled by dynamic, temporally and somatotopical distinct changes within grey and white matter of the corticomotor system. These changes are followed by and relate to dynamic and behavioural relevant changes in the hippocampus. These findings suggest a critical spatio-temporal interplay between changes in the corticomotor system and hippocampus during the period of procedural learning.

6.2 Introduction

Procedural learning, such as dancing, requires physical and cognitive effort and relies on changes in the central nervous systems (CNS) function (Dayan and Cohen 2011). Music and dance together require spatiotemporal coordination. These functional changes have been shown to have grey and white matter changes in the human brain (Draganski and May 2008; Zatorre et al. 2012). Volumetric changes in the hippocampus have been implicated during spatial navigation (Maguire et al. 2000) or dancing (Hüfner et al. 2011) and in the motor cortex (M1) during balance training (Taubert, Mehnert, et al. 2016). In individuals with a temporarily immobilised upper limb, a relative grey matter decrease occurred in the contralateral M1 with a concomitant decrease in corticomotor excitability (Granert et al. 2011). Subsequent training once immobilisation was discontinued re-established previous levels of regional grey matter density and M1 excitability (Granert et al. 2011). Training-induced white matter changes were also observed in human studies in the left intraparietal sulcus and left parieto-occipital sulcus while performing motor practice in a semi-immersive virtual reality (Lakhani et al. 2016); in the occipital and temporal lobe in gymnasts (Deng et al. 2018); or in the fronto-parietal network in a balance task (Taubert et al. 2011). These findings propose that learning-related neural processes follow a sequence of expansion, selection, and renormalization (Draganski et al. 2006; Fu and Zuo 2011; Makino et al. 2016; Wenger et al. 2016). Experimentally, performance improvements have been linked to myelination (Badea et al. 2019; Gibson et al. 2014; Lamprecht and LeDoux 2004; Theodosios, et al. 2008). Myelin is crucial for rapid neuronal signal conduction and can be modified by experience (McKenzie et al. 2014).

However, little is known about the spatio-temporal dynamics within and across brain networks and how these structural changes are related to performance improvement. This study investigates the spatio-temporal evolution of microstructural changes during one month of intensive dance training based on a computer-controlled motion game on a dance platform to probe (i) the spatio-temporal evolution of training-induced changes; (ii) the spatio-temporal interactions between white and grey matter across the areas of interested; (iii) the somatotopological changes characterizing upper and lower limb training; and (iv) the associations between structural changes and behavioural improvements. We use cutting edge computational modelling of multi-parametric mapping (MPM) data which has shown significant potential to characterize indirectly changes in myelin content by means of longitudinal relaxation rate ($R1 = 1/T1$) and magnetisation transfer (MT) saturation and volume changes (Dick et al. 2012; Draganski et al. 2011; Helms, et al. 2008; Sereno et al. 2013; Weiskopf 2013).

6.3 Materials and Methods

6.3.1 Participants

Thirty-two healthy adult males (age = 37.42 ± 11.65 years, all males) were recruited. All participants were right-handed (Oldfield 1971), with normal or corrected-to-normal vision, no history of psychological or neurological diseases, and did not have any contraindication to participate in an MR study. All participants were naive to the experimental setup with no prior experience in the training task. Participants were randomly assigned to one of the following three groups: upper limb training (n=9, age= 34 ± 10.22 years), lower limb training (n=9, age= 38.67 ± 13.22 years) and no training group (n=14, age= 38.71 ± 10.98 years).

6.3.2 Standard protocol approvals, registrations, and patient consents

The study was approved by the local ethics committee of Zurich the 'Kantonale Ethik kommission Zurich' (EK-2013-0559), and the study protocols were in accordance with the Declaration of Helsinki. All participants provided written informed consent prior to enrolment.

6.3.3 Experimental design and training task

The Training was performed over a period of 4 weeks (c.a. 30 minutes, 4 times per week, figure 6.1A) and involved a motor task on a dance platform (Impact Dance Platform, Positive Gaming BV, Haarlem, Netherlands). In particular, participants have to move upper or lower limbs – based on an open source software (StepMania 5 Beta 3 in Windows, www.stepmania.com) – where arrows with different directions (up, down, right and left) were rising from the bottom to the top of the screen (figure 6.1B). Whenever the rising arrow matched with the corresponding grey-one at the top, participants had to press the appropriate button of the dancing platform with their foot/hand, respectively (figure 6.1C, D). The behavioural outcome measure was the time (in milliseconds) in which participants pressed each button. We used a discovery learning approach (Orrell, et al. 2006) in which no information about the performance strategy was provided during learning. Therefore, participants had to discover their optimal strategy to improve the motor task (e. g. identify the right time to press the buttons) based on real-time visual feedback from the software during training (whenever the button was precisely pressed, the word 'perfect' was shown on the screen). In order to assess training improvements and microstructural changes over time, a longitudinal behavioural assessment (training test) and MRI

acquisition were performed before (day 0), during the training period at 7, 14, 28 days, and at 84 days follow-up. Scanning was performed before the training sessions.

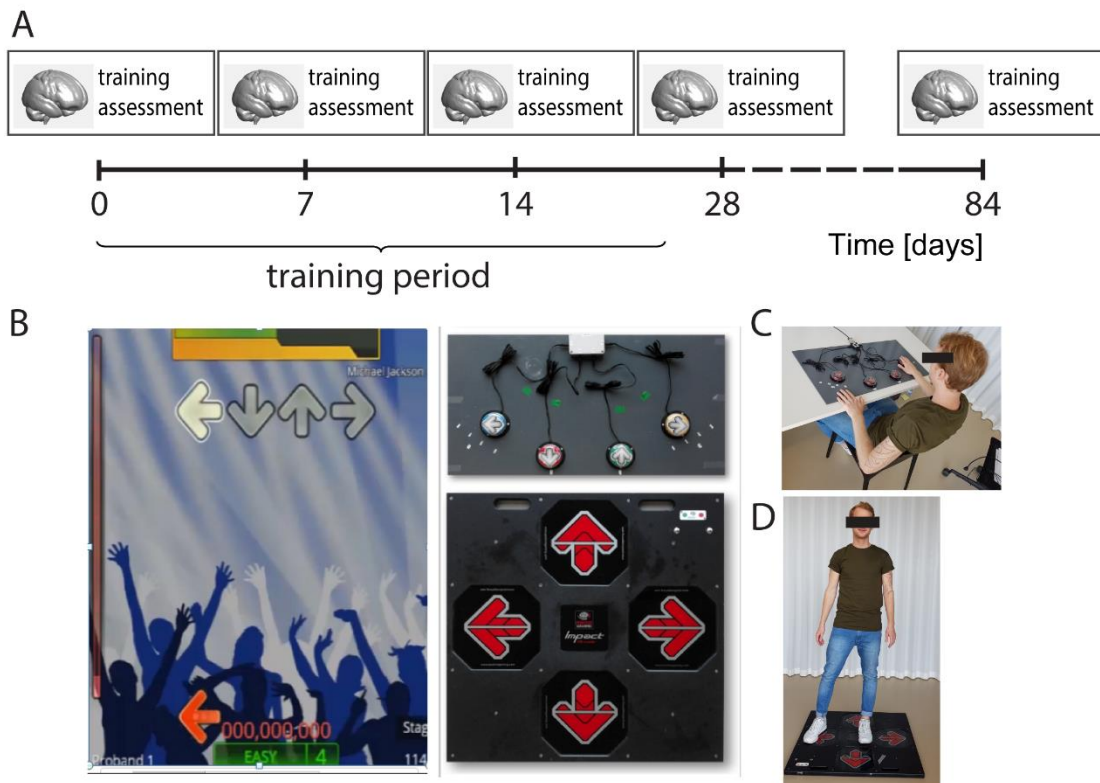


Figure 6.1: Experimental design and training task. The experimental design (A) included MRI acquisition and training assessments at baseline (day 0) during training period (day 4,14 and 28) and at final follow up (day 84). The training (c.a. 30 minutes) was performed four times a week (for 4 consecutive weeks) and involved a motor-skill training task in which, arrows with different directions (up, down, right and left) were rising from the bottom to the top of the screen (B). Whenever the rising arrow matched with the corresponding grey-one at the top, participants had to press the appropriate button of the dancing platform with their hand (C) or foot (D).

6.3.4 Behavioural analysis

Behavioural data were analysed in Matlab 1016b using custom-written routines and following parameters were computed: (i) the percentage of correct pressed button, defined as the sum of correct pressed buttons (within a delay of 90 ms) normalized by total amount of arrows; and (ii) the reaction time, defined as the average of the (absolute) time to press the correct buttons.

Skill acquisition was quantified by an exponential fit of the quantified behavioural parameters over the training period (from baseline to day 28) for each participant using equation (equation 1).

$$y = \alpha - \beta e^{-\gamma*t} \quad (1)$$

Where y is the training parameter (percentage of correct pressed buttons and reaction time); t is the time (baseline or 0, day 7, 14 and 28) and the three greek letters are estimated by the model. In particular, α is the 'asymptote', the value which the training parameter eventually settles on (the plateau); β is the 'recovery climb', the extent of improvement from baseline to asymptote; and γ controls the speed of improvement (how sharp the bend is, or rate of skill acquisition). The random error is assumed to be Normal.

Skill improvement is represented by β which represents the improvement from baseline to asymptote; and by a small γ which is an indicator of improvement speed (time to reach 63% of the asymptotic value). The improvement of all participants (in terms of β and γ) was checked using one-sample Wilcoxon test and median values were reported. Successively, to assess improvement differences in training upper or lower limb training, a two-sample Wilcoxon test was performed on the γ and β of all training parameters. Finally, to assess if the acquired skill was preserved at follow-up, a paired t-test was performed on training parameters (percentage of correct pressed buttons and reaction time) from days 28 and 84.

6.3.5 MRI acquisition

All participants underwent a multi-parameter mapping (MPM) MRI protocol which provides estimates of longitudinal relaxation rate ($R1=1/T1$), and magnetization transfer saturation (MT) Callaghan et al. 2015ba; Helms, et al. 2008a; Helms et al. 2009; Weiskopf et al. 2011a, 2013). The protocol for MPM involves acquisition of three images using a 3D multi-echo FLASH sequence (based on the Siemens "gre" FLASH product sequence) with 1 mm isotropic resolution, field of view (FoV) = 240×256×176 mm³. Total acquisition time was 23 min applying parallel imaging in the phase-encoding direction using a generalized auto-calibration partially parallel acquisition algorithm (GRAPPA) factor 2×2 and readout bandwidth of 480 Hz/pixel. Each set of echoes was acquired using a different TR and flip angle (α) to achieve images with either T1-weighting: 25 ms / 23°, PD-weighting: 25 ms / 4°, or MT-weighting: 37 ms / 9° with off-resonance RF pulse prior to excitation. Echoes were acquired at six equidistant echo times (TE) from 2.46 ms to 17.22 ms for all weightings, with an additional echo at 19.68 ms for the PD-weighted and T1-weighted volumes.

6.3.6 MRI processing

In total five MRI scans were acquired for each participant (one at baseline (day 0), 3 over the training period (days 7, 14, 28) and the last one at 84 days follow-up). MPM maps were generated using the hMRI toolbox (Tabelow et al. 2019; Weiskopf et al. 2013)(www.hmri.info) using UNICORT with bias-field inhomogeneities correction in SPM12 (Wellcome Trust Centre for Neuroimaging, London, UK, <http://www.fil.ion.ucl.ac.uk/spm>) and Matlab r2016b. All maps were pre-processed using a longitudinal pipeline (Ziegler, Dahnke, and Gaser 2012), in which, (1) MT maps were used to create a group specific template using Dartel Template(Ashburner 2007b); (2) MT maps were skull-stripped (3) and then used for within participants group wise co-registration (Ashburner and Ridgway 2013). This step generates participants specific midpoint map and corresponding deformation fields; (4) all MPM maps were mapped to such midpoint space using the deformation fields from the previous step; (5) all participants specific midpoint maps were then segmented using unified segmentation algorithm (Ashburner and Friston 2005) and corresponding deformation fields were used to map all MPM maps into MNI space. Finally all MPM maps were spatially smoothed using a 3-mm (in for the GM) and 5-mm (in the WM) full width at half maximum (FWHM) preserving GM/WM tissue boundaries (Draganski, et al. 2011).

To relate these quantitative (voxel-based quantification (VBQ)) to more conventional metrics (such as voxel-based morphometry (VBM)), segmented MT maps (GM and WM) were normalized using within- and between-participants modulation; and spatially smoothed using an isotropic Gaussian smoothing (4-mm for WM and 6-mm for GM FWHM). For statistical analysis, we excluded all voxels with a GM value below 0.2 (with a maximum value of 1) to avoid possible partial volume effects near the border between GM and white matter (WM).

6.3.7 MRI Statistics

Training induced structural changes

In this longitudinal study, we used the sandwich estimator (SwE) method to assess: (i) the training-induced brain changes over the training period; (2) the topological changes and (3) how, training improvements (in terms of β and γ from the behavioural analysis) are related to brain trajectories.

The SwE was developed for voxel-based longitudinal image analysis (<http://www.nisox.org/Software/SwE>) and it is based on a marginal model where the expected

variability is described as a function of predictors in a design matrix, while additionally accounting for correlations due to repeated measurements and unexplained variations across individuals as an enriched error term. The model incorporated time and time² factors in order to investigate permanent (linear term) or transient (temporary or quadratic term) training-induced brain changes over the training period (equation 2) by comparing trained (upper + lower limb training groups) with not trained group. Moreover, to assess somatotopic changes the same model was used to compare lower-limb with upper limb trainees.

$$y_i = X_i\beta + \epsilon_i \quad (2)$$

where y indicated the tissue volumes or MPM maps, X =design matrix including group interactions [intercept time time²] and covariates [age TIV] and ϵ_i is the error with mean 0.

For the association analysis we enriched the models by adding each improvement parameters at a time. In particular we investigated the association between linear and quadratic structural changes with the behavioural improvement (β), the speed of improvement (γ) and baseline value (α - β) of each participant specific model using both training parameters (percentage of correct pressed buttons and reaction time) as well as their interaction with change over time and time². These metrics allowed us to assess how linear or quadratic brain changes were associated with training improvements (for example, linear increase of MT map is associated with higher percentage of correct pressed buttons (β)). In all models the mean age of a participants over all scans and total intracranial volume (TIV) were included as covariates of no interest. All results exceeding a threshold of $p < 0.05$ FDR (false discovery rate) at the peak-level were considered significant.

In order to ensure no global effects in the maps (e.g. due to B1 mapping correction), the mean value from the WM was plotted over time for trained and not trained groups and visually checked for any time varying effect.

Temporal association along the corticomotor system and within the hippocampus

To investigate temporal associations along the corticomotor system and within the hippocampus, the mean value from significant clusters were extracted from the pre-processed maps from all participants using Matlab r2016 and further analysed in STATA 15.0 (Stata Corp 15.0, College Station, TX). To investigate the correlations of microstructural changes from different brain regions, a linear mixed effect model across time and between values from different ROIs was conducted. The association was

additionally checked across clusters from different time points (i.e. how microstructural changes from one region are related to microstructural changes from another region one time point before/after).

Follow up analysis

In order to investigate if structural changes were visible after a period of no training, paired t-test was performed comparing follow-up (day 84) and end of training (day 28); as well as follow-up (day 84) and beginning of training (day 0 or baseline). Here results exceeding a threshold of $p < 0.05$ FWE (family-wise error) at the cluster-level were considered significant.

Region of interest (ROI)

Region of interest (ROI) approach was used in this study including sub-regions from the hippocampus (entorhinal cortex (EC) and Cornu Ammonis (CA) and corticospinal tract (CST); primary sensory (S1) and motor cortex (M1). These ROIs were selected based on the task-related characteristics and previous training study (Draganski et al. 2006; Hüfner et al. 2011; Lakhani et al. 2016; Schlegel, et al. 2012; Wenger et al. 2016). Hippocampus and CST sub-regions were defined based on FSL Templates in MNI space; whereas S1 and M1 were defined from Anatomy toolbox in SPM (Eickhoff et al. 2005, 2007).

6.4 Results

6.4.1 Demographics and behavioural results

All participants were male, right-handed (Oldfield 1971) and the three groups did not differ with respect to age (ANOVA: $F=0.49$, $p=0.61$).

All trained participants improved (in terms of β) in the percentage of correct pressed buttons ($p<0.001$, $z= 3.72$) and reaction time ($p<0.001$, $z=3.72$), during the 28 days of training period (figure 6.2A). All trained participants were able to press about 18% more correct buttons than at baseline (interquartile range (IQR)=11 – 23 %), and this improvement was achieved in approximately 6 days (from the inverse of $\gamma= 0.17$, IQR: 0.11- 0.26, which is the time to reach 63% of the asymptotic value); all trained participants were 25.77 ms (IQR=15.00 – 34.82) faster in pressing the correct buttons, and this improvement was also achieved in approximately 6 days ($\gamma= 0.17$, IQR: 0.10- 0.28).

Participants training lower limbs improved more (approximately 22%, IQR= 22-29 %) than participants training upper limbs (only 11%, IQR= 9-12 %) in the percentage of correct pressed buttons ($p=0.004$,

$z=2.87$). At follow-up (comparing behavioural parameters from day 28 and 84) no significant differences in the percentage of correct pressed buttons, and reaction time ($p=0.307$ and $p=0.464$, respectively) were observed.

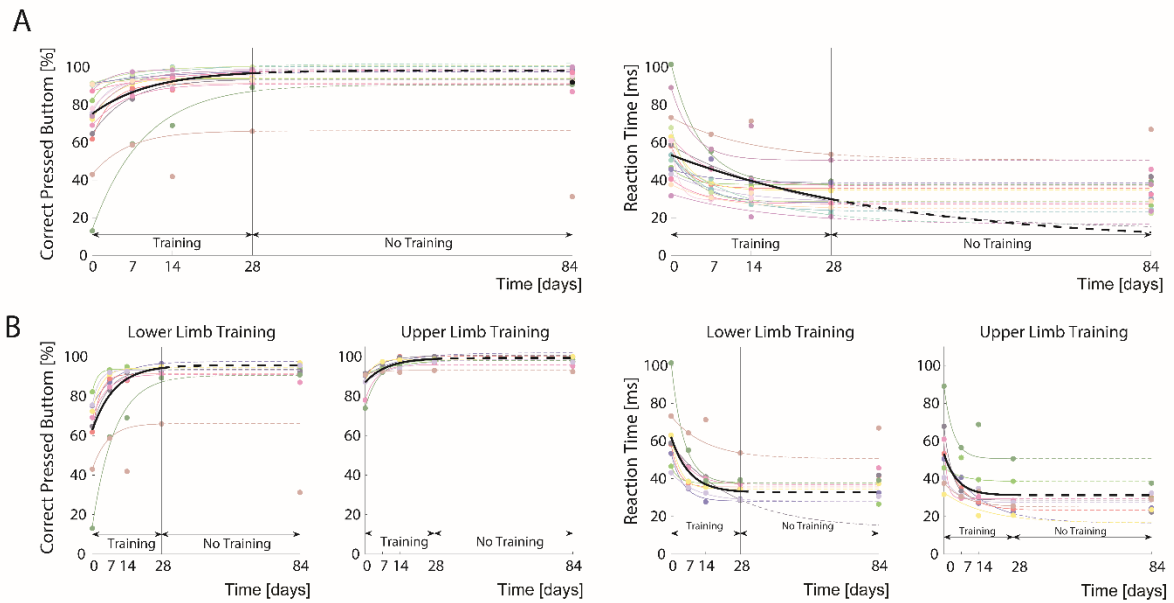


Figure 6.2: Behavioural assessment. Behavioural data were analysed, first by computing the percentage of correct pressed buttons and the reaction time (average time to press the correct buttons) (coloured dots in the figure), and then by computing the participants-specific behavioural curve ($y = \alpha - \beta e^{-\gamma * t}$) over the training period (light coloured lines) and the corresponding group mean (thick black line) on top. The dashed lines are connecting the last training point (day 28) and the follow-up (day 84) following the curve fit. In A all plots relative to all participants (upper and lower limb together) and in B for lower and upper limb training separately. These plots show that all participants could improve over time ($p < 0.05$) and that only the improvement in the percentage of correct pressed buttons was different between training upper and lower limbs ($p = 0.004$).

6.4.2 Training induced structural changes

In order to ensure no global effects in the results (e.g. due to B1 mapping correction), the mean value from the WM was plotted over time for trained and not trained groups and no changes were occurring over time, therefore we can be confident that there is no bias or any global effect that affect the results (results not shown).

During the training period, transient R1 decreases (u-shape pattern) occurred in the left primary sensorimotor cortex ($z=2.82$, $p=0.048$ FDR and $z=3.099$, $p=0.047$ FDR, respectively), and in the CST at the level of the right posterior limb of the internal capsule ($z=1.938$, $p=0.052$ FDR), bilaterally at the level of the cerebral peduncle ($z=3.502$, $p=0.021$ FDR, $z=3.199$, $p=0.025$ FDR, left and right side respectively), and brainstem ($z=3.607$, $p=0.012$ FDR; $z=2.944$, $p=0.033$ FDR, left and right side respectively); in the trained group when compared to not trained participants (figure 6.3, table 6.1).

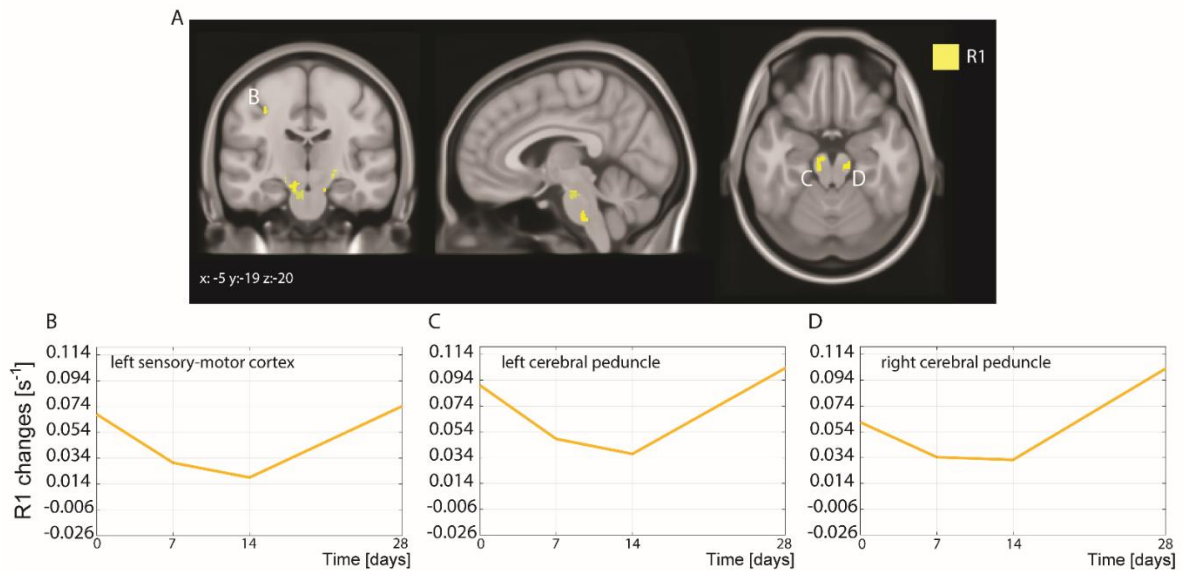


Figure 6.3: Training-induced changes in the corticomotor system. Quadratic microstructural changes (R1) were shown in the bilateral corticospinal tract (i.e. cerebral peduncle) and left sensory-motor motor cortex. All changes followed a 'u' shape as shown the longitudinal plots in B, C and D.

During the training period, transient microstructural R1 decrease in CA1 ($z=3.232$, $p=0.040$ FDR) and MT decrease in CA3 ($z=2.766$, $p=0.034$ FDR), was shown in the trained group compared to not trained, following a u-shape pattern. This transient microstructural decrease was accompanied by a transient volumetric increase occurred in the left CA3 ($z=3.036$, $p=0.036$ FDR) with an initial increase followed by a re-normalization process (inverted u-shape) (figure 6.4 and table 6.1).

Moreover, myelin-related R1 and MT linearly increased over time in the bilateral hippocampus-EC ($z>3$, $p<0.05$ FDR peak-corrected) in the trained group compared to not trained (figure 6.4 and table 6.1).

Macro- and micro-structural changes were unchanged (paired t-test) when compared to before and after training period values (i.e. day 84 vs day 28 and day 84 vs day 00) in all ROIs used in this study ($p>0.05$).

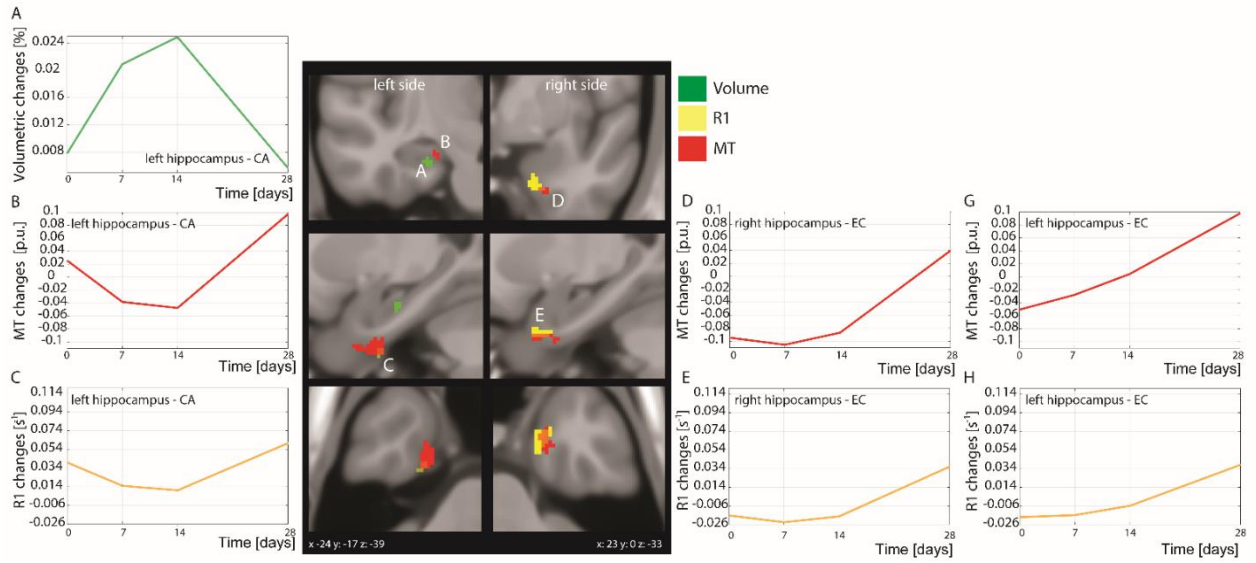


Figure 6.4: Training-induced changes in hippocampus sub-regions. Quadratic changes were shown in the left Hippocampus-CA following an inverted 'u' shape in the GM macrostructure (volume changes, A) and a 'u' shape in the microstructure (MT and R1 respectively shown in B and C). Linear microstructural increase was shown in the bilateral hippocampus-EC (both MT and R1, D-H).

ROI	Map	Contrast	Cluster size	peak_p (FDR-corr)	peak_Z	x [mm]	y [mm]	z [mm]
Hippocampus (Hipp)								
left Hipp-EC	MT	linear Trained>NotTrained	85	0.020	3.790	-24	-9	-38
left Hipp-EC	R1	linear Trained>NotTrained	20	0.047	3.099	-27	-11	-41
right Hipp-EC	R1	linear Trained>NotTrained	93	0.039	3.038	21	2	-30
left Hipp-CA3	Volume (GM)	quadr Trained<NotTrained	11	0.036	3.036	-24	-17	-21
left Hipp-CA3	MT	quadr Trained>NotTrained	6	0.034	2.766	-20	-17	-18
left Hipp-CA1	R1	quadr Trained>NotTrained	37	0.040	3.232	-33	-36	-9
CST								
left Cerebral peduncle	R1	quadr Trained>NotTrained	146	0.021	3.502	-15	-24	-15
right Cerebral peduncle	R1	quadr Trained>NotTrained	86	0.025	3.199	17	-12	-8
right Posterior Limb Internal Capsule	R1	quadr Trained>NotTrained	59	0.052	2.938	20	-15	-5
left cst at the level of brainstem	R1	quadr Trained>NotTrained	64	0.012	3.607	-5	-18	-26
right cst at the level of brainstem	R1	quadr Trained>NotTrained	25	0.033	2.944	3	-27	-42
sensory-motor cortex								
left primary motor cortex	R1	quadr Trained>NotTrained	18	0.047	3.099	-33	-20	44
left primary sensory cortex	R1	quadr Trained>NotTrained	17	0.048	2.824	-38	-24	39

Table 6.1: Results table for linear/quadratic differences between trained and not trained group. SPM longitudinal SwE results table testing for linear/quadratic differences between trained and not trained group on grey matter (GM) volume, myelin-sensitive R1 and MT maps. We report p-values from non-parametric voxel-wise FDR ($p < 0.05$).

6.4.3 Temporal association between the motor cortex, the corticospinal tract and the hippocampus

At any given time, there was a significant positive association between R1 changes in the left M1 and R1 changes in the left CST at the level of the cerebral peduncle one time unit before (coefficient= 0.138, $p=0.026$, CI:0.016 to 0.258); indicating that R1 changes in the CST are preceding changes in left M1. At any given time there was a significant negative association between R1 changes in the left EC and R1 changes in the left M1 one time unit before (coefficient= -0.360, $p=0.003$, CI: -0.598 to -0.122); indicating that negative R1 changes in M1 are preceding positive changes in the left Hippocampus EC. At any given time, there was a significant negative association between R1 changes in the left EC and R1 changes in left CA1 values one-time unit before (coefficient=-0.298, $p=0.006$, CI :-0.509 to -0.086); indicating that negative R1 changes in left CA1 are preceding positive changes in left EC (figure 6.5 and table 3.2).

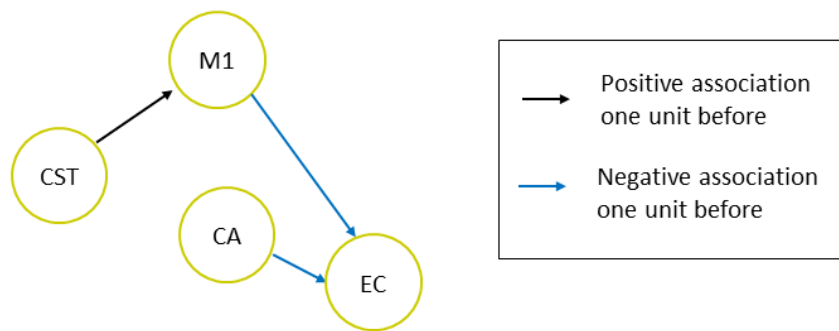


Figure 6.5: schematic representation of the temporal changes between corticomotor and Hippocampi circuits. Yellow circles indicate R1 changes. Note these associations refer only to the left side of the brain.

R1 map temporal association	Coefficient	Standard deviation error	z	$p> z $	95% Confidence interval
primary motor cortex and Cerebral peduncle one time point before (left side)	0.137	0.062	2.220	0.026	0.016
Hipp-EC and primary motor cortex one time point before (left side)	-0.360	0.121	-2.970	0.003	-0.598
Hipp-EC and Hipp-CA1 one time point before (left side)	-0.298	0.108	-2.760	0.006	-0.509

Table 6.2: Temporal association. Table testing for R1 map temporal association within the hippocampus (Hipp) and along the corticomotor system. We report only significant results ($p<0.05$).

6.4.4 Somatotopy of lower vs upper limb training

In the search for somatotopic differences, we found more transient MT changes in the lower-limb area of the CST at the level of the left internal capsule ($z=2.338$, $x=-24$, $y=-20$, $z=9$, $p=0.023$ FDR, cluster extent (CE)=48) and left cerebral peduncle ($z=3.079$, $x=-21$, $y=-21$, $z=-8$, $p=0.047$ FDR, CE=23) in participants from the lower-limb group when compared to the upper limb cohort (figure 6.6).



Figure 6.6: Somatotopy associated with training the upper vs lower limb. Microstructural (MT) differences in training the lower limbs induced more myelin sensitive MT changes in the lower limb area in the left posterior limb of the internal capsule (pink) and the left cerebral peduncle (green). Overlay of the left posterior limb capsule (light blue) and left cerebral peduncle (red) ROIs are shown (computed from FSL).

6.4.5 MRI correlations with behavioural improvements

Correlation analysis between structural MRI changes and behavioural improvements revealed negative correlations between transient volumetric changes and improvement in the percentage of correct pressed buttons ($z=2.885$, $p=0.019$ FDR, table 6.3) in the left CA3; indicating that more transient volume increase (represented by a negative quadratic term) are related to better improvement in the percentage of correct pressed button. In the same region, a positive correlation between transient volume changes and improvement in the reaction time ($z=2.834$, $p=0.028$ FDR, table 6.3) was shown; indicating that more transient volume increase is related to better reaction time. Positive correlations were found between linear MT changes in the right EC, and faster improvement (γ) in the percentage of correct pressed buttons and reaction time ($z=3.568$, $p=0.04$ FDR; $z=3.797$, $p=0.028$ FDR, respectively, figure 6.7 and table 6.3). Baseline percentage of correct pressed button correlated negatively with quadratic MT changes in the left EC ($z=3.607$, $p=0.026$ FDR, table 6.3).

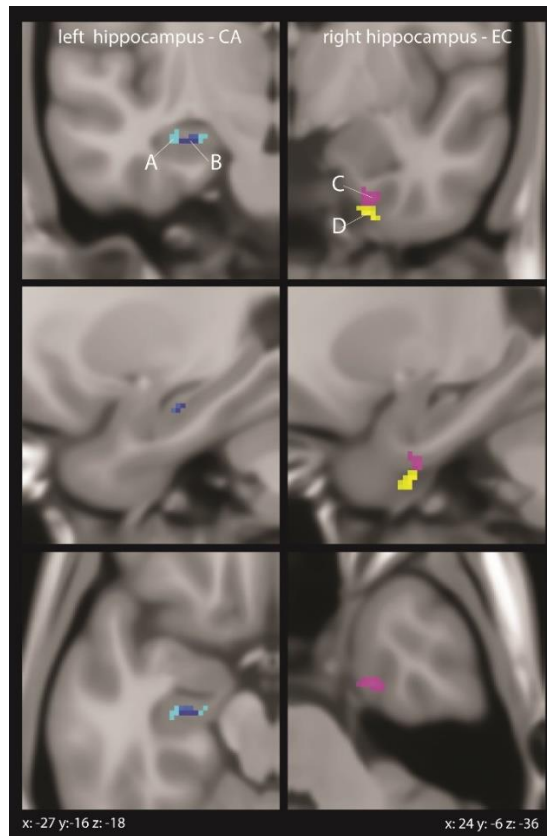


Figure 6.6: Associations between microstructural changes and training improvements. In the left hippocampus-CA, negative correlation between quadratic macrostructural changes and improvement in the number of pressed button(A); and positive correlation between quadratic macrostructural changes and accuracy improvement (B) were shown. In the right hippocampus-EC, positive correlations between linear MT changes and faster accuracy improvement (γ) (C) and positive correlation between linear MT changes and faster improvement (γ) in the number of pressed button (D) were shown.

ROI	Map	Contrast	Cluster size	peak_p (FDR-corr)	peak_Z	x [mm]	y [mm]	z [mm]
left CA3	Volume (GM)	negative correlation between quadratic time term and the percentage of correct pressed button	22	0.019	2.885	-30	-15	-18
left CA3	Volume (GM)	positive correlation between quadratic time term and accuracy improvement	15	0.028	2.834	-25	-15	-18
right EC	MT	positive correlations between linear time term and faster accuracy improvement (γ)	36	0.028	3.797	25	-7	-36
right EC	MT	positive correlation between linear time term and faster improvement (γ) in the percentage of correct pressed button	37	0.040	3.568	24	-6	-40
left EC	MT	negative correlation between quadratic time term and baseline	38	0.026	3.607	-18	-14	-32

		percentage of correct pressed button (α - β)						
--	--	---	--	--	--	--	--	--

Table 6.3: Correlation table. SPM longitudinal SwE results table testing for correlations between linear/quadratic structural changes and behavioural improvements. We report p-values from non-parametric voxel-wise FDR ($p < 0.05$).

6.5 Discussion

This longitudinal training study provides insights into the intimate relationships between training associated microstructural changes in the white and grey matter of the corticomotor system and its interplay with transient intra-hippocampal changes; its magnitude being associated with performance improvements. These findings allow us to elucidate possible underlying mechanisms of brain plasticity that might be used as biomarker in rehabilitation and clinical practice.

6.5.1 Training-induced structural changes

Transient microstructural R1 decrease was observed in left sensorimotor cortex and bilateral CST. In the grey matter, training-induced cellular mechanisms might be related to changes in dendritic spines (Kleim, et al. 2002) or rewiring of specific circuitry (Kolb et al. 2008). It was shown that during motor skill acquisition or new sensory experiences, novel dendritic spines rapidly grow and form new synapses in sensory and motor cortices; these new synapses stabilize during learning and others were eliminated (renormalization) showing a transient training-induced synaptic plasticity in the motor cortex (Moore et al. 2017). This behaviour was first described by Hebb's in 1949 (Hebb 1949) and then confirmed by others (Caroni, et al. 2014; Hofer et al. 2009; Xu et al. 2009; Yang et al. 2009). Interestingly, in our study changes in the motor cortex showed transient changes only in the left side. This is not surprising, considering that all participants were right-handed and that individuals with a temporarily immobilised upper limb showed grey matter decrease in the contralateral M1 (Granert et al. 2011).

In the white matter, transient reduction of R1 maps in the bilateral corticospinal tract at the level of the cerebral peduncle and brainstem, might be related to myelin modulation that promotes conduction through task-specific fibers (Lakhani et al. 2016). Increased excitability in the CST was observed in a visuomotor training study (Jensen, Marstrand, and Nielsen 2005) or in motor skill learning (Jensen et al. 2005). Crucially, the somatotopic analysis revealed accelerated myelin sensitive

MT changes in the lower limb trainees compared to upper limb trainees suggesting more microstructural (MT) changes in the appropriate area. Training lower limbs was more difficult, as they started with worst performance in the percentage of correct pressed buttons compared to upper limbs trainees; and this might explain the increased MT in the leg area. These findings were also in line with animal studies showing myelin plasticity following learning (Sampaio-Baptista et al. 2013) which might be related to increased conduction velocity and optimized timing in white matter circuitry (Fields 2015b; Hofstetter et al. 2013).

The hippocampus supports basic cognitive functions important for the formation and retrieval of declarative memories (Basu and Siegelbaum 2015; O'Keefe; Nadel 1978); and has shown to be implicated during spatial navigation (Maguire et al. 2000) or dancing (Hüfner et al. 2011).

In support of the importance of the direct EC inputs in spatial memory, chemical and electrolytic lesions of the inputs to CA1 were found to lead to a degradation of place-field precision (Brun et al. 2008) and deficits in consolidation of spatial long-term memory (Remondes and Schuman 2004). The cellular biological mechanisms underlying hippocampus plasticity are still controversial. Even if there is good evidence for adult neurogenesis occurring with learning in the hippocampus (Tronel et al. 2010), newborn neurons were mainly observed in the DG (Deng et al. 2009; Eriksson and Perfilieva 1998). Crucially, the transient decrease in R1 and MT accompanied by a transient volume increase in the left CA are more in line with the temporal changes of glia cells angiogenesis or rapid remodelling of dendritic spines and axonal terminals. Increased regional cerebral blood flow in the hippocampus (CA1 and DG) was shown comparing skilled or simple walking with rest rats (Guo et al. 2017). In the bilateral EC, the progressive increase of R1 and MT maps might be related to myelin modulation which might speed the conduction velocity in these regions, however further analysis is needed to investigate such cellular changes.

As an alternative possibility, the net effect of a reduction in MT and R1 might be related to a lengthening in T1 which is related to volume fraction, and therefore these changes might be related to angiogenesis or gliogenesis. Training induced transient vasculature changes were shown in animal study, where physical exercise induced a temporary increase (histologically-quantified) of vascular volume in the cerebral cortex of middle-aged monkeys (Rhyu et al. 2010). Gliogenesis, which includes changes in non-neuronal cells, such as astrocytes and oligodendrocyte progenitor cells (OPCs), was also shown during training (Dong and Greenough 2004). McKenzie et al. (2014) discovered that oligodendrocyte generation is accelerated when learning a complex, new skill and that if

oligodendrocyte precursor cells are genetically blocked, acquisition of the new skill remains incomplete (McKenzie et al. 2014). These changes could account to our observed transient changes in both GM and WM.

6.5.2 Temporal association between the motor cortex, the corticospinal tract and the hippocampus

The temporal association analysis across sensorimotor cortices, its descending projection and the hippocampus, revealed that transient R1 decrease in the CST are preceding transient R1 decrease in M1 suggesting a cortico-motor circuit, in which microstructural changes in CST are triggering similar changes in M1. Training-induced changes in the CST and motor cortex was shown during motor skill acquisition (Lakhani et al. 2016), however the temporal relationship was not investigated. Moreover, transient decreased R1 in the M1 and CA are linked to a linear increase of R1 in the EC, suggesting a motor-hippocampus and within-hippocampus circuits loop. The involvement of sensory-motor and hippocampus regions was shown in performing a visual-motor task (Kodama et al. 2018a), but the temporal association across these regions was also not investigated. The presence of a within-hippocampus circuits was already shown in animal studies, where deep layers' pyramidal neurons from EC projected to CA1 (Suh et al. 2011; Yamamoto et al. 2014). CA1 pyramidal neurons provide the major output from the hippocampus, sending projections to a number of brain regions, including the neighbouring subiculum, perirhinal cortex, prefrontal cortex, amygdala (van Groen and Wyss 1990) and back to the EC (completing an EC -> hippocampus -> EC loop (Naber, Lopes da Silva, and Witter 2001)). This training-induced corticomotor-hippocampi circuit might be related to the complex multi joint movement acquisition. The characteristic spatio-temporal microstructural changes in different circuits showed the significant functional interplay between different brain regions in performing a complex motor skill task.

6.5.3 MRI correlations with behavioural improvements

In this study, the transient volumetric changes in the left hippocampus was associated with improvements in the percentage of correct pressed buttons and reaction time, meaning that left CA encodes learning processes (Albouy et al. 2008; Yasuda et al. 2011); whereas linear microstructural changes in the right hippocampus EC was correlated with the speed of improvement, suggesting that faster learning is encoded in the microstructure of the EC. The EC has shown to have an important role in temporal, spatial and long-term memory (Brun et al. 2008; Remondes and Schuman 2004; Suh et al. 2011). One suggestion is that CA1 acts as a novelty detector, comparing stored memory-related

information in Dentate Gyrus (DG) and CA3 with ongoing direct sensory representations from the EC (Duncan et al. 2012; Lisman and Grace 2005).

The negative correlation, between the baseline percentage of correct pressed button and the quadratic MT changes in the EC, indicates that lower behavioural performance at baseline can induce more (transient) microstructural changes in the EC. Participants with lower baseline behavioural performance have more margin of improvement and therefore more microstructural changes are induced.

6.5.4 Limitations

This study has some limitations, which should be considered when interpreting the findings. First, MPM maps have a limited sensitivity and specificity to intra-voxel changes, therefore the direct investigation of cellular and molecular changes induced by training is not possible. However, animal studies supported the biological underlying mechanisms induced by training and learning new motor skills. The decision to train participants over a period of 4 weeks was based on previous studies (Draganski et al. 2004; Taubert, et al. 2016; Wenger et al. 2012). The behavioural improvement curves suggested that most of the participants reached the asymptotic value during training. However, several factors may influence the training and the improvements such as motivation, personal interest, tiredness and effort. In this study we tried to uphold motivation at a high level by written feedbacks on the screen while training and by implementing different difficulty levels of the task (i.e. faster upward transition of arrows). The level of the task was adjusted for each participant to keep the training interesting and enforce the same difficulty across participants. Tiredness was observed during training; however, the behavioural parameters were computed using a standardized test at the beginning of each training session to reduce tiredness bias. An additional point to consider is the training length and intensity, as well as the initial proficiency level of each participants at baseline. The training length was fixed to 4 weeks and the number of training sessions were constant across participants (c.a. 30 minutes, 4 times per week). The baseline proficiency level indicates the margin of possible improvement, where participants with worst baseline proficiency, might show more plastic changes (Jensen et al. 2005). The behavioural data lack of a control group, however the improvement was clearly visible from the behaviour curves and was assessed using quantitative measure in terms of α , β and γ . The small sample size is a further limitation, although the high number of scans (five MRI acquisition) per person yielded a more reliable analysis of training-induced changes. Given the high number of scans over time, MRI acquisition was limited to MPM protocol to keep reasonable

acquisition time, therefore volume changes were analysed based on MT maps. Finally, in this study only linear and quadratic temporal changes were investigated, but other temporal patterns could also be possible. However based on previous studies (Wenger et al. 2016) the quadratic model was the best model to describe brain changes over time because it is able to capture expansion and potential renormalization processes over time.

6.6 Conclusion

In this longitudinal qMRI study, transient microstructural changes were induced by learning a skilled motor task (i.e. dancing) using lower and upper limbs. Specifically, parallel to performance improvement, transient microstructural decrease was shown across the left sensorimotor cortex, bilateral CST and in the hippocampus. The underlying pathobiology might be related to more glia cells, angiogenesis or rapid remodelling of dendritic spines and axonal terminals. These changes were affecting persistent corticomotor-hippocampi and intra-hippocampi circuits. Specifically, microstructural changes in the CST were preceding changes in the motor cortex and microstructural changes in the corticomotor neurons were preceding those in the hippocampus. Lower limb training led to greater changes in myelin-sensitive MT in the posterior part of the limb of the internal capsule, suggesting a somatotopy of learning. Interestingly structural changes were associated with training improvement showing the importance of the hippocampus in learning a motor skill. Crucially, the transient volumetric changes in the left CA were associated with performance improvement; whereas linear progressive microstructural changes in the right EC were associated with speed of improvement.

This study showed the potential of neuroimaging biomarkers to investigate training-induced changes in the brain circuits and might be used as biomarker for the monitoring of neurorehabilitation therapies.

7 Study IV: Tracking the neurodegenerative gradient after spinal cord injury

Michela Azzarito, Maryam Seif, Sreenath Kyathanahally, Armin Curt, and Patrick Freund

NeuroImage Clinical 2020

Authors thank all participants for taking part in this study; Patrick Grabher for recruiting the subjects and the staff of the Department of Radiology and Neurology at the University Hospital Balgrist for their help in acquiring the MR images.

This study is funded by ERA-NET NEURON (hMRlofSCI no: 32NE30_173678), the European Union's Horizon 2020 research and innovation program under the grant agreement No 681094, and the Swiss State Secretariat for Education, Research and Innovation (SERI) under contract number 15.0137, grants from Wings for life charity (INSPIRED) (No WFL-CH-007/14), and Eccellenza fellowship/181362 by SNSF.

Final publication is available from <https://www.ncbi.nlm.nih.gov/pmc/articles/PMC7058923>.

Copyright ©2020 IEEE. Reprinted, with permission from Michela Azzarito, Maryam Seif, Sreenath Kyathanahally, Armin Curt, and Patrick Freund.

7.1 Abstract

Objective: To quantify neurodegenerative changes along the cervical spinal cord rostral to a spinal cord injury by means of quantitative MRI (qMRI) and to determine its relationship with clinical impairment.

Methods: Thirty chronic SCI patients (15 tetraplegics and 15 paraplegics) and 23 healthy controls underwent a high-resolution T1-weighted and myelin-sensitive magnetization transfer (MT) MRI. We assessed macro- and microstructural changes along cervical cord from levels C1 to C4, calculating cross-sectional spinal cord area, its anterior-posterior and left-right width and myelin content (i.e. MT). Regression analysis determined associations between qMRI parameters and clinical impairment.

Results: In SCI patients, atrophy ($p < 0.001$) and decreased myelin-sensitive MT ($p < 0.001$) is evident across all cervical cord segments when compared to the healthy controls. These changes were greater in tetraplegic than paraplegic SCI patients, and more prominent closer to the epicenter of the injury (i.e. neurodegenerative gradient). Higher lesion level correlated with greater neurodegeneration. Sensory integrity and level of functional independence were associated with cord atrophy and myelin-sensitive MT.

Conclusions: A tract-specific neurodegenerative gradient with more pronounced degeneration in the ascending as compared to the descending spinal pathways is evident after traumatic SCI; its magnitude is reduced with increasing distance from the lesion level. The clinicopathologic associations suggest that remote secondary neurodegenerative changes are clinically eloquent. Monitoring the neurodegenerative gradient could be used to track treatment effects of regenerative and neuroprotective agents.

7.2 Introduction

Traumatic spinal cord injury (SCI) leads most often to paralysis below the level of injury and functional recovery is limited (Ahuja et al. 2017). Based on the lesion level, SCI patients can be dichotomized into tetraplegics (tSCI) and paraplegics (Steven C Kirshblum et al. 2011b) (pSCI). Evidence from experimental SCI have shown that axonal degeneration and demyelination of the spinal pathways is greatest close to the injury and reduces with increasing distance (Freund et al. 2007; Grumbles and Thomas 2017; Kalil and Schneider 1975; Kerschensteiner et al. 2005a). In human SCI, tissue-specific neurodegenerative changes have been quantified in the spinal cord either at the C2/C3 level (Freund

et al. 2011, 2013; Huber, et al. 2018; Lundell et al. 2011; Seif et al. 2018) or at the lumbar enlargement (David et al. 2019) but not along the spinal cord. Thus it is unknown whether a tract-specific neurodegenerative gradient exists (Kalil and Schneider 1975; Kerschensteiner et al. 2005b) that could be quantified in-vivo to for example monitor the effects of regenerative and neuroprotective treatments. However, due to technical constraints, voxel-wise neurodegenerative changes adjacent to a focal injury or over several spinal segments are understudied. Here we use the spinal cord toolbox (SCT) (De Leener et al. 2016) to analyse volumetric T1-weighted MRI data (Tardif, Collins, and Pike 2009) and myelin-sensitive magnetisation transfer saturation (MT) maps (Helms, et al. 2008b) along the cervical cord from C1 to C4 to assess changes to the cords' morphometry (Huber, et al. 2018) and its myelin content (Schmierer et al. 2004), respectively.

Based on the literature, we hypothesized that (i) a neurodegenerative gradient will be present in SCI patients with more atrophy closer to the injury epicentre (i.e. changes at level C4>C3>C2>C1); (ii) these atrophic changes are more pronounced in tetraplegics when compared to paraplegics; (iii) the pathophysiological underpinning of the atrophy is related to demyelination by means of myelin-sensitive MT and; (iv) the magnitude of neurodegeneration is associated with clinical impairment.

7.3 Materials and methods

7.3.1 Participants and study design

Thirty patients with traumatic SCI, 15 tetraplegic (age: mean 42.61 ± SD 17.64 years, 1 female), 15 paraplegic (age: mean 46.73 ± SD 16.09 years, 2 females), and 23 healthy subjects (age= mean 36.87 ± SD 11.76 years, 10 females) were recruited at the University Hospital Balgrist between August 2011 and May 2015. The exclusion criteria for SCI patients were: time since injury <2 months, pregnancy, head or brain lesions associated with spinal cord injury, pre-existing neurological and medical disorders leading to functional impairments, mental disorder, or contraindications to MRI. Note that one of the paraplegics patients recovered from AIS score D to E during this study (see Table 7.1). The exclusion criteria for healthy subjects were: any neurological or mental disorder or pregnancy.

pSCI	Age (years)	Time since injury (months)	sex	AIS	Site of impairment (motor/sensory)	Lower limb motor score	Upper limb motor score	Pinprick	Light touch	SCIM
1	69	12.2	F	D	T11/T11	32	49	74	92	42
2	45	13.4	M	D	L3/L4	45	50	106	106	100
3	53	12.0	M	D	T10/T10	48	50	90	90	100

4	30	10.3	M	A	T10/T10	16	50	78	82	80
5	70	9.5	M	A	T7/T7	0	50	68	67	49
6	72	12.0	F	E	T3/T3	50	50	112	112	97
7	53	54.6	M	A	T3/T3	0	50	44	47	53
8	36	185.5	M	A	T12/T12	4	50	78	78	70
9	60	68.2	M	A	T1/T1	0	49	40	52	32
10	53	8.0	M	A	T9/T9	0	50	66	68	69
11	32	10.8	M	B	T11/T11	0	50	72	78	66
12	29	22.8	M	B	T6/T6	0	50	52	77	66
13	26	10.8	M	A	T4/T4	0	50	46	48	67
14	39	9.3	M	A	T7/T7	0	50	58	60	65
15	31	12.3	M	B	T4/T4	0	50	46	74	54
tSCI	Age (years)	Time since injury (months)	sex	AIS	Site of impairment (motor/sensory)	Lower limb motor score	Upper limb motor score	Pinprick	Light touch	SCIM
1	19	13.5	M	A	C6/C7	0	23	33	33	37
2	24	12.2	M	D	T1/C6	19	48	37	72	70
3	43	15.7	M	A	C6/C4	0	25	18	20	37
4	72	11.9	M	D	C6/C7	41	48	41	112	36
5	21	12.3	M	A	C6/C5	0	23	26	53	34
6	31	12.3	M	B	T1/C7	0	48	46	68	38
7	48	12.1	M	D	C5/C3	47	35	97	98	98
8	52	9.7	M	C	C7/C5	12	32	44	67	31
9	68	12.1	M	D	C3/C3	50	50	102	107	100
10	34	12.2	M	A	C7/C7	0	35	29	32	26
11	55	18.6	F	D	C3/C3	49	42	94	62	84
12	32	10.3	M	A	C6/C5	0	26	20	33	30
13	29	12.1	M	A	C5/C4	0	14	13	16	19
14	43	186.8	M	B	C6/C4	0	25	32	77	29
15	69	290.5	M	D	T1/C3	40	49	78	69	NA

Table 7.1: Demographic and clinical information of the spinal cord injury patients. Abbreviations: AIS: American Spinal Injury Association Impairment; F: female; M: male; pSCI: patients with paraplegia; SCIM: Spinal Cord Independence Measure; tSCI: patients with tetraplegia.

7.3.2 Standard protocol approvals, registrations, and patient consents

The study was approved by the local ethics committee of Zurich the 'Kantonale Ethik kommission Zurich' (EK-2010-0271), and the study protocols were in accordance with the Declaration of Helsinki. All subjects provided written informed consent prior to enrolment.

7.3.3 Clinical assessments

SCI patients underwent a comprehensive clinical protocol including the International Standards for Neurological Classification of Spinal Cord Injury (ISNCSCI) (Steven C Kirshblum et al. 2011b) for motor, light touch, and pinprick score; the Spinal Cord Independence Measure (SCIM)(Catz et al. 2007); and the Graded Redefined Assessment of Strength, Sensibility, and Prehension (GRASSP) particularly in tetraplegics patients(Kalsi-Ryan, et al. 2012)(Table 7.1).

7.3.4 Image acquisition

Participants underwent a T1-weighted 3D Magnetization Prepared Rapid Acquisition Gradient-Echo (MPRAGE) scan(whole-brain including the cervical cord down to C4 level) on a 3T MRI scanner (MagnetomSkyra^{Fit} and Verio, Siemens Healthcare, Erlangen, Germany). The system was equipped with a 16-channel radiofrequency (RF) receive head and neck coil and RF body transmit coil. The MRI parameters used in T1-weighted scan were as follows: field of view (FoV) of 224 x 256 mm², matrix size of 224 x 256, isotropic resolution of 1 mm³, repetitiontime (TR)=2420 ms, echo time (TE)= 4.18 ms, flip angle(α)= 9°, inversion time = 960 ms, and readout bandwidth of 150 Hz per pixel.

To assess microstructural changes (myelination) associated with quantitative MR parameters, a whole-brain multi-parameter mapping (MPM) protocol(Callaghan et al. 2015ba; Helms et al. 2009; Helms, et al. 2008b; Weiskopf et al. 2011a, 2013)was performed using a 3D multi-echo fast low-angle shot (FLASH) gradient-echo sequence. MPM protocol is designed to provide MR parameter measures of longitudinal relaxation rate ($R1=1/T1$), effective proton density (PD*), magnetization transfer saturation (MT) and effective transverse relaxation rate ($R2^*=1/T2^*$). MRI scans cover the whole brain and cervical corddown to the C4 level with 1 mm isotropic resolution, FoV=240x256 mm² and matrix-size=5240x256, with 176 partitions. Total scan time was 23 minutes applying parallel imaging in the phase-encoding direction using a generalized auto-calibration partially parallel acquisition algorithm (GRAPPA) factor 2x2 and readout bandwidth of 480 Hz/pixel. MPM protocol consists of three different MRI weighted contrasts, each acquired using a different TR and flip angle (α):(1) T1-weighted scan: 25

ms / 23°, (2) PD-weighted scan: 25 ms / 4°, and (3) MT-weighted scan: 37 ms / 9° with off-resonance RF pulse prior to excitation. Echoes were acquired at six equidistant times of echo (TE) from 2.46 ms to 17.22 ms for all volumes and an additional echo time at 19.68 ms for PD-weighted and T1-weighted scans.

7.3.5 MRI Data processing

MT-weighted, PD-weighted, and T1-weighted images acquired from MPM protocol were used to compute quantitative maps of MT, R1 and R2* using SPM12 (University College London, London, UK). The quality at lower cervical levels for R1 and R2* maps, after visual inspection, was insufficient and therefore could not be reliably analysed.

T1-weighted images (MPRAGE) and MT maps were analysed using spinal cord toolbox (SCT) (De Leener et al. 2016) following the automatic pipeline to register, warp, and extract morphometric and microstructural parameters. The pipeline included automatic spinal cord segmentation followed by visual inspection and manual correction of the generated masks if necessary (in FSL; <https://fsl.fmrib.ox.ac.uk/>). Next, the generated spinal cord mask was registered to the MNI-Poly-AMU template (De Leener et al. 2018) using a combination of affine and nonlinear registrations, and the reverse deformation field (template to subject) was applied to the white matter (WM) and gray matter (GM) atlases, projecting them into the subject space. Finally, morphometric and microstructural parameters were extracted automatically from the spinal cord at each level (from cervical level C1 down to cervical level C4). Morphometric SC parameters consisting of anterior-posterior width (APW), left-right width (LRW) and spinal cord cross-sectional area (SCA) were extracted from the segmented T1-weighted. Myelin sensitive MT values were extracted from the segmented MT map. Figure 7.1 demonstrates the processing pipeline. Voxel-wise analysis was performed on the MT maps in SPM12 after applying a smoothing (gaussian kernel with sigma 3 mm in SCT) and warping into template space (PAM50).

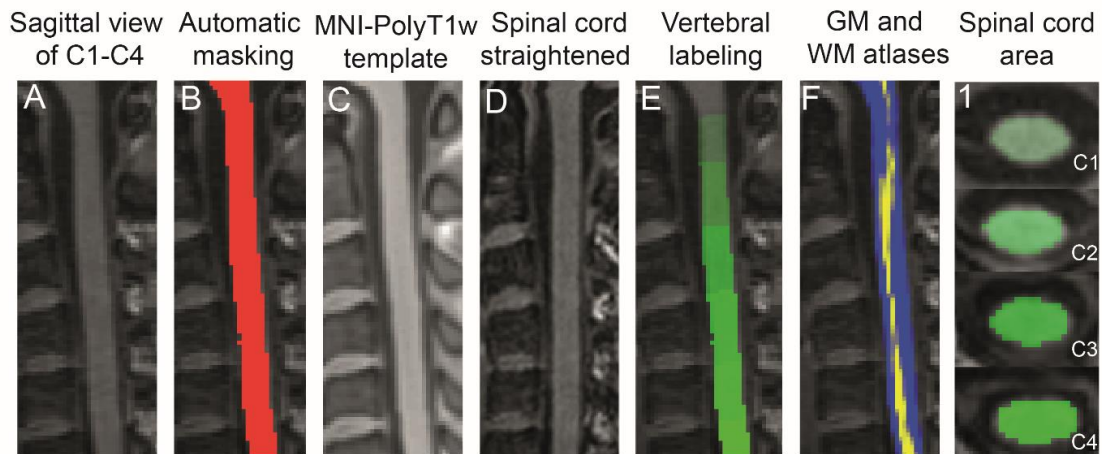


Figure 7. 1: Pre-processing steps for the analysis of MRI scans. Image registration pipeline for T1-weighted MRI from a healthy subject to PAM50 template using the spinal cord toolbox. The original T1-weighted image (A) was segmented using deep segmentation (Perone, Calabrese, and Cohen-Adad 2018) and the spinal cord mask was generated (B). Next, the template (MNI-poly T1w) was warped into subject space (C) and the T1-weighted image was warped into template space (straightened) (D). Vertebral levels were automatically labelled (E) and GM (yellow) and WM (blue) probabilistic atlases were warped back to native space (sagittal view in F) (De Leener et al. 2016). Segmented SC from C1 level down to C4 is presented in column 1.

7.3.6 Statistical analysis

To investigate the difference between SCI patients and healthy controls in spinal cord morphometry (i.e. cord area, APW and LRW) and microstructure (i.e. MT), a linear mixed effect model across the cervical segments (from C1 to C4) and across groups (healthy controls, both patients groups combined, as well as pSCI and tSCI separately) was conducted in Stata (Stata Corp 13.0, College Station, TX). Post-hoc pairwise comparisons were performed, adjusted for multiple comparisons using Bonferroni correction. To assess lesion completeness effects (AIS scores), spinal cord parameters at all spinal cord levels were compared between AIS A/B and AIS C/D in tetraplegics and paraplegics patients using a 2-sample ttest (1-tailed, unequal variances, $\alpha = 0.05$).

The correlation between lesion level and spinal cord MRI (using the mean value along the levels C2 to C4) measures was assessed using an ordinal logit regression, entering an indicator of the lesion level, defined on the basis of the neurological lesion level, as response variable. Furthermore, linear regressions were used to assess the correlation between qMRI parameters (using the mean value along the levels C2 to C4) and sensorimotor outcome measures (light touch, pin-prick, and SCIM scores). MT maps in PAM50 space were additionally analysed using general linear models (GML). Uncorrected voxel threshold of $p=0.001$ was initially considered, and to account for multiple comparisons, family

wise error correction (FWE) based on Gaussian random field theory, was applied. Only clusters surviving a corrected cluster threshold of $p=0.05$ were reported (Friston et al. 1994). ANOVA tests were used in each voxel of interest to investigate spinal cord changes in SCI patients compared to healthy controls; and tSCI compared to pSCI. Additionally, associations between myelin sensitive microstructural changes and functional recovery (LEMS, light-touch, pinprick and SCIM scores) were investigated. All Statistical tests were corrected for age as a cofactor of no interest and only results with a significant threshold of $p<0.05$ were reported.

7.4 Results

7.5 Demographic, clinical, and radiologic characteristics

There was no significant differences in age (ANOVA, $f = 2.08$ $p = 0.135$) or in sex (chi-square, $p = 0.435$) across the three groups (controls, tSCI and pSCI). Paraplegics patients were scanned on average 3.6 ± 6.8 years following the injury and were classified according to the American Spinal Injury Association Impairment Scale (AIS) as 8 AIS A, 4 AIS B, 2 AIS D and 1 AIS E. Tetraplegics patients were scanned on average $2.5 \pm SD 3.9$ years following the injury and were classified as 6 AIS A, 2 AIS B, 1 AIS C and 6 AIS D.

7.5.1 Neurodegenerative gradient

Cross-sectional cord area and its APW were decreased across all cervical cord levels in SCI patients when compared to healthy controls ($p<0.05$), while LRW showed decreases at levels C2, C3 and C4 ($p<0.05$) (figure 7.2A-C, table 7.2). The magnitude of spinal cord area and shape changes were greater at lower cervical levels (i.e. closer to the lesion level, $C4>C3>C2>C1$), defining a neurodegenerative gradient. Cord area decreased by 2.67 mm^2 per cervical cord level in the caudal direction [95% CI -4.48 to -0.86] ($p=0.004$) and LRW decreased by 0.35 mm [95% CI -0.57 to -0.13] ($p=0.002$) in SCI patients compared to healthy controls. APW presented a negative gradient in caudal direction for both SCI (APW decreased by 0.31 mm per cord level [95% CI -0.33 to -0.16] ($p<0.001$)) and healthy controls (APW decreased by 0.24 mm per cord level [95% CI -0.39 to -0.24] ($p<0.001$)), without a significant difference in the rate of change of the gradient ($p=0.197$).

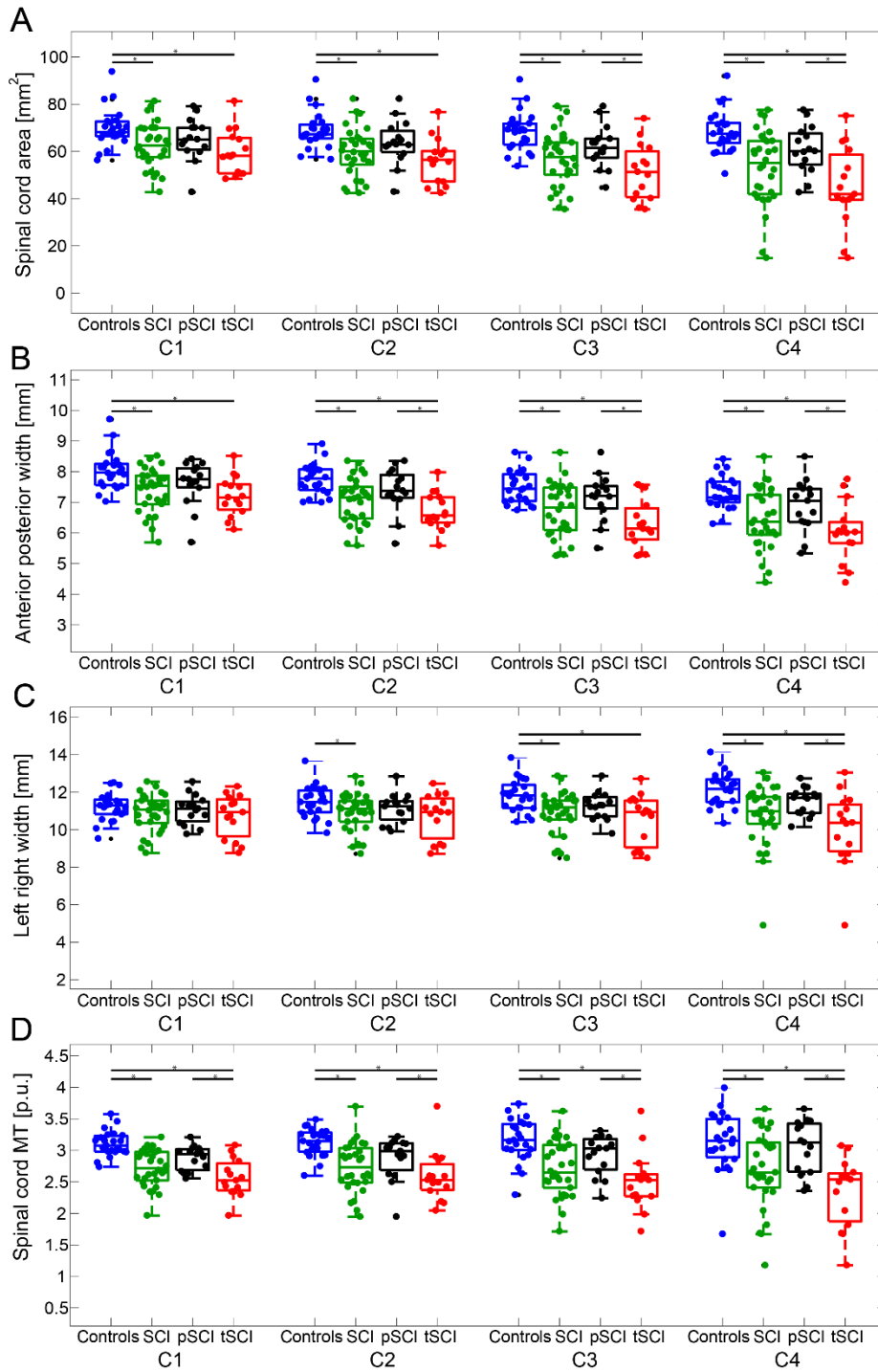


Figure 7.2: Spinal cord parameters from level C1 to C4. Morphometric and myelin-sensitive magnetization transfer parameters (coloured dots) at each individual cervical cord level (from C1 to C4) are shown (controls (blue), SCI (tSCI + pSCI, green), paraplegics (pSCI, black) and tetraplegics (tSCI, red)). Spinal cord parameters include: cross-section spinal cord area in A, its anterior posterior width (APW) in B, its left right width (LRW) in C and mean cord MT in D. Boxplots show the median (central mark), the 25th and 75th percentiles (bottom and top edges, respectively). The * symbol indicates significant differences ($p < 0.05$, family-wise corrected) between the connected groups.

In tSCI patients, cord area decreased by 3.28 mm² per cord level more than in pSCI in caudal direction, $p=0.011$, [95% CI -5.99 to -0.57] (figure 7.3A). APW showed a trend decrease in tSCI when compared to pSCI patients (tSCI decreased by 0.15 mm more than in pSCI in the caudal direction, $p=0.07$ [95% CI -0.31 to 0.0084]) (figure 7.3B); whereas LRW decreased by 0.36 mm more in tSCI than in pSCI in the caudal direction, $p=0.03$ [95% CI -0.70 to -0.03]) (figure 7.3C). Comparing MRI metrics of AIS A/B vs AIS C/D in paraplegics and tetraplegic patients across all spinal cord levels did not show significant differences ($p>0.05$).

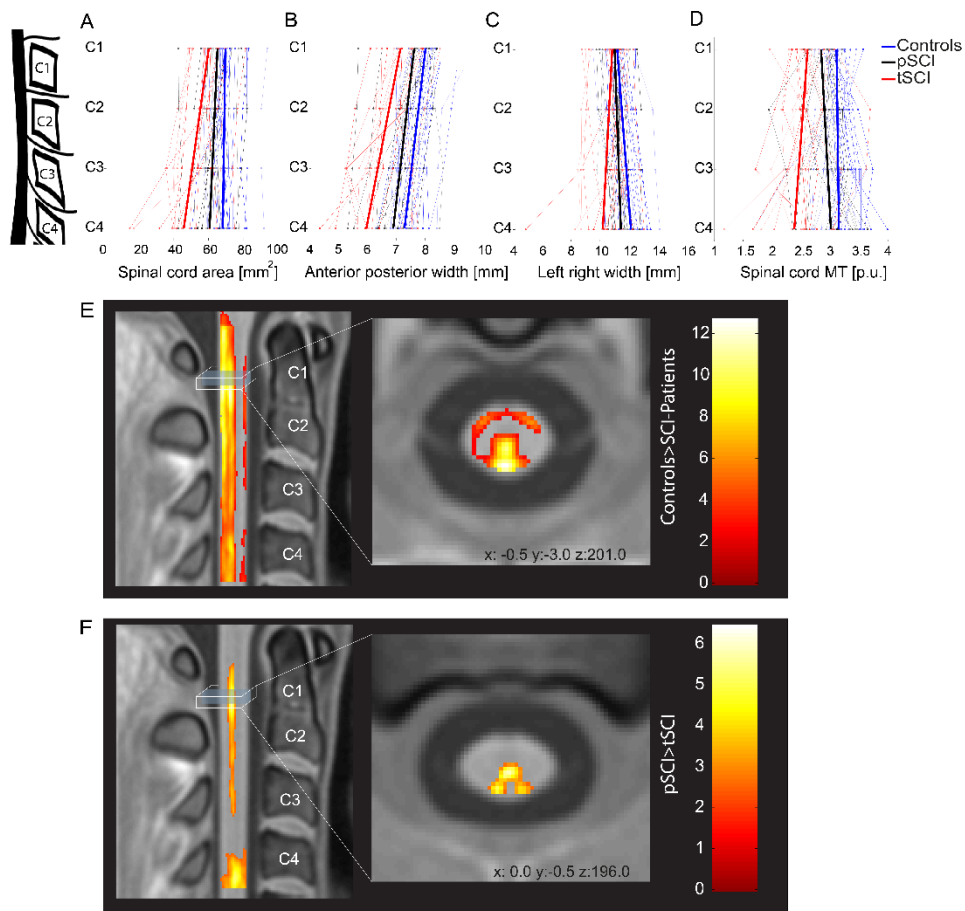


Figure 7. 3: Neurodegeneration along the spinal cord. Spinal cord area (A), anterior posterior width (B), left right width (C) and myelin-sensitive magnetization transfer MT (D) parameters (coloured dots) along the cervical cord (from C1 to C4) in controls (blue), paraplegics (pSCI, black) and tetraplegics (tSCI, red). The light-coloured lines are connecting subject specific data; bold lines represent changes along the cervical cord axis for each group. Changes in myelin-sensitive magnetization transfer (MT) from the voxel-wise analysis in template space (PAM50(De Leener et al. 2018)) are shown in E and F. Overlay of statistical parametric maps (uncorrected $p<0.01$, for illustrative purposes only) shows decreased myelin-sensitive MT in SCI patients compared to controls (E); and tetraplegic compared to paraplegic patients (F). The colour bar indicates the t score.

MRI Parameters	Healthy controls mean \pm sdt	SCI patients (pSCI+tSCI) mean \pm sdt	Group differences [%]	p-value	[95% Confidence Interval]
cord area					
c1	70.01 \pm 8.15	62.44 \pm 9.48	10.80	0.003	-12.49 to -2.65
c2	68.88 \pm 7.59	59.79 \pm 10.19	13.19	<0.001	-14.13 to -4.05
c3	68.42 \pm 8.37	56.61 \pm 11.64	17.26	<0.001	-17.47 to -6.13
c4	68.58 \pm 8.77	53.02 \pm 15.76	22.69	<0.001	-22.25 to -8.88
APW					
c1	8.04 \pm 0.61	7.40 \pm 0.71	7.96	<0.001	-0.99 to -0.29
c2	7.74 \pm 0.50	7.06 \pm 0.74	8.75	<0.001	-1.04 to -0.33
c3	7.49 \pm 0.53	6.72 \pm 0.88	10.28	<0.001	-1.16 to -0.39
c4	7.32 \pm 0.54	6.46 \pm 0.99	11.75	<0.001	-1.30 to -0.42
LRW					
c1	11.21 \pm 0.74	10.89 \pm 0.98	2.85	0.22	-0.83 to 0.19
c2	11.48 \pm 0.85	10.93 \pm 1.00	4.79	0.03	-1.05 to -0.05
c3	11.82 \pm 0.85	10.91 \pm 1.12	7.70	<0.001	-1.47 to -0.35
c4	12.15 \pm 0.90	10.78 \pm 1.63	11.28	<0.001	-2.06 to -0.69
Mean MT					
c1	3.10 \pm 0.20	2.72 \pm 0.29	12.26	<0.001	-0.54 to -0.23
c2	3.13 \pm 0.22	2.73 \pm 0.39	12.78	<0.001	-0.57 to -0.22
c3	3.17 \pm 0.34	2.71 \pm 0.44	14.51	<0.001	-0.68 to -0.23
c4	3.14 \pm 0.47	2.69 \pm 0.60	14.33	<0.001	-0.72 to -0.17

Table 7.2. MRI measures per cervical level in controls and spinal cord injury patients. APW: anterior posterior width; LRW: left right width; MT: magnetization transfer.

7.5.2 Pathophysiological changes

In SCI patients, myelin-sensitive MT was decreased across all cervical levels (z-score=5.85, x=3.5, y=2.0, z=195.5, p<0.001, CE=2752) when compared to healthy controls (figure 7.2D, 7.3E; table 7.2). The decrease in myelin-sensitive MT in the cord was greater in tSCI patients at level C1 (z-score=5.04, x=0, y=-0.5, z=195, p<0.001, CE=1036) and C4 (z-score=5.41, x=-0.5, y=-3, z=201, p<0.001, cluster extent (CE)=2621) (figure 7.3F) when compared to pSCI. The extracted mean MT in the cord using SCT showed a gradient along the spinal cord in tSCI compared to pSCI, specifically mean MT decreased by 0.13% per cord level in tSCI patients when compared to pSCI in the caudal direction, p=0.04 [95% CI -0.26 to -0.004] (figure 7.3D).

7.5.3 Associations between structural changes, lesion level and clinical outcome

Lesion level was associated with smaller mean cross-sectional cord area ($p < 0.001$, $r^2 = 0.146$, [95% Confidence interval (CI): 0.081-0.243]), mean APW ($p < 0.001$, $r^2 = 0.134$; [CI: 1.011-3.228]), mean LRW ($p = 0.003$, $r^2 = 0.085$; [CI: 0.369-1.792]), and mean cord MT ($p < 0.001$, $r^2 = 0.139$; [CI: 1.923-6.083]) (figure 7.4).

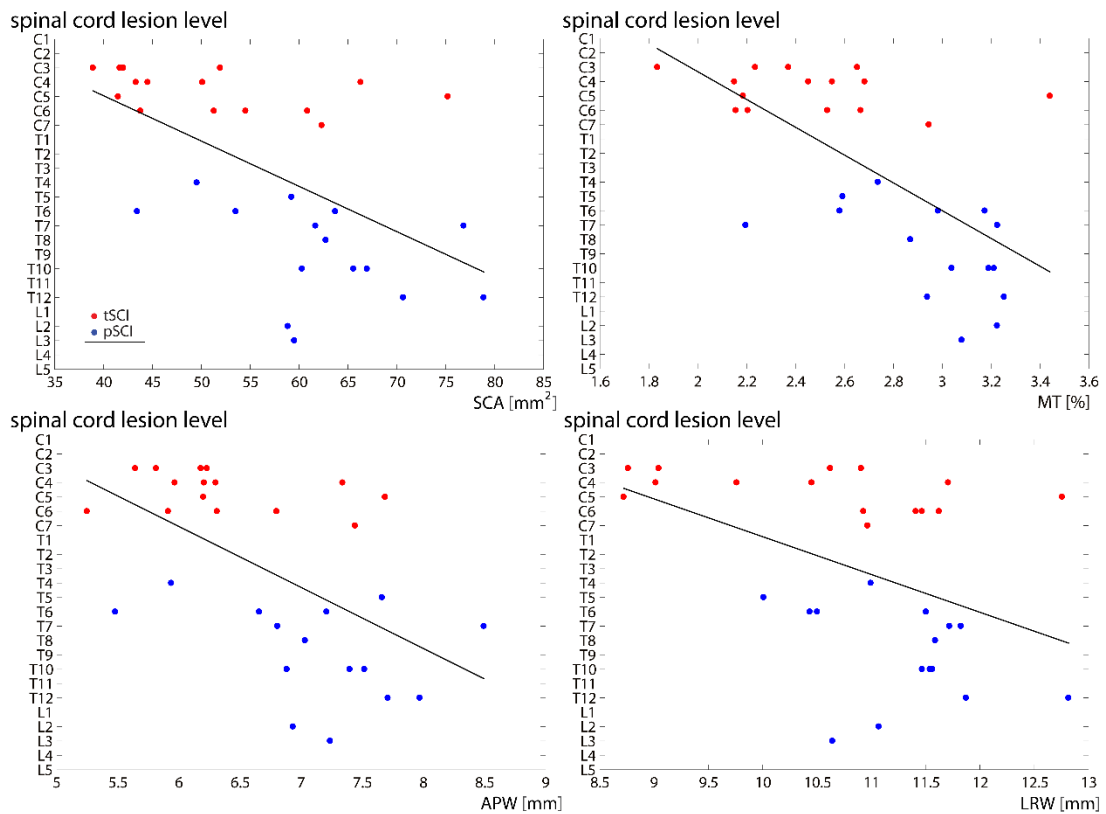


Figure 7.4: Correlations between lesion level and spinal cord parameters. On the y-axis the lesion level is represented defined on the basis of the neurological lesion level; on the x-axis the mean value of the individual MRI indices over cervical levels (from C1 to C4) in tSCI (red) and pSCI (blue) patients.

Better pinprick score was associated with greater mean cord area ($p = 0.016$, $r^2 = 0.416$; [CI: 0.201-1.826]) and APW ($p = 0.007$, $r^2 = 0.450$; [CI: 4.869-27.646]). Higher light touch score was associated with greater mean APW ($p = 0.033$, $r^2 = 0.389$; [CI: 1.069-23.248]) and higher SCIM score was associated with greater mean cord area ($p = 0.041$, $r^2 = 0.215$; [CI: 0.042-1.805]) and mean APW ($p = 0.035$, $r^2 = 0.223$; [CI: 1.041-25.902]). Greater mean MT in the dorsal column was associated with greater light touch score (z-score=4.86, $x=2$, $y=-3$, $z=143$, $p=0.016$, $CE=1166$) (figure 7.5A). Greater mean MT in the dorsal column (z-score=5.07, $x=-1$, $y=-3$, $z=200.5$, $p < 0.001$, $CE=3830$) and spinothalamic tract (z-score=4.85,

$x=-3, y=2, z=175, p=0.024, CE=1048$) was associated with better pinprick score (figure 7.5B). Greater mean MT in the dorsal column ($z\text{-score}=4.39, x=-1, y=-2.5, z=187, p<0.001, CE=3576$) and spinothalamic tract ($z\text{-score}=4.06, x=-3, y=2.5, z=173, p=0.045, CE=839$) was associated with better SCIM score (figure 7.5C).

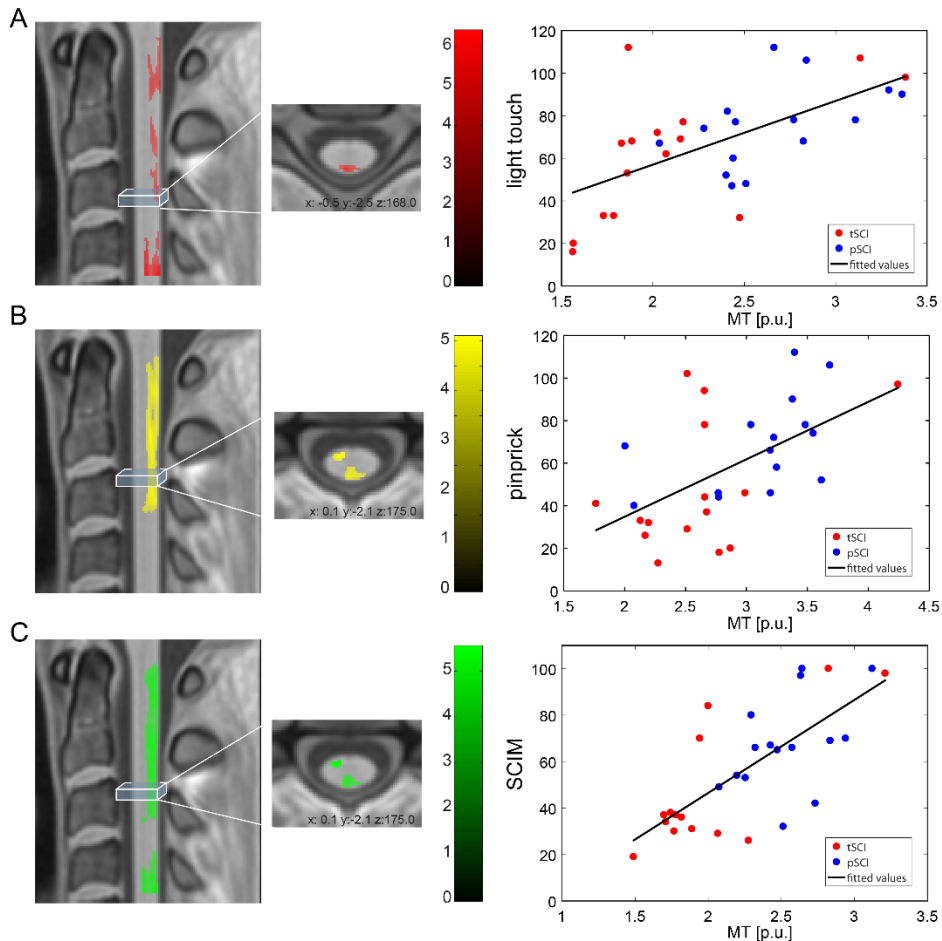


Figure 7.5: Correlations between clinical measures and spinal cord parameters. Correlations between myelin-sensitive magnetization transfer (MT) and light touch score (A); pinprick score (B), and SCIM score (C). Overlay of statistical parametric maps (uncorrected $p<0.01$, for illustrative purposes only) on the left side (the colour bar indicates the t-score); correlation with extracted mean values from the significant clusters in the right column (for illustrative purposes only).

7.6 Discussion

This study shows a lesion level dependent neurodegenerative gradient across the cervical cord with greater atrophic and myelin-sensitive MT reductions occurring in the proximity of the injury. These changes are less pronounced with increasing distance from the injury showing a gradient of

neurodegeneration. In addition, changes in the spinal cord macro- and microstructure were associated with tract-specific clinical outcomes. Tracking of a neurodegenerative gradient holds potential as a new neuroimaging biomarker to monitor treatment effects of regenerative and neuroprotective agents in interventional trials.

7.6.1 Characteristics of the neurodegenerative gradient

This is the first study to reveal a neurodegenerative gradient over several cervical segments (from C1 to C4) in chronic traumatic SCI patients. The extent of neurodegeneration was greatest in the proximity of the lesion and declining with increasing distance from the injury. Interestingly, only changes in the cords' left-right direction showed a neurodegenerative gradient while the observed decrease in the anterior-posterior direction was equally decreased across all cervical levels. Changes in the cords' LRW (Lundell 2011) have been associated with retrograde degeneration of the corticospinal tract (Lemon 2008); whereas changes in the APW (Grabher et al. 2015; Jutzeler et al. 2016; Lundell et al. 2011) have been associated with anterograde degeneration in the posterior columns (Daniel and Strich 1969). The lack of a neurodegenerative gradient within the dorsal columns – despite showing significant neurodegeneration – suggests that the magnitude of anterograde axonal degeneration in the posterior columns (i.e. Wallerian degeneration) (Daniel and Strich 1969) is equally distributed across cervical levels (i.e. no gradient); while degeneration of the CST (captured by the LRW gradient) is greatest in the proximity of the injury epicentre and declines with increasing distance (Kalil and Schneider 1975; Kerschensteiner et al. 2005b).

Higher lesion level was directly associated with the magnitude of neurodegeneration. In other words, the neurodegenerative gradient was more pronounced in tSCI patients when compared to pSCI. This is not surprising, as a lesion to a higher spinal level affects a greater number of neuronal structures and thus results in more neurodegenerative changes when compared to a lower spinal lesion (Jutzeler et al. 2016). However, the fact that significant neurodegenerative changes were detected in pSCI patients even in the cervical cord suggests that a neurodegenerative gradient occurs above a SCI at any level. Interestingly, the completeness of the lesion does not influence the neurodegenerative gradient. It remains to be revealed whether a similar neurodegenerative gradient exists caudally to a SCI. This is of particular importance for repair studies which would aim to reduce the amount of degeneration in the caudal proximity of the injury via regenerating fibres. The fact that the lumbar cord undergoes neurodegenerative changes after a cervical SCI (David et al. 2019) speaks however for a neurodegenerative gradient occurring also below the level of injury.

7.6.2 Pathophysiological changes

By means of myelin-sensitive MT (Helms, et al. 2008b) we were able to disentangle one of the underlying pathophysiological mechanisms contributing to cord atrophy. Previous studies showed a centrifugal pattern of axonal degeneration starting from the lesion site (Kalil and Schneider 1975; Kerschensteiner et al. 2005b) with a gradual myelin loss propagation (Buss et al. 2004, 2005). This demyelination was shown to be a slow and continuous process covering more years after injury (Buss et al. 2004, 2005). Specifically, myelin proteins were still detectable 3 years after injury in the degenerating fibre tracts, long after the disappearance of the corresponding axons (Beirowski et al. 2005; Buss et al. 2004). In agreement with the atrophic changes, myelin-sensitive MT showed a neurodegenerative gradient and the magnitude of decrease was greater in tSCI when compared to pSCI patients. Therefore, myelin-sensitive MT can be applied as a biomarker to monitor tract-specific myelin changes of the major spinal pathways.

7.6.3 Associations between structural changes and clinical outcome

We found tract-specific associations with appropriate clinical outcomes. For instance, greater myelin-sensitive MT decreases in the dorsal column were directly linked to worse light touch scores, while a greater decrease of myelin-sensitive MT was associated with reduced pinprick and SCIM scores in both, dorsal column and spinothalamic tracts. In agreement with previous reports, greater changes in the cords' APW were related to worse pinprick and light touch scores (Grabher et al. 2015; Lundell et al. 2011). The simultaneous associations between sensory outcomes with atrophy in anterior posterior direction (APW) and sensory outcomes as well as functional independence with decreased myelin-sensitive MT in the ascending pathways, supports the notion that demyelination is a critical factor in the pathobiology of human SCI (Buss et al. 2004, 2005). Therefore, both APW and MT readouts hold promise as biomarkers for assessing changes of sensory function in traumatic SCI patients.

7.6.4 Limitations

This study has some limitations. Patients were on average 8 years older than healthy controls. However, all statistical analyses were corrected for the linear effect of age. The automatic segmentation tool used to process the data (reducing bias) required manual editing. MPM protocols (Weiskopf et al. 2013) provide maps sensitive to myelin (R1 and MT) and to iron content (R2*). However, the quality of R1 and R2* maps at lower cervical cord levels was poor and could not be used for the analysis. Moreover, the interpretation of myelin-sensitive MT maps should be handled with

caution as MT is an indirect marker for myelin and cannot directly describe underlying biological changes at the microscopic level. Nevertheless, histopathological studies have shown association between changes in MT and myelination(Schmierer et al. 2004; Turati et al. 2015).

7.7 Conclusion

In conclusion, this study shows that the magnitude of neurodegeneration decreases along the cervical SC. In particular, the extent of neurodegeneration was more pronounced closer to the injury and directly correlated with the level of the injury and clinical impairments. Tracking remote cord pathology over several spinal segments is clinically eloquent and the MRI based neurodegenerative gradient measures could be used to monitor treatment effects of regenerative and neuroprotective agents.

Study funding

This study is funded by ERA-NET NEURON (hMRI of SCI no: 32NE30_173678), the European Union's Horizon 2020 research and innovation program under the grant agreement No 681094, and the Swiss State Secretariat for Education, Research and Innovation (SERI) under contract number 15.0137, grants from Wings for life charity (INSPIRED) (No WFL-CH-007/14), and Eccellenza fellowship/181362 by SNSF.

8 General discussion

In this chapter, after a short summary of the key finding, the results of all studies are discussed with a broader perspective. In particular, I would like to emphasize the scientific relevance of the work, the limitations, outlooks and future directions.

8.1 Key findings

The work of this thesis focused on the development of new tools for the application of MPM maps for the investigation of the spinal cord. Furthermore, MPM maps, which provide an indirect measure of myelin and iron content, were used for different clinical studies in order to investigate the underlying microstructural changes due to trauma and neuropathic pain in SCI patients or training-induced plasticity in healthy controls. In this section a list of the studies and relative key findings are presented.

Study I: Simultaneous analysis of brain and spinal cord multi-parametric maps based on SPM framework

- A tool for the simultaneous analysis of brain and cervical spinal cord was developed in the framework of VBM/VBQ in SPM (Matlab r2016b)
- These tools can be used to assess morphological and microstructural MRI changes
- Validation based on comparing SCI-patients and healthy controls showed that simultaneous analysis of brain and spinal cord is as sensitive as available tools in detecting trauma-induced changes occurring in the brain and spinal cord

Study II: Microstructural signature of neuropathic pain across the neuraxis after spinal cord injury

- The tool for the simultaneous analysis of brain and cervical spinal cord (from study I) was used to assess the pathophysiology of neuropathic pain in SCI-patients
- SCI-patients with neuropathic pain showed microstructural alterations, in terms of myelin and iron content, in ascending and descending nociceptive pathways
- These changes were related to pain intensity, and can be potentially used as biomarker to track microstructural plasticity that might facilitate the investigation and monitoring of neuropathic pain

Study III: The interplay between corticomotor system and hippocampus circuit changes during procedural learning

- A longitudinal processing pipeline was optimized for MPM maps
- This study showed evidence for brain plasticity as a consequence of motor skill learning
- The training-induced changes in healthy controls presented a quadratic shape showing transient microstructural changes that lead to skill improvement and memory consolidation
- MPM maps offer a novel quantitative measure of training-induced brain plasticity

Study IV: Tracking the neurodegenerative gradient after spinal cord injury

- SCT routines were optimized to analyse MPM maps in the spinal cord and were used to investigate macro- and micro- structural changes along the spinal cord (from level C1 to C4) of SCI patients and healthy controls
- A gradient of neurodegeneration was evident along the spinal cord showing more pronounced neurodegeneration closer to the injury.
- This gradient of neurodegeneration was directly correlated with the level of the injury and clinical impairments
- MRI based neurodegenerative gradient measures could be used to monitor treatment effects of regenerative and neuroprotective agents

8.2 Discussion of methodological improvements

The main methodological advancements carried out in this thesis were (i) the development of image processing tools for the simultaneous analysis of brain and spinal cord using qMRI (chapter 4), (ii) optimization of longitudinal processing pipelines for MPM maps to be more sensitive to subtle macro- and micro-structural changes over time (chapter 6) and (iii) definition of a pipeline to assess MPM maps along the spinal cord based on SCT routines. These processing tools were applied to qMRI data from SCI patients and healthy controls in order to assess trauma- or neuropathic pain- related changes in SCI patients and training-induced changes in healthy controls. The simultaneous analysis of brain and spinal cord was optimized for cross-sectional studies as well as for longitudinal studies.

8.2.1 Simultaneous analysis of brain and cervical spinal cord

In order to assess simultaneously brain and cervical spinal cord changes, a template covering brain and cervical spinal cord was incorporated in the framework of VBM and VBQ in SPM12. The development of this processing tool is based on a generative model in which the simultaneous segmentation, registration, normalization and bias correction is performed according to the unified algorithm from Ashburner et al. (Ashburner and Friston 2005).

To assess how well this pipeline is sensitive to neural changes, qMRI data of SCI patients and healthy controls were analysed with this new pipeline, and additionally with the standard VBM/VBQ and SCT covering only the Brain and spinal cord, respectively.

The ICC computed comparing maps from the 'Brain-neck' and standard 'brain' approach showed good to excellent values for most of the brain regions, suggesting that brain maps generated from the standard and brain-neck approach are similar. Nevertheless, by comparing the template covering brain and spinal cord and the old template covering only the brain (i.e. by subtracting the two templates), some misalignment was shown in the internal structures of the brain such as thalamus and CST. This might explain the moderate ICCs reported in the thalamus and CST (for MT and Volume maps). However, this misalignment did not alter results comparing SCI-patients and healthy controls, which showed the same macro- and micro-structural changes. Therefore, we are confident that results from the 'Brain-neck' analysis were similar to those from the standard VBM/VBQ pipeline covering only the brain.

In the spinal cord, the brain-neck analysis revealed similar changes as shown in the analysis using the SCT, with myelin-sensitive reductions in MT and R1 maps in SCI-patients compared to healthy controls. However, there are several differences between the two tools: in order to be consistent with the brain smoothing and be able to assess simultaneously brain-neck in the framework of random field theory (Flandin and Friston 2016), the brain-neck analysis in SPM requires a weighted isotropic Gaussian kernel smoothing as in (Draganski, et al. 2011); whereas in the SCT approach, since the spinal cord is disconnected from the brain, more flexibility is allowed for smoothing algorithms in the spinal cord. In SCT a centerline smoothing algorithm was implemented which works by straightening the cord, applying a 1-D Gaussian smoothing kernel and then un-straightening the cord back into the original space (De Leener et al. 2016). However, even if different smoothing algorithms were applied, group comparison revealed the same microstructural differences. Note that SCT does not provide probability maps of GM/WM, therefore no macrostructural analysis in template space is possible for data analysed

in SCT. Macrostructural spinal cord changes in SCT could be assessed only using subject specific cross-sectional area measurements which showed atrophy along the cord similarly as in the brain-neck analysis. In addition, both tools (brain-neck SPM and SCT) were able to show the same associations between cord changes and clinical outcomes. Therefore, this 'Brain-neck' approach is sensitive as available tools in discovering diseases associated effects in SCI-patients compared to healthy subjects with the advantage of analysing brain and spinal cord simultaneously.

8.2.2 Optimization of longitudinal pipeline

Longitudinal studies are of increasing importance in neuroimaging, because they offer the possibility to investigate processes that are inherently longitudinal, such as growth, plasticity, aging, and degeneration. Longitudinal studies involve repeated acquisitions of the same subjects over time and have well-established advantages over cross-sectional designs in terms of increasing power and reducing confounds. However, longitudinal study requires appropriate processing and statistical models in order to account for the dependence of repeated measurements within-subject.

In the past, longitudinal pre-processing tools were based on asymmetric methods where (moving) data were registered to one (fixed) image chosen as reference (i.e. baseline). However, this method has the potential to introduce false positive differences. Specifically, pair-wise registration results have been shown to differ depending on which image is chosen as the reference (Thomas et al. 2009; Yushkevich et al. 2010). For example, the sum of changes from A to B and B to C differs from the change estimated directly from A to C (Leung et al. 2012). Results, from a study based on three time-points, showed decelerating changes over the first two time points that are not biologically plausible (Hua et al. 2011; Thompson, Holland, and Bull 2011), therefore, any technique that is not symmetric with respect to the multiple time-points has the potential to introduce false positive differences.

Many of the solutions proposed to address asymmetry across multiple time points can be summarized as three distinct approaches (Ashburner, Andersson, and Friston 1999; Cachier and Rey 2000): (i) cross-sectional procedure, where all time-points are treated independently (e.g., (Giedd et al. 1999)); (ii) multiple co-registrations procedure, where each time-point can be registered to every other time-point within-subject (e.g., (Leung et al. 2012)); (iii) or some form of within-subject co-registration where all time-points of a subject are registered to a subject-specific average image (Reuter et al. 2012; Škrinjar, et al. 2008). The first approach showed low bias but very high variance while the second is computationally infeasible for high-dimensional diffeomorphic image registration. Therefore, the last approach offers the best solution so far. This method was introduced by Tagare et al. (2009) (Tagare,

et al. 2009) and it is based on the derivation of a “half-way” space between two images. This approach was further developed by Ashburner (Ashburner and Ridgway 2013) including more than two images and it was incorporated into SPM12 as the longitudinal registration tool. This longitudinal registration was implemented in a generative modelling framework, which combines rigid alignment, diffeomorphic warping and a correction for the intensity inhomogeneity artefact.

In our study, this longitudinal pipeline was optimized for MPM maps. Specifically, the five MT maps of each subject, were first skull-stripped and then used for within subject group wise co-registration (Ashburner and Ridgway 2013), this step generates subject specific midpoint map and corresponding deformation fields. These deformation fields were used to warp all MPM maps to such midpoint space. Finally, the subject specific midpoint maps were segmented using unified segmentation algorithm (Ashburner and Friston 2005) and corresponding deformation fields were used to map all MPM maps into MNI space. As usually, all MPM maps were spatially smoothed using a 3-mm (in for the GM) and 5-mm (in the WM) full width at half maximum (FWHM) preserving GM/WM tissue boundaries (Draganski, et al. 2011) before performing statistics.

To relate these quantitative MRI (voxel-based quantification (VBQ)) to more conventional metrics (such as voxel-based morphometry (VBM)), segmented MT maps (GM and WM) were additionally, normalized using within- and between-subject modulation; and spatially smoothed using an isotropic Gaussian smoothing (4-mm for WM and 6-mm for GM FWHM). This MT-based VBM pipeline offers the possibility to perform morphometric analysis based on MT segmentation which showed to be a good alternative in case traditional T1w maps are missing.

The longitudinal registration tool showed consistent solutions irrespective of the order of the images (Ashburner and Ridgway 2013). However, the algorithm is based on some regularizations, that are still relatively unexplored. An additional limitation for the validation of longitudinal tools is the lack of ground truth which limits the validation on the use of simulated data (where a specific change over time is artificially introduced), or data where changes are expected (i.e. reduction of myelin over time in MS patients).

8.2.3 Optimization of SCT routines for MPM maps analysis

The recently developed spinal cord toolbox (SCT) provides several tools for the analysis of spinal cord MRI. In particular, automatic segmentation techniques for the spinal cord (Horsfield et al. 2010; De

Leener, et al. 2014) and grey matter (Dupont et al. 2017; Perone et al. 2018) replace time-consuming and operator-dependent manual segmentations. In this way the spinal cord and relative GM/WM tissues can be analysed in a comparable and reproducible way. Another big advance in spinal cord image processing was the development of the first, multi-contrast, spinal cord template, the PAM50 template covering the full spinal cord (De Leener et al. 2018). This template provides atlases of GM, WM and white matter tracts which can be used to perform template-based analysis and facilitating group and multi-center studies comparison. These tools were developed for the analysis of DTI, fMRI or MTR. In our work (chapter 7), we optimized a processing pipeline based on the available routines from SCT to assess MPM maps. The optimized pipeline was able to segment properly MT maps, co-register them to template space and compute the corresponding deformation fields. These subject specific deformation fields could be applied to all MPM maps and warp them to PAM50 space allowing voxel-wise analysis in SPM. A tract-specific analysis using PAM50 atlases allowed a better investigation of the pathophysiological changes and the corresponding associations with the clinical measurements. Additionally, the MPM metrics can be extracted in subject space as previously done in the spinal cord community. The subject space metrics were very close to those computed using gold standard tools (i.e. Jim) therefore we are confident that SCT routines can be successfully applied to MPM maps.

8.3 Discussion of clinical studies

The development of the new cross-sectional pipeline including the brain and cervical spinal cord offered the possibility to investigate (i) macro- and micro-structural changes occurring across the full injured cervical cord and brain after a SCI and (ii) the underlying pathophysiological changes that lead to neuropathic pain in chronic SCI-patients. Additionally, optimized longitudinal processing pipelines for MPM maps allowed the investigation of training-induced changes in healthy subject. The developed methods and corresponding clinical applications clearly demonstrated the ability of MPM maps to detect microstructural changes induced by trauma, pain and training.

8.3.1 Trauma-induced changes in SCI

After the primary injury, coming from the direct physical trauma to the spinal cord, a cascade of secondary changes is occurring at the cellular, structural, and functional level. These changes start at the lesion site and propagates up- and down-stream along the nervous system leading to different macro- and microstructural changes. In agreement with previous reports, in our study trauma-induced

atrophic changes, as well as myelin and iron changes, were evident across the sensory-motor and limbic system (for review, see (Freund, et al. 2019a)) in SCI-patients compared to healthy controls. Specifically, atrophy in the thalamus was parallelized by myelin-sensitive R1 reduction in SCI-patients compared to healthy controls even by analysing brain and spinal cord simultaneously. Additionally, myelin-sensitive R1 and MT reductions in the sensory-motor cortex and R1 reduction in the CST were shown in SCI-patients compared to healthy controls.

Microstructural changes occurring in the spinal cord were revealed using the combined brain spinal cord SPM as well as SCT. Both analysis tools, showed that the spinal cord undergoes atrophy and myelin-related changes in SCI patients compared to healthy controls. This atrophy and myelin-sensitive MT reductions were more pronounced in the proximity of the injury, showing a gradient of neurodegeneration (chapter 7).

Interestingly, only changes in the cords' left-right direction showed a neurodegenerative gradient. This indicates that that degeneration of the CST (captured by the LRW gradient) is greatest in the proximity of the injury epicentre and declines with increasing distance (Kalil and Schneider 1975; Kerschensteiner et al. 2005b). In anterior-posterior direction, the neurodegeneration was equally decreased across all cervical levels, meaning that the magnitude of anterograde axonal degeneration in the posterior columns (i.e. Wallerian degeneration)(Daniel and Strich 1969) is equally distributed across cervical levels (i.e. no gradient).

The gradient of neurodegeneration was more evident in tSCI patients when compared to pSCI. This is not surprising, if we consider that a lesion at higher level affects a greater number of neuronal axons and therefore the neurodegenerative gradient is directly associated with the magnitude of neurodegeneration. However, the fact that significant neurodegenerative changes were detected in pSCI patients even in the cervical cord suggests that a neurodegenerative gradient occurs above a SCI at any level.

By means of myelin-sensitive MT (Helms, et al. 2008a) we were able to disentangle one of the underlying pathophysiological mechanisms contributing to cord atrophy. Previous studies showed axonal degeneration starting from the lesion site (Kalil and Schneider 1975; Kerschensteiner et al. 2005b) with a gradual (slow and continuous) myelin loss propagation covering more years after injury (Buss et al. 2004, 2005). Moreover, it was shown that myelin proteins are still detectable 3 years after injury in the degenerating fibre tracts (Beirowski et al. 2005; Buss et al. 2004). Interestingly, myelin-

sensitive MT showed a neurodegenerative gradient which was more pronounced in tSCI when compared to pSCI patients.

The association analysis between spinal cord microstructure and clinical disability showed that higher MT values in the spinal cord were associated with better sensory and motor outcome. More specifically, SCT analysis revealed a tract-specific association with appropriate clinical outcomes; showing that greater myelin-sensitive MT decreases in the dorsal column were directly linked to worse light touch scores, while a greater decrease of myelin-sensitive MT was associated with reduced pinprick and SCIM scores in both, dorsal column and spinothalamic tracts. In agreement with previous reports, greater changes in the cords' APW were related to worse pinprick and light touch scores (Grabher et al. 2015; Lundell et al. 2011).

Hence, sensory outcomes were associated with both atrophy in anterior posterior direction (APW) as well as decreased myelin-sensitive MT suggesting demyelination a critical factor in the ascending pathways after a SCI (Buss et al. 2004, 2005).

Therefore, both APW and MT can be used as biomarkers for assessing changes of sensory function in traumatic SCI patients. The definition of such biomarkers could facilitate monitoring effects of regenerative and neuroprotective treatments.

8.3.2 Microstructural signature of neuropathic pain after SCI

It was shown that volumetric increases and decreases in the cervical cord, thalamus, primary somatosensory cortex, ACC, and dorsolateral prefrontal cortex (DLPFC) have been also associated with neuropathic pain (NP) following SCI (Jutzeler et al. 2016; Wrigley et al. 2009). We demonstrate the microstructural substrates of such pain-associated volumetric changes by revealing changes in myelin and iron content along the trajectories of ascending and descending nociceptive pathways.

Specifically, microstructural alterations that are related to pain intensity, were detected within the spinal cord and periaqueductal gray (PAG); providing an important predictive biomarker for neuropathic pain. The PAG receives input from the frontal lobe, amygdala, hypothalamus, and anterior cingulate cortex and engages the rostral ventral medulla which in turn controls nociceptive processing in the spinal dorsal horn (Basbaum and Fields 1979). The involvement of PAG in pain modulation was also confirmed by other studies, where the direct stimulation of the PAG was used as a treatment

option for NP including pain following SCI (Jermakowicz et al. 2017). Therefore, microstructural changes revealed from R2* map might indicate molecular changes in the PAG that compromise descending inhibition of nociceptive processing and subsequent increased spinal gain of incoming information. This dysregulation in descending pain modulation has been shown to contribute to central sensitization as the hallmark of NP (Ossipov et al. 2010).

Additional evidence for an impaired descending pain modulatory system can be inferred from macro- and microstructural changes in other key constituents of this network such as the ACC (i.e., increased iron accumulation) and DLPFC circuitry (Wiech 2016) (i.e., reduced volume and myelin content). These alterations in DLPFC might indicate an individual's predisposition to develop persistent pain (Gustin et al. 2009) through decreased myelin content which might lead to a pathological nociceptive gain control in NP after SCI (Albu et al. 2015; Finnerup and Jensen 2004).

Interestingly, somatotopic changes in Thalamus were revealed in medial and lateral side, showing trauma-induced volumetric changes in medial thalamus, and pain-related iron accumulation in the lateral thalamic nuclei. This study highlighted the complex interplay between myelin and iron changes in areas related to ascending and descending nociceptive pathways. The microstructural signature of neuropathic pain was identified and might be used to investigate maladaptive plastic processes and may facilitate patient monitoring during clinical trials for NP.

8.3.3 Training-induced plastic changes in SCI

The adult brain preserves the ability to change morphometry and structure in response to altered environment or learning new skills. To date, alterations in brain structure were identified in circuits relevant to the task, for example, it has been found that London taxi drivers' presented more grey matter volume in the hippocampus which was related to the capability to store a detailed mental map of the city (Maguire et al. 2000); the cortico-motor system was altered after several months of juggling training (Draganski et al. 2004), spatial navigation training (Lövdén et al. 2012), or after few sessions of complex whole-body balancing (Taubert, Mehnert, et al. 2016). Apart from early studies showing macrostructural brain plasticity, much more attention nowadays has been focused on the spatio-temporal dynamics and microstructural changes underlying this training-induced plasticity (Kodama et al. 2018b). It was shown that myelin regulation might be a novel form of brain plasticity which speeds neuronal signal conduction and can be modified by experience (McKenzie et al. 2014). However, these

microstructural changes cannot be directly examined in the human brain and therefore the application of novel qMRI techniques might bring some light on the underlying mechanisms that lead to adult neuroplasticity.

In our longitudinal study, 18 healthy adult males performed a motor task on a dance platform (Impact Dance Platform, Positive Gaming BV, Haarlem, Netherlands) using upper (n=9) or lower (n=9) limbs for a period of 4 weeks. Spatio-temporal brain changes were investigated comparing trained participant to healthy controls (n=14) without training. All trained subject could improve in the number of correct pressed buttons as well as in the reaction time (time to press the button), and these improvements persisted after a period of no training. Parallel to the behavioural improvement, transient (or temporary) changes in the hippocampus, CST and sensory-motor cortex were shown. Interestingly changes in the CST are preceding those in the M1, and then, both M1 and CA changes are preceding those in EC showing a possible motor-Hippocampus and within-hippocampus loops. These distinct spatio-temporal microstructural changes in Hippocampi-corticomotor circuits showed the significant functional interplay between different brain regions related to the complex multi joint movement acquisition.

Additional confirmation about the behavioural relevance of structural changes comes from the correlation between structural changes in the hippocampus and performance improvements. Crucially, transient volumetric changes in the left hippocampus were associated with improvements in the percentage of correct pressed buttons and reaction time, meaning that left CA encodes learning processes; whereas linear microstructural changes in the right hippocampus EC was correlated with the speed of improvement, meaning that faster learning is encoded in the microstructure of the EC.

In this study temporary microstructural R1 changes were observed in the bilateral CST and left sensory motor cortex, showing a characteristic “u” shape with a transient microstructural decrease followed by a normalization phase. The net effect of a reduction in MT and R1 might be related to a lengthening in T1 which is related to volume fraction. Therefore, possible underlying mechanisms behind the transient microstructural reduction might be related to vascular changes or gliogenesis. An alternative interpretation of such temporary changes might be related to synaptic changes in the grey matter (M1) or myelin modulation in the CST (white matter). All these interpretations were supported by animal studies showing neurogenesis in the hippocampus (Deng et al. 2009; Eriksson and Perfilieva 1998; Tronel et al. 2010), novel dendritic spines and synapses in sensory and motor cortices (Chen et al. 2015; Sonja B. Hofer et al. 2009) and myelin changes in the CST (Sampaio-Baptista et al. 2013). In addition,

our study showed that participant training lower limbs presented greater temporary changes in the myelin-sensitive MT compared to those training upper limbs, in the posterior part of the limb of the internal capsule suggesting a somatotopy of learning.

In this study, we elucidated possible underlying mechanisms of training-induced neuroplasticity revealing the characteristic spatio-temporal pattern and the interplay of different brain regions. These findings suggest that intra-hippocampi and hippocampi-corticomotor interplay occurs during motor-skill training and may play an important role in tracking rehabilitation and recovery in clinical practice.

8.4 Limitations and considerations

8.4.1 Technical limitations for the spinal cord analysis

The simultaneous analysis of brain and cervical spinal cord in SPM offers the great advantage of performing the simultaneous analysis of brain and cervical spinal cord in the same framework and using the same algorithm, but it has several limitations. Firstly, the template covers only cervical spinal cord until level C3; however, a template including more spinal cord levels can be generated by including MRI data covering more spinal cord segments in the generation of a new template covering brain and more spinal cord levels. Furthermore, the GM/WM classification in the spinal cord is sub-optimal. In our studies (chapter 4 and 5), the probability maps of GM and WM were combined to generate a probability map of neural tissue (NT) which is an indirect measure of spinal cord volume. In future, a better GM/WM classification in the spinal cord might be achieved by combining high resolution spinal cord data and lower resolution brain MRI in the template. Some differences were evident between the standard SPM template and the new template incorporating brain and cervical spinal cord, especially in the internal structures of the brain. In addition, the standard template showed more smoothed probably maps in the brain than the brain-neck' template, this is due to the different amount of MRI data used for the templates' generation; by including more data, the two templates might look more similar.

In our study (chapter 7) a pipeline based on SCT routines was optimized for MPM maps. The automatic segmentation tool used to segment MT maps required manual editing, however the mean values from MPM maps were very close to those computed using Jim (which represents the gold standard for MRI processing). The big difference between SCT and the brain-neck processing consists in the smoothing algorithm applied in the spinal cord. Specifically, the SCT uses an adaptive Gaussian kernel oriented

along the spinal cord centreline (De Leener et al. 2016); whereas in the brain-neck approach a weighted smoothing is applied. Unfortunately, no standards for the correct shape and size of smoothing algorithms are defined in the spinal cord community and further investigation is needed.

8.4.2 MPM maps as indirect measure of microstructural changes

MPM protocols (Weiskopf et al. 2013) provide maps sensitive to myelin (R1 and MT) and to iron content (R2*). However, the interpretation of myelin-sensitive MT or R1 maps should be handled with caution as they are indirect markers for myelin and cannot directly describe underlying biological changes at the microscopic level. A big limitation for the development of qMRI in the spinal cord consists in the lack of the ground truth. The most controlled approach is based on numerical phantoms and in silico simulation of MRI signals against models of tissue microstructure and the corresponding analysis. However, they suffer from poor realism as they don't necessarily account for all the MRI signal variance (such as susceptibility artifacts, physiological noise, etc.). A more realistic approach involves scanning synthetic phantoms (e.g., type-I bovine brain extract), which account for the experimental variance related to MRI acquisition, but still they are poorly realistic with respect to the true microstructural tissue. In vivo validation using literature evidence is limited and it is usually difficult to generalize because it is often derived from single individuals. In addition, all approaches might differ in pathological conditions. Validation using ex vivo samples is more realistic so far. In this procedure, the same tissue is scanned both with MRI and with high resolution microscopy, and then compared using statistical tests of correlation and levels of agreement. Even if this procedure sound easy and straightforward, every step is tricky and can affect the overall precision and accuracy of the ground truth itself (Cohen-adad 2018).

8.5 Outlook and future directions

8.5.1 Generation of a brain and spinal cord template covering more spinal cord segments

In our studies (chapter 4 and 5) the simultaneous analysis of brain and spinal cord was limited until level C3; however, by developing a template covering all spinal cord segments, the analysis could incorporate more segments covered in the MRI. Therefore, the development of a better template represents the first step to take. A template including more spinal cord levels can be generated by

including MRI data covering more spinal cord segments. Furthermore, by including high resolution spinal cord data and lower resolution brain MRI, a better GM/WM classification in the spinal cord might be achieved, and therefore more tissue specific analysis could be possible also in the spinal cord. Further development of the template might include labelling of the spinal cord segments (i.e. C1, C2) as well as for the spinal cord tracts (i.e. corticospinal tract). Labelling of the spinal cord segments might be incorporated using information from the other probability maps such as bone structures (which presents specific shape feature at each level), whereas more limitations are related to the classification of the tracts because of the restricted resolution and acquisition protocols. In the future better acquisitions of spinal cord imaging might lead to a better visualization of the tracts and therefore better tissue classification.

8.5.2 Improvement in the generation of MPM map in the spinal cord

Map generation from the MPM acquisition is based on rigid registration between the echoes before computing the maps. This rigid registration is used to correct for head motion during the acquisition protocol and it represents a valid assumption in the brain. However, the spinal cord, is a more flexible structure and more motion is allowed even between the internal structures. Therefore, MPM maps in the spinal cord could be improved by incorporating some degree of non-rigid deformation, which might improve the alignment between the echoes and therefore improve the quality of the generated maps. This might improve the contrast in the spinal cord and allow a better coregistration and GM/WM segmentation in the spinal cord.

8.5.3 Multi-contrast MPM data

The idea of in vivo histology based on MRI (hMRI) is based on the possibility to infer microstructural changes related to myelin, axonal changes and iron content in neural tissues using MRI data. MPM approach is one possible acquisition protocol to get qMRI maps that are sensitive to myelin and iron content. However, they do not provide any information related to axonal changes. The idea of including more modalities in new biophysical models might provide more information for in vivo histology. In this direction the MR g-ratio (the ratio between inner and outer diameter of a myelinated axon) model (Ellerbrock and Mohammadi 2018b; Mohammadi et al. 2015b; Stikov et al. 2011b); or the DTI & Fiber tools (Reisert et al. 2013) were developed.

The g-ratio quantifies the ratio between the inner to the outer diameter of the myelin sheath and it is based on the combination of MT and diffusion data. This ratio provides a measure of the myelin

thickness that complements axon morphology (diameter and density) with high specificity for assessment of demyelination; and therefore, it is functionally related to conduction velocity. The MR g-ratio presented good agreement with histological findings (Duval et al. 2017; Mohammadi et al. 2015a) and holds promise as an important non-invasive biomarker due to its microstructural and functional relevance in neurodegeneration.

The estimation of fiber orientation densities can be used for a more accurate description of the fiber architecture (Reisert et al. 2013). This approach is based on the biophysical assumption that fibers do not terminate in white matter and using inter-voxel relations from a single q-shell DWI measurement, the global coherent fiber density (also defined as tensor fiber density (TFD)) is computed.

8.6 Concluding remarks

In this thesis, we have developed a tool for the simultaneous analysis of brain and cervical spinal cord in the framework of VBM/VBQ in SPM12. The proposed method yielded successful results on qMRI and offered the possibility to investigate morphological and microstructural MRI changes in different clinical studies. Validation based on comparing SCI-patients and healthy controls showed that the 'Brain-neck' analysis is as sensitive as available tools in detecting trauma-induced changes occurring in the brain and spinal cord. This tool was further used to investigate the microstructural signature of NP, affecting key constituents of the ascending and descending nociceptive pathways. The magnitude of microstructural changes is directly linked to NP intensity. The complex interplay between myelin and iron changes in areas related to sensory and affective processing, highlights maladaptive plastic processes likely involved in the maintenance of NP. Beyond the understanding of the intimate pathophysiology of NP, tracking microstructural plasticity may facilitate patient monitoring during clinical trials for NP. Closer investigation of trauma-induced changes in the spinal cord was possible using SCT routines, that were optimized for the analysis of MPM maps. Using such routines, it was possible to assess the magnitude of neurodegeneration along the cervical SC, showing a gradient of neurodegeneration. The extent of neurodegeneration was more pronounced closer to the injury and directly correlated with the level of the injury and clinical impairments. Additionally, longitudinal processing workflow were optimized for MPM maps allowing the investigation of subtle time dependent changes induced by intensive motor training in healthy subjects. In conclusion, the studies of this work showed that tracking MPM changes might be used in clinical trials to investigate

neurodegenerative structural changes occurring after SCI and can potentially provide biomarkers of microstructural integrity in clinical diagnosis and monitoring of treatment and rehabilitation outcomes.

References

- Acosta-Cabronero, Julio, Carlos Milovic, Hendrik Mattern, Cristian Tejos, Oliver Speck, and Martina F. Callaghan. 2018. "A Robust Multi-Scale Approach to Quantitative Susceptibility Mapping." *NeuroImage* 183:7–24.
- Adams, Beth, Melvin Lee, Margaret Fahnstock, and Ronald J. Racine. 1997. "Long-Term Potentiation Trains Induce Mossy Fiber Sprouting." *Brain Research* 775(1–2):193–97.
- Adams, Raymond D. and Maria Salam-Adams. 1991. "Chronic Nontraumatic Diseases of the Spinal Cord." *Neurologic Clinics* 9(3):605–23.
- Ahuja, Christopher S., Jefferson R. Wilson, Satoshi Nori, Mark R. N. Kotter, Claudia Druschel, Armin Curt, and Michael G. Fehlings. 2017. "Traumatic Spinal Cord Injury." *Nature Reviews. Disease Primers* 3(2, Spinal Cord Disorders):17018.
- Al-Louzi, Omar, Julia Button, Scott D. Newsome, Peter A. Calabresi, and Shiv Saidha. 2017. "Retrograde Trans-Synaptic Visual Pathway Degeneration in Multiple Sclerosis: A Case Series." *Multiple Sclerosis (Houndmills, Basingstoke, England)* 23(7):1035–39.
- Albouy, Geneviève, Virginie Sterpenich, Evelyne Balteau, Gilles Vandewalle, Martin Desseilles, Thanh Dang-Vu, Annabelle Darsaud, Perrine Ruby, Pierre-Hervé Hervé Luppi, Christian Degueldre, Philippe Peigneux, André Luxen, and Pierre Maquet. 2008. "Both the Hippocampus and Striatum Are Involved in Consolidation of Motor Sequence Memory." *Neuron* 58(2):261–72.
- Albu, Sergiu, Julio Gomez-Soriano, Gerardo Avila-Martin, and Julian Taylor. 2015. "Deficient Conditioned Pain Modulation after Spinal Cord Injury Correlates with Clinical Spontaneous Pain Measures." *Pain* 156(2):260–72.
- Alonso-Ortiz, Eva, Ives R. Levesque, and G. Bruce Pike. 2018. "Impact of Magnetic Susceptibility Anisotropy at 3 T and 7 T on T2*-Based Myelin Water Fraction Imaging." *NeuroImage* 182:370–78.
- Apkarian, A. Vania, M. Catherine Bushnell, Rolf-Detlef Treede, and Jon-Kar Zubieta. 2005. "Human Brain Mechanisms of Pain Perception and Regulation in Health and Disease." *European Journal of Pain (London, England)* 9(4):463–84.
- Ashburner, J., J. Andersson, and K. J. Friston. 2000. "Image Registration Using a Symmetric Prior - in Three-Dimensions." *Human Brain Mapping* 9(4):212–25.
- Ashburner, J., J. L. Andersson, and K. J. Friston. 1999. "High-Dimensional Image Registration Using Symmetric Priors." *NeuroImage* 9(6 Pt 1):619–28.
- Ashburner, John. 2007. "A Fast Diffeomorphic Image Registration Algorithm." *Neuroimage*. 38(1):95–113.
- Ashburner, John and Karl J. Friston. 2005. "Unified Segmentation." 26:839–51.
- Ashburner, John and Gerard R. Ridgway. 2013. "Symmetric Diffeomorphic Modeling of Longitudinal Structural MRI." *Frontiers in Neuroscience* 6(FEB):1–19.

- Badea, Alexandra, Kwan L. Ng, Robert J. Anderson, Jiangyang Zhang, Michael I. Miller, and Richard J. O'Brien. 2019. "Magnetic Resonance Imaging of Mouse Brain Networks Plasticity Following Motor Learning." *PLoS ONE* 14(5):1–21.
- Balteau, Evelyne, Karsten Tabelow, John Ashburner, Martina F. Callaghan, Bogdan Draganski, Gunther Helms, Ferath Kherif, Tobias Leutritz, Antoine Lutti, Christophe Phillips, Enrico Reimer, Lars Ruthotto, Maryam Seif, Nikolaus Weiskopf, Gabriel Ziegler, and Siawoosh Mohammadi. 2018. "HMRI-A Toolbox for Using Quantitative MRI in Neuroscience and Clinical Research." (2527).
- Bareyre, Florence M., Martin Kerschensteiner, Olivier Raineteau, Thomas C. Mettenleiter, Oliver Weinmann, and Martin E. Schwab. 2004. "The Injured Spinal Cord Spontaneously Forms a New Intraspinal Circuit in Adult Rats." *Nature Neuroscience* 7(3):269–77.
- Barnabé-Heider, Fanie, Christian Göritz, Hanna Sabelström, Hirohide Takebayashi, Frank W. Pfrieger, Konstantinos Meletis, Jonas Frisen, Fanie Barnabe-Heider, Christian Goritz, Hanna Sabelstrom, Hirohide Takebayashi, Frank W. Pfrieger, Konstantinos Meletis, and Jonas Frisen. 2010. "Origin of New Glial Cells in Intact and Injured Adult Spinal Cord." *Cell Stem Cell* 7(4):470–82.
- Barnes, Josephine, Gerard R. Ridgway, Jonathan Bartlett, Susie M. D. Henley, Manja Lehmann, Nicola Hobbs, Matthew J. Clarkson, David G. MacManus, Sebastien Ourselin, and Nick C. Fox. 2010. "Head Size, Age and Gender Adjustment in MRI Studies: A Necessary Nuisance?" *NeuroImage* 53(4):1244–55.
- Bartzokis, George, Todd A. Tishler, Il-Seon Shin, Po H. Lu, and Jeffrey L. Cummings. 2004. "Brain Ferritin Iron as a Risk Factor for Age at Onset in Neurodegenerative Diseases." *Annals of the New York Academy of Sciences* 1012:224–236.
- Basbaum, A. I. and H. L. Fields. 1979. "The Origin of Descending Pathways in the Dorsolateral Funiculus of the Spinal Cord of the Cat and Rat: Further Studies on the Anatomy of Pain Modulation." *The Journal of Comparative Neurology* 187(3):513–31.
- Basu, Jayeeta and Steven A. Siegelbaum. 2015. "The Corticohippocampal Circuit, Synaptic Plasticity, and Memory." *Cold Spring Harbor Perspectives in Biology* 7(11).
- Beattie, M. S., J. C. Bresnahan, J. Komon, C. A. Tovar, M. Van Meter, D. K. Anderson, A. I. Faden, C. Y. Hsu, L. J. Noble, S. Salzman, and W. Young. 1997. "Endogenous Repair after Spinal Cord Contusion Injuries in the Rat." *Experimental Neurology* 148(2):453–63.
- Beauparlant, Janine, Rubia Van Den Brand, Quentin Barraud, Lucia Friedli, Pavel Musienko, Volker Dietz, and Grégoire Courtine. 2013. "Undirected Compensatory Plasticity Contributes to Neuronal Dysfunction after Severe Spinal Cord Injury." *Brain* 136(11):3347–61.
- Beirowski, Bogdan, Robert Adalbert, Diana Wagner, Daniela S. Grumme, Klaus Addicks, Richard R. Ribchester, and Michael P. Coleman. 2005. "The Progressive Nature of Wallerian Degeneration in Wild-Type and Slow Wallerian Degeneration (WldS) Nerves." *BMC Neuroscience* 6:1–27.
- Benarroch, E. E. 2012. "Periaqueductal Gray: An Interface for Behavioral Control." *Neurology* 78(3):210–17.
- Bengtsson, Sara L., Zoltán Nagy, Stefan Skare, Lea Forsman, Hans Forssberg, and Fredrik Ullén. 2005. "Extensive Piano Practicing Has Regionally Specific Effects on White Matter Development."

Nature Neuroscience 8(9):1148–50.

- Benjamini, Yoav and Yoel Hochberg. 1995. "Controlling the False Discovery Rate: A Practical and Powerful Approach to Multiple Testing." *Journal of the Royal Statistical Society: Series B (Methodological)* 57(1):289–300.
- Berman, Shai, Kathryn L. West, Mark D. Does, Jason D. Yeatman, and Aviv A. Mezer. 2018. "Evaluating G-Ratio Weighted Changes in the Corpus Callosum as a Function of Age and Sex." *NeuroImage* 182:304–13.
- Bermudez, Patrick, Jason P. Lerch, Alan C. Evans, and Robert J. Zatorre. 2009. "Neuroanatomical Correlates of Musicianship as Revealed by Cortical Thickness and Voxel-Based Morphometry." *Cerebral Cortex (New York, N.Y. : 1991)* 19(7):1583–96.
- Berry, M., W. L. Maxwell, A. Logan, A. Mathewson, P. McConnell, D. E. Ashhurst, and G. H. Thomas. 1983. "Deposition of Scar Tissue in the Central Nervous System." *Acta Neurochirurgica. Supplementum* 32:31–53.
- Bingel, Ulrike and Irene Tracey. 2008. "Imaging CNS Modulation of Pain in Humans." *Physiology (Bethesda, Md.)* 23:371–80.
- Blaiotta, Claudia, Patrick Freund, M. Jorge Cardoso, and John Ashburner. 2018b. "Generative Diffeomorphic Modelling of Large MRI Data Sets for Probabilistic Template Construction." *NeuroImage* 166:117–34.
- Blaiotta, Claudia, M. Jorge Cardoso, and John Ashburner. 2016. "Variational Inference for Medical Image Segmentation." *Computer Vision and Image Understanding* 151:14–28.
- Blakemore, W. F. 1974. "Remyelination of the Superior Cerebellar Peduncle in Old Mice Following Demyelination Induced by Cuprizone." *Journal of the Neurological Sciences* 22(1):121–26.
- Blight, A. R. and V. Decrescito. 1986. "Morphometric Analysis of Experimental Spinal Cord Injury in the Cat: The Relation of Injury Intensity to Survival of Myelinated Axons." *Neuroscience* 19(1):321–41.
- Bloch, F. 1946. "Nuclear Induction." *Physical Review* 70(7–8):460–74.
- Bloembergen, N., E. M. Purcell, and R. V. Pound. 1948. "Relaxation Effects in Nuclear Magnetic Resonance Absorption." *Phys. Rev.* 73(7):679–712.
- Borsook, David, Jaymin Upadhyay, Eric H. Chudler, and Lino Becerra. 2010. "A Key Role of the Basal Ganglia in Pain and Analgesia--Insights Gained through Human Functional Imaging." *Molecular Pain* 6:27.
- Boulenguez, Pascale, Sylvie Liabeuf, Rémi Bos, Hélène Bras, Céline Jean-Xavier, Cécile Brocard, Aurélie Stil, Pascal Darbon, Daniel Cattaert, Eric Delpire, Martin Marsala, and Laurent Vinay. 2010. "Down-Regulation of the Potassium-Chloride Cotransporter KCC2 Contributes to Spasticity after Spinal Cord Injury." *Nature Medicine* 16(3):302–7.
- Bozzo, Anthony, Judith Marcoux, Mohan Radhakrishna, Julie Pelletier, and Benoit Goulet. 2011a. "The Role of Magnetic Resonance Imaging in the Management of Acute Spinal Cord Injury." *Journal of*

- Neurotrauma* 28(8):1401–11.
- Bozzo, Anthony, Judith Marcoux, Mohan Radhakrishna, Julie Pelletier, and Benoit Goulet. 2011b. "The Role of Magnetic Resonance Imaging in the Management of Acute Spinal Cord Injury." *Journal of Neurotrauma* 28(8):1401–11.
- Bradbury, Elizabeth J. and Stephen B. McMahon. 2006. "Spinal Cord Repair Strategies: Why Do They Work?" *Nature Reviews. Neuroscience* 7(8):644–53.
- Brown, Mark, Richard Semelka, and Thomas Nishino. 2004. "MRI: Basic Principles and Applications." *Medical Physics* 31:170.
- Bruehlmeier, M., V. Dietz, K. L. Leenders, U. Roelcke, J. Missimer, A. Curt, P. E. T. Program, and Ch-Villigen. 1998. "SHORT COMMUNICATION How Does the Human Brain Deal with a Spinal Cord Injury?" 10(June):3918–22.
- Brun, Vegard Heimly, Stefan Leutgeb, Hui-Qiu Wu, Robert Schwarcz, Menno P. Witter, Edvard I. Moser, and May-Britt Moser. 2008. "Impaired Spatial Representation in CA1 after Lesion of Direct Input from Entorhinal Cortex." *Neuron* 57(2):290–302.
- Bryce, T. N., F. Biering-Sørensen, N. B. Finnerup, D. D. Cardenas, R. Defrin, T. Lundeberg, C. Norrbrink, J. S. Richards, P. Siddall, T. Stripling, R. D. Treede, S. G. Waxman, E. Widerström-Noga, R. P. Yezierski, and M. Dijkers. 2012. "International Spinal Cord Injury Pain Classification: Part I. Background and Description." *Spinal Cord* 50(6):413–17.
- Bunge, RP, WR Puckett, JL Becerra, A. Marcillo, and RM Quencer. 1993. "Observations on the Pathology of Human Spinal Cord Injury. A Review and Classification of 22 New Cases with Details from a Case of Chronic Cord Compression with Extensive Focal Demyelination." *Neurology Advance* 59:75–89.
- Burke, D., B. M. Fullen, D. Stokes, and O. Lennon. 2017. "Neuropathic Pain Prevalence Following Spinal Cord Injury: A Systematic Review and Meta-Analysis." *European Journal of Pain* 21(1):29–44.
- Burns, S. P., D. G. Golding, W. A. Jr Rolle, V. Graziani, and J. F. Jr Ditunno. 1997. "Recovery of Ambulation in Motor-Incomplete Tetraplegia." *Archives of Physical Medicine and Rehabilitation* 78(11):1169–72.
- Buss, Armin, G. A. Brook, B. Kakulas, D. Martin, R. Franzen, J. Schoenen, J. Noth, and A. B. Schmitt. 2004. "Gradual Loss of Myelin and Formation of an Astrocytic Scar during Wallerian Degeneration in the Human Spinal Cord." *Brain* 127(1):34–44.
- Buss, Armin, K. Pech, D. Merkler, B. A. Kakulas, D. Martin, J. Schoenen, J. Noth, M. E. Schwab, and G. A. Brook. 2005. "Sequential Loss of Myelin Proteins during Wallerian Degeneration in the Human Spinal Cord." *Brain* 128(2):356–64.
- Cachier, Pascal and David Rey. 2000. "Symmetrization of the Non-Rigid Registration Problem Using Inversion-Invariant Energies: Application to Multiple Sclerosis BT - Medical Image Computing and Computer-Assisted Intervention – MICCAI 2000." Pp. 472–81 in *Lecture Notes in Computer Science (including subseries Lecture Notes in Artificial Intelligence and Lecture Notes in*

Bioinformatics). Vol. 1935, edited by S. L. Delp, A. M. DiGoia, and B. Jaramaz. Berlin, Heidelberg: Springer Berlin Heidelberg.

- Calhoun, V. D., T. Adali, G. D. Pearlson, and J. J. Pekar. 2001. "A Method for Making Group Inferences from Functional MRI Data Using Independent Component Analysis." *Hum.Brain Mapp.* 14(3):140–51.
- Callaghan, M. F., P. Freund, Draganski, E. Anderson, M. Cappelletti, R. Chowdhury, J. Diedrichsen, T. H. B. FitzGerald, P. Smittenaar, G. Helms, A. Lutti, and N. Weiskopf. 2014. "Widespread Age-Related Differences in the Human Brain Microstructure Revealed by Quantitative Magnetic Resonance Imaging." *Neurobiology of Aging* 35(8):1862–72.
- Callaghan, Martina F, Gunther Helms, Antoine Lutti, Siawoosh Mohammadi, and Nikolaus Weiskopf. 2015. "A General Linear Relaxometry Model of R 1 Using Imaging Data." *Magnetic Resonance in Medicine* 73(3):1309–14.
- Callaghan, Martina F., Oliver Josephs, Michael Herbst, Maxim Zaitsev, Nick Todd, and Nikolaus Weiskopf. 2015. "An Evaluation of Prospective Motion Correction (PMC) for High Resolution Quantitative MRI." *Frontiers in Neuroscience* 9(MAR):1–9.
- Callaghan, Martina F., Siawoosh Mohammadi, and Nikolaus Weiskopf. 2016. "Synthetic Quantitative MRI through Relaxometry Modelling." *NMR in Biomedicine* 29(12):1729–38.
- Campbell, Jennifer S. W., Ilana R. Leppert, Sridar Narayanan, Mathieu Boudreau, Tanguy Duval, Julien Cohen-Adad, G. Bruce Pike, and Nikola Stikov. 2017. "Promise and Pitfalls of G-Ratio Estimation with MRI." *NeuroImage*.
- Caroni, Pico, Ananya Chowdhury, and Maria Lahr. 2014. "Synapse Rearrangements upon Learning: From Divergent-Sparse Connectivity to Dedicated Sub-Circuits." *Trends in Neurosciences* 37(10):604–14.
- Catz, A., M. Itzkovich, L. Tesio, F. Biering-Sorensen, C. Weeks, M. T. Laramee, B. C. Craven, M. Tonack, S. L. Hitzig, E. Glaser, G. Zeilig, S. Aito, G. Scivoletto, M. Mecci, R. J. Chadwick, W. S. El Masry, A. Osman, C. a Glass, P. Silva, B. M. Soni, B. P. Gardner, G. Savic, E. M. Bergström, V. Bluvshstein, and J. Ronen. 2007. "A Multicenter International Study on the Spinal Cord Independence Measure, Version III: Rasch Psychometric Validation." *Spinal Cord* 45(4):275–91.
- Chen, Jerry L., David J. Margolis, Atanas Stankov, Lazar T. Sumanovski, Bernard L. Schneider, and Fritjof Helmchen. 2015. "Pathway-Specific Reorganization of Projection Neurons in Somatosensory Cortex during Learning." *Nature Neuroscience* 18(8):1101–8.
- Chen, Xin, Lu Wan, Wen Qin, Weimin Zheng, Zhigang Qi, Nan Chen, and Kuncheng Li. 2016. "Functional Preservation and Reorganization of Brain during Motor Imagery in Patients with Incomplete Spinal Cord Injury: A Pilot fMRI Study." *Frontiers in Human Neuroscience* 10(February):46.
- Chung, Sohae, Daniel Kim, Elodie Breton, and Leon Axel. 2010. "Rapid B1+ Mapping Using a Preconditioning RF Pulse with TurboFLASH Readout." *Magnetic Resonance in Medicine* 64(2):439–46.
- Cohen-adad, J. 2018. "Microstructural Imaging in the Spinal Cord and Validation Strategies." *NeuroImage* (September 2017):1–15.

- Cohen-Adad, J., M. M. El Mendili, S. Lehericy, P. F. Pradat, S. Blancho, S. Rossignol, and H. Benali. 2011. "Demyelination and Degeneration in the Injured Human Spinal Cord Detected with Diffusion and Magnetization Transfer MRI." *NeuroImage* 55(3):1024–33.
- Cohen-Adad, Julien. and Claudia A. M. Wheeler-Kingshott. 2014. *Quantitative MRI of the Spinal Cord*. 1st ed. Elsevier.
- Colloca, Luana, Taylor Ludman, Didier Bouhassira, Ralf Baron, Anthony H. Dickenson, David Yarnitsky, Roy Freeman, Andrea Truini, Nadine Attal, Nanna B. Finnerup, Christopher Eccleston, Eija Kalso, David L. Bennett, Robert H. Dworkin, and Srinivasa N. Raja. 2017. "Neuropathic Pain." *Nature Reviews Disease Primers* 3(1):17002.
- Connor, J. R. and S. L. Menzies. 1996. "Relationship of Iron to Oligodendrocytes and Myelination." *Glia* 17(2):83–93.
- Connor, J. R., S. L. Menzies, S. M. St Martin, and E. J. Mufson. 1990. "Cellular Distribution of Transferrin, Ferritin, and Iron in Normal and Aged Human Brains." *Journal of Neuroscience Research* 27(4):595–611.
- Cripps, R. A., B. B. Lee, P. Wing, E. Weerts, J. MacKay, and D. Brown. 2011. "A Global Map for Traumatic Spinal Cord Injury Epidemiology: Towards a Living Data Repository for Injury Prevention." *Spinal Cord* 49(4):493–501.
- Curt, A. and V. Dietz. 1996. "Traumatic Cervical Spinal Cord Injury: Relation between Somatosensory Evoked Potentials, Neurological Deficit, and Hand Function." *Archives of Physical Medicine and Rehabilitation* 77(1):48–53.
- Curt, A. and V. Dietz. 1999. "Electrophysiological Recordings in Patients with Spinal Cord Injury: Significance for Predicting Outcome." *Spinal Cord* 37(3):157–65.
- Curt, Armin, Hubertus J. A. Van Hedel, Daniel Klaus, and Volker Dietz. 2008. "Recovery from a Spinal Cord Injury: Significance of Compensation, Neural Plasticity, and Repair." *Journal of Neurotrauma* 25(6):677–85.
- Dancause, Numa, Scott Barbay, Shawn B. Frost, Erik J. Plautz, Daofen Chen, Elena V Zoubina, Ann M. Stowe, and Randolph J. Nudo. 2005. "Extensive Cortical Rewiring after Brain Injury." *The Journal of Neuroscience : The Official Journal of the Society for Neuroscience* 25(44):10167–79.
- Daniel, P. M. and Sabina J. Strich. 1969. "Histological Observations on Wallerian Degeneration in the Spinal Cord of the Baboon, Papio Papio." *Acta Neuropathologica* 12(4):314–28.
- David, Gergely, Maryam Seif, Eveline Huber, Markus Hupp, Jan Rosner, Volker Dietz, Nikolaus Weiskopf, Siawoosh Mohammadi, and Patrick Freund. 2019. "In Vivo Evidence of Remote Neural Degeneration in the Lumbar Enlargement after Cervical Injury." *Neurology* 92(12):e1367–77.
- Dayan, Eran and Leonardo G. Cohen. 2011. "Neuroplasticity Subservicing Motor Skill Learning." *Neuron* 72(3):443–54.
- Debarnot, Ursula, Chieko Huber, Aymeric Guillot, and Sophie Schwartz. 2018. "Sensorimotor Representation and Functional Motor Changes Following Short-Term Arm Immobilization." *Behavioral Neuroscience* 132(6):595–603.

- Deng, Feng, Ling Zhao, Chunlei Liu, Min Lu, Shufei Zhang, Huiyuan Huang, Lixiang Chen, Xiaoyan Wu, Chen Niu, Yuan He, Jun Wang, and Ruiwang Huang. 2018. "Plasticity in Deep and Superficial White Matter: A DTI Study in World Class Gymnasts." *Brain Structure & Function* 223(4):1849–62.
- Deng, Wei, Michael D. Saxe, Iryna S. Gallina, and Fred H. Gage. 2009. "Adult-Born Hippocampal Dentate Granule Cells Undergoing Maturation Modulate Learning and Memory in the Brain." *The Journal of Neuroscience : The Official Journal of the Society for Neuroscience* 29(43):13532–42.
- Deoni, Sean C. L., Terry M. Peters, and Brian K. Rutt. 2005. "High-Resolution T1 and T2 Mapping of the Brain in a Clinically Acceptable Time with DESPOT1 and DESPOT2." *Magnetic Resonance in Medicine* 53(1):237–41.
- Deoni, Sean C.L., Steven C. R. Williams, Peter Jezzard, John Suckling, Declan G. M. Murphy, and Derek K. Jones. 2008. "Standardized Structural Magnetic Resonance Imaging in Multicentre Studies Using Quantitative T1 and T2 Imaging at 1.5 T." *NeuroImage* 40(2):662–71.
- Deoni, Sean C L, Steven C. R. Williams, Peter Jezzard, John Suckling, Declan G. M. Murphy, and Derek K. Jones. 2008. "Standardized Structural Magnetic Resonance Imaging in Multicentre Studies Using Quantitative T1 and T2 Imaging at 1.5 T." *NeuroImage* 40(2):662–71.
- Diaz, Eric and Humberto Morales. 2016. "Spinal Cord Anatomy and Clinical Syndromes." *Seminars in Ultrasound, CT and MRI* 37(5):360–71.
- Dick, Frederic, Adam Taylor Tierney, Antoine Lutti, Oliver Josephs, Martin I. Sereno, and Nikolaus Weiskopf. 2012. "In Vivo Functional and Myeloarchitectonic Mapping of Human Primary Auditory Areas." *Journal of Neuroscience* 32(46):16095–105.
- Dietz, V. 2010. "Behavior of Spinal Neurons Deprived of Supraspinal Input." *Nat.Rev.Neurol.* 6(3):167–74.
- Dietz, Volker and Karim Fouad. 2014. "Restoration of Sensorimotor Functions after Spinal Cord Injury." *Brain* 137(3):654–67.
- Dobkin, Bruce H. 2004. "Neurobiology of Rehabilitation." *Annals of the New York Academy of Sciences* 1038:148–70.
- Does, Mark D. 2018. "Inferring Brain Tissue Composition and Microstructure via MR Relaxometry." *NeuroImage* 182(December 2017):136–48.
- Mac Donald, Christine L., Krikor Dikranian, Philip Bayly, David Holtzman, and David Brody. 2007. "Diffusion Tensor Imaging Reliably Detects Experimental Traumatic Axonal Injury and Indicates Approximate Time of Injury." *The Journal of Neuroscience : The Official Journal of the Society for Neuroscience* 27(44):11869–76.
- Dong, Willie K. and William T. Greenough. 2004. "Plasticity of Nonneuronal Brain Tissue: Roles in Developmental Disorders." *Mental Retardation and Developmental Disabilities Research Reviews* 10(2):85–90.
- Dowell, Nicholas G., Thomas M. Jenkins, Olga Ciccarelli, David H. Miller, and Claudia A. M. M. Wheeler-Kingshott. 2009. "Contiguous-Slice Zonally Oblique Multislice (CO-ZOOM) Diffusion Tensor Imaging: Examples of in Vivo Spinal Cord and Optic Nerve Applications." *Journal of Magnetic*

Resonance Imaging 29(2):454–60.

- Draganski, B, J. Ashburner, C. Hutton, F. Kherif, R. S. Frackowiak, G. Helms, and N. Weiskopf. 2011. "Regional Specificity of MRI Contrast Parameter Changes in Normal Ageing Revealed by Voxel-Based Quantification (VBQ)." *Neuroimage* Volume 55(Issue 4):1423–34.
- Draganski, B, J. Ashburner, C. Hutton, F. Kherif, R. S. J. Frackowiak, G. Helms, and N. Weiskopf. 2011. "NeuroImage Regional Specificity of MRI Contrast Parameter Changes in Normal Ageing Revealed by Voxel-Based Quantification (VBQ)." *NeuroImage* 55(4):1423–34.
- Draganski, B. and A. May. 2008. "Training-Induced Structural Changes in the Adult Human Brain." *Behavioural Brain Research* 192(1):137–42.
- Draganski, B, T. Moser, N. Lummel, S. Ga, U. Bogdahn, F. Haas, and A. May. 2006. "Decrease of Thalamic Gray Matter Following Limb Amputation." 31:951–57.
- Draganski, Bogdan, Christian Gaser, Volker Busch, Gerhard Schuierer, Ulrich Bogdahn, and Arne May. 2004. "Changes in Grey Matter Induced by Training." *Nature* 427(6972):311–12.
- Draganski, Bogdan, Christian Gaser, Gerd Kempermann, H. Georg Kuhn, Jurgen Winkler, Christian Buchel, and Arne May. 2006. "Temporal and Spatial Dynamics of Brain Structure Changes during Extensive Learning." *The Journal of Neuroscience: The Official Journal of the Society for Neuroscience* 26(23):6314–17.
- Duff, Susan, Michael G. Fehlings, Sukhvinder Kalsi-Ryan, Milos R. Popovic, Claudia Rudhe, Dorcas Beaton, Armin Curt, and Mary C. Verrier. 2011. "The Graded Redefined Assessment of Strength Sensibility and Prehension: Reliability and Validity." *Journal of Neurotrauma* 29(5):905–14.
- van Duijn, Sara, Marjolein Bulk, Sjoerd G. van Duinen, Rob J. A. Nabuurs, Mark A. van Buchem, Louise van der Weerd, and Remco Natté. 2017. "Cortical Iron Reflects Severity of Alzheimer's Disease." *Journal of Alzheimer's Disease: JAD* 60(4):1533–45.
- Dumont, R. J., D. O. Okonkwo, S. Verma, R. J. Hurlbert, P. T. Boulos, D. B. Ellegala, and A. S. Dumont. 2001. "Acute Spinal Cord Injury, Part I: Pathophysiologic Mechanisms." *Clinical Neuropharmacology* 24(5):254–64.
- Duncan, Katherine, Nicholas Ketz, Souheil J. Inati, and Lila Davachi. 2012. "Evidence for Area CA1 as a Match/Mismatch Detector: A High-Resolution FMRI Study of the Human Hippocampus." *Hippocampus* 22(3):389–98.
- Dupont, Sara M., Benjamin De Leener, Manuel Taso, Arnaud Le Troter, Sylvie Nadeau, Nikola Stikov, Virginie Callot, and Julien Cohen-Adad. 2017. "Fully-Integrated Framework for the Segmentation and Registration of the Spinal Cord White and Gray Matter." *NeuroImage* 150(June 2016):358–72.
- Dusart, I. and M. E. Schwab. 1994. "Secondary Cell Death and the Inflammatory Reaction after Dorsal Hemisection of the Rat Spinal Cord." *Eur.J.Neurosci.* 6(5):712–24.
- Duval, T., S. Le Vy, N. Stikov, J. Campbell, A. Mezer, T. Witzel, B. Keil, V. Smith, L. L. Wald, E. Klawiter, and J. Cohen-Adad. 2017. "G-Ratio Weighted Imaging of the Human Spinal Cord in Vivo." *NeuroImage* 145(Pt A):11–23.

- Edwards, Luke J., Evgeniya Kirilina, Siawoosh Mohammadi, and Nikolaus Weiskopf. 2018. "Microstructural Imaging of Human Neocortex in Vivo." *NeuroImage* 182(February):184–206.
- Eickhoff, Simon B., Tomas Paus, Svenja Caspers, Marie Helene Grosbras, Alan C. Evans, Karl Zilles, and Katrin Amunts. 2007. "Assignment of Functional Activations to Probabilistic Cytoarchitectonic Areas Revisited." *NeuroImage* 36(3):511–21.
- Ellerbrock, Isabel and Siawoosh Mohammadi. 2018a. "Four in Vivo G-Ratio-Weighted Imaging Methods: Comparability and Repeatability at the Group Level." *Human Brain Mapping* 39(1):24–41.
- Eriksson, PS and E. Perfilieva. 1998. "Neurogenesis in the Adult Human Hippocampus." *Nature Medicine* 4(11):1313–17.
- Ernst, R. R. and W. A. Anderson. 1966. "Application of Fourier Transform Spectroscopy to Magnetic Resonance." *Review of Scientific Instruments* 37(1):93–102.
- Evans, A. C., S. Marrett, P. Neelin, L. Collins, K. Worsley, W. Dai, S. Milot, E. Meyer, and D. Bub. 1992. "Anatomical Mapping of Functional Activation in Stereotactic Coordinate Space." *NeuroImage* 1(1):43–53.
- Fatouros, P. P. and A. Marmarou. 1999. "Use of Magnetic Resonance Imaging for in Vivo Measurements of Water Content in Human Brain: Method and Normal Values." *Journal of Neurosurgery* 90(1):109–15.
- Fehlings, Michael G. and Charles H. Tator. 1995. "The Relationships among the Severity of Spinal Cord Injury, Residual Neurological Function, Axon Counts, and Counts of Retrogradely Labeled Neurons after Experimental Spinal Cord Injury." *Experimental Neurology* 132(2):220–28.
- Fehlings, Michael G., Lindsay A. Tetreault, Jefferson R. Wilson, Brian K. Kwon, Anthony S. Burns, Allan R. Martin, Gregory Hawryluk, and James S. Harrop. 2017. "A Clinical Practice Guideline for the Management of Acute Spinal Cord Injury: Introduction, Rationale, and Scope." *Global Spine Journal* 7(3_supplement):84S-94S.
- Fields, R. Douglas. 2008. "White Matter in Learning, Cognition and Psychiatric Disorders." *Trends in Neurosciences* 31(7):361–70.
- Fields, R. Douglas. 2015. "A New Mechanism of Nervous System Plasticity: Activity-Dependent Myelination." *Nature Reviews. Neuroscience* 16(12):756–67.
- Figley, C. R. and P. W. Stroman. 2007. "Investigation of Human Cervical and Upper Thoracic Spinal Cord Motion: Implications for Imaging Spinal Cord Structure and Function." *Magnetic Resonance in Medicine* 58(1):185–89.
- Finnerup, N. B. and T. S. Jensen. 2004. "Spinal Cord Injury Pain--Mechanisms and Treatment." *European Journal of Neurology* 11(2):73–82.
- Finsterbusch, Jürgen. 2009. "High-Resolution Diffusion Tensor Imaging with Inner Field-of-View EPI." *Journal of Magnetic Resonance Imaging : JMRI* 29(4):987–93.
- Flandin, Guillaume and Karl J. Friston. 2016. "Analysis of Family-Wise Error Rates in Statistical

Parametric Mapping Using Random Field Theory." 1–4.

- Florence, S. L., H. B. Taub, and J. H. Kaas. 1998. "Large-Scale Sprouting of Cortical Connections after Peripheral Injury in Adult Macaque Monkeys." *Science (New York, N.Y.)* 282(5391):1117–21.
- Fonov, Vladimir, Alan C. Evans, Kelly Botteron, C. Robert Almli, Robert C. McKinsty, and D. Louis Collins. 2011. "Unbiased Average Age-Appropriate Atlases for Pediatric Studies." *NeuroImage* 54(1):313–27.
- Frens and P. C. LAUTERBUR. 1973. "Image Formation by Induced Local Interactions: Examples Employing Nuclear Magnetic Resonance." *Nature* 242(5394):190–91.
- Freund, Patrick., THIERRY Wannier, ERIC Schmidlin, JOCELYNE Bloch, ANIS Mir, Martin E. M. E. E. Schwab, Rouiller Eric M., and E. M. M. Rouiller. 2007. "Anti-Nogo-A Antibody Treatment Enhances Sprouting of Corticospinal Axons Rostral to a Unilateral Cervical Spinal Cord Lesion in Adult Macaque Monkey." *Comparative and General Pharmacology* 1156(August 2006):1138–56.
- Freund, Patrick, Karl Friston, Alan J. Thompson, Klaas E. Stephan, John Ashburner, Dominik R. Bach, Zoltan Nagy, Gunther Helms, Bogdan Draganski, Siawoosh Mohammadi, Martin E. Schwab, Armin Curt, and Nikolaus Weiskopf. 2016. "Embodied Neurology : An Integrative Framework for Neurological Disorders." 1855–61.
- Freund, Patrick, Maryam Seif, Nikolaus Weiskopf, Karl Friston, Michael G. Fehlings, Alan J. Thompson, and Armin Curt. 2019a. "MRI in Traumatic Spinal Cord Injury: From Clinical Assessment to Neuroimaging Biomarkers." *The Lancet Neurology* 18(12):1123–35.
- Freund, Patrick, Maryam Seif, Nikolaus Weiskopf, Karl Friston, Michael G. Fehlings, Alan J. Thompson, and Armin Curt. 2019b. "MRI in Traumatic Spinal Cord Injury: From Clinical Assessment to Neuroimaging Biomarkers." *The Lancet Neurology* 18(12):1123–35.
- Freund, Patrick, Nikolaus Weiskopf, John Ashburner, Katharina Wolf, Reto Sutter, Daniel R. Altmann, Prof Karl Friston, Alan Thompson, and Armin Curt. 2013. "MRI Investigation of the Sensorimotor Cortex and the Corticospinal Tract after Acute Spinal Cord Injury: A Prospective Longitudinal Study." *The Lancet Neurology* 12(9):873–81.
- Freund, Patrick, Nikolaus Weiskopf, Nick S. Ward, Chloe Hutton, Angela Gall, Olga Ciccarelli, Michael Craggs, Karl Friston, and Alan J. Thompson. 2011. "Disability, Atrophy and Cortical Reorganization Following Spinal Cord Injury." *BRAIN A JOURNAL OF NEUROLOGY* Brain 1610–22.
- Friston, K. J., K. J. Worsley, R. S. Frackowiak, J. C. Mazziotta, and A. C. Evans. 1994. "Assessing the Significance of Focal Activations Using Their Spatial Extent." *Human Brain Mapping* 1(3):210–20.
- Fu, Min and Yi Zuo. 2011. "Experience-Dependent Structural Plasticity in the Cortex." *Trends in Neurosciences* 34(4):177–87.
- Fukunaga, Masaki, Tie-Qiang Li, Peter van Gelderen, Jacco A. de Zwart, Karin Shmueli, Bing Yao, Jongho Lee, Dragan Maric, Maria A. Aronova, Guofeng Zhang, Richard D. Leapman, John F. Schenck, Hellmut Merkle, and Jeff H. Duyn. 2010. "Layer-Specific Variation of Iron Content in Cerebral Cortex as a Source of MRI Contrast." *Proceedings of the National Academy of Sciences of the United States of America* 107(8):3834–39.

- Fullerton, G. D., J. L. Potter, and N. C. Dornbluth. 1982. "NMR Relaxation of Protons in Tissues and Other Macromolecular Water Solutions." *Magnetic Resonance Imaging* 1(4):209–26.
- Gaser, Christian and Gottfried Schlaug. 2003. "Brain Structures Differ between Musicians and Non-Musicians." *The Journal of Neuroscience* 23(27):9240–45.
- Gensel, John C. and Bei Zhang. 2015. "Macrophage Activation and Its Role in Repair and Pathology after Spinal Cord Injury." *Brain Research* 1619:1–11.
- Ghadery, Christine, Lukas Pirpamer, Edith Hofer, Christian Langkammer, Katja Petrovic, Marisa Loitfelder, Petra Schwingenschuh, Stephan Seiler, Marco Duering, Eric Jouvent, Helena Schmidt, Franz Fazekas, Jean-Francois Mangin, Hugues Chabriat, Martin Dichgans, Stefan Ropele, and Reinhold Schmidt. 2015. "R2* Mapping for Brain Iron: Associations with Cognition in Normal Aging." *Neurobiology of Aging* 36(2):925–32.
- Gibson, Erin M., David Purger, Christopher W. Mount, Andrea K. Goldstein, Grant L. Lin, Lauren S. Wood, Ingrid Inema, Sarah E. Miller, Gregor Bieri, J. Bradley Zuchero, Ben A. Barres, Pamelyn J. Woo, Hannes Vogel, and Michelle Monje. 2014. "Neuronal Activity Promotes Oligodendrogenesis and Adaptive Myelination in the Mammalian Brain." *Science (New York, N.Y.)* 344(6183):1252304.
- Giedd, J. N., J. Blumenthal, N. O. Jeffries, F. X. Castellanos, H. Liu, A. Zijdenbos, T. Paus, A. C. Evans, and J. L. Rapoport. 1999. "Brain Development during Childhood and Adolescence: A Longitudinal MRI Study." *Nature Neuroscience* 10(2):861–63.
- Good, Catriona D., Ingrid S. Johnsrude, John Ashburner, Richard N. A. Henson, Karl J. Friston, and Richard S. J. Frackowiak. 2001. "A Voxel-Based Morphometric Study of Ageing in 465 Normal Adult Human Brains." *NeuroImage* 14(1 I):21–36.
- Goto, Noboru and Naruhito Otsuka. 1997. "Development and Anatomy of the Spinal Cord." *Neuropathology* 17(1):25–31.
- Gould, Elizabeth, AJ Reeves, MSA Graziano, and CG Gross. 1999. "Neurogenesis in the Neocortex of Adult Primates." *Science* 286(October):548–52.
- Grabher, Patrick, Martina F. M. F. Martina F. Callaghan, John Ashburner, Nikolaus Weiskopf, A. J. Alan J. Thompson, Armin Curt, and Patrick Freund. 2015. "Tracking Sensory System Atrophy and Outcome Prediction in Spinal Cord Injury." *Annals of Neurology* 78(5):751–61.
- Granert, Oliver, Martin Peller, Christian Gaser, Sergiu Groppa, Mark Hallett, Arne Knutzen, Günther Deuschl, Kirsten E. Zeuner, and Hartwig R. Siebner. 2011. "Manual Activity Shapes Structure and Function in Contralateral Human Motor Hand Area." *NeuroImage* 54(1):32–41.
- Green, J. B., E. Sora, Y. Bialy, A. Ricamato, and R. W. Thatcher. 1999. "Cortical Motor Reorganization after Paraplegia: An EEG Study." *Neurology* 53(4):736–43.
- van Groen, T. and J. M. Wyss. 1990. "Extrinsic Projections from Area CA1 of the Rat Hippocampus: Olfactory, Cortical, Subcortical, and Bilateral Hippocampal Formation Projections." *The Journal of Comparative Neurology* 302(3):515–28.
- Groppa, S., A. Oliviero, A. Eisen, A. Quartarone, L. G. Cohen, V. Mall, A. Kaelin-Lang, T. Mima, S. Rossi, G. W. Thickbroom, P. M. Rossini, U. Ziemann, J. Valls-Solé, and H. R. Siebner. 2012. "A Practical

- Guide to Diagnostic Transcranial Magnetic Stimulation: Report of an IFCN Committee." *Clinical Neurophysiology: Official Journal of the International Federation of Clinical Neurophysiology* 123(5):858–82.
- Grumbles, Robert M. and Christine K. Thomas. 2017. "Motoneuron Death after Human Spinal Cord Injury." *Journal of Neurotrauma* 34(3):581–90.
- Guo, Yumei, Zhuo Wang, Sandhya Prathap, and Daniel P. Holschneider. 2017. "Recruitment of Prefrontal-Striatal Circuit in Response to Skilled Motor Challenge." *Neuroreport* 28(18):1187–94.
- Gupta, Cota Navin, Jessica A. Turner, and Vince D. Calhoun. 2019. "Source-Based Morphometry: A Decade of Covarying Structural Brain Patterns." *Brain Structure and Function* 224(9):3031–44.
- Gustin, S. M., P. J. Wrigley, P. J. Siddall, and L. A. Henderson. 2009. "Brain Anatomy Changes Associated with Persistent Neuropathic Pain Following Spinal Cord Injury." *Cereb.Cortex*.
- Gustin, S. M., P. J. Wrigley, A. M. Youssef, L. McIndoe, S. L. Wilcox, C. D. Rae, R. A. E. Edden, P. J. Siddall, and L. A. Henderson. 2014. "Thalamic Activity and Biochemical Changes in Individuals with Neuropathic Pain after Spinal Cord Injury." *Pain* 155(5):1027–36.
- Gustin, Sylvia M., Chris C. Peck, Sophie L. Wilcox, Paul G. Nash, Greg M. Murray, and Luke A. Henderson. 2011. "Different Pain, Different Brain: Thalamic Anatomy in Neuropathic and Non-Neuropathic Chronic Pain Syndromes." *The Journal of Neuroscience: The Official Journal of the Society for Neuroscience* 31(16):5956–64.
- Harlow, Danielle E., Justin M. Honce, and Augusto A. Miravalle. 2015. "Remyelination Therapy in Multiple Sclerosis." *Frontiers in Neurology* 6(DEC):1–13.
- Harrison, B. M. and W. I. McDonald. 1977. "Remyelination after Transient Experimental Compression of the Spinal Cord." *Annals of Neurology* 1(6):542–51.
- Hebb, D. O. 1949. "Organization of Behavior." *New York: Wiley* 6(3):335.
- Helms, Gunther, Henning Dathe, and Peter Dechent. 2008. "Quantitative FLASH MRI at 3T Using a Rational Approximation of the Ernst Equation." *Magnetic Resonance in Medicine* 59(3):667–72.
- Helms, Gunther, Henning Dathe, Kai Kallenberg, and Peter Dechent. 2008a. "High-Resolution Maps of Magnetization Transfer with Inherent Correction for RF Inhomogeneity and T1 Relaxation Obtained from 3D FLASH MRI." *Magnetic Resonance in Medicine* 60(6):1396–1407.
- Helms, Gunther, Henning Dathe, Kai Kallenberg, and Peter Dechent. 2008b. "High-Resolution Maps of Magnetization Transfer with Inherent Correction for RF Inhomogeneity and T1 Relaxation Obtained from 3D FLASH MRI." *Magnetic Resonance in Medicine: Official Journal of the Society of Magnetic Resonance in Medicine / Society of Magnetic Resonance in Medicine* 60(6):1396–1407.
- Helms, Gunther, Bogdan Draganski, Richard Frackowiak, John Ashburner, and Nikolaus Weiskopf. 2009. "NeuroImage Improved Segmentation of Deep Brain Grey Matter Structures Using Magnetization Transfer (MT) Parameter Maps." *NeuroImage* 47(1):194–98.
- Henderson, Luke A., Chris C. Peck, Esben T. Petersen, Caroline D. Rae, Andrew M. Youssef, Jenna M.

- Reeves, Sophie L. Wilcox, Rahena Akhter, Greg M. Murray, and Sylvia M. Gustin. 2013. "Chronic Pain: Lost Inhibition?" *The Journal of Neuroscience: The Official Journal of the Society for Neuroscience* 33(17):7574–82.
- Hendrix, Abernethy, Sloane, Misuraca, & Moore. 2013. "Correlation between Electrophysiological Properties, Morphological Maturation, and Olig Gene Changes during Postnatal Motor Tract Development Jun." *Bone* 23(1):1–7.
- Hofer, Sonja B, Thomas D. Mrsic-Flogel, Tobias Bonhoeffer, and Mark Hübener. 2009. "Experience Leaves a Lasting Structural Trace in Cortical Circuits." *Nature* 457(7227):313–17.
- Hofer, Sonja B., Thomas D. Mrsic-Flogel, Tobias Bonhoeffer, and Mark Hübener. 2009. "Experience Leaves a Lasting Structural Trace in Cortical Circuits." *Nature* 457(7227):313–17.
- Hofstetter, Shir, Ido Tavor, Shimrit Tzur Moryosef, and Yaniv Assaf. 2013. "Short-Term Learning Induces White Matter Plasticity in the Fornix." *The Journal of Neuroscience: The Official Journal of the Society for Neuroscience* 33(31):12844–50.
- Horsfield, Mark a, Stefania Sala, Mohit Neema, Martina Absinta, Anshika Bakshi, Maria Pia Sormani, Maria A. Rocca, Rohit Bakshi, and Massimo Filippi. 2010. "Rapid Semi-Automatic Segmentation of the Spinal Cord from Magnetic Resonance Images: Application in Multiple Sclerosis." *Neuroimage*. 50(2):446–55.
- Hua, Xue, Boris Gutman, Christina P. Boyle, Priya Rajagopalan, Alex D. Leow, Igor Yanovsky, Anand R. Kumar, Arthur W. Toga, Clifford R. Jack, Norbert Schuff, Gene E. Alexander, Kewei Chen, Eric M. Reiman, Michael W. Weiner, Paul M. Thompson, and =Alzheimer's Disease Neuroimaging Initiative. 2011. "Accurate Measurement of Brain Changes in Longitudinal MRI Scans Using Tensor-Based Morphometry." *NeuroImage* 57(1):5–14.
- Huang, Junting, Vinicius M. Gadotti, Lina Chen, Ivana A. Souza, Shuo Huang, Decheng Wang, Charu Ramakrishnan, Karl Deisseroth, Zizhen Zhang, and Gerald W. Zamponi. 2019. "A Neuronal Circuit for Activating Descending Modulation of Neuropathic Pain." *Nature Neuroscience* 22(10):1659–68.
- Huber, Eveline, Gergely David, Alan J. Thompson, and Nikolaus Weiskopf. 2018. "Dorsal and Ventral Horn Atrophy Is Associated with Clinical Outcome after Spinal Cord Injury." 0.
- Huber, Eveline, Gergely David, Alan J. Thompson, Nikolaus Weiskopf, Siawoosh Mohammadi, and Patrick Freund. 2018. "Dorsal and Ventral Horn Atrophy Is Associated with Clinical Outcome after Spinal Cord Injury." *Neurology* 90(17):e1510–22.
- Huber, Eveline, Patrice Lachappelle, Reto Sutter, Armin Curt, and Patrick Freund. 2017. "Are Midsagittal Tissue Bridges Predictive of Outcome after Cervical Spinal Cord Injury?" *Annals of Neurology* 81(5):740–48.
- Hüfner, Katharina, Carolina Binetti, Derek A. Hamilton, Thomas Stephan, Virginia L. Flanagin, Jennifer Linn, Kirsten Labudda, Hans Markowitsch, Stefan Glasauer, Klaus Jahn, Michael Strupp, and Thomas Brandt. 2011. "Structural and Functional Plasticity of the Hippocampal Formation in Professional Dancers and Slackliners." *Hippocampus* 21(8):855–65.
- Itzkovich, M., I. Gelernter, F. Biering-Sorensen, C. Weeks, M. T. Laramée, B. C. Craven, M. Tonack, S. L.

- Hitzig, E. Glaser, G. Zeilig, S. Aito, G. Scivoletto, M. Mecci, R. J. Chadwick, W. S. El Masry, A. Osman, C. A. Glass, P. Silva, B. M. Soni, B. P. Gardner, G. Savic, E. M. Bergstrom, V. Bluvshstein, J. Ronen, A. Catz, E. M. Bergström, V. Bluvshstein, J. Ronen, and A. Catz. 2007. "The Spinal Cord Independence Measure (SCIM) Version III: Reliability and Validity in a Multi-Center International Study." *Disability and Rehabilitation* 29(24):1926–33.
- Jackson, Amie B., Marcel Dijkers, Michael J. DeVivo, and Robert B. Poczatek. 2004. "A Demographic Profile of New Traumatic Spinal Cord Injuries: Change and Stability over 30 Years." *Archives of Physical Medicine and Rehabilitation* 85(11):1740–48.
- Jankowska, Elzbieta. 2013. "Spinal Interneurons." Pp. 1063–99 in *Neuroscience in the 21st Century: From Basic to Clinical*.
- Jeanmonod, D., M. Magnin, and A. Morel. 1993. "Thalamus and Neurogenic Pain: Physiological, Anatomical and Clinical Data." *Neuroreport* 4(5):475–78.
- Jensen, Jesper Lundbye, Peter C. D. D. Marstrand, and Jens B. Nielsen. 2005. "Motor Skill Training and Strength Training Are Associated with Different Plastic Changes in the Central Nervous System." *Journal of Applied Physiology* 99(4):1558–68.
- Jermakowicz, Walter J., Ian D. Hentall, Jonathan R. Jagid, Corneliu C. Luca, James Adcock, Alberto Martinez-Arizala, and Eva Widerström-Noga. 2017. "Deep Brain Stimulation Improves the Symptoms and Sensory Signs of Persistent Central Neuropathic Pain from Spinal Cord Injury: A Case Report." *Frontiers in Human Neuroscience* 11:177.
- Jindahra, Panitha, Aviva Petrie, and Gordon T. Plant. 2012. "The Time Course of Retrograde Trans-Synaptic Degeneration Following Occipital Lobe Damage in Humans." *Brain: A Journal of Neurology* 135(2):534–41.
- Johansen-Berg, Heidi. 2007. "Structural Plasticity: Rewiring the Brain." *Current Biology* 17(4):141–44.
- Jørgensen, L. M., J. E. Nielsen, and M. Ravnborg. 2005. "MEP Recruitment Curves in Multiple Sclerosis and Hereditary Spastic Paraplegia." *Journal of the Neurological Sciences* 237(1):25–29.
- Jurkiewicz, M. T., A. P. Crawley, M. C. Verrier, M. G. Fehlings, and D. J. Mikulis. n.d. "Cortical Atrophy after Spinal Cord Injury : A Morphometry Study." di:64–67.
- Jutzeler, C. R. R. Catherine R., Eveline Huber, Martina F. M. F. Callaghan, Roger Luechinger, Armin Curt, John L. K. J. L. K. Kramer, and Patrick Freund. 2016. "Association of Pain and CNS Structural Changes after Spinal Cord Injury." *Scientific Reports* 6:18534.
- Jutzeler, Catherine R., Eveline Huber, Martina F. Callaghan, Roger Luechinger, Armin Curt, John L. K. Kramer, and Patrick Freund. 2016. "Association of Pain and CNS Structural Changes after Spinal Cord Injury." *Nature Publishing Group* (April 2015):1–13.
- Kalil, K. and G. E. Schneider. 1975. "Retrograde Cortical and Axonal Changes Following Lesions of the Pyramidal Tract." *Brain Res.* 89(1):15–27.
- Kalsi-Ryan, Sukhvinder, Armin Curt, Mary C. Verrier, and Michael G. Fehlings. 2012. "Development of the Graded Redefined Assessment of Strength, Sensibility and Prehension (GRASSP): Reviewing Measurement Specific to the Upper Limb in Tetraplegia." *Journal of Neurosurgery. Spine* 17(1

Suppl):65–76.

- Kalsi-Ryan, Sukhvinder, Armin Curt, Mary C Verrier, and Michael G. Fehlings. 2012. "Development of the Graded Redefined Assessment of Strength, Sensibility and Prehension (GRASSP): Reviewing Measurement Specific to the Upper Limb in Tetraplegia." *Journal of Neurosurgery. Spine* 17(1 Suppl):65–76.
- Kasperek, Tomas, Radek Marecek, Daniel Schwarz, Radovan Prikryl, Jiri Vanicek, Michal Mikl, and Eva Ceskova. 2010. "Source-Based Morphometry of Gray Matter Volume in Men with First-Episode Schizophrenia." *Human Brain Mapping* 31(2):300–310.
- Kerschensteiner, Martin, Martin E. Schwab, Jeff W. Lichtman, and Thomas Misgeld. 2005a. "In Vivo Imaging of Axonal Degeneration and Regeneration in the Injured Spinal Cord." *Nat.Med.* 11(5):572–77.
- Kerschensteiner, Martin, Martin E. Schwab, Jeff W. Lichtman, and Thomas Misgeld. 2005b. "In Vivo Imaging of Axonal Degeneration and Regeneration in the Injured Spinal Cord In Vivo Imaging of Axonal Degeneration and Regeneration in the Injured Spinal Cord." 11(May):572–77.
- Kim, Byung G., Hai-Ning Dai, Marietta McAtee, Stefano Vicini, and Barbara S. Bregman. 2006. "Remodeling of Synaptic Structures in the Motor Cortex Following Spinal Cord Injury." *Experimental Neurology* 198(2):401–15.
- Kinam Park. 2014. "Effects of Aerobic Exercise Training on Cognitive Function and Cortical Vascularity in Monkeys." *Bone* 23(1):1–7.
- Kirshblum, Steven C., Stephen P. Burns, Fin Biering-Sorensen, William Donovan, Daniel E. Graves, Amitabh Jha, Mark Johansen, Linda Jones, Andrei Krassioukov, M. J. Mulcahey, Mary Schmidt-Read, and William Waring. 2011. "International Standards for Neurological Classification of Spinal Cord Injury (Revised 2011)." *Journal of Spinal Cord Medicine* 34(6):535–46.
- Kirshblum, Steven C, William Waring, Fin Biering-Sorensen, Stephen P. Burns, Mark Johansen, Mary Schmidt-Read, William Donovan, Daniel Graves, Amit Jha, Linda Jones, M. J. Mulcahey, and Andrei Krassioukov. 2011a. "Reference for the 2011 Revision of the International Standards for Neurological Classification of Spinal Cord Injury." *The Journal of Spinal Cord Medicine* 34(6):547–54.
- Kirshblum, Steven C, William Waring, Fin Biering-Sorensen, Stephen P. Burns, Mark Johansen, Mary Schmidt-Read, William Donovan, Daniel Graves, Amit Jha, Linda Jones, M. J. Mulcahey, and Andrei Krassioukov. 2011b. "Reference for the 2011 Revision of the International Standards for Neurological Classification of Spinal Cord Injury." *J.Spinal Cord Med.* 34(6):547–54.
- Kleim, Jeffrey B, Scott, Natalie R. Cooper, Theresa M. Hogg, Chelsea N. Reidel, Michael S. Remple, and Randolph J. Nudo. 2002. "Motor Learning-Dependent Synaptogenesis Is Localized to Functionally Reorganized Motor Cortex." *Neurobiology of Learning and Memory* 77(1):63–77.
- Kodama, Midori, Takashi Ono, Fumio Yamashita, Hiroki Ebata, Meigen Liu, Shoko Kasuga, and Junichi Ushiba. 2018a. "Structural Gray Matter Changes in the Hippocampus and the Primary Motor Cortex on An-Hour-to-One- Day Scale Can Predict Arm-Reaching Performance Improvement." *Frontiers in Human Neuroscience* 12:209.

- Kodama, Midori, Takashi Ono, Fumio Yamashita, Hiroki Ebata, Meigen Liu, Shoko Kasuga, and Junichi Ushiba. 2018b. "Structural Gray Matter Changes in the Hippocampus and the Primary Motor Cortex on An-Hour-to-One- Day Scale Can Predict Arm-Reaching Performance Improvement." *Frontiers in Human Neuroscience* 12:209.
- Kolb, Bryan, Jan Cioe, and Wendy Comeau. 2008. "Contrasting Effects of Motor and Visual Spatial Learning Tasks on Dendritic Arborization and Spine Density in Rats." *Neurobiology of Learning and Memory* 90(2):295–300.
- Koo, Terry K. and Mae Y. Li. 2016. "A Guideline of Selecting and Reporting Intraclass Correlation Coefficients for Reliability Research." *Journal of Chiropractic Medicine* 15(2):155–63.
- Kramer, John L. K., Nikita K. Minhas, Catherine R. Jutzeler, Erin L. K. S. Erskine, Lisa J. W. Liu, and Matt S. Ramer. 2017. "Neuropathic Pain Following Traumatic Spinal Cord Injury: Models, Measurement, and Mechanisms." *Journal of Neuroscience Research* 95(6):1295–1306.
- Lakhani, Bimal, Michael R. Borich, Jacob N. Jackson, Katie P. Wadden, Sue Peters, Anica Villamayor, Alex L. MacKay, Irene M. Vavasour, Alexander Rauscher, and Lara A. Boyd. 2016. "Motor Skill Acquisition Promotes Human Brain Myelin Plasticity." *Neural Plasticity* 2016.
- Lamprecht, Raphael and Joseph LeDoux. 2004. "Structural Plasticity and Memory." *Nature Reviews. Neuroscience* 5(1):45–54.
- Langkammer, Christian, Nikolaus Krebs, Walter Goessler, Eva Scheurer, Franz Ebner, Kathrin Yen, Franz Fazekas, and Stefan Ropele. 2010. "Quantitative MR Imaging of Brain Iron: A Postmortem Validation Study 1." *Radiology* 257(2):455–62.
- Laule, Cornelia, Irene M. Vavasour, Shannon H. Kolind, David K. B. Li, Tony L. Traboulsee, G. R. Wayne Moore, and Alex L. MacKay. 2007. "Magnetic Resonance Imaging of Myelin." *Neurotherapeutics : The Journal of the American Society for Experimental NeuroTherapeutics* 4(3):460–84.
- Lawrence, D. G. and H. G. Kuypers. 1968. "The Functional Organization of the Motor System in the Monkey. I. The Effects of Bilateral Pyramidal Lesions." *Brain : A Journal of Neurology* 91(1):1–14.
- Lee, Jee Eun, Moo K. Chung, Mariana Lazar, Molly B. DuBray, Jinsuh Kim, Erin D. Bigler, Janet E. Lainhart, and Andrew L. Alexander. 2009. "A Study of Diffusion Tensor Imaging by Tissue-Specific, Smoothing-Compensated Voxel-Based Analysis." *NeuroImage* 44(3):870–83.
- Lee, Jongho, Yoonho Nam, Joon Yul Choi, Eung Yeop Kim, Se-Hong Oh, and Dong-Hyun Kim. 2017. "Mechanisms of T(2) * Anisotropy and Gradient Echo Myelin Water Imaging." *NMR in Biomedicine* 30(4).
- De Leener, Benjamin, Vladimir S. Fonov, D. Louis Collins, Virginie Callot, Nikola Stikov, and Julien Cohen-Adad. 2018. "PAM50: Unbiased Multimodal Template of the Brainstem and Spinal Cord Aligned with the ICBM152 Space." *NeuroImage* 165(October 2017):170–79.
- De Leener, Benjamin, Samuel Kadoury, and Julien Cohen-Adad. 2014. "Robust, Accurate and Fast Automatic Segmentation of the Spinal Cord." *NeuroImage* 98:528–36.
- De Leener, Benjamin, Simon Lévy, Sara M. Dupont, Vladimir S. Fonov, Nikola Stikov, D. Louis Collins, Virginie Callot, and Julien Cohen-Adad. 2016. "SCT: Spinal Cord Toolbox, an Open-Source

- Software for Processing Spinal Cord MRI Data." *NeuroImage* 145(October 2016):24–43.
- Lemon, Roger N. 2008. "Descending Pathways in Motor Control." *Annu.Rev.Neurosci.* 31(1):195–218.
- Leung, Kelvin K., Gerard R. Ridgway, Sébastien Ourselin, and Nick C. Fox. 2012. "Consistent Multi-Time-Point Brain Atrophy Estimation from the Boundary Shift Integral." *NeuroImage* 59(4):3995–4005.
- Lisman, John E. and Anthony A. Grace. 2005. "The Hippocampal-VTA Loop: Controlling the Entry of Information into Long-Term Memory." *Neuron* 46(5):703–13.
- Liu, Yuanyuan, Alban Latremoliere, Xinjian Li, Zicong Zhang, Mengying Chen, Xuhua Wang, Chao Fang, Junjie Zhu, Chloe Alexandre, Zhongyang Gao, Bo Chen, Xin Ding, Jin-Yong Zhou, Yiming Zhang, Chinfai Chen, Kuan Hong Wang, Clifford J. Woolf, and Zhigang He. 2018. "Touch and Tactile Neuropathic Pain Sensitivity Are Set by Corticospinal Projections." *Nature* 561(7724):547–50.
- Lorio, S., S. Fresard, S. Adaszewski, F. Kherif, R. Chowdhury, R. S. Frackowiak, J. Ashburner, G. Helms, N. Weiskopf, A. Lutti, and Draganski. 2016. "NeuroImage New Tissue Priors for Improved Automated Classification of Subcortical Brain Structures on MRI ☆." *NeuroImage* 130:157–66.
- Lorio, S., A. Lutti, F. Kherif, A. Ruef, J. Dukart, R. Chowdhury, R. S. Frackowiak, J. Ashburner, G. Helms, N. Weiskopf, and Draganski. 2014. "Disentangling in Vivo the Effects of Iron Content and Atrophy on the Ageing Human Brain." *NeuroImage* 103:280–89.
- Lövdén, Martin, Sabine Schaefer, Hannes Noack, Nils Christian Bodammer, Simone Kühn, Hans-Jochen Heinze, Emrah Düzel, Lars Bäckman, and Ulman Lindenberger. 2012. "Spatial Navigation Training Protects the Hippocampus against Age-Related Changes during Early and Late Adulthood." *Neurobiology of Aging* 33(3):620.e9-620.e22.
- Lundell, H. 2011. "Independent Spinal Cord Atrophy Measures Correlate to Motor and Sensory Deficits in Individuals with Spinal Cord Injury." *Spinal Cord* 49(1):70–75.
- Lundell, H., D. Barthelemy, A. Skimminge, T. B. Dyrby, F. Biering-Sørensen, and J. B. Nielsen. 2011. "Independent Spinal Cord Atrophy Measures Correlate to Motor and Sensory Deficits in Individuals with Spinal Cord Injury." *Spinal Cord* 49(1):70–75.
- Lutti, Antoine, Frederic Dick, Martin I. Sereno, and Nikolaus Weiskopf. 2014. "Using High-Resolution Quantitative Mapping of R1 as an Index of Cortical Myelination." *NeuroImage* 93:176–88.
- Lutti, Antoine, Joerg Stadler, Oliver Josephs, Christian Windischberger, Oliver Speck, Johannes Bernarding, Chloe Hutton, and Nikolaus Weiskopf. 2012. "Robust and Fast Whole Brain Mapping of the RF Transmit Field B1 at 7T." *PLoS ONE* 7(3):1–7.
- Lynskey, James V, Adam Belanger, and Ranu Jung. 2008. "Activity-Dependent Plasticity in Spinal Cord Injury." *Journal of Rehabilitation Research and Development* 45(2):229–40.
- Maguire, E. A., D. G. Gadian, I. S. Johnsrude, C. D. Good, J. Ashburner, R. S. Frackowiak, and C. D. Frith. 2000. "Navigation-Related Structural Change in the Hippocampi of Taxi Drivers." *Proceedings of the National Academy of Sciences of the United States of America* 97(8):4398–4403.
- Makino, Hiroshi, Eun Jung Hwang, Nathan G. Hedrick, and Takaki Komiyama. 2016. "Circuit Mechanisms of Sensorimotor Learning." *Neuron* 92(4):705–21.

- Mansfield, P. and P. K. Grannell. 1973. "NMR 'diffraction' in Solids?" *Journal of Physics C: Solid State Physics* 6(22):L422–26.
- Markl, Michael and Jochen Leupold. 2012. "Gradient Echo Imaging." *Journal of Magnetic Resonance Imaging : JMRI* 35(6):1274–89.
- Marques, José P., Diana Khabipova, and Rolf Gruetter. 2017. "Studying Cyto and Myeloarchitecture of the Human Cortex at Ultra-High Field with Quantitative Imaging: R(1), R(2)(*) and Magnetic Susceptibility." *NeuroImage* 147:152–63.
- Matt B A, Kevin K F, Xiaohong Z. J. n.d. "Handbook of MRI Pulse Sequences." *ISBN*.
- Mazziotta, J. C., A. W. Toga, A. Evans, P. Fox, and J. Lancaster. 1995a. "A Probabilistic Atlas and Reference System for the Human Brain: International Consortium for Brain Mapping (ICBM)." *NeuroImage* 2(2):89–101.
- Mazziotta, J. C., A. W. Toga, A. Evans, P. Fox, and J. Lancaster. 1995b. "A Probabilistic Atlas of the Human Brain: Theory and Rationale for Its Development. The International Consortium for Brain Mapping (ICBM)." *NeuroImage* 2(2):89–101.
- Mazziotta, J., A. Toga, A. Evans, P. Fox, J. Lancaster, K. Zilles, R. Woods, T. Paus, G. Simpson, B. Pike, C. Holmes, L. Collins, P. Thompson, D. MacDonald, M. Iacoboni, T. Schormann, K. Amunts, N. Palomero-Gallagher, S. Geyer, L. Parsons, K. Narr, N. Kabani, G. Le Goualher, J. Feidler, K. Smith, D. Boomsma, H. Hulshoff Pol, T. Cannon, R. Kawashima, and B. Mazoyer. 2001. "A Four-Dimensional Probabilistic Atlas of the Human Brain." *Journal of the American Medical Informatics Association : JAMIA* 8(5):401–30.
- McCoy, D. B., S. M. Dupont, C. Gros, J. Cohen-Adad, R. J. Huie, A. Ferguson, X. Duong-Fernandez, L. H. Thomas, V. Singh, J. Narvid, L. Pascual, N. Kyritsis, M. S. Beattie, J. C. Bresnahan, S. Dhall, W. Whetstone, and J. F. Talbott. 2019. "Convolutional Neural Network–Based Automated Segmentation of the Spinal Cord and Contusion Injury: Deep Learning Biomarker Correlates of Motor Impairment in Acute Spinal Cord Injury." *American Journal of Neuroradiology* 40(4):737–44.
- McGraw, Kenneth O. and S. P. Wong. 1996. "Forming Inferences About Some Intraclass Correlation Coefficients." *I(1)*:2292–94.
- McKenzie, Ian A., David Ohayon, Huiliang Li, Joana Paes de Faria, Ben Emery, Koujiro Tohyama, and William D. Richardson. 2014. "Motor Skill Learning Requires Active Central Myelination." *Science (New York, N.Y.)* 346(6207):318–22.
- McRobbie, Donald W., Elizabeth A. Moore, and Martin J. Graves. 2017. *MRI from Picture to Proton*.
- Meletis, Konstantinos, Fanie Barnabé-Heider, Marie Carlén, Emma Evergren, Nikolay Tomilin, Oleg Shupliakov, Jonas Frisén, Fanie Barnabe-Heider, Marie Carlen, Emma Evergren, Nikolay Tomilin, Oleg Shupliakov, and Jonas Frisen. 2008. "Spinal Cord Injury Reveals Multilineage Differentiation of Ependymal Cells." *PLoS Biology* 6(7):1494–1507.
- Mezer, Aviv, Jason D. Yeatman, Nikola Stikov, Kendrick N. Kay, Nam-Joon Cho, Robert F. Dougherty, Michael L. Perry, Josef Parvizi, Le H. Hua, Kim Butts-Pauly, and Brian A. Wandell. 2013. "Quantifying the Local Tissue Volume and Composition in Individual Brains with Magnetic

- Resonance Imaging." *Nature Medicine* 19(12):1667–72.
- van Middendorp, Joost J., Ben Goss, Susan Urquhart, Sridhar Atresh, Richard P. Williams, and Michael Schuetz. 2011. "Diagnosis and Prognosis of Traumatic Spinal Cord Injury." *Global Spine Journal* 1(1):001–007.
- Milhorat, T. H., A. L. Jr Capocelli, A. P. Anzil, R. M. Kotzen, and R. H. Milhorat. 1995. "Pathological Basis of Spinal Cord Cavitation in Syringomyelia: Analysis of 105 Autopsy Cases." *Journal of Neurosurgery* 82(5):802–12.
- Mohammadi, Siawoosh, Daniel Carey, Fred Dick, Joern Diedrichsen, Martin I. Sereno, Marco Reisert, Martina F. Callaghan, and Nikolaus Weiskopf. 2015a. "Whole-Brain in-Vivo Measurements of the Axonal G-Ratio in a Group of 37 Healthy Volunteers." *Frontiers in Neuroscience* 9(NOV):1–13.
- Mohammadi, Siawoosh, Daniel Carey, Fred Dick, Joern Diedrichsen, Martin I. Sereno, Marco Reisert, Martina F. Callaghan, and Nikolaus Weiskopf. 2015b. "Whole-Brain in-Vivo Measurements of the Axonal G-Ratio in a Group of 37 Healthy Volunteers." *Frontiers in Neuroscience* 9(NOV):1–13.
- Mole, Tom B., Kate Maciver, Vanessa Sluming, Gerard R. Ridgway, and Turo J. Nurmikko. 2014. "Specific Brain Morphometric Changes in Spinal Cord Injury with and without Neuropathic Pain." *NeuroImage: Clinical* 5:28–35.
- Moore, Jason J., Pascal M. Ravassard, David Ho, Lavanya Acharya, Ashley L. Kees, Cliff Vuong, and Mayank R. Mehta. 2017. "Dynamics of Cortical Dendritic Membrane Potential and Spikes in Freely Behaving Rats." *Science (New York, N.Y.)* 355(6331):1–38.
- Morris, C. M., J. M. Candy, A. E. Oakley, C. A. Bloxham, and J. A. Edwardson. 1992. "Histochemical Distribution of Non-Haem Iron in the Human Brain." *Cells Tissues Organs* 144(3):235–57.
- Naber, P. A., F. H. Lopes da Silva, and M. P. Witter. 2001. "Reciprocal Connections between the Entorhinal Cortex and Hippocampal Fields CA1 and the Subiculum Are in Register with the Projections from CA1 to the Subiculum." *Hippocampus* 11(2):99–104.
- Natu, Vaidehi S., Jesse Gomez, Michael Barnett, Brianna Jeska, Evgeniya Kirilina, Carsten Jaeger, Zonglei Zhen, Siobhan Cox, Kevin S. Weiner, Nikolaus Weiskopf, and Kalanit Grill-Spector. 2019. "Apparent Thinning of Human Visual Cortex during Childhood Is Associated with Myelination." *Proceedings of the National Academy of Sciences of the United States of America* 116(41):20750–59.
- Neumann, E., M. G. Ramos, L. M. Santos, A. C. P. Rodrigues, E. C. Vieira, L. C. C. Afonso, J. R. Nicoli, and L. Q. Vieira. 2009. "Lactobacillus Delbrueckii UFV-H2b20 Induces Type 1 Cytokine Production by Mouse Cells in Vitro and in Vivo." *Brazilian Journal of Medical and Biological Research = Revista Brasileira de Pesquisas Medicas e Biologicas* 42(4):358–67.
- Norenberg, Michael D., Jon Smith, and Alex Marcillo. 2004. "The Pathology of Human Spinal Cord Injury: Defining the Problems." *Journal of Neurotrauma* 21(4):429–40.
- Nudo, Randolph J. 1951. "Plasticity." *Physics Today* 4(3):17–23.
- O'Keefe; Nadel, Lynn. 1978. *The Hippocampus as a Cognitive Map*. Vol. 27.

- O'Shea, Timothy M., Joshua E. Burda, and Michael V Sofroniew. 2017. "Cell Biology of Spinal Cord Injury and Repair." *The Journal of Clinical Investigation* 127(9):3259–70.
- Oh, Se-Hong, Young-Bo Kim, Zang-Hee Cho, and Jongho Lee. 2013. "Origin of B0 Orientation Dependent R2(*) (=1/T2(*)) in White Matter." *NeuroImage* 73:71–79.
- Oldfield, R. C. 1971. "The Assessment and Analysis of Handedness: The Edinburgh Inventory." *Neuropsychologia* 9(1):97–113.
- Ong, Wei-Yi, Christian S. Stohler, and Deron R. Herr. 2019. "Role of the Prefrontal Cortex in Pain Processing." *Molecular Neurobiology* 56(2):1137–66.
- Orrell, A. J., F. F. Eves, and R. S. W. Masters. 2006. "Implicit Motor Learning of a Balancing Task." *Gait & Posture* 23(1):9–16.
- Ossipov, Michael H., Gregory O. Dussor, and Frank Porreca. 2010. "Central Modulation of Pain." *The Journal of Clinical Investigation* 120(11):3779–87.
- Papinutto, Nico, Carlo Asteggiano, Antje Bischof, Tristan J. Gundel, Eduardo Caverzasi, William A. Stern, Stefano Bastianello, Stephen L. Hauser, and Roland G. Henry. 2019. "Intersubject Variability and Normalization Strategies for Spinal Cord Total Cross-Sectional and Gray Matter Areas." *Journal of Neuroimaging* jon.12666.
- Papp, Daniel, Martina F. Callaghan, Heiko Meyer, Craig Buckley, and Nikolaus Weiskopf. 2016. "Correction of Inter-Scan Motion Artifacts in Quantitative R1 Mapping by Accounting for Receive Coil Sensitivity Effects." *Magnetic Resonance in Medicine* 76(5):1478–85.
- Perone, Christian S., Evan Calabrese, and Julien Cohen-Adad. 2018. "Spinal Cord Gray Matter Segmentation Using Deep Dilated Convolutions." *Scientific Reports* 8(1):5966.
- Peters, Alan, Ameigh Verderosa, and Claire Sethares. 2008. "The Neuroglial Population in the Primary Visual Cortex of the Aging Rhesus Monkey." *Glia* 56(11):1151–61.
- Pfyffer, Dario, Eveline Huber, Reto Sutter, Armin Curt, and Patrick Freund. 2019. "Tissue Bridges Predict Recovery after Traumatic and Ischemic Thoracic Spinal Cord Injury." *Neurology* 0:1–12.
- Preibisch, C. and R. Deichmann. 2009. "Influence of RF Spoiling on the Stability and Accuracy of T1 Mapping Based on Spoiled FLASH with Varying Flip Angles." *Magnetic Resonance in Medicine* 61(1):125–35.
- Psachoulia, Konstantina, Françoise Jamen, Kaylene M. Young, and William D. Richardson. 2009. "Cell Cycle Dynamics of NG2 Cells in the Postnatal and Ageing Brain." *Neuron Glia Biology* 5(3–4):57–67.
- Purcell, E. M., H. C. Torrey, and R. V Pound. 1946. "Resonance Absorption by Nuclear Magnetic Moments in a Solid." *Phys. Rev.* 69(1–2):37–38.
- Raineteau, O and M. E. Schwab. 2001. "Plasticity of Motor Systems after Incomplete Spinal Cord Injury." *Nature Reviews. Neuroscience* 2(4):263–73.
- Raineteau, Olivier and Martin E. Schwab. 2001. "Plasticity of Motor Systems after Incomplete Spinal

- Cord Injury." *Nature Reviews Neuroscience* 2(4):263–73.
- Rakic, Pasko. 2002. "Neurogenesis in Adult Primate Neocortex: An Evaluation of the Evidence." *Nature Reviews. Neuroscience* 3(1):65–71.
- Ramírez-Amaya, V. and ML Escobar. 1999. "Synaptogenesis of Mossy Fibers Induced by Spatial Water Maze Overtraining." *Hippocampus* 636(9):631–36.
- Reisert, Marco, Irina Mader, Roza Umarova, Simon Maier, Ludger Tebartz van Elst, and Valerij G. Kiselev. 2013. "Fiber Density Estimation from Single Q-Shell Diffusion Imaging by Tensor Divergence." *NeuroImage* 77:166–76.
- Remondes, Miguel and Erin M. Schuman. 2004. "Role for a Cortical Input to Hippocampal Area CA1 in the Consolidation of a Long-Term Memory." *Nature* 431(7009):699–703.
- Reuter, Martin, Nicholas J. Schmansky, H. Diana Rosas, and Bruce Fischl. 2012. "Within-Subject Template Estimation for Unbiased Longitudinal Image Analysis." *NeuroImage* 61(4):1402–18.
- Reuter, Martin, M. Dylan Tisdall, Abid Qureshi, Randy L. Buckner, André J. W. van der Kouwe, and Bruce Fischl. 2015. "Head Motion during MRI Acquisition Reduces Gray Matter Volume and Thickness Estimates." *NeuroImage* 107:107–15.
- Rhyu, I. J., J. A. Bytheway, S. J. Kohler, H. Lange, K. J. Lee, J. Boklewski, K. McCormick, N. I. Williams, G. B. Stanton, W. T. Greenough, and J. L. Cameron. 2010. "Effects of Aerobic Exercise Training on Cognitive Function and Cortical Vascularity in Monkeys." *Neuroscience* 167(4):1239–48.
- Ridgway, Gerard, Josephine Barnes, Tracey Pepple, and Nick Fox. 2011. "Estimation of Total Intracranial Volume; a Comparison of Methods." *Alzheimer's & Dementia* 7(4):S62–63.
- Ridgway, Gerard R., Susie M. D. Henley, Jonathan D. Rohrer, Rachael I. Scahill, Jason D. Warren, and Nick C. Fox. 2008. "Ten Simple Rules for Reporting Voxel-Based Morphometry Studies." *NeuroImage* 40(4):1429–35.
- Ridgway, John P. 2010. "Cardiovascular Magnetic Resonance Physics for Clinicians: Part I." *Journal of Cardiovascular Magnetic Resonance : Official Journal of the Society for Cardiovascular Magnetic Resonance* 12(1):71.
- Rioult-Pedotti, M. S., J. P. Donoghue, and A. Dunaevsky. 2007. "Plasticity of the Synaptic Modification Range." *Journal of Neurophysiology* 98(6):3688–95.
- Rooney, William D., Glyn Johnson, Xin Li, Eric R. Cohen, Seong-Gi Kim, Kamil Ugurbil, and Charles S. Springer. 2007. "Magnetic Field and Tissue Dependencies of Human Brain Longitudinal $^1\text{H}_2\text{O}$ Relaxation in Vivo." *Magnetic Resonance in Medicine* 57(2):308–18.
- Rosen, Adon F. G., David R. Roalf, Kosha Ruparel, Jason Blake, Kevin Seelaus, Lakshmi P. Villa, Rastko Ciric, Philip A. Cook, Christos Davatzikos, Mark A. Elliott, Angel Garcia de La Garza, Efsthios D. Gennatas, Megan Quarmley, J. Eric Schmitt, Russell T. Shinohara, M. Dylan Tisdall, R. Cameron Craddock, Raquel E. Gur, Ruben C. Gur, and Theodore D. Satterthwaite. 2018. "Quantitative Assessment of Structural Image Quality." *NeuroImage* 169:407–18.
- Rosenkranz, Karin, Aaron Williamson, Katherine Butler, Carla Cordivari, Andrew J. Lees, and John C.

- Rothwell. 2005. "Pathophysiological Differences between Musician's Dystonia and Writer's Cramp." *Brain : A Journal of Neurology* 128(4):918–31.
- Rotshenker, Shlomo. 2011. "Wallerian Degeneration: The Innate-Immune Response to Traumatic Nerve Injury." *Journal of Neuroinflammation* 8:109.
- Rowland, James W., Gregory W. J. Hawryluk, Brian Kwon, and Michael G. Fehlings. 2008. "Current Status of Acute Spinal Cord Injury Pathophysiology and Emerging Therapies: Promise on the Horizon." *Neurosurgical Focus* 25(5):E2.
- Roy, Mathieu, Daphna Shohamy, Nathaniel Daw, Marieke Jepma, G. Elliott Wimmer, and Tor D. Wager. 2014. "Representation of Aversive Prediction Errors in the Human Periaqueductal Gray." *Nature Neuroscience* 17(11):1607–12.
- Sampaio-Baptista, Cassandra, Alexandre A. Khrapitchev, Sean Foxley, Theresa Schlagheck, Jan Scholz, Saad Jbabdi, Gabriele C. DeLuca, Karla L. Miller, Amy Taylor, Naghme Thomas, Jeffrey Kleim, Nicola R. Sibson, David Bannerman, and Heidi Johansen-Berg. 2013. "Motor Skill Learning Induces Changes in White Matter Microstructure and Myelination." *The Journal of Neuroscience : The Official Journal of the Society for Neuroscience* 33(50):19499–503.
- Schlegel, Alexander A., Justin J. Rudelson, and Peter U. Tse. 2012. "White Matter Structure Changes as Adults Learn a Second Language." *Journal of Cognitive Neuroscience* 24(8):1664–70.
- Schmierer, Klaus, Francesco Scaravilli, Daniel R. Altmann, Gareth J. Barker, and David H. Miller. 2004. "Magnetization Transfer Ratio and Myelin in Postmortem Multiple Sclerosis Brain." *Annals of Neurology* 56(3):407–15.
- Scholz, Jan, Miriam C. Klein, Timothy E. J. Behrens, and Heidi Johansen-Berg. 2009. "Training Induces Changes in White-Matter Architecture." *Nature Neuroscience* 12(11):1370–71.
- Sehm, Bernhard, Marco Taubert, Virginia Conde, David Weise, Joseph Classen, Juergen Dukart, Bogdan Draganski, Arno Villringer, and Patrick Ragert. 2014. "Structural Brain Plasticity in Parkinson's Disease Induced by Balance Training." *Neurobiology of Aging* 35(1):232–39.
- Seif, Maryam, Armin Curt, Alan J. Thompson, Patrick Grabher, and Nikolaus Weiskopf. 2018. "Clinical Quantitative MRI of Rostral Spinal Cord and Brain Regions Is Predictive of Functional Recovery in Acute Spinal Cord Injury." *NeuroImage: Clinical* 20(July):556–63.
- Seif, Maryam, Claudia Am Gandini Wheeler-Kingshott, Julien Cohen-Adad, Adam E. Flanders, and Patrick Freund. 2019. "Guidelines for the Conduct of Clinical Trials in Spinal Cord Injury: Neuroimaging Biomarkers." *Spinal Cord* 57(9):717–28.
- Sereno, Martin I., Antoine Lutti, Nikolaus Weiskopf, and Frederic Dick. 2013. "Mapping the Human Cortical Surface by Combining Quantitative T1 with Retinotopy †." (September):2261–68.
- Siddall, Philip J., Joan M. McClelland, Susan B. Rutkowski, and Michael J. Cousins. 2003. "A Longitudinal Study of the Prevalence and Characteristics of Pain in the First 5 Years Following Spinal Cord Injury." *Pain* 103(3):249–57.
- Škrinjar, Oskar, Arnaud Bistoquet, and Hemant Tagare. 2008. "Symmetric and Transitive Registration of Image Sequences" edited by Y. Wang. *International Journal of Biomedical Imaging*

2008(1):686875.

- Smith, Stephen M., Mark Jenkinson, Heidi Johansen-Berg, Daniel Rueckert, Thomas E. Nichols, Clare E. Mackay, Kate E. Watkins, Olga Ciccarelli, M. Zaheer Cader, Paul M. Matthews, and Timothy E. J. Behrens. 2006. "Tract-Based Spatial Statistics: Voxelwise Analysis of Multi-Subject Diffusion Data." *NeuroImage* 31(4):1487–1505.
- Steiger, Tineke K., Nikolaus Weiskopf, and Nico Bunzeck. 2016. "Iron Level and Myelin Content in the Ventral Striatum Predict Memory Performance in the Aging Brain." *The Journal of Neuroscience : The Official Journal of the Society for Neuroscience* 36(12):3552–58.
- Stikov, Nikola, Lee M. Perry, Aviv Mezer, Elena Rykhlevskaia, Brian A. Wandell, John M. Pauly, and Robert F. Dougherty. 2011a. "Bound Pool Fractions Complement Diffusion Measures to Describe White Matter Micro and Macrostructure." *NeuroImage* 54(2):1112–21.
- Stroman, P. W., C. Wheeler-Kingshott, M. Bacon, J. M. Schwab, R. Bosma, J. Brooks, D. Cadotte, T. Carlstedt, O. Ciccarelli, J. Cohen-Adad, A. Curt, N. Evangelou, M. G. Fehlings, M. Filippi, B. J. Kelley, S. Kollias, A. Mackay, C. A. Porro, S. Smith, S. M. Strittmatter, P. Summers, and I. Tracey. 2014a. "The Current State-of-the-Art of Spinal Cord Imaging: Methods." *NeuroImage* 84:1070–81.
- Stroman, P. W., C. Wheeler-Kingshott, M. Bacon, J. M. Schwab, R. Bosma, J. Brooks, D. Cadotte, T. Carlstedt, O. Ciccarelli, J. Cohen-Adad, A. Curt, N. Evangelou, M. G. Fehlings, M. Filippi, B. J. Kelley, S. Kollias, A. Mackay, C. A. Porro, S. Smith, S. M. Strittmatter, P. Summers, and I. Tracey. 2014b. "The Current State-of-the-Art of Spinal Cord Imaging: Methods." *NeuroImage* 84.
- Stüber, Carsten, Markus Morawski, Andreas Schäfer, Christian Labadie, Miriam Wähnert, Christoph Leuze, Markus Streicher, Nirav Barapatre, Katja Reimann, Stefan Geyer, Daniel Spemann, and Robert Turner. 2014. "NeuroImage Myelin and Iron Concentration in the Human Brain : A Quantitative Study of MRI Contrast." *NeuroImage* 93:95–106.
- Suh, Junghyup, Alexander J. Rivest, Toshiaki Nakashiba, Takashi Tominaga, and Susumu Tonegawa. 2011. "Entorhinal Cortex Layer III Input to the Hippocampus Is Crucial for Temporal Association Memory." *Science (New York, N.Y.)* 334(6061):1415–20.
- Tabelow, Karsten, Evelyne Balteau, John Ashburner, Martina F. Callaghan, Bogdan Draganski, Gunther Helms, Ferath Kherif, Tobias Leutritz, Antoine Lutti, Christophe Phillips, Enrico Reimer, Lars Ruthotto, Maryam Seif, Nikolaus Weiskopf, Gabriel Ziegler, and Siawoosh Mohammadi. 2019. "HMRI - A Toolbox for Quantitative MRI in Neuroscience and Clinical Research." *NeuroImage* 194(September 2018):191–210.
- Tagare, Hemant D., David Groisser, and Oskar Skrinjar. 2009. "Symmetric Non-Rigid Registration: A Geometric Theory and Some Numerical Techniques." *Journal of Mathematical Imaging and Vision* 34(1):61–88.
- Takeuchi, Hikaru, Atsushi Sekiguchi, Yasuyuki Taki, Satoru Yokoyama, Yukihiro Yomogida, Nozomi Komuro, Tohru Yamanouchi, Shozo Suzuki, and Ryuta Kawashima. 2010. "Training of Working Memory Impacts Structural Connectivity." *Journal of Neuroscience* 30(9):3297–3303.
- Tardif, Christine L., D. Louis Collins, and G. Bruce Pike. 2009. "Sensitivity of Voxel-Based Morphometry Analysis to Choice of Imaging Protocol at 3 T." *Neuroimage*. 44(3):827–38.

- Tasker, R. R., J. Gorecki, F. A. Lenz, T. Hirayama, and J. O. Dostrovsky. 1987. "Thalamic Microelectrode Recording and Microstimulation in Central and Deafferentation Pain." *Applied Neurophysiology* 50(1–6):414–17.
- Tator, C. H. 1995. "Update on the Pathophysiology and Pathology of Acute Spinal Cord Injury." *Brain Pathology (Zurich, Switzerland)* 5(4):407–13.
- Taubert, M, Draganski, A. Anwander, K. Muller, A. Horstmann, A. Villringer, and P. Ragert. 2010. "Dynamic Properties of Human Brain Structure: Learning-Related Changes in Cortical Areas and Associated Fiber Connections 3." *J Neurosci.* 30(1529-2401 (Electronic)):11670–77.
- Taubert, Marco, Bogdan Draganski, Alfred Anwander, Karsten Müller, Annette Horstmann, Arno Villringer, and Patrick Ragert. 2010. "Dynamic Properties of Human Brain Structure: Learning-Related Changes in Cortical Areas and Associated Fiber Connections." *The Journal of Neuroscience : The Official Journal of the Society for Neuroscience* 30(35):11670–77.
- Taubert, Marco, Gabriele Lohmann, Daniel S. Margulies, Arno Villringer, and Patrick Ragert. 2011. "Long-Term Effects of Motor Training on Resting-State Networks and Underlying Brain Structure." *NeuroImage* 57(4):1492–98.
- Taubert, Marco, Jan Mehnert, Burkhard Pleger, and Arno Villringer. 2016. "Rapid and Specific Gray Matter Changes in M1 Induced by Balance Training." *NeuroImage* 133:399–407.
- Taubert, Marco, Thorsten Stein, Tommy Kreutzberg, Christian Stockinger, Lukas Hecker, Anne Focke, Patrick Ragert, Arno Villringer, and Burkhard Pleger. 2016. "Remote Effects of Non-Invasive Cerebellar Stimulation on Error Processing in Motor Re-Learning." *Brain Stimulation* 9(5):692–99.
- Theodosis, Dionysia T., Dominique A. Poulain, and Stéphane H. R. R. Oliet. 2008. "Activity-Dependent Structural and Functional Plasticity of Astrocyte-Neuron Interactions." *Physiological Reviews* 88(3):983–1008.
- Thomas, Adam G., Sean Marrett, Ziad S. Saad, Douglas A. Ruff, Alex Martin, and Peter A. Bandettini. 2009. "Functional but Not Structural Changes Associated with Learning: An Exploration of Longitudinal Voxel-Based Morphometry (VBM)." *NeuroImage* 48(1):117–25.
- Thompson, Wesley, Dominic Holland, and MRS Bull. 2011. "Bias in Tensor Based Morphometry Stat-ROI Measures May Result in Unrealistic Power Estimates." *NeuroImage* 57(1):1–4.
- Tinnermann, A., S. Geuter, C. Sprenger, J. Finsterbusch, and C. Büchel. 2017. "Interactions between Brain and Spinal Cord Mediate Value Effects in Nocebo Hyperalgesia." *Science* 358(6359):105–8.
- Totoiu, Minodora O. and Hans S. Keirstead. 2005. "Spinal Cord Injury Is Accompanied by Chronic Progressive Demyelination." *Journal of Comparative Neurology* 486(4):373–83.
- Trampel, Robert, Pierre-Louis Bazin, Kerrin Pine, and Nikolaus Weiskopf. 2019. "In-Vivo Magnetic Resonance Imaging (MRI) of Laminae in the Human Cortex." *NeuroImage* 197:707–15.
- Treede, Rolf-Detlef. 2016. "Gain Control Mechanisms in the Nociceptive System." *Pain* 157(6):1199–1204.
- Tremblay, Marie-Ève, Rebecca L. Lowery, and Ania K. Majewska. 2010. "Microglial Interactions with

- Synapses Are Modulated by Visual Experience." *PLoS Biology* 8(11):e1000527.
- Tronel, Sophie, Annabelle Fabre, Vanessa Charrier, Stéphane H. R. Oliet, Fred H. Gage, and Djoher Nora Abrous. 2010. "Spatial Learning Sculptures the Dendritic Arbor of Adult-Born Hippocampal Neurons." *Proceedings of the National Academy of Sciences of the United States of America* 107(17):7963–68.
- Turati, Laura, Marco Moscatelli, Alfonso Mastropietro, Nicholas G. Dowell, Ileana Zucca, Alessandra Erbetta, Chiara Cordiglieri, Greta Brenna, Beatrice Bianchi, Renato Mantegazza, Mara Cercignani, Fulvio Baggi, and Ludovico Minati. 2015. "In Vivo Quantitative Magnetization Transfer Imaging Correlates with Histology during De- and Remyelination in Cuprizone-Treated Mice." *NMR in Biomedicine* (November 2014).
- Turchick, Audrey, Emmanuel Pierrot-Deseilligny, and David Burke. 2012. "The Circuitry of the Human Spinal Cord: Spinal and Corticospinal Mechanisms of Movement." *The Circuitry of the Human Spinal Cord: Spinal and Corticospinal Mechanisms of Movement* 88(1):1–606.
- Vallotton, Kevin, Eveline Huber, Reto Sutter, Armin Curt, Markus Hupp, and Patrick Freund. 2019. "Width and Neurophysiologic Properties of Tissue Bridges Predict Recovery after Cervical Injury." *Neurology* 92(24):e2793–2802.
- Vavasour, Irene M., Cornelia Laule, David K. B. Li, Anthony L. Traboulsee, and Alex L. MacKay. 2011. "Is the Magnetization Transfer Ratio a Marker for Myelin in Multiple Sclerosis?" *Journal of Magnetic Resonance Imaging : JMRI* 33(3):713–18.
- Villanueva, L. and D. Le Bars. 1995. "The Activation of Bulbo-Spinal Controls by Peripheral Nociceptive Inputs: Diffuse Noxious Inhibitory Controls." *Biological Research* 28(1):113–25.
- Volz, Steffen, Ulrike Nöth, Alina Jurcoane, Ulf Ziemann, Elke Hattingen, and Ralf Deichmann. 2012. "Quantitative Proton Density Mapping: Correcting the Receiver Sensitivity Bias via Pseudo Proton Densities." *NeuroImage* 63(1):540–52.
- Wake, Hiroaki, Andrew J. Moorhouse, Shozo Jinno, Shinichi Kohsaka, and Junichi Nabekura. 2009. "Resting Microglia Directly Monitor the Functional State of Synapses in Vivo and Determine the Fate of Ischemic Terminals." *The Journal of Neuroscience : The Official Journal of the Society for Neuroscience* 29(13):3974–80.
- Wang, Jack T., Zachary A. Medress, and Ben A. Barres. 2012. "Axon Degeneration: Molecular Mechanisms of a Self-Destruction Pathway." *Journal of Cell Biology* 196(1):7–18.
- Weidner, N., A. Ner, N. Salimi, and M. H. Tuszynski. 2001. "Spontaneous Corticospinal Axonal Plasticity and Functional Recovery after Adult Central Nervous System Injury." *Proceedings of the National Academy of Sciences of the United States of America* 98(6):3513–18.
- Weiskopf. 2013. "Quantitative Multi-Parameter Mapping of R1, PD*, MT, and R2* at 3T: A Multi-Center Validation." *Frontiers in Neuroscience* 7(7 JUN):1–11.
- Weiskopf, Nikolaus, Martina F. Callaghan, Oliver Josephs, Antoine Lutti, and Siawoosh Mohammadi. 2014. "Estimating the Apparent Transverse Relaxation Time (R2*) from Images with Different Contrasts (ESTATICS) Reduces Motion Artifacts." *Frontiers in Neuroscience* 8(SEP):1–10.

- Weiskopf, Nikolaus and Gunther Helms. 2008. "Multi-Parameter Mapping of the Human Brain at 1mm Resolution in Less than 20 Minutes N." *Current* 16:57091–57091.
- Weiskopf, Nikolaus, Antoine Lutti, Gunther Helms, Marianne Novak, John Ashburner, and Chloe Hutton. 2011a. "Unified Segmentation Based Correction of R1 Brain Maps for RF Transmit Field Inhomogeneities (UNICORT)." *NeuroImage* 54(3):2116–24.
- Weiskopf, Nikolaus, Antoine Lutti, Gunther Helms, Marianne Novak, John Ashburner, and Chloe Hutton. 2011b. "Unified Segmentation Based Correction of R1 Brain Maps for RF Transmit Field Inhomogeneities (UNICORT)." *NeuroImage* 54(3):2116–24.
- Weiskopf, Nikolaus, Siawoosh Mohammadi, Antoine Lutti, and Martina F. Callaghan. 2015. "Advances in MRI-Based Computational Neuroanatomy: From Morphometry to in-Vivo Histology." *Current Opinion in Neurology* 28(4):313–22.
- Weiskopf, Nikolaus, John Suckling, Guy Williams, Marta M. Correia, Becky Inkster, Roger Tait, Cinly Ooi, Edward T. Bullmore, and Antoine Lutti. 2013. "Quantitative Multi-Parameter Mapping of R1, PD(*), MT, and R2(*) at 3T: A Multi-Center Validation." *Frontiers in Neuroscience* 7(June):95.
- Wenger, Elisabeth, Simone Kühn, Julius Verrel, Johan Mårtensson, Nils Christian Bodammer, Ulman Lindenberger, and Martin Lövdén. 2016. "Repeated Structural Imaging Reveals Nonlinear Progression of Experience-Dependent Volume Changes in Human Motor Cortex." *Cerebral Cortex (New York, N.Y. : 1991)* bhw141.
- Wenger, Elisabeth, Sabine Schaefer, Hannes Noack, Simone Kühn, Johan Mårtensson, Hans Jochen Heinze, Emrah Dözel, Lars Björckman, Ulman Lindenberger, and Martin Lövdén. 2012. "Cortical Thickness Changes Following Spatial Navigation Training in Adulthood and Aging." *NeuroImage* 59(4):3389–97.
- West, Janne. 2014. *Quantitative Magnetic Resonance Imaging of the Brain Applications for Tissue Segmentation and Multiple Sclerosis*.
- Wharton, Samuel and Richard Bowtell. 2012. "Fiber Orientation-Dependent White Matter Contrast in Gradient Echo MRI." *Proceedings of the National Academy of Sciences of the United States of America* 109(45):18559–64.
- Wiech, Katja. 2016. "Deconstructing the Sensation of Pain: The Influence of Cognitive Processes on Pain Perception." *Science (New York, N.Y.)* 354(6312):584–87.
- Wilm, B. J., J. Svensson, A. Henning, K. P. Pruessmann, P. Boesiger, and S. S. Kollias. 2007. "Reduced Field-of-View MRI Using Outer Volume Suppression for Spinal Cord Diffusion Imaging." *Magnetic Resonance in Medicine* 57(3):625–30.
- Wirth, Brigitte, Hubertus J. A. A. Van Hedel, and Armin Curt. 2008. "Changes in Corticospinal Function and Ankle Motor Control during Recovery from Incomplete Spinal Cord Injury." *Journal of Neurotrauma* 25(5):467–78.
- Worsley, K. J., S. Marrett, P. Neelin, and A. C. Evans. 1996. "Searching Scale Space for Activation in PET Images." *Human Brain Mapping* 4(1):74–90.
- Wrigley, P. J., S. R. Press, S. M. Gustin, V. G. Macefield, S. C. Gandevia, M. J. Cousins, J. W. Middleton,

- L. A. Henderson, and P. J. Siddall. 2009. "Neuropathic Pain and Primary Somatosensory Cortex Reorganization Following Spinal Cord Injury." *Pain* 141(1–2):52–59.
- Xu, Lai, Karyn M. Groth, Godfrey Pearlson, David J. Schretlen, and Vince D. Calhoun. 2009. "Source-Based Morphometry: The Use of Independent Component Analysis to Identify Gray Matter Differences with Application to Schizophrenia." *Human Brain Mapping* 30(3):711–24.
- Xu, Tonghui, Xinzhu Yu, Andrew J. Perlik, Willie F. Tobin, Jonathan A. Zweig, Kelly Tennant, Theresa Jones, and Yi Zuo. 2009. "Rapid Formation and Selective Stabilization of Synapses for Enduring Motor Memories." *Nature* 462(7275):915–19.
- Yamamoto, Jun, Junghyup Suh, Daigo Takeuchi, and Susumu Tonegawa. 2014. "Successful Execution of Working Memory Linked to Synchronized High-Frequency Gamma Oscillations." *Cell* 157(4):845–57.
- Yang, Guang, Feng Pan, and Wen-Biao Gan. 2009. "Stably Maintained Dendritic Spines Are Associated with Lifelong Memories." *Nature* 462(7275):920–24.
- Yarnykh, Vasily L. 2007. "Actual Flip-Angle Imaging in the Pulsed Steady State: A Method for Rapid Three-Dimensional Mapping of the Transmitted Radiofrequency Field." *Magnetic Resonance in Medicine* 57(1):192–200.
- Yarnykh, Vasily L. 2010. "Optimal Radiofrequency and Gradient Spoiling for Improved Accuracy of T1 and B1 Measurements Using Fast Steady-State Techniques." *Magnetic Resonance in Medicine* 63(6):1610–26.
- Yasuda, Masahiro, Erin M. Johnson-Venkatesh, Helen Zhang, Jack M. Parent, Michael a Sutton, and Hisashi Umemori. 2011. "Multiple Forms of Activity-Dependent Competition Refine Hippocampal Circuits in Vivo." *Neuron* 70(6):1128–42.
- Yoon, Eun Jin, Yu Kyeong Kim, Hyung Ik Shin, Youngjo Lee, and Sang Eun Kim. 2013. "Cortical and White Matter Alterations in Patients with Neuropathic Pain after Spinal Cord Injury." *Brain Research* 1540:64–73.
- Yushkevich, Paul A., Brian B. Avants, Sandhitsu R. Das, John Pluta, Murat Altınay, and Caryne Craige. 2010. "Bias in Estimation of Hippocampal Atrophy Using Deformation-Based Morphometry Arises from Asymmetric Global Normalization: An Illustration in ADNI 3 T MRI Data." *NeuroImage* 50(2):434–45.
- Zai, Laila J. and Jean R. Wrathall. 2005. "Cell Proliferation and Replacement Following Contusive Spinal Cord Injury." *Glia* 50(3):247–57.
- Zai, Laila J., Soonmoon Yoo, and Jean R. Wrathall. 2005. "Increased Growth Factor Expression and Cell Proliferation after Contusive Spinal Cord Injury." *Brain Research* 1052(2):147–55.
- Zatorre, Robert J., R. Douglas Fields, and Heidi Johansen-Berg. 2012. "Plasticity in Gray and White: Neuroimaging Changes in Brain Structure during Learning." *Nature Neuroscience* 15(4):528–36.
- Zhang, Jiangyang, Melina Jones, Cynthia A. DeBoy, Daniel S. Reich, Jonathan A. D. Farrell, Paul N. Hoffman, John W. Griffin, Kazim A. Sheikh, Michael I. Miller, Susumu Mori, and Peter A. Calabresi. 2009. "Diffusion Tensor Magnetic Resonance Imaging of Wallerian Degeneration in Rat Spinal

Cord after Dorsal Root Axotomy." *The Journal of Neuroscience : The Official Journal of the Society for Neuroscience* 29(10):3160–71.

Ziegler, Gabriel, Robert Dahnke, and Christian Gaser. 2012. "Models of the Aging Brain Structure and Individual Decline." *Frontiers in Neuroinformatics* 6(March):1–16.

Acknowledgments

This Thesis would not have been possible without the guidance and the support of several people around me. Firstly, I would like to thank my supervisor Patrick Freund for the continuous support, for his patience, motivation, and for guiding me through the projects. His desire to help patients inspired me. Patrick involved me in several exciting projects, in which I could learn and grow professionally.

Besides my advisor, I would like to thank the rest of the committee members especially Prof. Dr. Nicole Wenderoth, Prof. Dr. Dominik R. Bach, Prof. Dr. Armin Curt and Prof. Dr. Daniel Kiper; for their insightful comments and for the hard questions which incited me to widen my knowledge from various perspectives.

I would like to thank our collaborators such as John Ashburner, Yaël Balbastre, Claudia Blaiotta from the University College London. They were always very helpful in providing the right comment and tips to overcome technical implementations' problems. Thanks to Martina Callaghan for the great feedbacks and for always answering my questions.

I wish to express my gratitude to Gabriel Ziegler, who helped me in the analysis of longitudinal data and for the technical support.

A special thanks goes to Dr. Maryam Seif and Dr. Pruthvi Kyathanahally for giving the encouragement, useful advice and sharing insightful suggestions for my personal and professional development. I thank everyone in the Neuroimaging group: Gergely David, Eve Huber, Dario Pfyffer, Kevin Vallotton, Tim Emmenegger, Johanna Vannesjö, Sanne Kikkert and Patrick Grabher; for the stimulating discussions, for the sleepless nights before ISMRM deadlines, and for all the fun we spent together. They are great colleagues and friends. I really enjoyed working with them. I also thank my students, Sakana Jeyaraj and Mia Meyer for their support and help.

I would also like to say a heartfelt thank you to my Mum, Dad, Brother and Sister for always believing in me, supporting me in general and for encouraging me to follow my dreams.

Finally, I would like to thank my loved husband, Vincenzo, who was always present and supported me with his help and laughs. He gave me encouragement and motivation to accomplish the personal and professional goals.

Curriculum vitae

Michela Azzarito

Date of birth: 30th November 1987
Nationality: Italy
Address: Strübiweg 2B, 5600, Ammerswil AG
E-mail: michela.azzarito@yahoo.it



Research interest

- Application of novel machine learning techniques to improve diagnosis, therapy and prognosis
- Algorithm implementation and software development for medical applications
- Data analysis and modelling
- Signal and Image processing (i.e. computer vision, deep learning)
- Development of technical tools for medical applications

Education

- 06/2016 – 06/2020 PhD degree: **Doctor of sciences of ETH Zürich**
ETH Zurich, Zurich, Switzerland
Thesis: Development of Image Processing Tools for the Simultaneous Analysis of Brain and Spinal Cord Multi-Parametric Maps: implication for Spinal Cord Injury
- 03/2013 – 10/2013 **State Examination:** Exam for the qualification to the profession of Engineer
This examination (or Habilitation) allows the free exercise of the engineering profession
- 11/2010 – 03/2013 Master degree (MSc): **Biomedical Engineering**,
Turin Polytechnic, Italy
Thesis: Biomechanical Device for Rehabilitation in cardiovascular Paraplegics
Grade: **110/110** (top grade)
- 11/2007 - 10/2010 Bachelor degree: **Informatics and Biomedical Engineering**
"Magna Graecia" University (Italy)
Thesis: Implementation of Algorithms for Ulcers' Detection and Classifications
Grade: **110/110 with honors** (summa cum laude)
- 09/2002 - 07/2007 **High school leaving qualification in scientific studies**
With focus in languages (French and English) –CZ (Italy)
grade: **100/100** (top grade)

Work Experience

- 06/2016-06/2020 Research Assistant: MRI investigation of trauma induced structural changes in the brain and spinal cord
Balgrist University Hospital (Spinal Cord Injury Center) and ETH Zurich, Switzerland
- software development for the simultaneous analysis of brain and spinal cord MRI data
 - application of novel statistical and machine learning approaches to MRI data
 - motion correction and coregistration of multiple MRI data
 - image analysis and extraction of valuable multimodal biomarker for clinical practice
 - pre-processing pipeline development for cross-sectional and longitudinal quantitative MRI data

- designing, running and interpreting MRI data from healthy controls and spinal cord injury patients
 - presenting findings and developments at international conferences (ISMRR)
- 12/2014 – 02/2016 Research Assistant: investigation of action potential propagation in cardiac tissue under mechanical deformation
University of Bern, Switzerland
- computational modelling of cardiac electrophysiology and mechanics, i.e. implementation of the Luo-Rudy model for cardiac cells (in a cell, in 1D and 2D)
 - realization of flexible and stretchable micro-electrode arrays (MEAs) (in collaboration with the EPFL Lausanne)
 - experimental investigation of cardiac cells, i.e. extraction and culture of embryo cardiac cells on micro-electrode arrays (MEAs)
 - cell image analysis and extraction of valuable measurements
 - acquisition and processing of EMG signals
- 12/2013 - 08/2014 Postgraduate Internship: Video analysis for medical diagnostics
Novartis Pharma Basel, Switzerland
- quality check, i.e. identification of bad data and propose better values
 - implementation of a user interface for checking and fixing acquired data
 - video analysis (i.e. segmentation, motion tracking) and extraction of valuable clinical parameters
 - help clinicians in acquiring data and teach them the correct use of the tool
- 09/2012 - 03/2013 Internship during the master thesis in the Turin Polytechnic, Italy
- testing an Intermittent Pneumatic Compression (IPC) device for lower limb rehabilitation, i.e. using test bench for pressure, manometers, sensors, calibrators etc.
 - signal acquisition from the IPC device (Labview and Matlab to record and analyse signals)
 - computational modelling of the prototype to investigate better functionality
- 02/2011 - 02/2013 Part time job during the studies in the Turin Polytechnic, Italy
- management of computers and printers
 - IT support during the lessons
- 04/2010 - 10/2010 Internship e “Magna Graecia” University of Catanzaro, Italy
- implementation of an algorithm to recognize skin ulcers (image processing)
 - provide clinical measurements (i.e. wound area, stage classification etc)
 - implementation of a user interface for clinical trials

Skills

- IT skills Scripting: Matlab (SPM, image processing toolbox, Simulink, OOP), Python (i.e. pandas, numpy, sklearn, TensorFlow, PyTorch, Keras), Java, C #, C++ languages,
OS: Windows, Linux and bash scripts
CADs: Rhinoceros, AutoCAD,
other programs: Labview, Ansys, Adobe Illustrator, LaTeX, SQL, Github
Statistics tools: R-studio and STATA
- Language(s) Italian: Mother tongue
English: business fluent (IELTS’ qualification)
German: business fluent
French: basic

Publication list

Simultaneous analysis of brain and spinal cord multi-parametric maps based on SPM framework (under review)

Microstructural signature of neuropathic pain across the neuraxis after spinal cord injury (under review)

The interplay between corticomotor system and hippocampus circuit changes during procedural learning (in preparation)

Azzarito Michela, Maryam Seif, Sreenath Kyathanahally, Armin Curt, and Patrick Freund. 2020. "Tracking the Neurodegenerative Gradient after Spinal Cord Injury." *NeuroImage. Clinical* 26(February):102221.

Buccarello, A., **M. Azzarito**, F. Michoud, S. P. Lacour, and J. P. Kucera. 2018. "Uniaxial Strain of Cultured Mouse and Rat Cardiomyocyte Strands Slows Conduction More When Its Axis Is Parallel to Impulse Propagation than When It Is Perpendicular." *Acta Physiologica (Oxford, England)* 223(1):e13026.

Kucera, Jan P., Yann Prudat, Irene C. Marcu, **Michela Azzarito**, and Nina D. Ullrich. 2015. "Slow Conduction in Mixed Cultured Strands of Primary Ventricular Cells and Stem Cell-Derived Cardiomyocytes." *Frontiers in Cell and Developmental Biology* 3(SEP):1–13.

Kontschieder, Peter, Jonas F. Dorn, Cecily Morrison, Robert Corish, Darko Zikic, Abigail Sellen, Marcus D'Souza, Christian P. Kamm, Jessica Burggraaff, Prejaas Tewarie, Thomas Vogel, **Michela Azzarito**, Ben Glocker, Peter Chin, Frank Dahlke, Chris Polman, Ludwig Kappos, Bernard Uitdehaag, and Antonio Criminisi. 2014. "Quantifying Progression of Multiple Sclerosis via Classification of Depth Videos." *Medical Image Computing and Computer-Assisted Intervention : MICCAI ... International Conference on Medical Image Computing and Computer-Assisted Intervention* 17(Pt 2):429–37.